Contribution to optical wireless multi-stable micro-actuation

Xingxing Liu

▶ **To cite this version:**

Xingxing Liu. Contribution to optical wireless multi-stable micro-actuation. Mechanics [physics.med-ph]. Université de Technologie de Compiègne, 2015. English. NNT : 2015COMP2214 . tel-01301379

HAL Id: tel-01301379

https://theses.hal.science/tel-01301379

Submitted on 12 Apr 2016

HAL is a multi-disciplinary open access archive for the deposit and dissemination of scientific research documents, whether they are published or not. The documents may come from teaching and research institutions in France or abroad, or from public or private research centers.

L'archive ouverte pluridisciplinaire **HAL**, est destinée au dépôt et à la diffusion de documents scientifiques de niveau recherche, publiés ou non, émanant des établissements d'enseignement et de recherche français ou étrangers, des laboratoires publics ou privés.

Par **Xingxing LIU**

Contribution to optical wireless multi-stable micro-actuation

Thèse présentée pour l'obtention du grade de Docteur de l'UTC

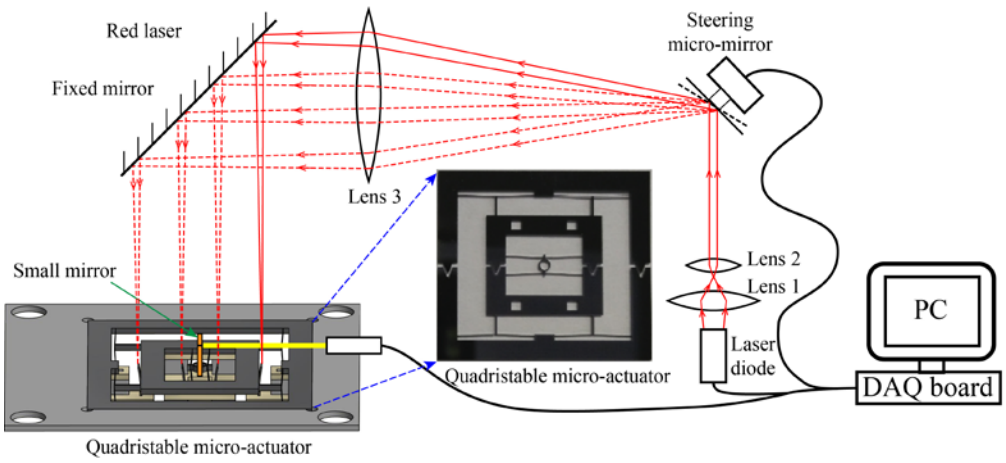

Soutenue le 07 octobre 2015
Spécialité : Advanced Mechanics

D2214

THÈSE
Présentée pour obtenir le grade de
DOCTEUR
de
UNIVERSITÉ DE TECHNOLOGIE DE COMPIÈGNE
Spécialité : Mécanique Avancée
par
Xingxing LIU

Contribution au Micro-actionnement Multi-stable Piloté par Radiations Optiques

Soutenance prévisionnelle le 7 Octobre 2015 devant le jury composé de :

Stéphane Régnier
Professeur à l'Université Pierre et Marie Curie, Paris (Rapporteur)
Fabien Formosa
Maître de Conférences-HDR à l'Université de Savoie Polytech'Savoie, Annecy (Rapporteur)
Elie Lefeuvre
Professeur à l'Université Paris-Sud – Institut D'Electronique Fondamentale, Orsay (Examinateur)
Arnaud Hubert
Professeur à l'Université de Technologie de Compiègne, Compiègne (Examinateur)
Frédéric Lamarque
Professeur à l'Université de Technologie de Compiègne, Compiègne (Directeur de Thèse)
Emmanuel Doré
Maître de Conférence à l'Université de Technologie de Compiègne, Compiègne (Directeur de Thèse)

Laboratoire Roberval, UMR 7337, UTC

THESIS
Submitted in partial fulfilment of the degree of
DOCTOR
in
UNIVERSITÉ DE TECHNOLOGIE DE COMPIÈGNE
Specialty: Advanced Mechanics
by
Xingxing LIU

Contribution to Optical Wireless Multi-stable Micro-actuation

Defense predicted on the 7th of October 2015 in front of the following jury:

Stéphane Régnier
Professor at the Université Pierre et Marie Curie, Paris (Reviewer)
Fabien Formosa
Maître de Conférences-HDR at the Université de Savoie Polytech'Savoie, Annecy (Reviewer)
Elie Lefeuvre
Professor at the Université Paris-Sud – Institut D'Electronique Fondamentale, Orsay (Examiner)
Arnaud Hubert
Professor at the Université de Technologie de Compiègne, Compiègne (Examiner)
Frédéric Lamarque
Professor at the Université de Technologie de Compiègne, Compiègne (Director of Thesis)
Emmanuel Doré
Maître de Conférences at the Université de Technologie de Compiègne, Compiègne (Director of Thesis)

Laboratory Roberval, UMR 7337, UTC

Acknowledgement

There are a number of people without whom this thesis might not have been written, and to whom I am greatly indebted.

This study was conducted in the « Laboratoire Roberval, UMR 7337 de l'Université de Technologie de Compiègne ». I would like to gratefully acknowledge the support and guidance provided by my PhD supervisors Pr. Frédéric LAMARQUE (Professeur des Universités) and Mr. Emmanuel Doré (Maître de Conférences) during the course of this PhD. Their patient explanations, help and co-operation were the keys to the successful completion of this research work. I am also thankful for their tireless efforts during the review of the thesis manuscripts. Working with them was a learning experience and one of the main gains of this PhD program. Their help on both the professional and personal fronts was invaluable. I would like to thank all the members of the jury (Pr. Stéphane Régnier, Dr. Fabien Formosa, Pr. Elie Lefeuvre and Pr. Arnaud Hubert) for my thesis. Thanks for your valuable time and advices.

I would also like to thank Dr. Muneeb Khan, Pr. Christine PRELLE, Dr. Emmanuel Doré, Dr. Jérôme Favergeon, Dr. Hani Al Hajjar, Dr. Laurent PETIT, Dr. Erwan DUPONT, Mr. Phillipe Pouille and all the other staff members of Laboratoire Roberval to provide me their valuable support during this research work. I would like to especially thank the team of « Laboratoire de Physique de la Matière Condensée, de l'Université de Picardie Jules Verne » to work with us on the deposition of SiO_2 layer for shape memory alloy elements.

My time at UTC was made enjoyable for the most part due to all my friends and colleagues (Yingfan HOU, Jing XU, Zaina El Rawashdeh, Neha ARORA, Zineb Yanha, Saadallah El Darazi …). I thank them for their moral support and also for the nice and cheerful office environment.

I am forever indebted to my mother and my father for their belief and confidence in me.

I owe my deepest gratitude to my wife, Jia, for being a pillar of support during all the hardships and difficulties that we encountered during this journey. I thank her for bearing with me in times of stress and despair. Without her constant support and encouragement this would not been possible. Finally, I thank my daughter Yuchen.

Lastly, I gratefully acknowledge my funding agency "China Scholarship Council".

Table of Contents

List of Figures

List of Tables

Introduction

At present, Micro electro mechanical system (MEMS) technology trend is reshaping modern micro-devices to achieve smaller dimensions. As a consequence, the integration of power supply modules or external sensors (e.g., position sensor, etc.) in these micro-devices becomes more difficult. Problems are arising with the transfer of energy and control when micro-systems are considered. In case of design with a group of micro-actuators that are distributed overs a surface to produce collective actuation, these problems are much crucial. Therefore, it is necessary to design some new concepts of actuation that favorize the integration of several micro-actuators into a smart surface. One of the solutions to solve these problems is to utilize digital actuators with contactless energy transfer methods. Because digital actuators can be controlled by sensorless method (open loop) and using wireless actuation can avoid the integration of power supply unit.

According to the output continuity, actuators are categorized by analog actuators and digital actuators. For an analog actuator, the output is smooth, every position within its output range is theoretically attainable. Thus, the analog actuators can have high output resolution. However, it is necessary to use closed-loop control methods with external position sensors to have precise output. Different from analog actuators, a digital actuator has several stable output positions that can be controlled using open-loop method, thus, avoiding the need to integrate additional sensors for position control. Furthermore, in these multistable actuators, the stable positions are self-maintained without the need of external input energy, which allow them to only consume energy during the switching cycle (no stand by power consumption). This results in low level power consumption which makes them suitable in special scenarios such as applications in which actuators are not frequently actuated. So, to economize the power, this feature of the digital actuators can reduce power dependence of the micro devices and it has also led to the possibility of being actuated by weak but wireless energy transfer approaches (e.g., laser and radio frequency electromagnetic waves) which can maximize the degrees of freedom of micro-actuators.

The digital actuators or multistable actuators are based on multistable mechanisms. According to the method used to maintain the stable position, they can be divided into multistable mechanisms with locking mechanisms and compliant multistable mechanisms. The locking mechanism could be additional locking actuators (active locking) or multiple energy field domains (passive locking), such as, gravity field and magnetic field. However, all the locking mechanisms will increase the complexity of the system which will have adverse effect on the minimization of the devices. On the contrary, the multiple stable positions of compliant mechanisms are realized by elastic deformation of the flexible part. As a consequence, the systems of compliant multistable mechanisms are simple. Among the compliant mechanisms, bistable buckled beam is one of the most commonly used mechanisms to form the multistable mechanisms. The bistable buckled beams can be divided into three groups: pre-compressed beams, pre-stressed beams and pre-shaped beams. The pre-compressed beams and pre-stressed beams have the advantages of symmetrical output force. However, the pre-load operation for pre-compressed beams and pre-stress process of pre-stressed beams are difficult to control. The pre-shaped beams need no pre-load or pre-stress, but their output force is asymmetrical. Furthermore, there is a geometrical limit for the pre-shaped beams, which will make the strokes of pre-shaped beams bigger than the pre-compressed and pre-stressed beam that have the same length and thickness.

For the wireless actuation method, electromagnetic system, inductive coupling and capacitive coupling are the most commonly used approaches. However, they all have common drawback: the energy transfer efficiency decreases rapidly with the increasing of distance between the energy emitter and

receiver. The used of radio frequency electromagnetic waves is an approach that can realize a long distance actuation, but additional receiving circuits are necessary, which will increase the complexity of the system. Another long distance wireless actuation approach is based on laser heated shape memory alloy (SMA) elements or more generally, active elements having a thermal sensitivity. It can realize the long distance actuation without extra circuits. Furthermore, laser beam can be easily oriented by optical systems and the SMA/thermal elements can provide a relative big actuation force.

Therefore, the main objective of this work is to design a bistable buckled beams based multistable mechanism which has easier pre-load operation and a symmetrical output force. At the same time a wireless actuation method will be proposed based on laser heated SMA elements, so that the designed multistable mechanism can be wirelessly actuated. These two main directions should make easier the design of new kind of smart surfaces composed of an array of distributed micro-actuators.

There will be five chapters in this study. The first chapter is the state of art. Then in the second chapter, antagonistic pre-shaped double beams based bistable mechanism will be proposed. The proposed bistable mechanism will be compared with other existing ones and the advantages will be discussed. The design, fabrication and test of a quadristable meso-scaled prototype using laser cutting machine will be described. Then, the designed prototype will be fabricated at the micro-scale on silicon wafer using deep reactive ion etching technique. In the third chapter, the wireless actuation method using laser heated SMA elements will be discussed. The artificial "two-way" memory effect using deposited SiO_2 on SMA as biasing spring will be described. Furthermore, the two way memory SMA element will be used to realize the wireless actuation of the quadristable micro-actuator. The test results will be analyzed and discussed in detail. However, the stroke of the quadristable micro-actuator is still big, therefore, the integration of a stroke reducing module is mandatory to get micrometric even submicrometric output resolution. So, in the fourth chapter, the design and verification of a bistable actuator including a stroke reducing structure will be presented. To minimize the output stroke more and generate more stable output positions, a multistable nano-actuator which has four combined bistable modules will be discussed. It is capable of generate 16 different stable positions. At the end, it is the conclusion and perspectives.

The work presented in this thesis has already been published in one international journal and has been presented in 3 international conferences. The detail of published and presented papers can be found in Annex I.

Résumé

Cette thèse traite le sujet du micro-actionnement multistable employant des radiations optiques pour atteindre les différentes positions offertes par le micro-actionneur. Dans le cadre des travaux réalisés, un mécanisme bistable reposant sur un principe de doubles poutres préformées situées en position antagoniste est proposé, et, sur cette brique élémentaire, un micro-actionneur quadristable a été conçu. Afin de valider le principe de fonctionnement de micro-actionneur, des procédés de fabrication Laser (sur le matériau « médium - MDF») puis DRIE (sur un wafer SOI de silicium) ont été utilisés. Sur le prototype en silicium, permettant une réduction des courses du rang interne et du rang externe du micro-actionneur, celles-ci ont été fixées à 300 µm et 200 µm respectivement. L'actionnement à distance de ce micro-actionneur a été prouvé en utilisant le chauffage laser d'un élément actif en Nitinol structuré par un dépôt de SiO_2, ceci générant un effet « deux sens » de l'élément actif permettant d'annuler la charge sur les poutres du micro-actionneur une fois celui-ci déclenché puis en position stable. L'utilisation d'un banc expérimental incluant une membrane MEMS de balayage laser a permis de démontrer la quadristabilité du micro-actionneur sur 90 000 cycles. Afin de réduire davantage la course de ce micro-actionneur, des concepts de dispositifs de réduction de course ont été développés pour démontrer, à partir de prototypes fabriqué en MDF par usinage laser, la capacité à atteindre une course de 1 µm. Enfin, à la suite de ces travaux de réduction de course, un concept de nano-actionneur multistable a été proposé. Ce nano-actionneur est composé de quatre modules bistables liés et disposés en parallèle pour offrir 16 positions discrètes sur une course rectiligne. Les simulations de cet actionneur montrent la possibilité d'atteindre les 15 positions espacées de 10 nm sur une course de 150 nm.

Le travail présenté dans cette thèse a déjà été publié dans une revue internationale et a été présenté en 3 conférences internationales. Le détail des documents publiés ou présentés se trouvent à l'annexe I.

Chapter I

State of the Art

1 Introduction

Due to the requirement of minimization for micro-actuators, the dimensions of micro-actuators become smaller. As a consequence, the integration of sensors and power supply units becomes more difficult. These problems are even more crucial for the applications of smart surfaces which need to integrate an actuators' array on a plane surface and actuate these actuators to complete certain tasks, e.g., transporting objects on the top of the smart surface. One solution for these problems is to use digital actuators [PETI 14, MOBE 12] with wireless actuation methods [ZAID 11, ZAID 12, BYUN 11, HYUN 14, OWEN 06, KHAN 12, STRA 12, IMBO 14, BOEI 08, KARU 10, BAGL 02, ALI 10, ALI 11].

As shown in figure 1 – 1, a digital actuator is the actuator with discrete output positions. Different from analog actuators which have continuous output, digital actuators only have several stable output positions. But, each of the stable position is self-maintained which makes it possible to be controlled in sensorless way (open loop method). Therefore, the exploitation of digital actuators can solve the sensors' integration problem. For the power supply issue, wireless energy transfer and actuation methods can provide power for the actuators without physical contacts, which can maximize the degrees of freedom of the actuators, especially for the micro-actuators.

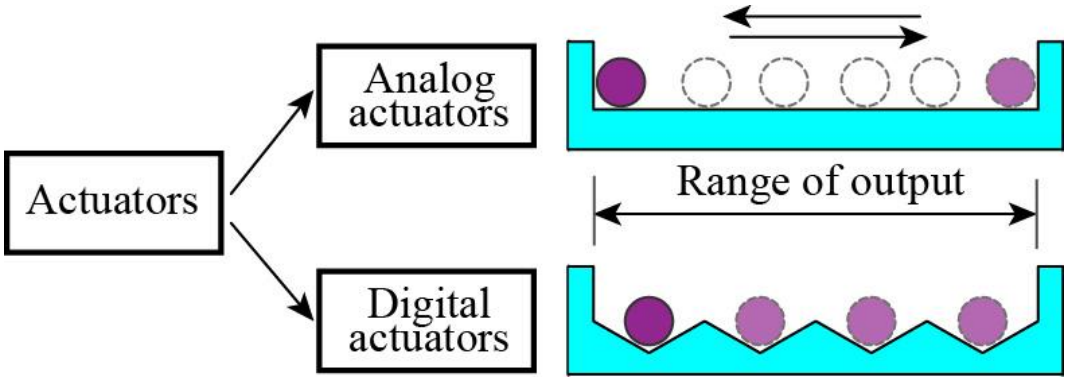

Figure 1- 1. Analog actuator and digital actuator.

Since the main task of this study is to design a digital micro-actuator (or multistable micro-actuator) actuated by wireless methods and this digital actuator is expected to be used for the smart surface application which is based on the actuators' array, the following parts of this chapter will focus on the surveying of literatures related to smart surfaces, multistable actuators and wireless actuation methods.

2 State of the art on the "Smart surfaces"

Here, smart surface means the surface formed by actuators' array for micro-conveyance purpose. By proper control of these actuators, the collective actuation can realize complex tasks, even if the surface is formed by actuators with only one degree of freedom. If the smart surface is formed by analog actuators, we call it smart surface with analog control. Likewise, if it is based on digital actuators, we call it smart surface with digital control.

2.1 Smart surface with analog control

The basic actuators in smart surface with analog control are analog actuators, due to the characteristic of their continuous stroke. The group behavior of the actuators' array is also continuous and adjustable.

In [BOHR 94a, BOHR 94b and BOHR 96], a smart surface with analog control was reported. The smart surface was based on an analog actuator shown in figure 1 - 2a. It has two electrodes and a grid which is suspended by a torsional rod. When the electrodes are charged, the static electric force makes the grid rotate.

When the rod is shifted from the central position of the grid, the output is biased, i.e., the output is not symmetrical. As a consequence, the biased output tends to move more in one direction than the other. Using this characteristic and distributing the actuators with different biased direction on a surface, a smart surface with analog control and three degrees of freedom can be formed. This design was fabricated on single crystal silicon wafer.

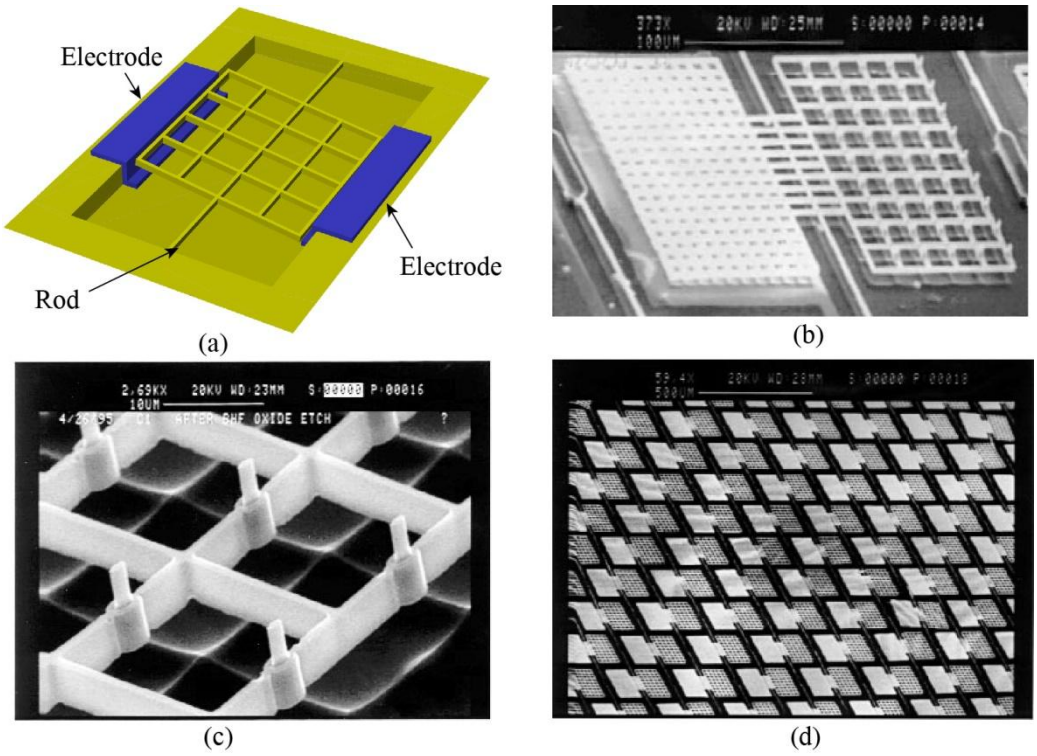

Figure 1- 2. A smart surface with analog control: (a) CAD model of a single analog micro-actuator (electrodes and torsional rod suspended grid); (b) SEM photograph of a single analog micro-actuator fabricated on single crystal silicon wafer; (c) A zoomed of a the suspended grid; (d) SEM photograph of the smart surface formed by the analog actuator shown in (b) [BOHR 94a, BOHR 94b and BOHR 96].

A scanning electron microscope (SEM) photo of a single actuator is shown in figure 1 - 2b and a zoomed view of the grid is shown in figure 1 - 2c. We can see that there are small tips onto the grid which can improve the contact between the grid and the object on the smart surface. Part of the fabricated actuator array is shown in figure 1 - 2d. In this smart surface design, the basic actuator is analog actuator, therefore, the output amplitude of a single actuator is not a discrete value and it depends on the voltage applied between the grid and the electrodes. Furthermore, it is necessary to provide the power supply when the actuated position of the actuator needs to be held. Therefore, large amount of stand by energy will be consumed and it is difficult to be actuated by wireless energy transfer methods which have low efficiency.

Besides the application for transporting objects, the smart surface can also be used in the application of tactile display. In [TALB 06], a smart surface formed by an electromagnetic actuator array (4 × 4) is reported for the application of tactile display interface (figure 1 – 3a). The discrete actuators can apply discrete vibrational excitations on the skin, which can be used in the entertainment industry (e.g. computer paddles), the medical world (e.g. virtual surgery training, remote surgery), sensory

substitution systems (e.g. displays for the blind persons), e-commerce (e.g. remote sensing of a material via the internet), the research world (e.g. study of mechanoreceptors), and many more [TALB 06]. As shown in figure 1 – 3a, each actuator is a cantilever with a permanent magnet installed on the tip. A coil is configured beneath the tip of the cantilever which can produce an electromagnetic field that can be used to attract or repulse the permanent magnet. Therefore, this is also a smart surface with analog control. As a consequence, stand-by energy consuming is necessary to hold a certain actuation pattern. Another 4 × 4 actuator array used as the tactile display is presented in [ZOLT 12] (figure 1 - 3b). The actuators were operating on the principle of voice-coil actuators. It can be used in similar applications as described for the former smart surface presented in [TALB 06].

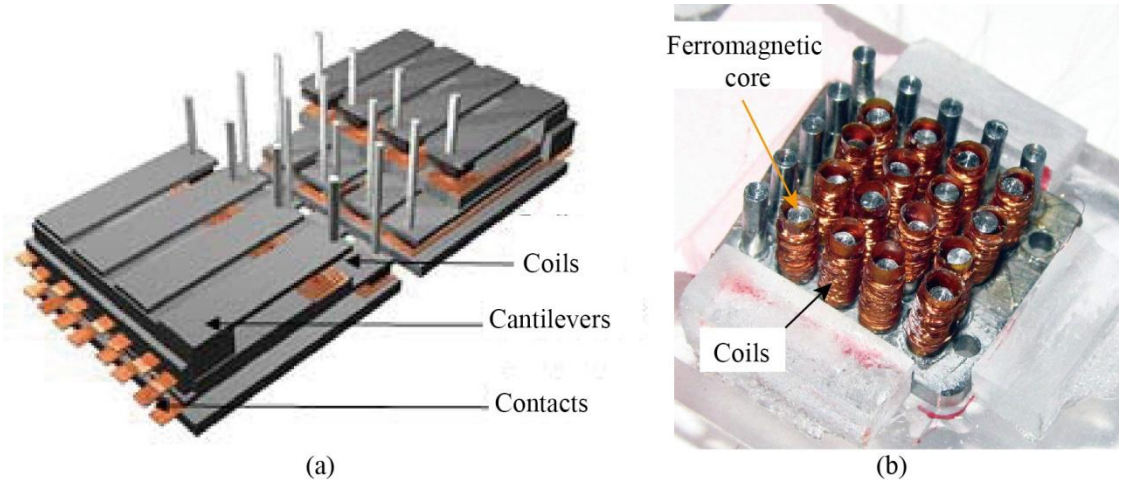

Figure 1- 3. (a) The general layout of an electromagnetic actuator array (4×4) for tactile display application [TALB 06]; (b) A wearable micro-actuator array (4×4) for 3-D virtual tactile displays [ZOLT 12].

There is a common point for the above described smart surfaces that they all have physical contacts between the surfaces and the objects. There is another group of smart surfaces which are using pneumatic force to transport or stimulating the objects, where there are no physical contacts between the surfaces and the objects. In [DELE 11], a smart surface based on pneumatic principle is reported (figure 1 – 4a and b). As it can be seen, there is an array of air flow outlets distributed in a plane surface. Some of the outlets are open all the time which are used to create an air cushion that can levitate the objects. The traction outlets, which are indicated as traction nozzle in figure 1 – 4b, are controlled by valves. When the traction nozzle is open, it can create a traction air-jet which will induce the air cushion to the attraction nozzle's location. As a consequence, the objects nearby can be attracted to the attraction nozzle's location. This attraction effect can be used to transport objects over the smart surface. Each attraction nozzle can be considered as valve controlled analog actuator. Therefore, this is also a smart surface with analog control. In the design, the shape and dimensions of the smart surface are fixed. Thus, the surface needs to be specially designed and fabricated for different installing spaces. In the aim of making it more adaptive, a smart surface operating on the same principle but based on smart blocks is proposed in [HABI 12] (figure 1 – 4c and d). The smart surface is separated into small and independent modules which are called smart blocks. Each smart block has both levitation outlets and attraction outlet. These smart blocks can be attached together to form a smart surface with different shapes. So it is more adaptive that the former design.

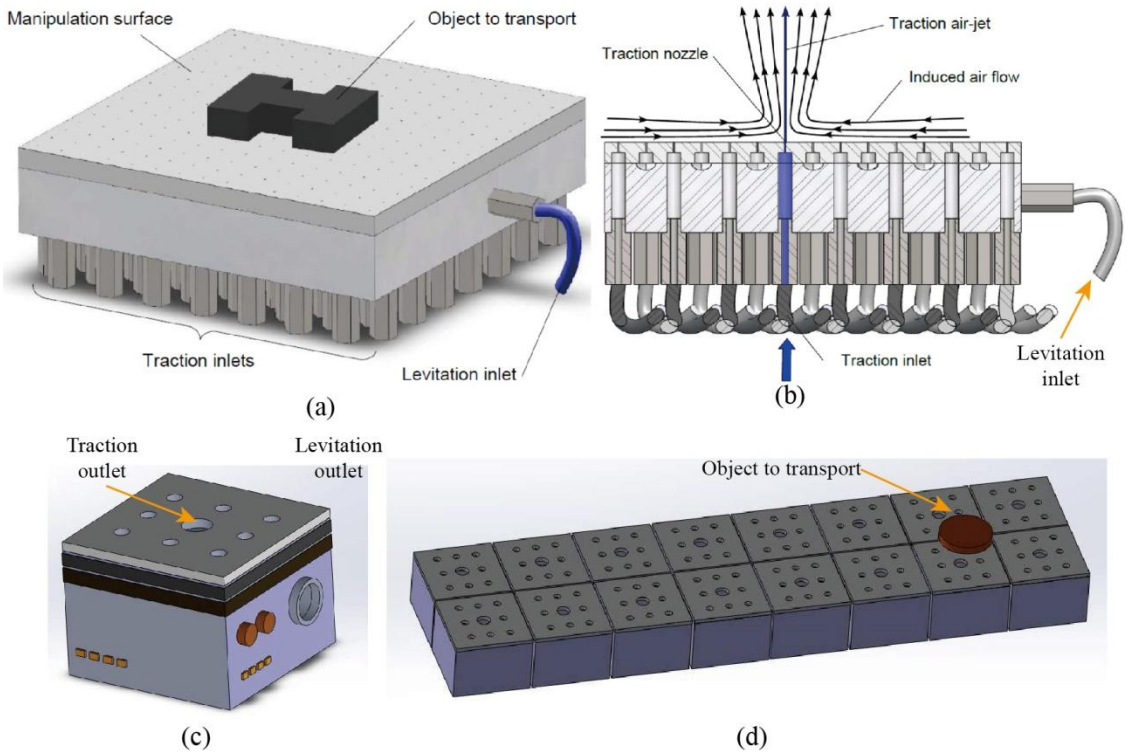

Figure 1- 4. (a) The global view (b) cross sectional view of the an induced air flow surface for contactless manipulation of objects [DELE 11]; (c) Schematic view of a smart block [HABI 12]; (d) Group of attached blocks making a bigger conveyance surface and an object over it [HABI 12].

Another smart surface design is reported in [FUKU 04, FUKU 06, MATI 10] (figure 1 - 5). Pneumatic force is also used to transport the objects. Its principle is different from the former described pneumatic smart surfaces. The micro-valves are directly integrated into the pneumatic modules. As shown in figure 1 – 5a, the micro-valve can be attracted by electrostatic force. When there is no electrostatic fore, it will generate a symmetrical air leakage which could be used to levitate the objects. When the micro-valve is attracted to one side, it can generate an asymmetrical air leakage which can be used to drive the objects. It is obvious that one module can only generate the driving force in one axis. Therefore, in order to form a smart surface with two degrees of freedom, there should be two groups of micro-valves oriented in two orthogonal directions and distributed properly onto the surface like it is shown in figure 1 – 5b.

Like the analog actuators, the smart surfaces with analog control need feedback sensors to realize the precise control, which will increase the complexity of the system and has adverse effect on the minimization of the devices. Moreover, the power consuming level is high due to the stand-by power consuming. In order to minimize and simplify the system, smart surfaces with digital control have attracted the attention of researchers due the characteristic that they can be controlled by sensorless methods at low power consuming level.

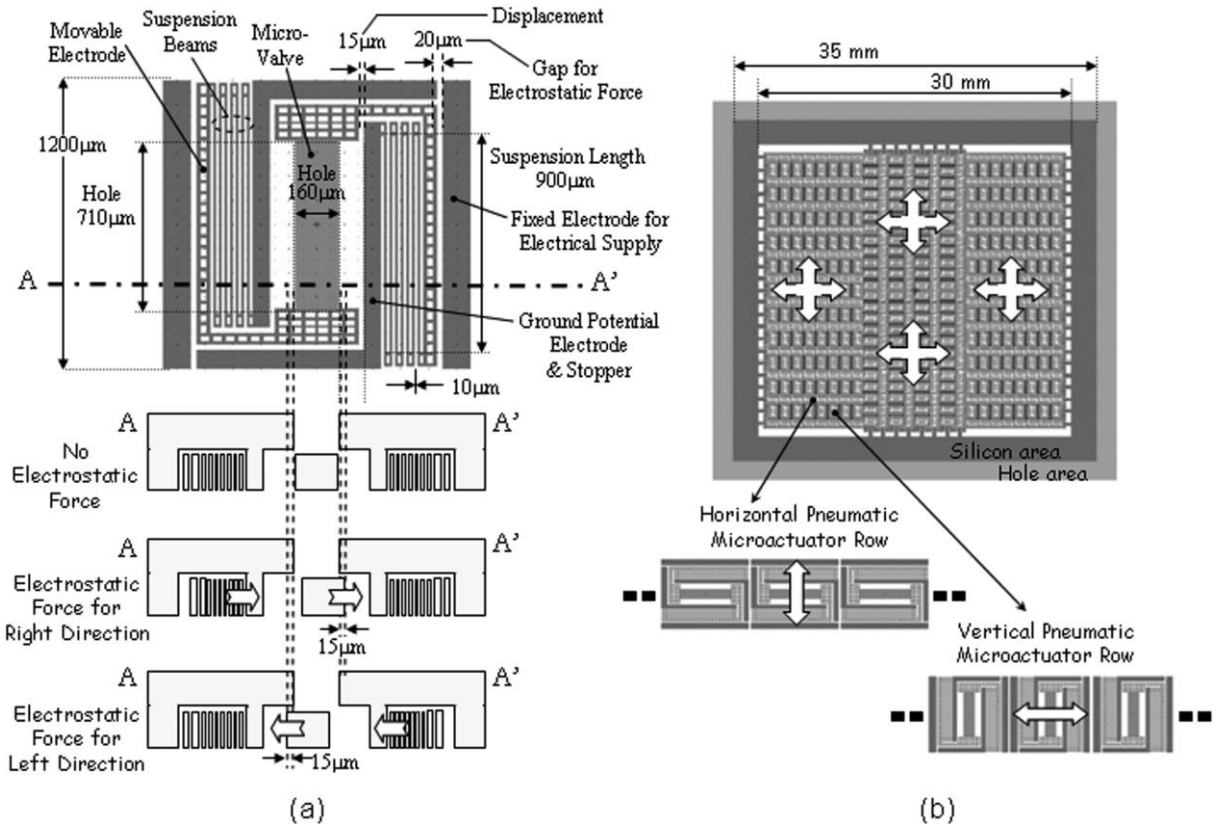

Figure 1- 5. (a) Mask design patterns and schematic diagram indicating the functions of the pneumatic micro-actuator in cross-section [FUKU 06]; (b) Mask design of pneumatic micro-actuator array for motion surface [FUKU 06].

2.2 Smart surface with digital control

As mentioned before, beside the smart surface with analog control, there is the smart surface with digital control. The actuator array is formed by digital actuators. Due to the characteristic of digital actuators, they could be actuated both independently and simultaneously with open loop method which can largely simplify the control system.

In [PETI 14], a smart surface with digital control was reported. Its actuators' array was formed by electromagnetic digital actuators with four discrete stable positions. The cross sectional view and top view of a single digital actuator's schematic are shown in figure 1 – 6a and b respectively. A single actuator was called elementary digital actuator (EDA). Each EDA has one mobile permanent magnet (MPM) and four fixed permanent magnets (FPMs). The movement of the MPM is confined into a square cavity. There are wires, configured in two orthogonal directions, placed under the MPM. Because the MPM and FPMs are magnetized in opposite directions, when there is no actuating current passing through the wires, the MPM will be pulled to one corner of the square cavity due to the magnetic attraction between MPM and FPMs. When some current passes through the wires under the MPM, due to the field interaction between the magnets and the wires, the MPM could be switched to another corner. The smart surface formed by a digital actuator array of 25 (5 × 5) EDAs is shown in figure 1 - 6c. These EDAs can be actuated independently or simultaneously and each EDA has two degrees of freedom. Hence, if a plate placed on the top of the smart surface covers at least 2 EDAs and control the EDAs properly, the collective actuation can produce complex movement with 3 degrees of freedom (two translations and one rotation). Moreover, due the characteristic of digital actuator, there is no stand-by power consumption and no need of the integration of sensors.

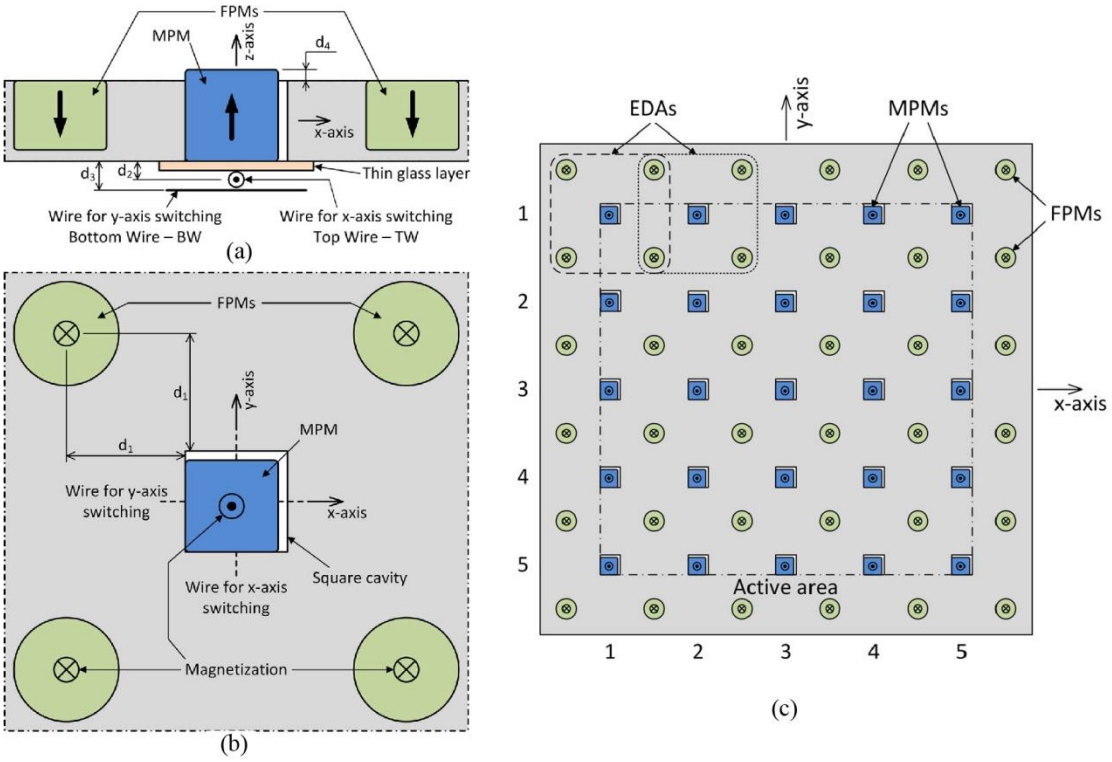

Figure 1- 6. A smart surface with digital control: (a) Cross sectional view and (b) top view of single digital actuator's schematic; (c) The schematic of a smart surface formed by actuator array of 25 (5 × 5) digital actuators [PETI 14].

In [MOBE 12], a reconfigurable smart surface based on block actuators is presented (figure 1 - 7). As it can be seen in figure 1 – 7a, these blocks can form smart surfaces with different shapes. A block is a cube with the dimension of 10 mm. It has three parts: the conveying surface, the upper magnet layer and the lower magnet layer. As shown in figure 1 – 7c and d, permanent magnets and electro-permanent magnets are installed in the magnet layers. The upper and lower magnet layers are oriented in two orthogonal directions. Therefore, each block has two degrees of freedom. The working principle is shown in figure 1 – 7e, it can be seen that by changing the polarized direction of electro-permanent magnets, the electro-permanent magnets in one block can be attracted or repulsed by the permanent magnets of the neighbor blocks, so that it can move along the lateral side of neighbor blocks which are fixed. Due to the characteristic of electro-permanent magnets, the positions of blocks are self-maintained. So, this is a smart surface with digital control which can be controlled by sensorless methods.

We can see that the smart surface with digital control has the advantages, such as able to be controlled by sensorless methods and low power consumption. These characteristics can facilitate the minimization and simplification of the system. Furthermore, it can reduce the power dependency of the system which makes it possible of being actuated by wireless methods which has lower power transfer efficiency. The smart surfaces with digital control are based on digital actuator arrays, so, in the following part, the research will be focused on digital actuators.

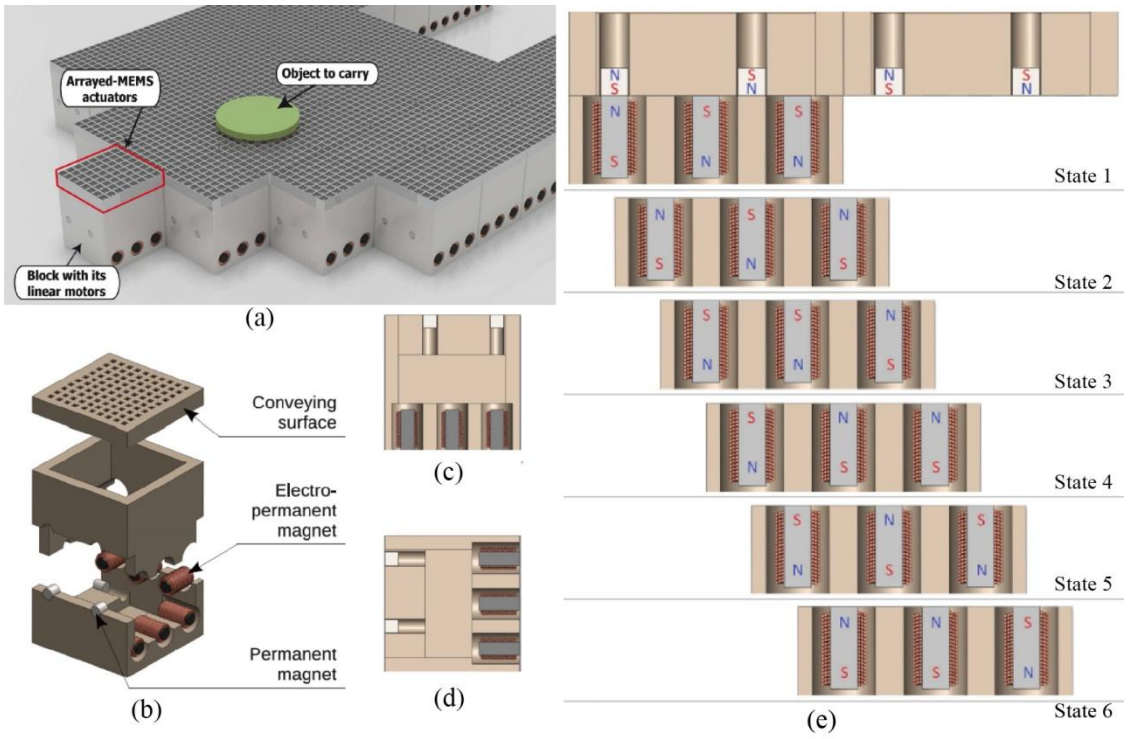

Figure 1- 7. (a) Example of using reconfigurable blocks for conveying objects [MOBE 12]; (b) Design of the block with the configuration of the electro-permanent and the neodymium magnets. The block is a 10mm cube and consists of two parts, an upper and a lower part, to make the final assembly easier [MOBE 12]; (c) Sectional view of the lower magnet layer [MOBE 12]; (d) Sectional view of the upper magnet layer [MOBE 12]; (e) State diagram of the linear motor showing the 6 different states of the EP magnets and their caused position in respect to the passive sides of two blocks. The magnetic poles are marked with S and N for South and North [MOBE 12].

3 Multistable micro-actuators

As mentioned in the introduction part, due the minimization of MEMS devices, problems, such as integration power unit and sensors without influencing the number of degrees of freedom and the autonomy, become more crucial, especially for the case of smart surface which has multiple micro-actuators. Therefore, we have to design some new concept which could be used without sensors (digital actuator or multistable actuators) and actuated by wireless method. Thus, in this part, we will do some study on multistable mechanism and wireless actuation methods.

3.1 Multistable Mechanisms

A multistable mechanism possesses multiple stable equilibrium positions within its range of motion [CHEN 10]. These stable positions are self maintained and no power supply is necessary to hold these positions, even when there are small disturbances. Multistable mechanisms can be roughly divided (by the number of stable positions) into two groups: bistable mechanisms with two stable positions and multistable mechanisms with more two stable positions, in which the bistable mechanisms are the basis of multistable mechanisms. Hereafter, bistable mechanism will be considered as a special multistable mechanism. Multistable mechanisms are widely employed in applications, such as switches, relays, valves, overload protection, digital robot and positioners [QIU 01, QIU 04, BART 12, PHAM 11, CHEN 08, CHAL 11, PETI 14].

The multistability can be achieved through using locking mechanisms or multiple energy domains (e.g., gravitational and magnetic fields). Another approach to multistability is compliant mechanism, whose

mobility is achieved through deformation of its flexible parts other than articulated joints only. The classification of multistable mechanisms is shown in figure 1 - 8.

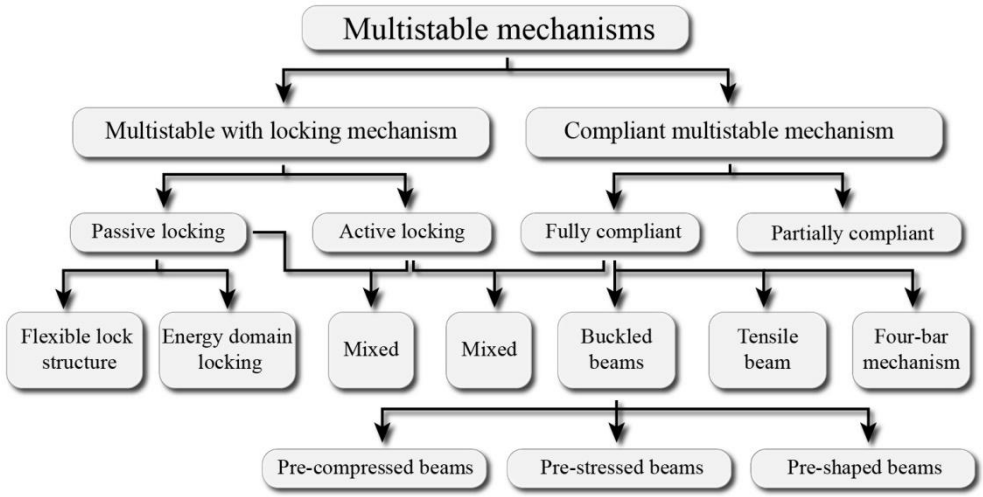

Figure 1- 8. Classification of multistable mechanisms.

The locking mechanisms can be divided into active and passive locking mechanism. The active mechanism needs additional locking and unlocking actuator to complete the locking and unlocking operation (figure 1 - 9a). During the operation energy is consumed to drive the locking and unlocking actuator. For the passive locking mechanism, the locking and unlocking operations are automatically completed when the mobile part passes the equilibrium point (Figure 1 - 9b) or reaches the stable positions (Figure 1 - 9c). The multistability of active locking mechanism is more robust, while the design of passive locking mechanism is simpler.

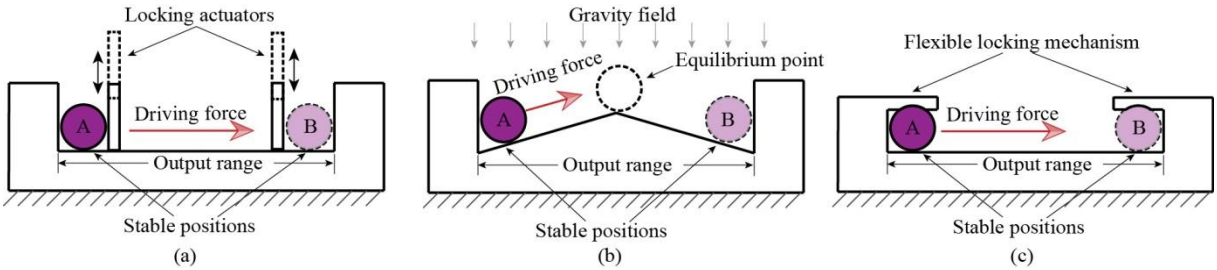

Figure 1- 9. Active (a) and passive (b), (c) locking mechanisms for bistable mechanisms: (a) Active locking mechanism with locking actuators; (b) Passive locking mechanism with gravity field or magnetic field; (c) Passive locking mechanism with flexible locking structure.

3.1.1 Multistable mechanisms with active locking mechanisms

An active multistable locking mechanism based on rank-and-tooth structure was reported in [SYMS 03, SYMS 05] (figure 1 - 10). The rank-and-tooth structure was locked and unlocked by electrothermal shape bimorph actuators. The locking mechanism is employed in the variable optical attenuator. The attenuator is fabricated in silicon by deep reactive etching (DRIE) using bonded silicon on insulator (SOI) wafer. Two electrothermal shape bimorph actuators (actuator A and actuator B) are integrated into the system. When actuator B is powered by current I_B, the rank part will be rotated in clockwise direction, then the tooth part could be driven by actuator A and move between different positions on the rank, finally the position will be locked when the rank recover to the locking position by cutting off the power supply of actuator B. In [UNAM 06, UNAM 13], a similar active multistable locking mechanism was demonstrated (figure 1 - 11). Electrothermal shape bimorph actuators and chevron actuator were utilized to drive the multistable latching mechanism.

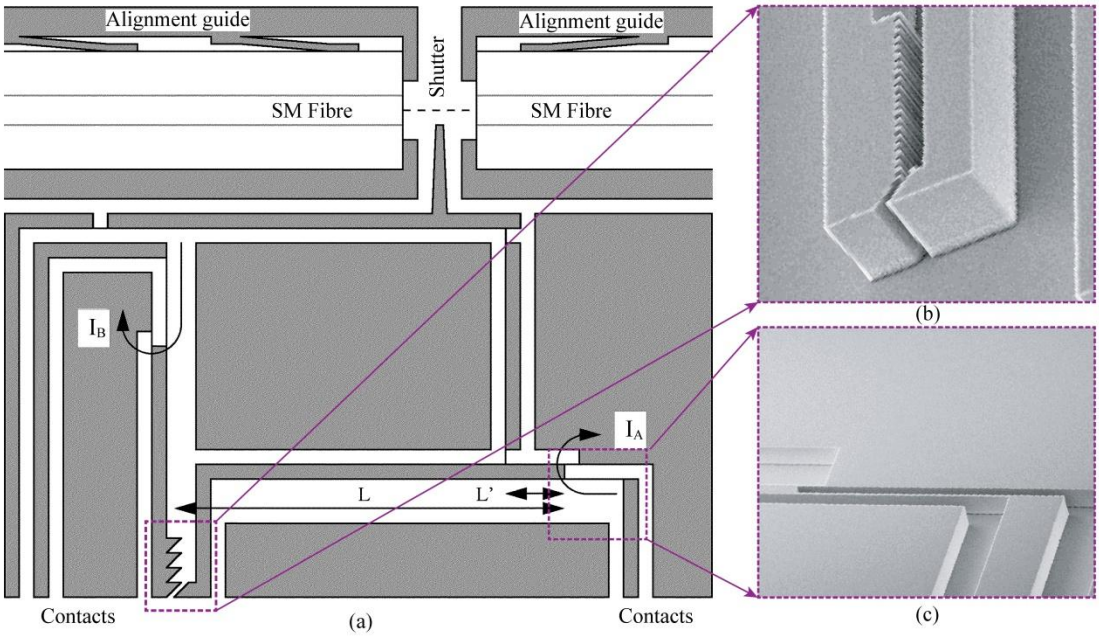

Figure 1- 10 A MEMS latching shutter-insertion variable optical attenuator (not to scale): (a) Layout of the optical attenuator; (b) SEM photograph of the rank-and tooth latching; (c) SEM photograph of the electrothermal bimorph actuator A [SYMS 03].

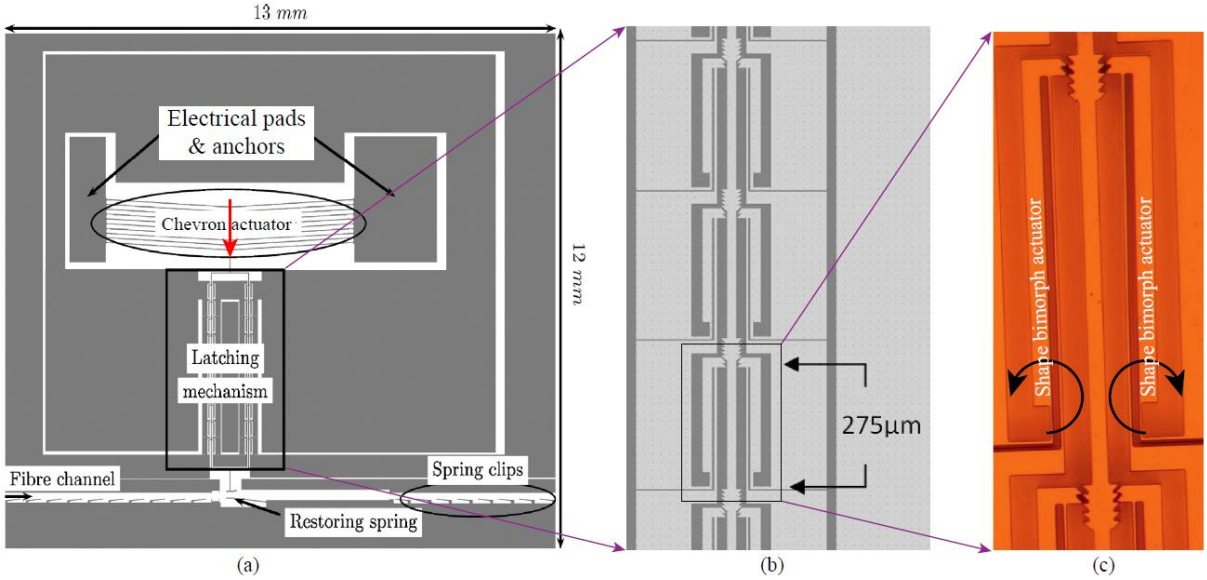

Figure 1- 11. MEMS device highlighting of Vernier latching mechanism: (a) Layout of the optical attenuator; (b) One branch of the latching mechanism; (c) One single latching mechanism [UNAM 06, UNAM 13].

3.1.2 Multistable mechanism with passive locking mechanisms

3.1.2.1 Locking with magnetic field.

In [PETI 14], a quadristable mechanism with the passive locking mechanism through magnetic field is reported. Four fixed permanent magnets with same magnetization directions were configured at outside of four corners of a square cavity to create four magnetic fields. One mobile permanent magnet with opposite magnetization direction was placed inside the square cavity (figure 1 - 12a). When the mobile permanent magnet is near one of the four corners and the magnetic attracting force created by the nearest fixed permanent magnet is big enough to overcome the force caused by the other three magnets and friction, the mobile permanent magnet would be attracted and locked to the nearest corner. This practical scenario could be abstracted to the potential energy model (figure 1 - 12b). There are two stable zones, which stand for the case when force generated by the nearest magnet is bigger than the force caused by

friction and other three magnets. Once the mobile magnet enters the stable zone, it is locked to the stable position. Between two stable zones, there is a unstable equilibrium zone, where the resultant force of friction and magnets is zero. Since the force between two magnets is monotonic to the distance between them, the unstable equilibrium zone is caused by friction. Therefore, it could be inferred that in the ideal condition, when there is no friction between the mobile permanent magnet and the thin glass layer placed at the bottom of it, the central lines would be the equilibrium lines and the cavity area will be divide into four parts. Once the mobile magnet passes the central line under driving Lorentz force, it will be attracted to the stable corner position. The potential energy model is shown in figure 1 - 12c.

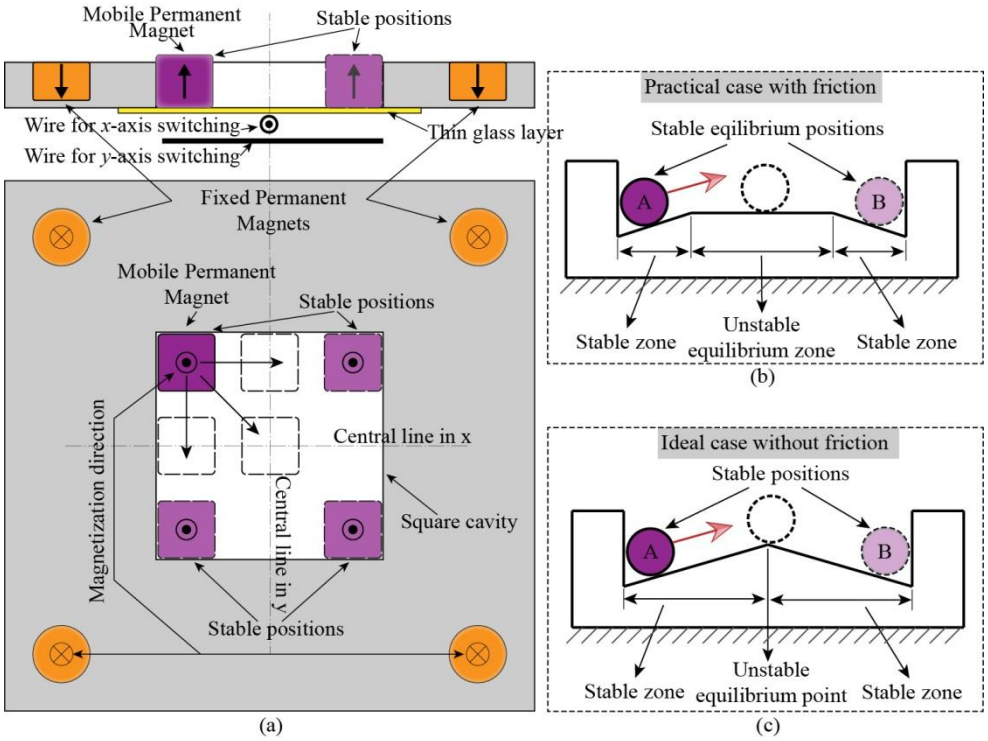

Figure 1- 12. Passive locking mechanism through magnetic field: (a) Schematic layout of the quadristable mechanism locking through magnetic field [PETI 14]; (b) Potential energy model of the magnetic locking mechanism in practical case; (c) Potential energy model for the magnetic locking mechanism in ideal case.

In [BART 12], a bistable micro-valve with magnetic latches was reported (figure 1 - 13). The bistable system consists two fixed soft magnetic structures and a centrally located movable hard magnetic structure that can be actuated in both directions.

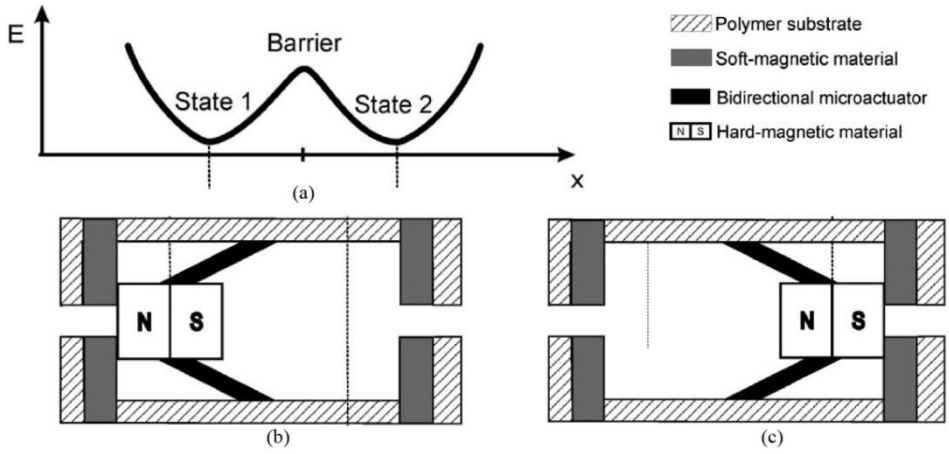

Figure 1- 13. (a) Schematic free energy-displacement characteristic of a bistable system. (b) Stable state 1 (c) stable state 2 of the bistable system consisting soft magnetic structures and a movable hard magnetic structure that can be driven by a shape memory alloy bidirectional micro-actuator. [BART 12]

3.1.2.2 Flexible locking structure.

In [CHEN 08, CHAL 11], a bistable module for micro-robots was designed using flexible locking mechanisms (figure 1 - 14). When actuation force, from thermal actuator, was applied on the central part of the bistable structure, the deformable beams were bended by the stop blocks to the mid side. Finally, the central part go through the gap defined by the two stop blocks and go to the other stable position. Similarly, the central part could come back by bending the deformable beams and go through the gap. Similarly, in [MAO 10] a micro-switch (bistable mechanism) is designed (figure 1 - 15), a metal contact pair was attached to two electrothermal bimorph actuators and they were partially overlapped. Between the two metal contact a gap was defined by a heighten block. When actuator A is powered, it will force the upper contact against the lower contact, then, due the deformation of the contact pair, the upper contact would snap to the low position beneath the lower contact. After the power of actuator A is cut off and actuator is cooled down, the recovering trend of actuator A will exert a force on lower contact, making the contact pair touching each other, which is the "ON" state. Similarly, the micro-switch could be recovered to initial "OFF" state by powering actuator B.

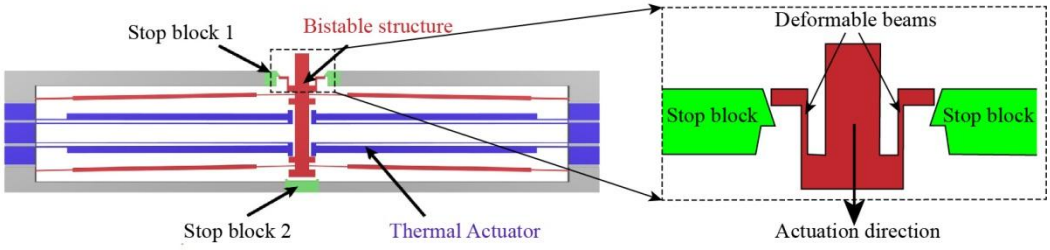

Figure 1- 14. Bistable module with flexible locking structure [CHEN 08, CHAL 11].

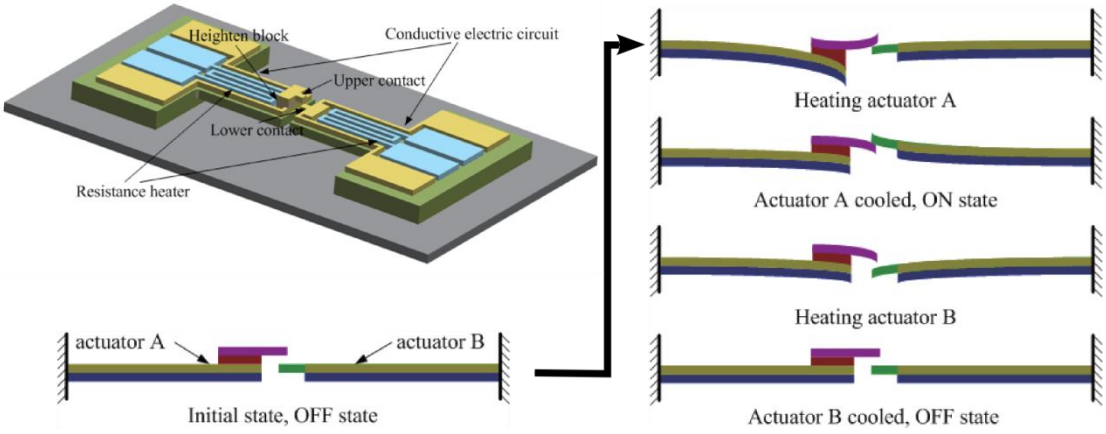

Figure 1- 15. Schematic diagram and the working principle of the micro-switch [MAO 10].

In [LUKE 10], a half passive (lock) half passive (release) locking mechanism used in shock sensor was reported (figure 1-16). Quarter round surfaces were employed as flexible locking interface. When the sensor was subjected to an acceleration along *Y-axis*, the mass part would move and deform the springs. If the acceleration was big enough, two quarter round surface of mass would go against the quarter round surface of the latch. Due to the round surface, a component of the contacting force would bend the thin beam of the latch. Moreover, when the magnitude of the acceleration is bigger, the mass will pass the latch and when the acceleration was removed, the mass would be locked behind the latch under the restoring force generated by springs. Then, it could be released by the reset arm.

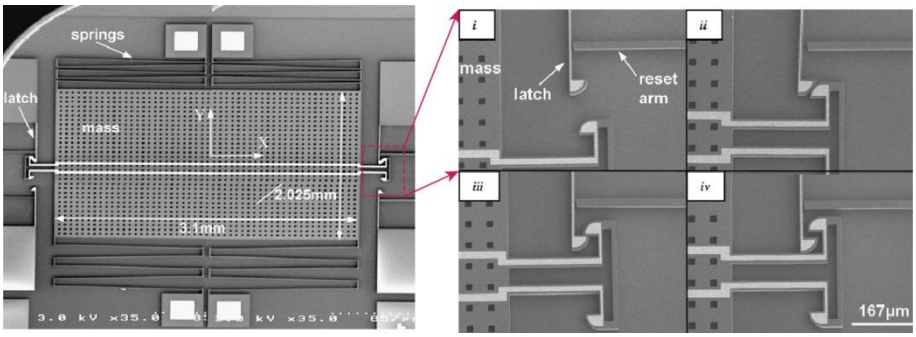

Figure 1- 16. SEM of latching shock sensor design and sequence of events during sensor latching: (i) before mass contact latch, (ii) during contact, mass is sliding past latch, (iii) still in contact, mass has just moved past latch and (iv) after contact, when mass has moved past latch for large acceleration [LUKE 10].

3.1.3 Compliant multistable mechanisms

A compliant mechanism achieves at least some of its mobility from the elastic deformation of the flexible parts other than through traditional joints. It offers an effective and economical way to achieve multistability because the mechanism's energy storage and motion characteristic are directly related [HOWE 01]. Moreover, compliant mechanisms are usually monolithic. As a consequence, it is compatible with micro fabrication techniques and there is no need of assembly. Because they are jointless, rubbing and friction between parts is absent. Furthermore, they do not have the backlash error, which is commonly seen in rigid body mechanisms [WIKI 14]. Due to these merits, compliant mechanisms are quite suitable for micro precise applications.

3.1.3.1 Partially compliant multistable mechanisms

For a compliant multistable mechanism, if some of its mobility is not achieved through deformation of its flexible part, it is called a partially compliant multistable mechanism. (Partially compliant multistable mechanism can have bigger motion than fully compliant multistable mechanism.) Figure 1 - 17a shows a partially compliant bistable mechanism [UMIT 08]. It is symmetrical structure which consists of two flexible arm beams, two flexible shoulder beams and a slider. When the slider is pushed by driving force from the first stable position to the second stable position, two shoulder beams will be bended aside, two flexible arm beam will be buckled. After the slider gets to the second stable position, these flexible beams will recover to original straight shape. When these flexible beams are deformed, energy is stored in form of deformation. As consequence, an energy barrier is created between two positions and make them stable.

The research group of Chen Guimin has done a series of work on how to realize multistability through a single bistable mechanism [CHEN 11]. Figure 1 - 17b shows the schematic diagram and a polypropylene prototype of the partially compliant tristable mechanism. One bistable mechanism based on buckled beams and a link-slider module were employed to achieve the tristability. As shown in figure 1 - 17b, l, which is the length of the link, equals to a, which is the distance between the bistable mechanism and the slider path when the bistable mechanism is at upper bistable position. Therefore, when the link is at vertical position, it is stable. Furthermore, there are two stable positions distributed symmetrically at two sides, when the bistable mechanism is at lower stable position. Then, this mechanism is tristable. If $a<l$, as shown in figure 1 - 17c, when the bistable mechanism is at upper stable position, the link is not at vertical position, so there will be two symmetrical stable positions correspond to the upper stable position of bistable mechanism. Similarly there are another two stable positions correspond to the lower stable position of bistable mechanism. So, this is partially compliant quadristable mechanism. It could be inferred that, if more link-slider modules are employed, more stable positions will be created. The maximal number of stable positions is $M_n=2^n$, where n is the number of

link-slider modules. Figure 1 - 17d shows the schematic diagram of a partially compliant octostable mechanism who consists one bistable mechanism and two link-slider modules. Because the stable positions are symmetrically distributed, so only half of the stable positions are presented in figure 1 - 17d.

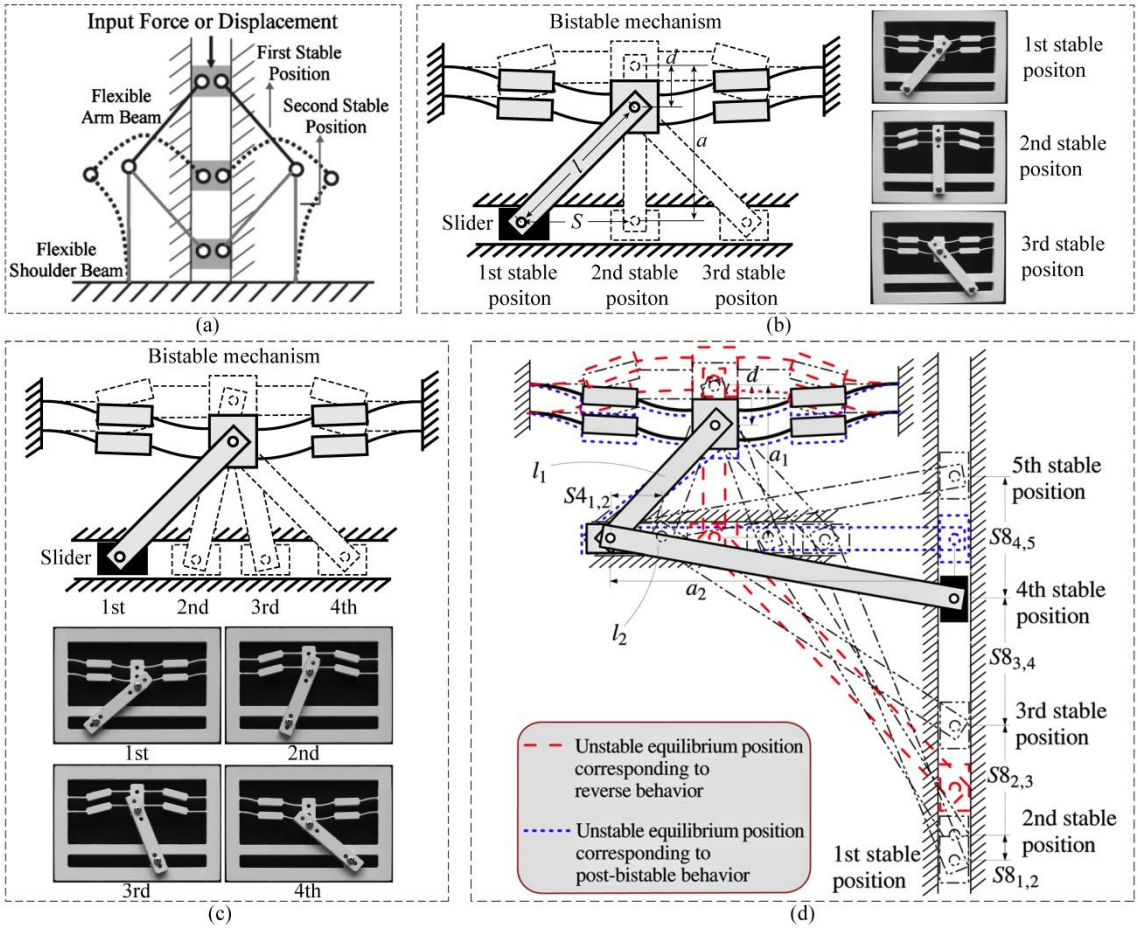

Figure 1- 17. Partially compliant multistable mechanism: (a) Schematic of a partially compliant bistable mechanism [UMIT 08]; (b) Schematic and polypropylene prototype of a partially compliant tristable mechanism [CHEN 11]; (c) Schematic and polypropylene prototype of a partially compliant quadristable mechanism [CHEN 11]; (d) Schematic of a partially compliant octostable mechanism [CHEN 11].

3.1.3.2 Fully compliant multistable mechanisms

If all the motion of a compliant multistable mechanism is achieved through deformation of its flexible part, it is called a fully compliant multistable mechanism. Three kinds of fully compliant multistable mechanism will be surveyed in this study: Four-bar mechanism, buckled beam and tensile beam.

Four-bar mechanism.

The pseudo-rigid-body model (PRBM) method [HOWE 01] leads to the possibility of applying the knowledge available in rigid body field to compliant mechanisms. Employing PRBM method, researchers started to explore the multistability of four-bar mechanisms. Figure 1 - 18 presented a tristable four-bar mechanism [FEND 07]. Both partially and fully compliant four-bar tristable mechanisms were fabricated and tested. The fact proves that the pin joints in partially compliant version can be easily replaced by flexible connections. In [JENS 99], another partially compliant four-bar bistable mechanism was reported. In this bistable mechanism, two pin joints were utilized to allow the rotation, but with the help of PRBM, these two pin joints could be replaced by flexible connections without losing the bistability, which allows researchers to develop fully compliant bistable mechanisms

with four-bar mechanism. In [JENS 03], Jensen and Howell have developed the theory to identify mechanism and guarantee the bistability.

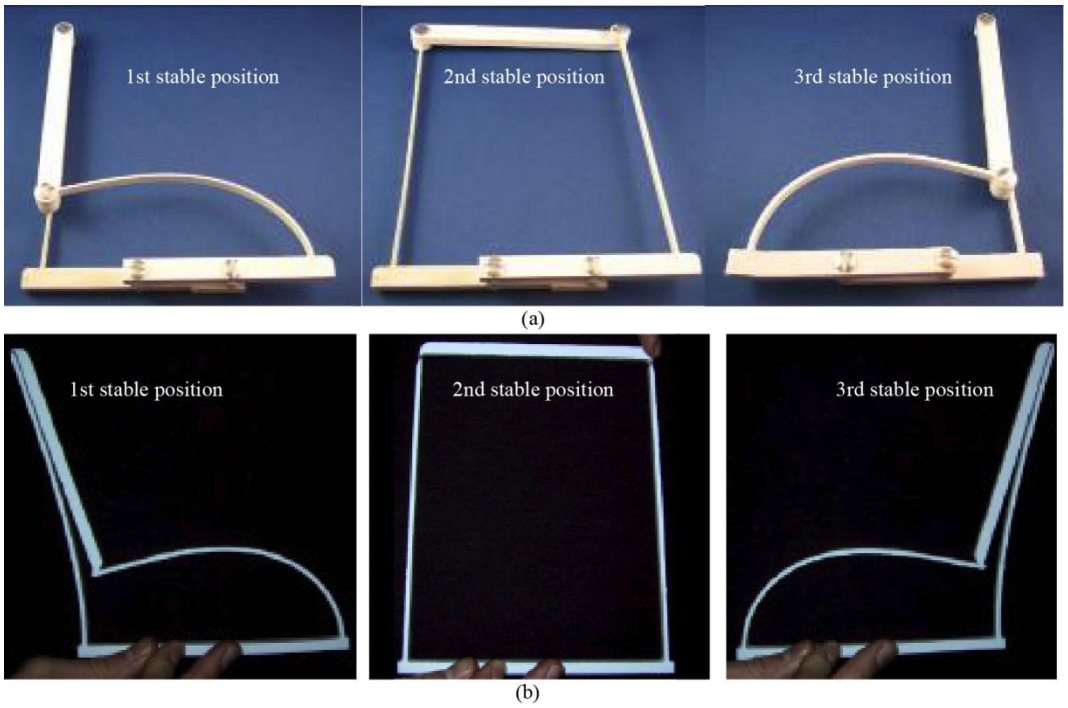

Figure 1- 18. A tristable four-bar compliant mechanism [FEND 07]: (a) The partially compliant version; (b) The fully compliant version.

Buckled beams

Buckled beam is one of the most commonly used mechanisms for bistable or multistable designs. The structure is simple and it can provide a relatively big output force. Furthermore, buckled beam is compatible with fully compliant design, which gains a lot of attention in fully compliant multistable fields. Buckled beams achieve their bistability or multistability through snap effect. During the switching process from one stable position to another stable position, the buckled beam is under the combined loads of compression and bending. There is another group of bistable or multistable beams under combined loads of tensile and bending which is called tensile beams. They will be discussed in the following part.

The buckled beams could be generally divided into three groups: pre-compressed beams, pre-stressed beams and pre-shaped beams.

A **pre-compressed** beam is fabricated with a straight shape (figure 1 - 19), then, it could be compressed and buckled, under axial load, to one of the lateral side to a cosine shape. The already buckled beam could be switched to the other lateral side by external force. Both the two positions are stable and based on the fact that it is initially straight, so, the strain conditions at two stable positions are identical. Therefore, it is not difficult to infer that, the output force of pre-compressed beam would be symmetrical with respect to the central position [ZAID 11c].

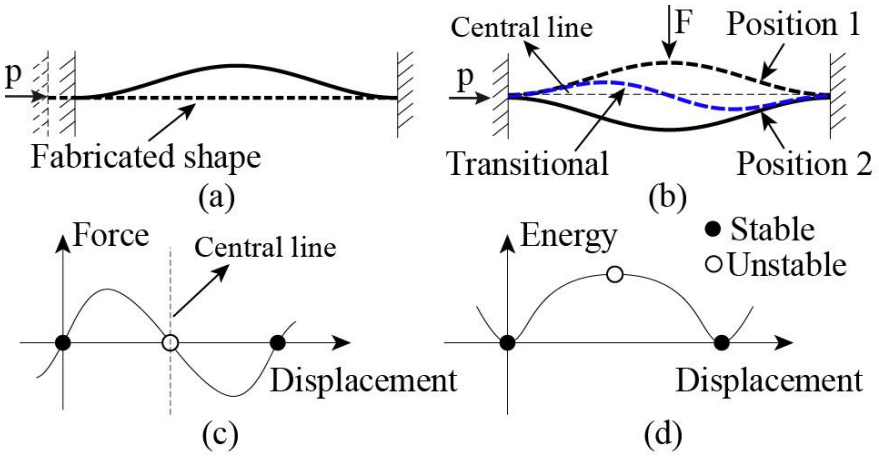

Figure 1- 19. Pre-compressed beam: (a) Pre-compression; (b) Switching process; (c) Force-displacement chart; (d) Energy-displacement chart [ZAID 11c].

In [ZAID 10, ZAID 11a, ZAID 11b, ZAID 12], Zaidi S. et al reported a bistable mechanism using pre-compressed beam. The beam is fabricated with a flat form through 3D printing using ABS+ material (figure 1 - 20). Two support parts were designed with two installation holes, so that the beam could be fixed onto two precise linear stages (PLS). With the help of one of these stages, the flat beam could be compressed and buckled to one stable position which has a cosine shape and it could be switched to the other symmetrical stable position.

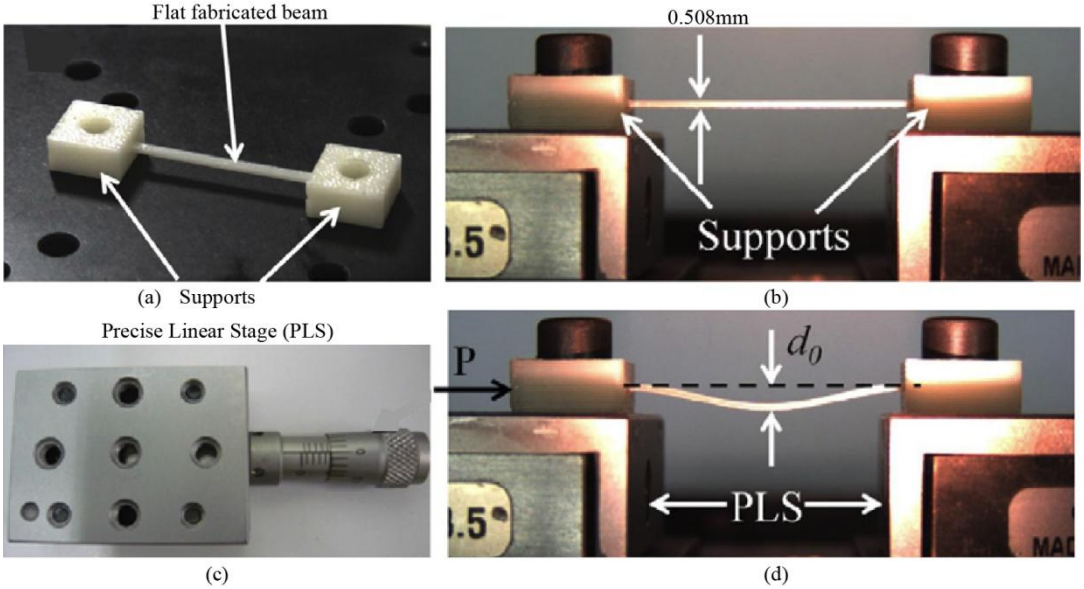

Figure 1- 20. A bistable mechanism using pre-compressed beam: (a) Flat beam fabricate by 3D printing using ABS+ material; (b) Flat beam fixed on precise linear stage; (c) Precise linear stage; (d) Curved beam after the application of compressive force, P, using one linear stage [ZAID 12].

Based on pre-compressed bistable buckled beam, B. Andò et al have developed a vibrational energy harvesting approach [ANDO 12, ANDO 14] (figure 1 - 21). The flexible polyethylene terephthalate pre-compressed beam was used as the bistable mechanism. The beam could be switched between two stable states by environmental vibrations. The mechanical-to-electrical energy conversion was performed by two piezoelectric transducer laterally installed on the beam. Each time the beam was switched, the energy of beam's impacts would be harvested by the piezoelectric transducer. As a consequence of the wide bandwidth of the devices, the efficiency was improved at very low cost.

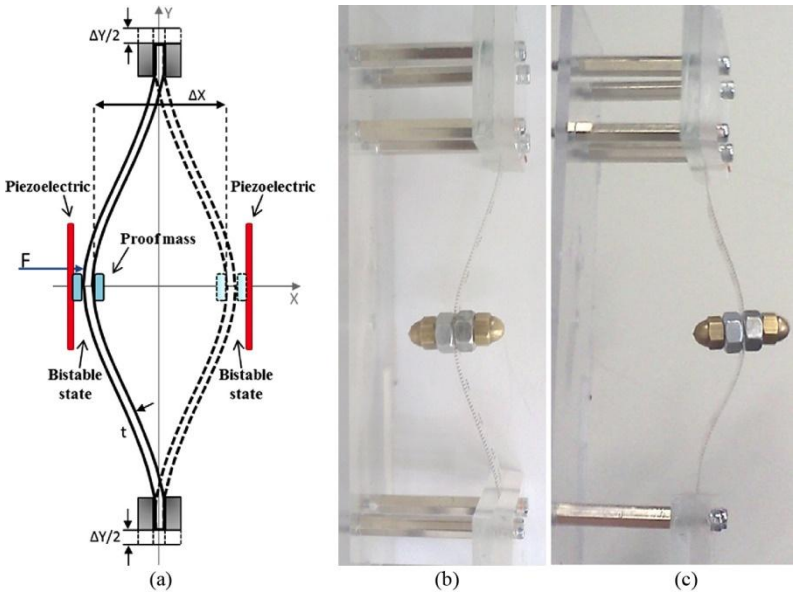

Figure 1- 21. Bistable buckled beam based approach for vibration energy harvesting: (a) Working principle of the double piezo-nonlinear harvester; (b) First stable state of the flexible polyethylene terephthalate (PET) beam; (c) Second stable state of the PET beam [ANDO 14].

Different from pre-compressed beam, the **pre-stressed** beam is curved by artificially creating stress during the fabrication process. I. Z. Pane et al. designed and fabricated a bistable pre-stressed curved beam by patterning the active silicon (Si) layer of SOI wafer [PANE 07, PANE 08, PANE 09] (figure 1 - 22). The stress is introduced by the difference in thermal expansion ratio between Si and SiO_2 layers during the oxidation process. The pre-compress operation was replace by the oxidation of silicon layer. The stroke of the pre-stressed bistable curved beam could be controlled with different thickness of oxidized layers.

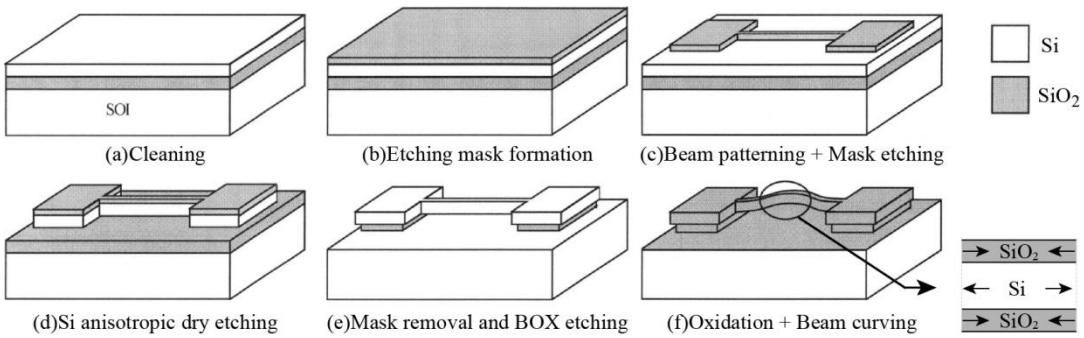

Figure 1- 22. Fabrication process of pre-stressed curved beam [PANE 07].

Because the beam is curved by stress and the unstressed shape is straight, so, the strain energy stored at two stable positions theoretically should be the same. Thus, the force-displacement chart of pre-stressed beam should be similar with the pre-compressed beam, which is symmetrical with respect to the central position (figure 1 - 19c, d). The force-displacement and energy-displacement chart based on Euler beam theory was presented in [PANE 07] (figure 1 - 23).

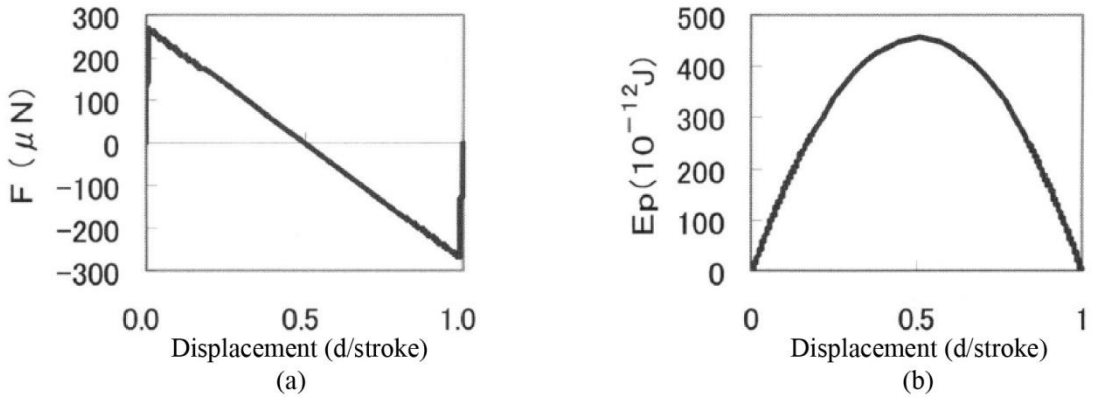

Figure 1- 23. (a) Force-Displacement chart of pre-stressed beam; (b) Energy-Displacement chart of pre-stressed beam (here d is the displacement of beam's midpoint and the displacement axis in chart is relative displacement).

Another approach of bistable buckled beams is **pre-shaped** beam which is fabricated with a certain shape. Thus, the pre-load (pre-compress or pre-stress) operation is not necessary to achieve the desired curved shape. A centrally clamped parallel pre-shaped double beams based bistable mechanism was presented by J. Qiu et al. in [QIU 01, QIU 04] (figure 1 - 24). Two beams were fabricated with a cosine shape without residual stress and centrally clamped at the midpoints. It is fabricated utilizing deep reactive ion etching (DRIE) technique and another dry isotropic etching process of 15 seconds using SF_4 was applied to smooth out the sidewall surface roughness created during DRIE. This dry etch process could significantly increase the fracture stress of a DRIE structure [CHEN 98]. According J. Qiu's work, a single pre-shaped beam (with cosine shape) could not be bistable because of the rotation of the midpoint, i.e. after withdraw the actuation force the beam would recover to the original position. So, they clamped two beams together to constrain the rotation of the midpoints so that the transitional buckling mode would be the third buckling mode which stores more strain energy than the transitional buckling mode for a single pre-shaped beam.

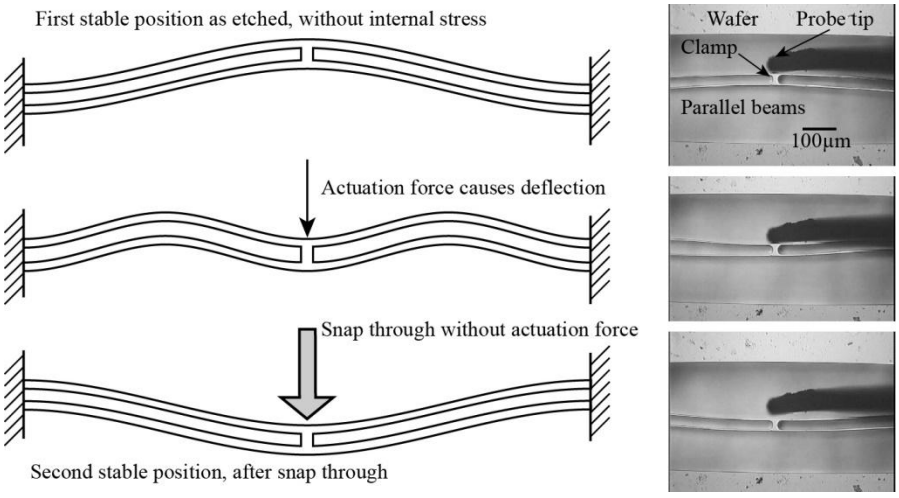

Figure 1- 24. The schematic diagram and photos of the centrally clamped parallel-beam bistable mechanism and its deflection and snap through behavior.

Then the energy barrier between two positions would be high enough to create two local minimal energy point, i.e., the structure would be bistable. However, the strain state at two stable positions were different, the force-displacement chart of the pre-shaped bistable beam is not symmetrical with respect to the central position (figure 1 - 25). If we take the original fabricated shape as the first stable position, it is obvious that the switching from first stable position would be more difficult than the switching back. More detailed discuss could be found in [QIU 01, QIU 04].

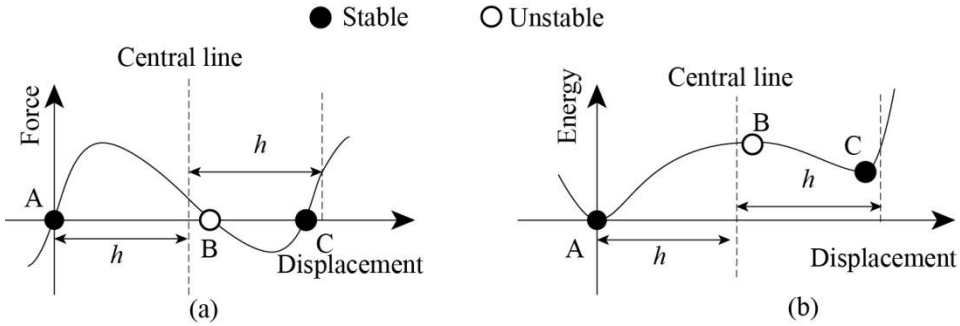

Figure 1- 25. (a) Force-Displacement and (b) Energy-Displacement curves of central clamped parallel pre-shaped beam.

In [PHAM 11a, PHAM 11b], a quadristable mechanism based on central clamped parallel pre-shaped beams was reported. As we see in figure 1 - 26a-d, there are two sets of beams in the structure: the inner curved beams and outer curved beams. So it is a combination of two bistable structures: the inner one is surrounded by the outer one. Due to the fact that these two bistable structures were serially coupled along the same direction, its four stable positions were distributed in a single axis. In [WANG 13], only the three forward stable positions are used, so the same structure was clamed to be a tristable structure. Based on this structure, a constant force bistable mechanism (CFBM) was presented in [PHAM 11b] (figure 1 - 26e), which has an almost constant force output behavior in a wide actuation range and could be used as overload protection mechanism. In the CFBM structure, additional upper and lower lateral beams were added. The lateral beams together with outer curved beams functioned as flexible hinges. They can deflect initially and store the strain energy when there is load F applied on the shuttle mass. When the load is increased to a certain value, the CFBM snaps to the second stable position so that the device will not be destroyed by the big load.

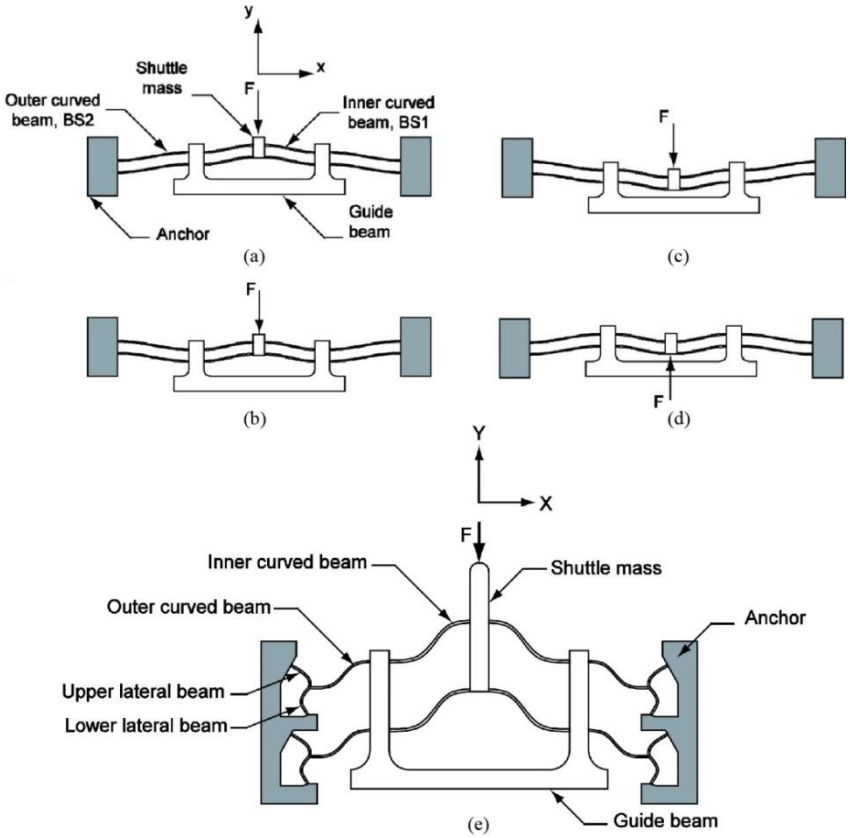

Figure 1- 26. (a) - (d) Operational principle of a quadristable mechanism [PHAM 11a, WANG 13]; (e) Schematic of a constant force bistable mechanism [PHAM 11b].

In [SAM 06], a quadristable mechanism based on centrally clamped parallel pre-shaped beams was presented, this mechanism was capable of output four stable positions distributed in two orthogonal directions: two in x-direction and two in y-direction (figure 1 - 27). One bistable mechanism is embedded into another bistable mechanism. These two bistable mechanisms were configured in two orthogonal directions. So, the combined output would be the four vertices of a rectangle. One prototype of this design was fabricated on brass wafer using milling machine and the quadristability of the design was experimentally verified.

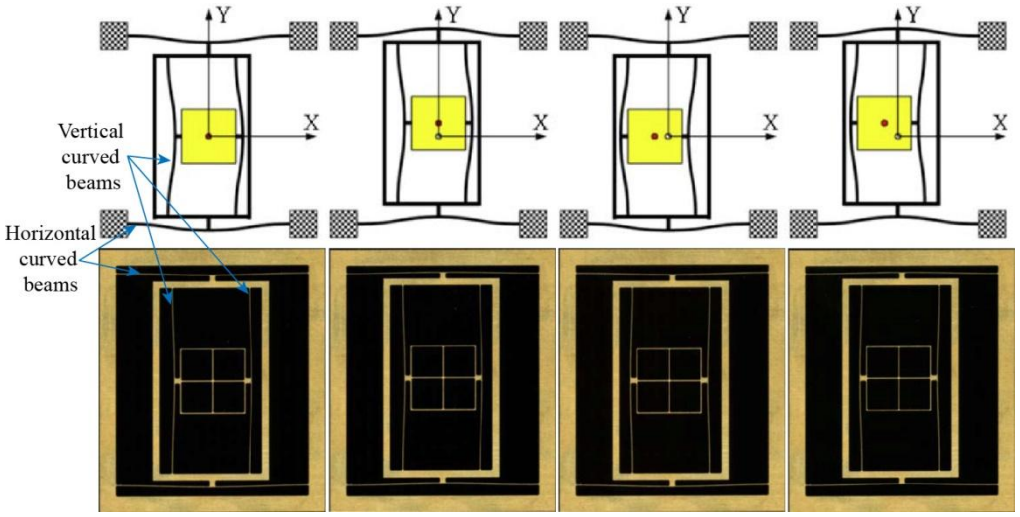

Figure 1- 27. Schematic and photos of four stable positions for a quadristable mechanism with X- and Y-Directional bistable curved beams [SMA 06].

In former part, all the pre-shaped bistable curved beams have uniform sections. There is another approach for bistable curved pre-shaped beams which consist in beams with non-uniform sections. A general bistable mechanisms based on non-uniform sectional beams is presented in figure 1 - 28a [CHEN 08, CHAL 11, CHEN 11, CHEN 09, WANG 09].

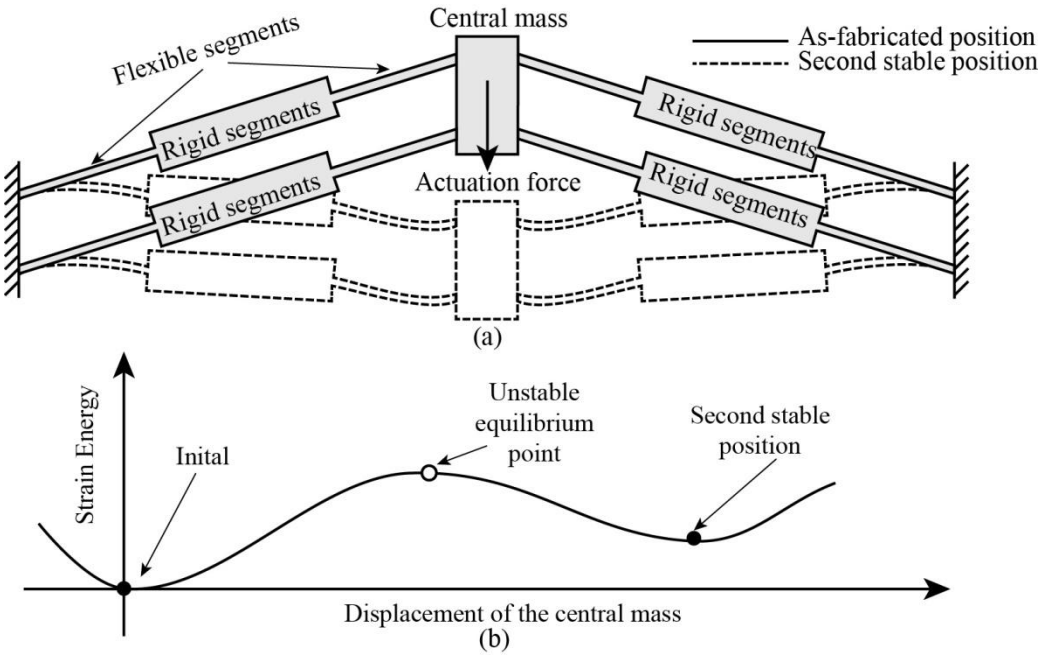

Figure 1- 28. (a) Bistable mechanism based on centrally clamped non-uniform sectional pre-shaped beams; (b) Strain energy trend curve.

We can see that there are three parts in a beam: two flexible segments and one rigid segment. The flexible segments act as flexible hinges and the rigid segment acts as springs. When the central mass is push downward under the actuation force, the rigid segment would be compressed and the strain energy caused by compression would be largely increased. After the central mass pass an equilibrium position, the compression on the rigid segment will decrease and the compression energy also decreases. If the actuation force continues to push the central mass the beam will be stretched then the strain energy will increase again. As a consequence, there will be local minimal energy point, which is the second stable position (figure 1 - 28b).

Based on the non-uniform sectional bistable curved pre-shaped beam, Chen G. et al. developed a series of multistable mechanisms, which were called multistable mechanisms through single bistable mechanism [CHEN 09, CHEN 11]. Figure 1 - 29a is an in plane fully compliant tristable mechanism, presented in [CHEN 11], using one bistable mechanism. The partially compliant design of the tristable mechanism is shown in figure 1 - 17b where link-slider structure was used to increase the number of stable positions. In the fully compliant structure the link-slider structure was replaced by compliant end effector with linear motion. In [CHEN 09b], an out of plane tristable mechanism was reported (figure 1 – 29b), the motion direction of the end effector was configured to the normal direction of the device plane. Furthermore, by adding a second end effector with a linear motion, a multistable mechanism with five stable positions was proposed in [CHEN 11]. These five stable positions are shown in figure 1 – 29c. Six pairs of pre-shaped centrally clamped pre-shaped beams were used to increase the output force of the bistable mechanism, so that it could drive two levels of end effector mechanisms.

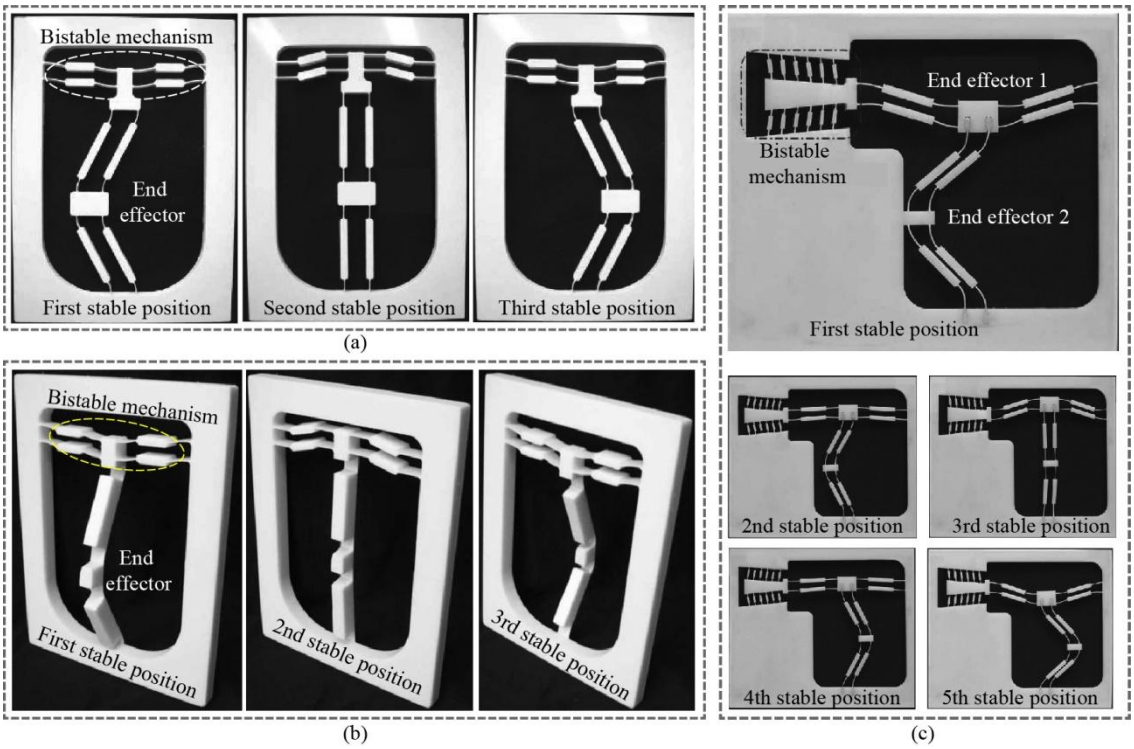

Figure 1- 29. Multistable mechanisms with non-uniform sectional pre-shaped beams: (a) An in plane tristable mechanism using single bistable mechanism [CHEN 11]; (b) An out of plane tristable mechanism using single bistable mechanism [CHEN 09b]; (c) An in plane multistable mechanism with five stable positions [CHEN 11].

Unlike the method used by Chen G. et al., there is another approach to synthesis a multistable mechanism by coupling multiple bistable mechanisms [CHEN 08, CHAL 11, PHAM 11a, PHAM 11b, WANG 13, SAM 06, CHAL 13]. In [12], Qiao Chen et al. designed a bistable mechanism using non-uniform sectional beams with flexible locking structure (figure 1 - 30b), by parallel coupling multiple this bistable mechanisms in a parallel configuration (figure 1 - 30a and b). Figure 1-30a shows

the CAD model of the digital micro-robot whose kinematic structure is shown in figure 1 - 30c. Chalvet V. et al. designed and fabricated a digital micro-robot with multiple stable positions (2^6 = 64) with a combination of 6 bistable modules) distributed on a planar workspace (figure 1 - 30d). These bistable modules were coupled through levers connected by flexible hinges. Due to the stroke reducing effect of levers, the initial output stroke (30µm) of bistable modules at the third level (bl3 and br3) was reduced to 1.5µm at the end effector. To prove the concept a device with four bistable modules of this design was fabricated on SOI wafer using DRIE technique (figure 1-30e).

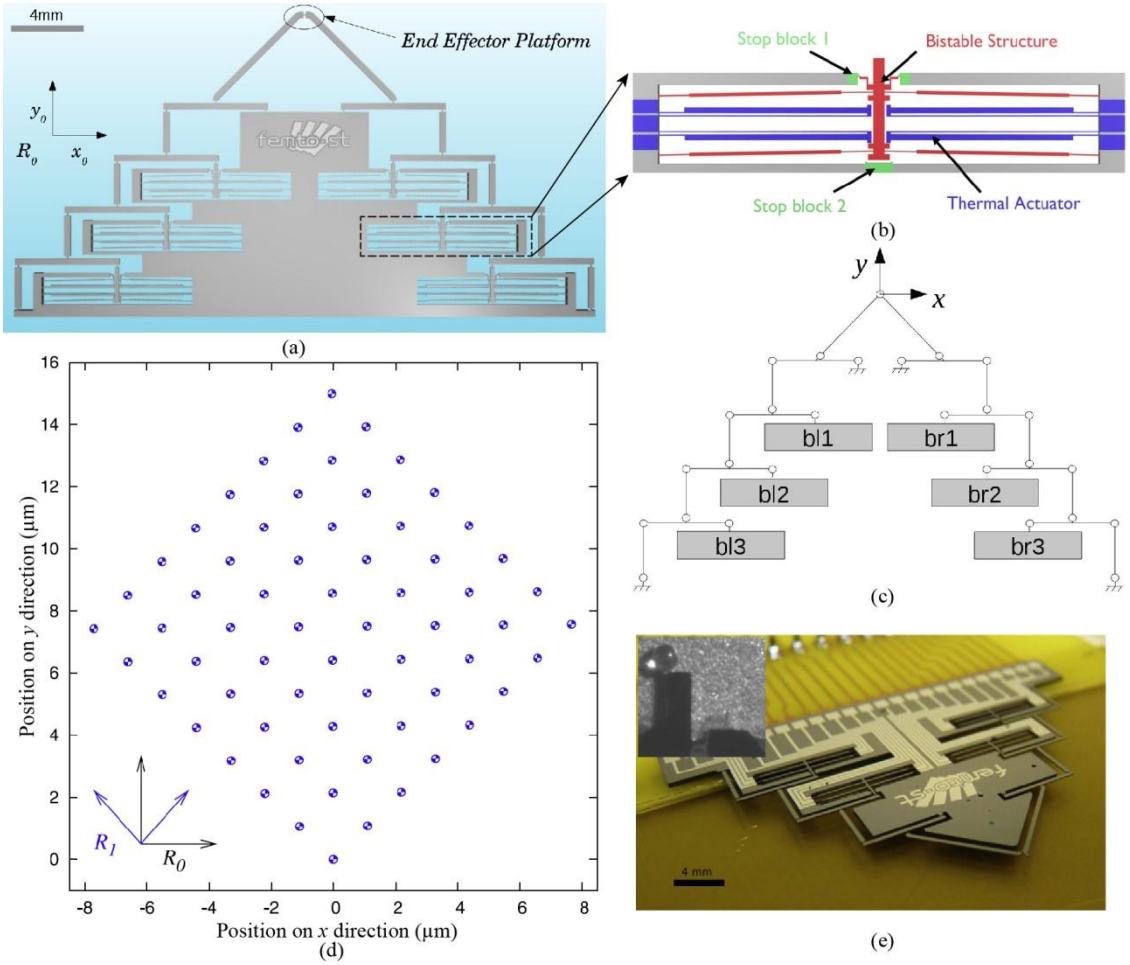

Figure 1- 30. A planar digital micro-robot based on bistable modules: (a) CAD model of the digital micro-robot with six bistable modules [CHAL 11]; (b) One bistable module which is based on non-uniform sectional pre-shaped beam [CHEN 08, CHAL 11]; (c) Kinematic structure of the robotic structure [CHAL 11]; (d) Theoretical workspace generated by the robotic structure with six bistable modules [CHAL 13]; (e) Digital micro-robot containing four bistable modules and zoom on its end-effector while manipulating a 150µm diameter glass ball [CHAL 13].

A comparison of buckled beams based bistable mechanisms are shown in table 1 - 1. We can see that the pre-compressed beams and pre-stressed beams have the advantage of symmetrical output force and smaller attainable stroke with a certain thickness of beam. However, the pre-load operation (pre-stress for pre-stressed beam) is quite difficult, especially for actuator which contains multiple bistable beams. Pre-shaped beam has the advantage of no pre-load operation, which makes it is possible of bulk fabrication. But, the output force is not symmetrical and due to the geometrical limit, its attainable smallest stroke is bigger than the other two kinds of beams with the same beam thickness. To combine the advantages and reduce the drawbacks of different beams, a new bistable mechanism based on antagonistic pre-shaped double beams was proposed four our design. It has symmetrical output force, smaller stroke and easier pre-load operation. More detailed information will be discussed in chapter 2.

Table 1 - 1. Comparison of buckled beams based bistable mechanisms

	Pre-compressed beam	Pre-stressed beam	Pre-shaped beam
Pre-load operation	difficult	difficult	no pre-load
Symmetry of output	symmetrical	symmetrical	asymmetrical
Stroke	small	small	big

Tensile beam

As mentioned in former part, when beam is under the combined loads of tensile and bending, the beam is called tensile beam. It is another approach for multistable mechanisms [WILC 05, MAST 03, CHEN 09]. In [WILC 05], a bistable mechanism using both buckled beams and tensile beams was presented (figure 1 - 31a). The exploitation of tensile beam shared the bending strain at the ends of the buckled beams. As a consequence the asymmetry of the force output was reduced. In [MAST 03], a bistable mechanism purely based on tensile beams was reported (figure 1 - 31b). In [CHEN 09a], a tristable mechanism based on two pairs of symmetrically configured tensile beams was realized (figure 1 - 31c). In figure 1 - 31c, only the fabricated position and an upper stable position was presented, but it is clear that there is a third stable position which is at the lower position.

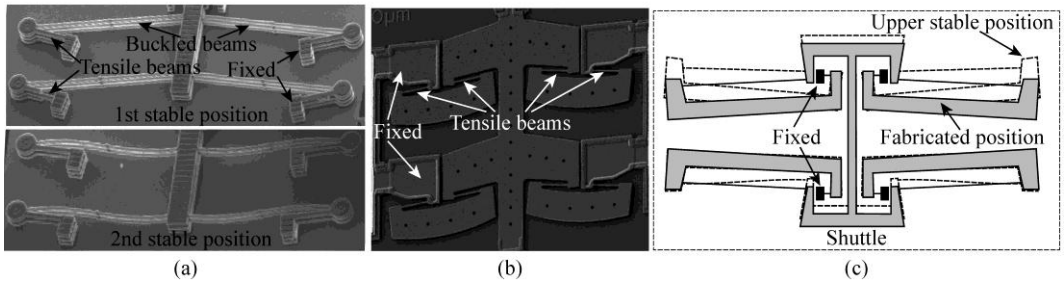

Figure 1- 31. Multistable mechanisms based on tensile beams: (a) A bistable mechanism using buckled beams and tensile beams [WILC 05]; (b) A bistable mechanism using only tensile beams [MAST 03]; (c)A tristable mechanism using only tensile beams [CHEN 09a].

3.1.4 Stroke reducing system

Because of the nature of the multistable actuators, only a series of the discrete positions are attainable. Thus, for the applications where high output resolution is required it is necessary to add a stroke reducing system to the multistable actuators. Because the aim of this study is to design a micro system, the traditional reducing systems based on lead screw or gears, which are not compatible with micro fabrication techniques, will not be discussed. Our attention will be focused on compliant reducing mechanisms. According to the literature survey we have done [CHAL 11, QIN 07, CHEN 15, DAVI 14, NI 14, XU 10, XU 14, TANG 14], the compliant displacement reducing or amplifying mechanisms[1] could be divided into two groups. For the first group the reducing or amplifying effect is accomplished through the rotation of levers. So, the reducing factor is not a constant value. In the second group the reducing or amplifying effect is achieved using the law of lever and the reducing factor is constant (does not depend on the input). The calculation and the modeling of the second group are simpler, while the first group can have very big reducing factor.

In [QIN 07], a nano-positioning compliant displacement reducing mechanism based on flexible hinges connected levers was reported (figure 1 - 32a). Two reducing levels were employed: first, the horizontal

[1] When input and output point is exchanged, the displacement amplifying mechanism will become the reducing mechanism.

level; second, the vertical level. The output direction was changed twice by two reducing levels, so, the final output was aligned in the same direction with input. The structure was designed to be symmetrical, so that the coupled unwanted displacement caused by rotation of the lever could be eliminated. Furthermore, the using of two reducing levels could lead to a big reducing factor, so, it could have an output resolution at nano-scale. In [CHEN 15], a rhombic displacement amplifier was proposed for the piezoelectric actuator in a single level amplifier configuration. The input of piezoelectric actuator in the horizontal direction will cause the rotation of the edges of the rhombus, then, the rotation will cause an amplified output in vertical direction (figure 1 - 32b).

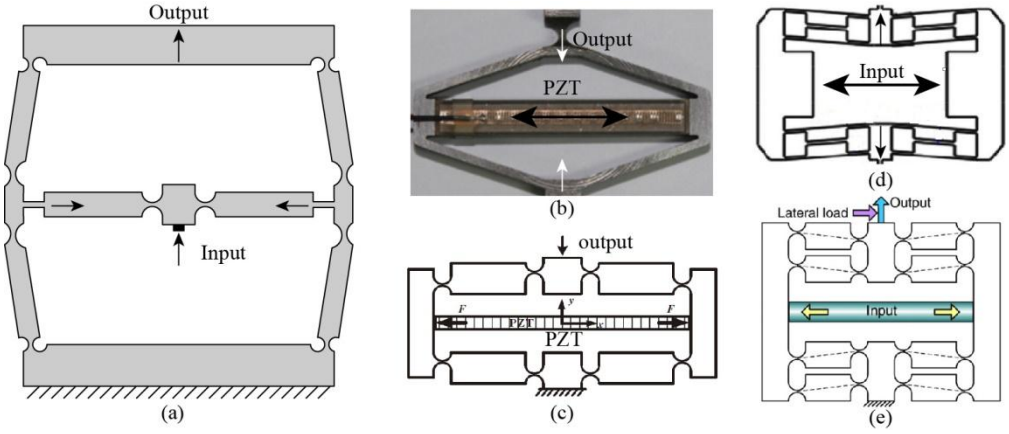

Figure 1- 32. Stroke reducing mechanisms with non-constant reducing or amplifying factor : (a) A nano-positioning compliant mechanism for motion reduction [QIN 07]; (b) A prototype of mechanical micro-displacement amplifier [CHEN 15]; (c) A bridge type displacement amplifier [NI 14]; (d) A bridge type displacement amplifier [XU 14]; (e) A compound bridge type displacement amplifier [XU 10].

In [DAVI 14], a displacement amplifier which is a half rhombic structure of the design in [CHEN 15] was studied. In [NI 14], a bridge type displacement amplifier was represented. In fact, the bridge type amplifier could be regarded as an extension of the rhombic type. For a rhombic type amplifier, the output is always towards the inside of the rhombus. But for the bridge type, the output direction could be customized by changing the relative position of flexible hinges. For example, the output direction in figure 1 - 32c is towards inside, while the output direction for the mechanisms in figure 1 - 32d and e are towards outside. The amplifiers represented in figure 1 - 32d and e were called compound bridge typed displacement amplifier. Two pairs of flexible hinges connected levers were employed for each side. As a consequence, the resistance to lateral load is largely increased.

The stroke reducing or amplifying mechanisms in the second group are based on the law of lever. The output is a linear function of the input, which is simple for modeling. As a consequence, it is possible to utilize multiple reducing (or amplifying) levels without the issue of increasing the complexity of the model. A coupling system based on flexible hinges connected levers was utilized in [CHAL 11] to combine the output from multiple bistable modules, so that, the designed digital micro-robot could have a planar workspace. Figure 1 - 33a shows the schematic of the coupling system of the micro-robot. Because of the nature of lever, beside the combination of inputs from bistable modules, the coupling system has stroke reducing effect. If we take the bistable module left in level 3 (bl3 in figure 1 - 33a) as an example, the output of bl3 would be reduced to a half of the original when it is transferred to the second level, then it will reduced to one fourth when it goes to the first level. In [TANG 14], a flexible hinges connected lever based displacement amplifier used to increase the workspace range of piezoelectric actuator was reported (figure 1 - 33b). Similarly, it was based on law of lever to realize the amplifying effect. Parallel coupled two branches of levers were employed in the first reducing level, so that it could achieve a bigger amplifying factor.

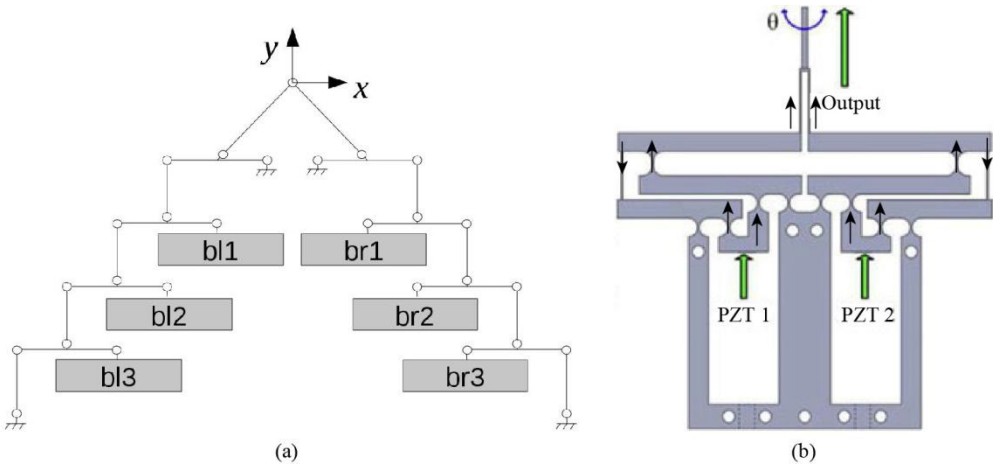

Figure 1- 33. Stroke reducing mechanisms: (a) The kinematic model of a digital micro-robot [CHAL 11]; (b) A flexure based nano-manipulator [TANG 14].

3.2 Wireless micro-actuation

The contactless energy transfer methods have attracted the attention of researchers in developments of micro devices. Electrical energy, which is the basic input energy source, can be supplied internally by integrating the batteries units or externally through wires. However, integration of batteries will largely limit the autonomy of the micro systems, while the exploitation of wire for power transfer will influence the mobility and reduce the number of degrees of freedom [ZAID 12]. Therefore, the contactless energy transfer is preferable for micro devices.

Hence, to realize a multistable actuator, beside the multistable mechanism, an actuation method is necessary to drive the multistable mechanism from one stable state to another. So, different actuation methods have been surveyed and will be presented in the following part. Moreover, based on the fact that our aim is to design a micro multistable actuator with contactless actuation methods, the literature surveying has been focused on contactless approaches which could maximize the degrees of freedoms of a micro-actuator. According to the working principles of contactless energy transfer systems, energy could be transferred from energy source to micro devices without physical contact through electromagnetic system, capacitive (electrostatic) coupling system, inductive coupling system, magnetostrictive effect, opto-thermal systems based on laser heated thermo-active materials, opto-fluidic system, etc.

3.2.1 Electromagnetic systems.

In electromagnetic actuating systems, the mobile part (normally, the permanent magnets) is driven by the magnetic field excited via the current carried by the coils or wires (fixed part). No physic connection exists between the mobile and fixed part, so, it could be regarded as an approach of contactless actuation methods.

Based on the electromagnetic principle, a biomimetic swimming tadpole micro-robot using Helmholtz coils was presented in [BYUN 11, HYUN 14]. Like it is shown in figure 1 - 34, three pairs of Helmholtz coils were configured perpendicular to each other to create a 3D controllable magnetic field. The robot body consists of buoyant body, a NdFeB magnet and a silicone fin which was directly connected on the magnet. The propulsion and steering forces were provided the swing action of the silicone fin, which was driven by the interaction of the NdFeB magnet and the electromagnetic system.

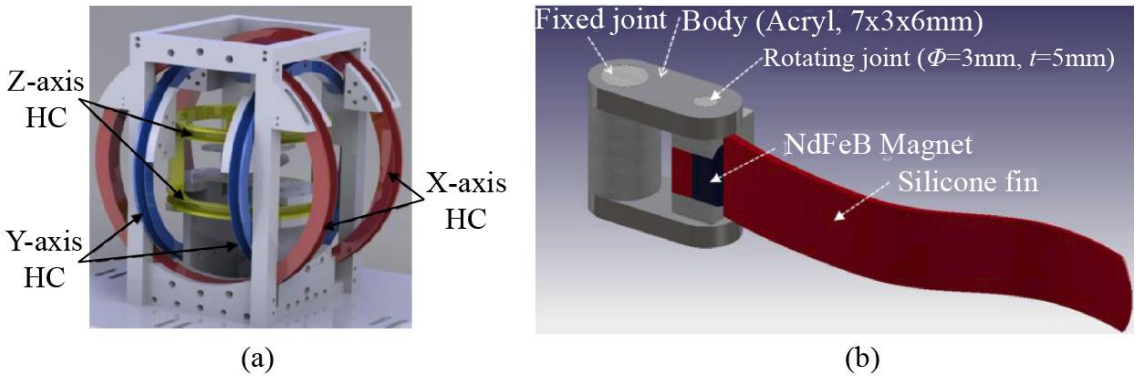

Figure 1- 34. (a) Schematic diagram of 3 pairs Helmholtz Coil; (b) Design of the swing tadpole micro-robot [HYUN 14].

Another electromagnetic actuator was reported in [PETI 14]. It is a quadristable actuator which is actuated by the current carrying wires located beneath the mobile permanent magnet (figure 1 - 12a).

To realize contactless actuation for industrial manufacturing, a high-precision magnetically levitated positioning stage was reported in [OWEN 06]. This iron-cored permanent magnet linear synchronous motors (PMLSM) is composed of two parts: a stator and a mover (figure 1 - 35). The stator has slots hosting a three-phase winding. The mover, placed below the stator, hosts a series of permanent magnets of alternating polarity. For the typical configurations of PMLSMs, the normal axis (y-axis) is constrained at a fixed air gap by means of bearing and the force generated by stator is only used to propel the mover along the longitudinal axis (x-axis). In this design the attractive/repulsive force, generated by the interaction between permanent magnets and the magnetic field of the stator coil, together with the attractive force between the permanent magnets of the mover and the iron core of the stator were used to levitate the mover. The attractive force was designed slightly stronger than the gravity force, then, via controlling the current in stator's coil to produce a small repulsive force, the mover could reach a balanced position with desired air gap. This magnetically levitated positioning stage could be used in semiconductor industry to reduce the dust generated by friction between mover and stator and the cost of maintenance.

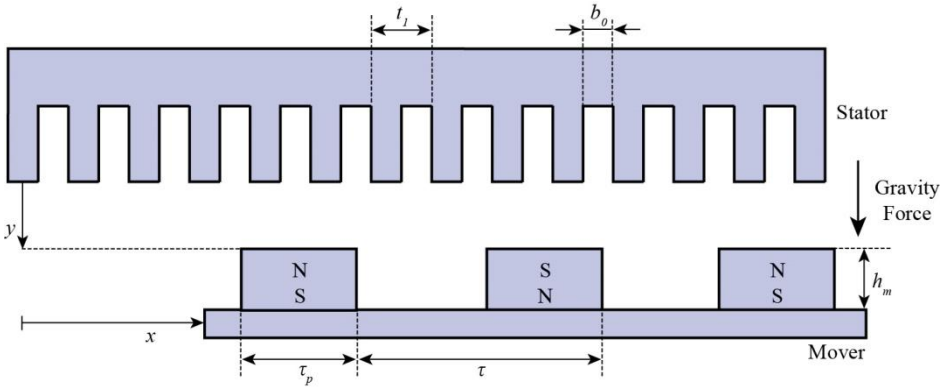

Figure 1- 35. Structure of a flat, single sided, iron-cored permanent magnet linear synchronous motor (PMLSM) [OWEN 06].

In [KHAN 12], a long stroke electromagnetic XY positioning stage for micro applications was reported (figure 1 - 36). The positioning stage consists of four linear motors (LMs) as shown in figure 1 - 36a, each LM is an electromagnetic actuator based on Lorentz principle. Figure 1 - 36b shows the cross-sectional view of LM1; it is composed of a fixed 2-phase planar coil and a mobile permanent magnet array with alternative polarity. Similar with the PMLSM in [OWEN 06], the coil could exert a magnetic field on the permanent magnet array and propel it to move along the longitudinal axis. The

combination of the movements of LMs could generate a 3-degrees-of-freedom motion, including two translations along x- and y- axis and a rotation with respect to the z-axis.

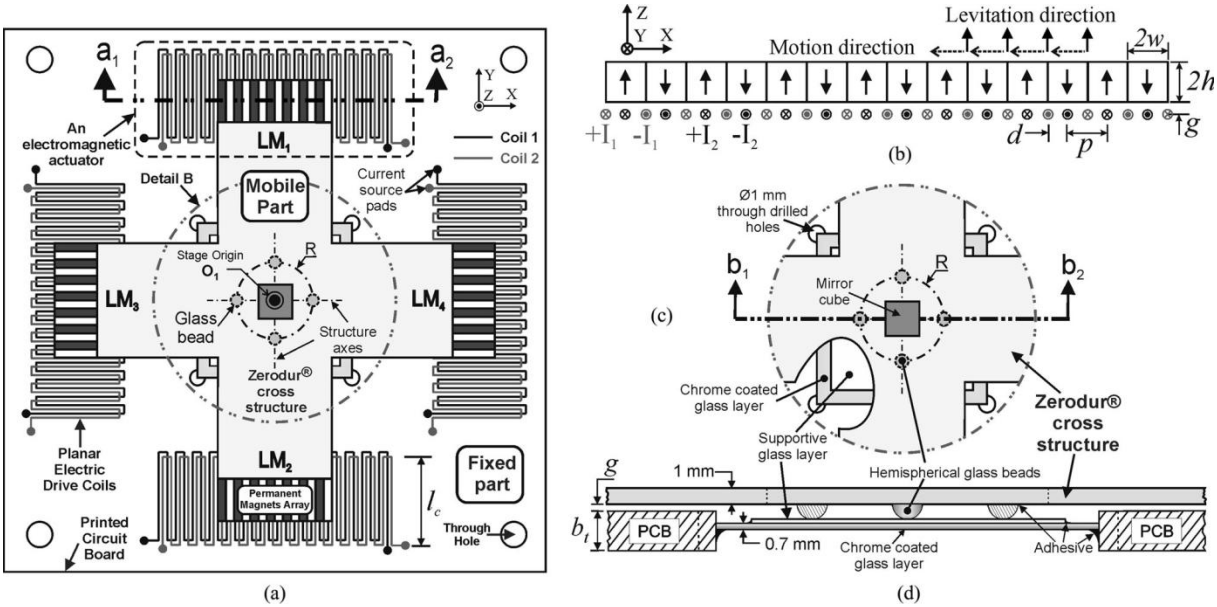

Figure 1- 36. (a) Top view of the positioning stage; (b) a_1-a_2 cross-sectional view of linear motor 1 (LM1); (c) Top view of detail B; (d) b_1-b_2 cross-sectional view. [KHAN 12]

3.2.2 Capacitive coupling system

The capacitive coupling system is another approach to realize the contactless actuation. Instead of employing the magnetic field, the electric field is used to generate the electrostatic force, which could be utilized to drive the mobile part of an actuator. Due to the merits of low power consumption, high response speed and the ability to generate a large linear motion, the capacitive coupling mechanisms are widely used for the design of micro-motors (linear motors, rotatory motors and planar manipulator), high precision sensors (gyroscopes, accelerometers and displacement sensors), oscillators, energy harvesters, etc.

Comb drive actuator is one of the most important configurations of capacitive coupling systems. As the name suggests, the electrodes of a comb actuator have the comb like shape with fingers (figure 1-37), so that the capacitance between electrodes could be largely increased (parallel arrangement), as well as the electrostatic force. When there is potential difference between the electrodes, the electrostatic force is intended to increase the capacitance at each elementary capacitor, so that the moving comb will be pulled to the fixed comb. In [IMBO 14], a thin capacitive comb actuator was demonstrated (figure 1 - 37a). To reduce the effect of the fringe fields, a configuration with alternate potential fingers was proposed. Like it is shown in figure 1 - 37a, the moving comb was held to the ground and the fixed comb fingers were alternatively polarized. The alternative design was proved successful in decreasing out-of-plane motion by 75%, while enhancing the in-plane displacement of the linear comb actuator by over 35%. In [LASZ 10], a two directional electrostatic comb-drive *X*-*Y* micro stage was presented (figure 1 - 37b). The two directional motions were realized by a configuration called “stage-in-stage” construction. The internal stage, which was in charge of the output in *Y* direction, was connected with the external stage via flexure springs, so that the internal stage could be driven by the external stage to generate the motion in *X* direction.

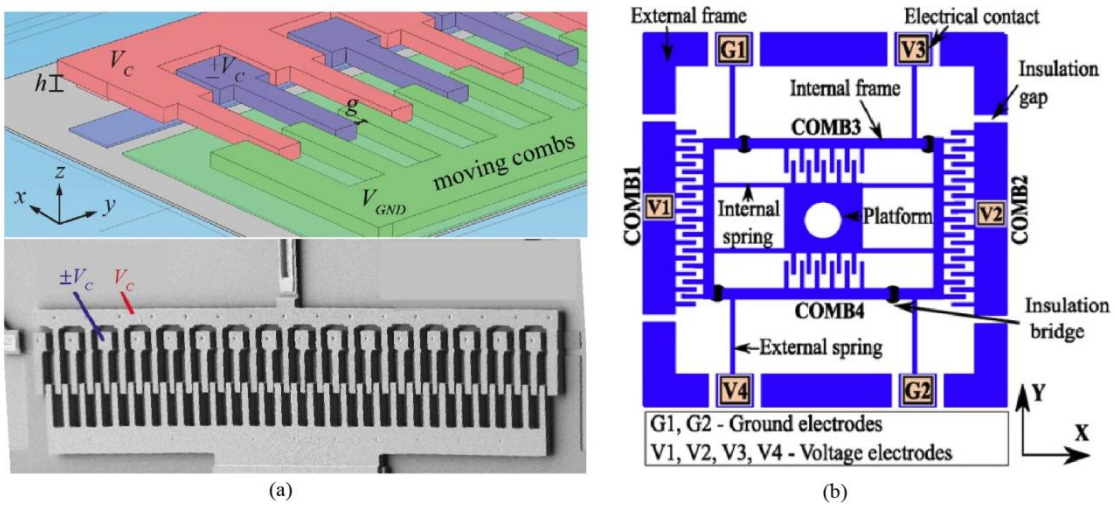

Figure 1- 37. Comb drive actuators: (a) Diagram and SEM image of a comb actuator with alternating finger potentials [IMBO 14]; (b) A design of the silicon comb drive *X-Y* micro-stage [LASZ 10].

Beside the comb like electrostatic actuators, there are un-comb-like ones. A high angular range electrostatic rotatory stepper micro-motor (figure 1 - 38a) was reported in [STRA 12]. The structure and the working principle were similar with the traditional stepper motor, except that the magnetic field coupling in traditional stepper was replace by capacitive coupling. Moreover, the rotatory joint of rotor was replaced by a butterfly flexure pivot so that it is compatible with silicon based micro-fabrication process. Another rotatory motor based on electrostatic forces was reported in [JEON 99]. Like it is shown in figure 1 - 38b, there are two groups of electrodes in the stator: the big electrodes (E_1, E_2 and E_3) are responsible for creating the levitation force for the rotor; the small electrodes located at the edge of stator are excited with sinusoidal potentials to generate the propelling rotary torque. Unlike the motor in [STRA 12], this electrostatically suspended rotor could rotate continually like a traditional motor. Figure 1 - 38c shows another application based electrostatic force, which could be used for the contactless glass panel transportation in mobile phone assembly industry [JEON 07].

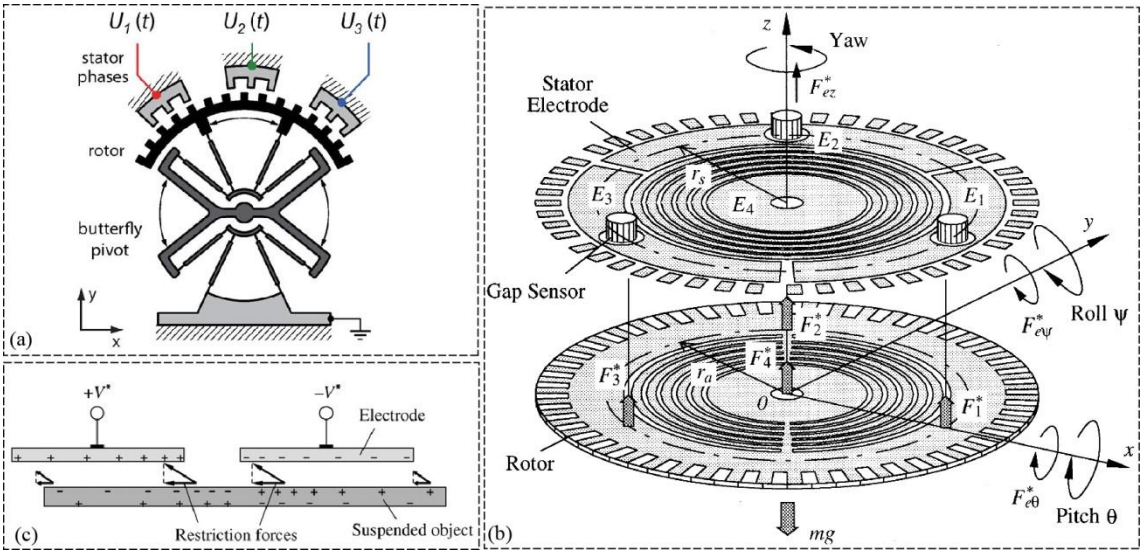

Figure 1- 38. Un-comb like electrostatic actuators: (a) A high angular range electrostatic rotary stepper micro-motor [STRA 12]; (b) Variable-capacitance motors with electrostatic suspension [JEON 99]; (c) Contactless suspension and transportation of glass panels by electrostatic forces [JEON 07].

3.2.3 Inductive coupling system

The inductive coupling system is usually employed as the energy transfer method in the contactless actuation systems. Generally, the primary coil, which is the energy source, is bonded with the fixed part in the system. There are one or several secondary coils fixed with the mobile part. When the primary coil carries alternative current, it generates a varying magnetic field. If the secondary coil is close to the primary coil (coupled), the magnetic flux is changed. According the Faraday's law of induction, the changed magnetic flux generates an electromotive force, which can be used to drive the mobile part.

In [BOEI 08], a contactless motion system was demonstrated (figure 1 - 39a). It consists of a contactless planar actuator with 6-DOF and long stroke movement in the x-y plane, with a 2-DOF manipulator on top of a floating platform. The floating platform was levitated by magnetic bearing and the contactless energy transfer (100W continuous) was transferred to the mobile floating part through the inductive coupling system (primary coil on the fixed world, secondary coil on the mobile part). The energy generated from the secondary coil was used to drive the manipulator on the floating platform.

In [PAPA 07a, PAPA 07b], the inductive coupling system based rotating transformer was used to transform energy from the stationary base to the revolving platform of an airborne radar system (figure 1 - 39b). Similarly, the inductive coupling was employed in a rotatable transformer with FPGA controlled resonant converter [MORA 10]. This energy transfer method was also used for the power supply for automobiles [ELLI 10], robots and manipulators [MORA 08], robotic capsular endoscopes [CART 10].

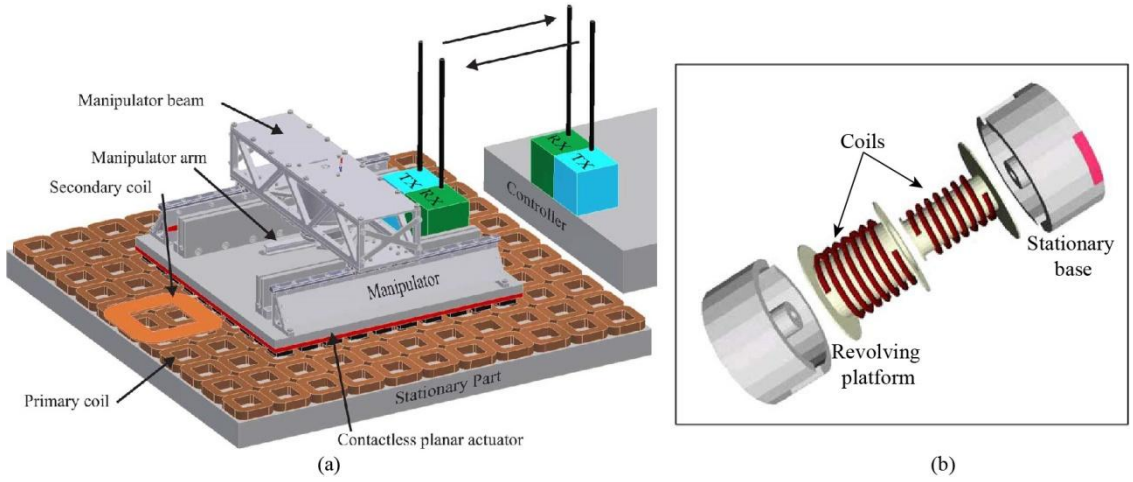

Figure 1- 39. Inductive coupling systems: (a) A planar actuator powered by inductive coupling system [BOEI 08]; (b) An airborne radar using inductive coupling system for energy transfer from stationary base to the revolving platform [PAPA 07].

3.2.4 Magnetostrictive effect

Magnetostriction is a property of ferromagnetic materials that causes them to change their shape or dimensions during the process of magnetization. Due to the change of magnetic field the material's magnetostrictive strain varies until it reaches the saturation value λ. When the magnetostrictive effect was firstly identified by James Joule in 1842 [JOUL 47], λ was very small (less than 10^{-5}) as compared to the piezoelectric effect, so it was not employed too much. Recently, materials with big magnetostrictive strain (around 10^{-3}) were found, this effect regained the attention of researchers. A magnetostrictive actuator for high dynamic servo valve was reported in [KARU 10]. Like it is shown in figure 1 - 40, Terfenol-D rod was used as the magnetostrictive material. It is surrounded by excitation coil. When the Terfenol-D rod was excited by the magnetic field, its dimension will change. Then the change of dimension could be used as high dynamic output for servo valve. Most of the magnetostrictive actuators have similar structure like the one shown in figure 1 - 40. A theoretical and experimental investigation of the temperature and thermal deformation of a giant magnetostrictive

actuator was carried by Yuchuan Zhu et al. [ZHU 14] and the research results provided the basis for precise micro-displacement giant magnetostrictive actuators. Another study focused on the mechanics of magnetostrictive composites was reported in [ABOU 14] and the analysis presented has provided an efficient tool for analyzing magnetostrictive composites with continuous and arbitrary inclusion phases. Due to the characteristic of high force output and high driven frequency, the magnetostrictive actuators are quite suitable for vibration control and high dynamic applications. A model of magnetostrictive actuators used for active vibration control was reported in [BRAG 11].

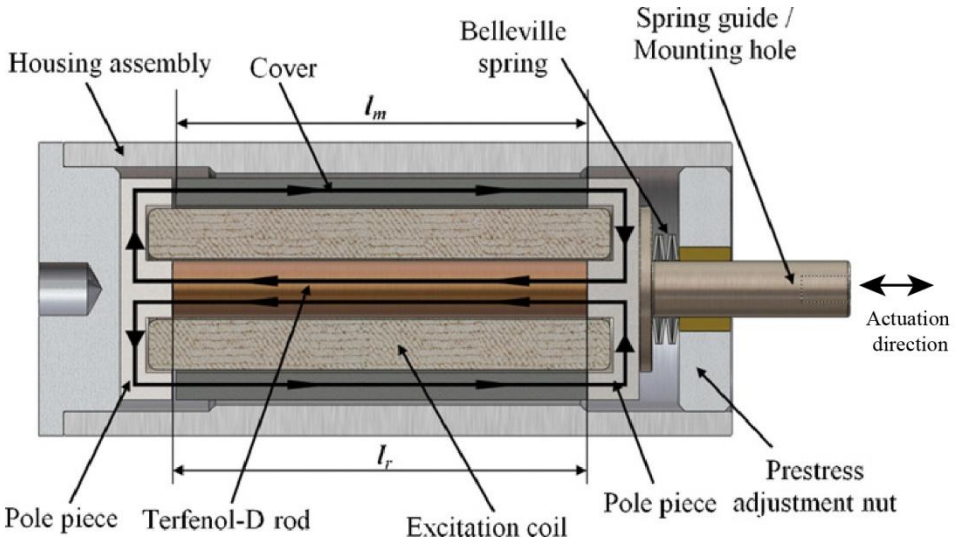

Figure 1- 40. Magnetostrictive actuator for high dynamic servo valve [KARU 10].

3.2.5 Optical actuation

Varieties of contactless actuation methods have been discussed in former part, but they all have a common point that the actuation efficiency depends on the distance between mobile part and fixed part. As the distance increases, the efficiency would be significantly decreased. This has created many limits for contactless applications. Thus, the contactless energy transfer via laser, which has a much small attenuation ratio as compared to magnetic or electric fields, was explored for long distance wireless actuation applications. As we know, laser could be easily focused and directionally oriented and usually has a wavelength in a very narrow bandwidth, which could lead to the possibility of selective actuation with the help of optical filters.

In [BAGL 02], a photo thermal mechanical contactless long range actuation method was proposed. The schematic of the proposed actuator structure is shown in figure 1 - 41a. Here a laser was employed as the long range contactless energy source. When the laser beam comes focused to the actuator via a micro machined lens, the bimorph cantilever, which consists two layers with different thermal expansion ratios, is bent. For example, here the top layer possessed a higher thermal expansion ratio, so, when the bilayer cantilever was heated, it will bend to downwards direction.

In [EMIR 14], an opto-fluidic effect based long range contactless actuator approach was demonstrated. As shown in figure 1 - 41b, laser beam was also used as the energy source. When it was focused onto a certain position on the petri dish with a thin layer of liquid, the caused thermal increase created a flow, which was used to manipulate the small object in the liquid (small glass beads). Via the high speed camera, the position of the beads was retrieved by the control system, which could adjust the parameters (focused position, heating duration) of the laser to manipulate the small beads along the desired trajectory.

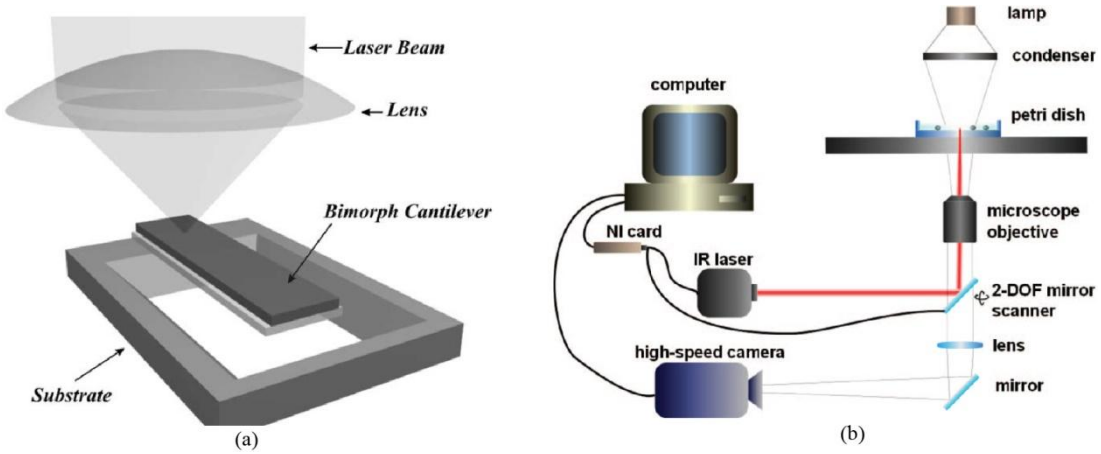

Figure 1- 41. (a) A photo thermal mechanical actuator structure [BAGL 02]; (b) The schematic of a manipulate system using opto-fluidic actuation and visual servoing [EMIR 14].

In [ZAID 12], the laser heated shape memory alloy (SMA) was adopted as the contactless actuation method for a bistable actuator. More precisely, as shown in figure 1 - 42, a pair of antagonistic configured shape memory alloy elements with flat austenite form is coupled to a laser heating system were utilized for the contactless actuation. At the original state, SMA 1 is bended by the curved beam. When SMA 1 is heated by the laser beam and reach the phase transform temperature, it starts to recover to its austenite form (flat). As a consequence, SMA 1 exerts a force on the curved beam and finally, curved beam is switched to its second stable position. During the switching process, SMA 2 is bended by curved beam. Then, if SMA 2 is heated, with same process, the curved beam can be switched back to the original state.

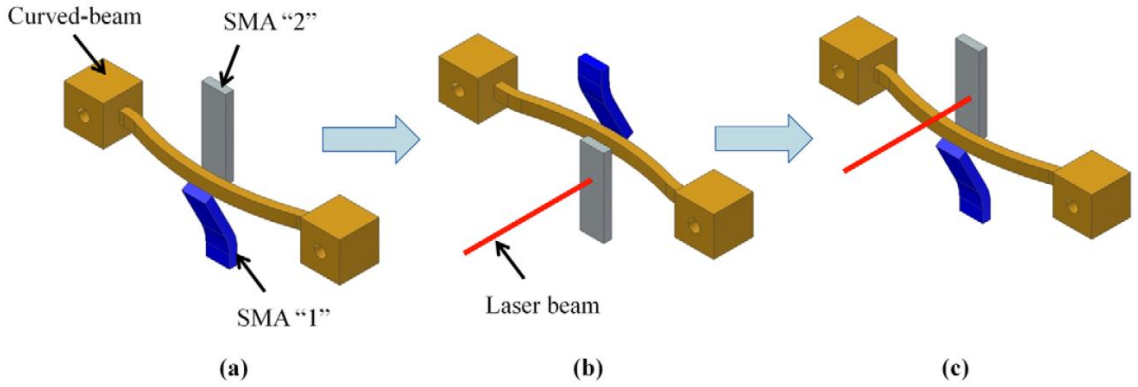

Figure 1- 42. Contactless actuation via laser heated shape memory alloy (SMA) [ZAID 12]: (a) Original state, (b) second stable state, (c) back to the original state.

Beside the laser beam, Radio Frequency (RF) electromagnetic radiation was also adopted as an approach for contactless actuation. In [ABDE 11, LEE 10], ionic polymer-metal composite (IPMC) was successfully actuated by RF electromagnetic radiation. It was also used to actuate SMA based actuator in [ALI 10, ALI 11] (figure 1 - 43). However, as compared to laser beam, additional RF receiving circuits are necessary to convert the radiation to electrical energy, then, this energy can be used to actuate the IPMC or SMA based actuators. Thus, it will increase the complexity of the mobile part as well as the dimensions, which is not the best option for micro designs.

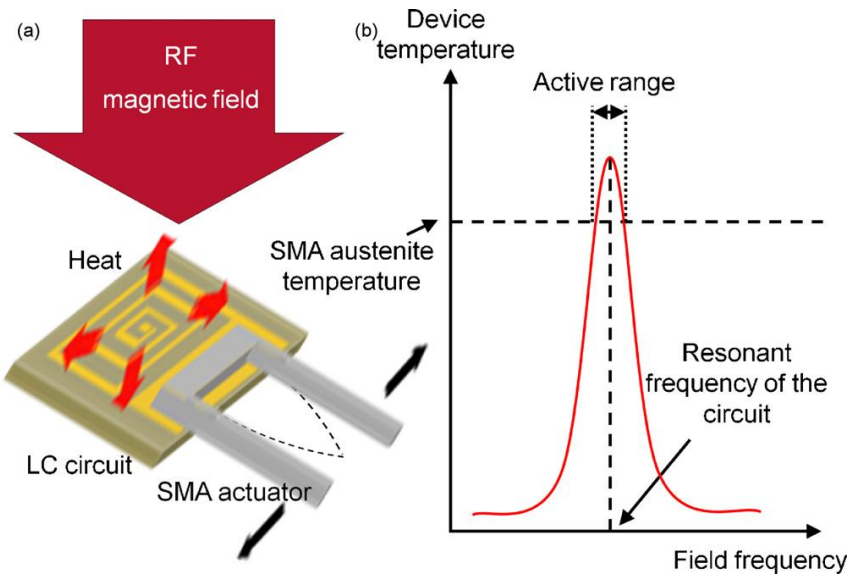

Figure 1- 43. RF electromagnetic radiation actuated SMA actuator [ALI 10].

3.2.6 Summary of wireless actuation

Above described wireless actuation approaches are compared in table 1 - 2. We can see that the laser heated SMA based approach has long working distance, big force output, simple system. The only drawback is the long response time. However, the response depends a lot on the volume of SMA elements and the power of laser beam. The response time can be shortened by using smaller SMA elements and laser beam with bigger power. Therefore, the laser heated SMA based approach is the best option four our wireless actuation method.

Table 1 - 2. Comparison of different wireless actuation approaches.

Wireless actuation approaches	Working distance	Force	Response time	Complexity
Electromagnetic system	short	medium	short	complex
Capacitive coupling	short	small	short	complex
Inductive coupling	short		short	complex
Magnetostrictive effect	short	big	short	complex
RF electromagnetic radiation with SMA	long	big	long	complex
Laser heated SMA	long	big	long	simple

4 Conclusion

Due to the minimization of micro devices, problems, such as sensor integration and power supply, are arising. Integration of sensors will increase the complexity of micro system which will have adverse effect on minimization of the system. For the power supply problem, if the power is provided by wires, it will limit the number of degrees of freedom. But, if the power is provided by internal battery unit, the autonomy of the micro-system will be influenced. In the case of smart surface, where a group of micro-actuators distributed onto a surface are controlled, these problems become more crucial.

Therefore, one way to solve these problems is to use multistable (digital actuator) actuator and wireless actuation method. The multistable actuator could be control with open loop method, i.e., extra sensors are not necessary. Furthermore, multistable actuator has low power consuming level, thus, it is possible to be actuated by wireless methods which have weaker energy transfer efficiency than wires. So, the work of this study will be focused on multistable mechanisms and wireless actuation methods.

Chapter II

Quadristable Micro-actuator

1 Introduction

As mentioned in the first chapter, problems, such as integration of power unit and sensors for micro devices, have become more crucial due to the minimization requirements. In the case of design a group of micro-actuators, it becomes even more difficult. Thus, the best option is to utilize digital (multistable) actuators which do not need sensors to control the output. Therefore, we will design a new multistable micro-actuator to fulfil the requirements of applications like smart surface (described in first chapter). In this chapter, a quadristable actuator based on antagonistic pre-shaped double beams will be presented. The designed actuator is formed by two rows of bistable actuators providing four stable positions. The bistable mechanism for each row is a pair of antagonistic pre-shaped double beams. This bistable mechanism has an easier pre-load operation as compared to pre-compressed bistable beams. Furthermore, it solves the asymmetrical output force problem of parallel pre-shaped bistable double beams. At the same time, the geometrical limit is lower than parallel pre-shaped bistable double beams which ensures a smaller stroke of the actuator with the same dimensions.

2 Modeling and Design

The bistable buckled beam, which has uniform cross section, based multistable mechanism is the best option to form a multistable micro-actuator because of its merits, such as, simple structure design, big force output and the fact that it is compatible with micro-fabrication, etc. Thus, the characteristics of different kinds of bistable buckled beams will be studied, analyzed and compared in the following part. Furthermore, a mathematical model will be constructed to help the design of the quadristable micro-actuator based on the antagonistic pre-shaped double beams principle.

2.1 Buckling modes

The switching process of a bistable buckled beam from one stable position to another is a buckling behavior. The force and energy characteristics of different buckling modes vary a lot. So, different buckling modes of a beam will largely influence the output force behavior and its bistability.

The bistable buckled beams are usually long and slender which agrees with the assumption of Euler-Bernoulli beam [TIMO 61]. According to Euler-Bernoulli beam theory, a two ends clamped beam has a series of buckling modes with the rising of axial applied force p. The first three buckling modes, which are the main influence factors of the force output behavior during the switching, are presented in figure 2 - 1. When the axial applied force p is increased to the critical value p_1 the first buckling mode will be observed (a cosine shape). If the midpoint of the beam is constrained to the middle position in vertical direction and at the same time the axial force p is increased to p_2 then the second buckling mode will be observed. Furthermore, if the rotation of the midpoint is also constrained and the axial force p is increased to p_3, the third buckling mode will appear. In an energy point of view, during the buckling process energy is stored in the beam and more energy is stored in higher buckling modes [QIU 01]. The critical axial load p could be calculated by the following equation:

$$p = \frac{\pi^2 EI}{(KL)^2} \tag{2.1}$$

Where, E is the modulus of elasticity, I is the inertial moment, L is the length of the buckled beam, K is the effective length factor. For buckling mode 1, $K = 0.5$, for bucking modes 2 and 3, K is 0.35 and 0.25 respectively.

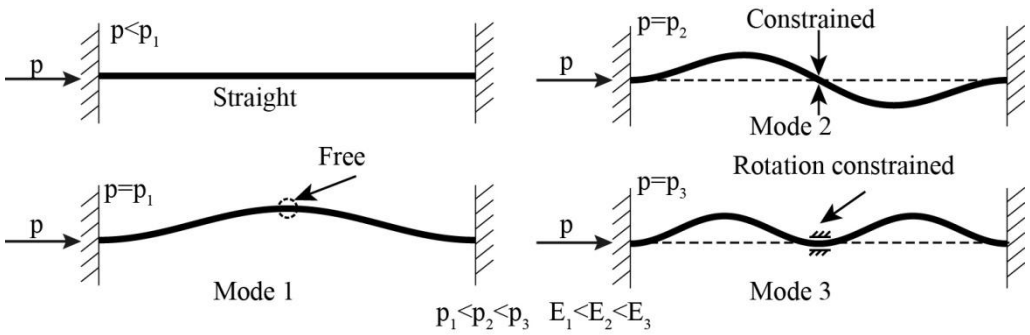

Figure 2 - 1. First three buckling modes of a two ends clamped beam. (p_1 p_2 p_3 and E_1 E_2 E_3 are the critical axial load and stored energy of buckling mode 1, 2 and 3 respectively)

2.2 Comparison of different bistable beams

The bistable buckled beams could be divided into three groups: pre-compressed beams, pre-stressed beams and pre-shaped beams. They have different force output behavior and different manufacturing and assembly processes. To optimize our design, the advantages and disadvantages will be discussed in the following part.

2.2.1 Pre-compressed beam and pre-stressed beam

A pre-compressed beam is fabricated with a flat form, then, an axial force *p* is applied to compress the beam to a curved shape (figure 2 - 2a). As it can be observed in figure 2 - 2b, a single pre-compressed beam has two stable positions with the shape of buckling mode 1. When the switching force *F* is applied to the midpoint, the beam will be deflected from stable position 1 to stable position 2. For the single pre-compressed beam the rotation of midpoint is not constrained and when the switching force constrains the midpoint in the vertical direction, the transitional buckling mode becomes buckling mode 2 (figure 2 - 2b).

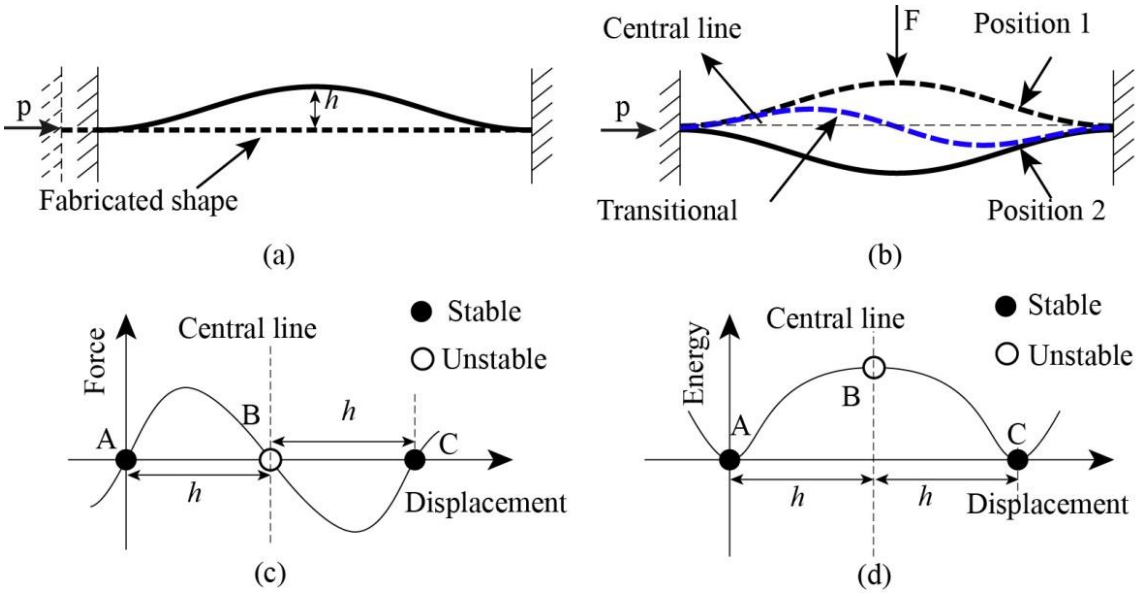

Figure 2 - 2. (a) Pre-compressed beam; (b) Transitional buckling mode (S-shaped) of pre-compressed beam; (c) Force-Displacement chart of pre-compressed beam; (d) Energy-Displacement chart of pre-compressed beam [ZAID 11a].

If a force *F* is applied at the midpoint of the beam to switch the beam (figure 2 - 2b), during the switching from position 1 to position 2, the beam's internal stress is caused by the combined load of compression in longitudinal direction and the bending. Due to the fact that the pre-compressed beam is fabricated as straight, so, the stresses caused by compression will increase firstly, after reaching the maximal value at the central position, then decrease until it gets the position 2. On the contrary, stress caused by bending will decrease first then increase again, after the beam passes the central position. Both the two kinds of stresses are symmetrical with respect to the central position. Thus, the stress states at two stable positions are equivalent. So, if the switching force is applied at the midpoint of the beam, the Force-Displacement curve of a single pre-compressed beam should be symmetrical with respect to the displacement axis [ZAID 11b] (figure 2 - 2c), i.e., the beam generates same force in forward and backward directions (figure 2 - 2c). As we see, there are three equilibrium positions (indicated as A, B and C) where the force is zero. Among them, A and C are stable equilibrium positions, because if there is a small disturbance at position A or C, according to the Force-Displacement curve, the beam could reset itself to position A or C after the disturbance is gone. However, if there is a disturbance around B, the beam will snap to position A or C instead of recovering to position B, so, B is an unstable equilibrium position.

In an energy point of view, the transitional buckling mode (mode 2) stores more energy than stable buckling modes [QIU 01]. As shown in figure 2-2d, buckling mode 2 created an energy barrier between two stable positions, so that the two stable positions are two local minimal energy points. Therefore, a single pre-compressed beam is bistable.

For the pre-stressed bistable beam [PANE 07, PANE 08, PANE 09], the curved shape of buckling mode 1 was realized by introduce the residual stress into the beam. It can be considered as a special way of compressing, so, the stress states for two stable positions are also equivalent. Thus, similar with pre-compressed beam, the Force-Displacement curve of pre-stressed beam is also symmetrical with respect to the displacement axis.

2.2.2 Pre-shaped beam

2.2.2.1 Single pre-shaped beam

Different from pre-compressed and pre-stressed beams the pre-shaped beam was fabricated with the shape of buckling mode 1 without residual stress (figure 2 - 3a). There are also two extreme positions: the fabricated shape and the position 2 (figure 2 - 3b). Similar with pre-compressed beam, the rotation of the mid-point is not constrained, so the transitional buckling mode is also the buckling mode 2. Due to the fact that the beam is fabricated to be curved without residual stress, during the switching from fabricated position to the other extreme position, the stress caused by bending will increase monotonically. Otherwise, the stress caused by compressing is similar with the situation for pre-compressed beam, i.e., the stress increase firstly and reach the maximal value at the middle position then started to decrease. Thus, it is apparent that the stress states at two extreme positions are different and the force needed to switch the beam from the fabricated shape to position 2 will be bigger than the force in the reverse direction.

According to the work in [QIU 01], during the switching process from fabricated shape (cosine shape) (position A in figure 2 - 3c) to position 2 (position C in figure 2 - 3c), the switching force will always be positive, i.e., after withdrawing the switching force, the beam will recover to the original fabricated shape (position A). In the energy point of view, as the consequence of the positive force between A and C, the energy stored in the beam, which is the integral of force with respect to the displacement, will monotonically increase (figure 2 - 3d). Therefore, there is no local minimal energy point for position C, indicating that a single pre-shaped beam with cosine shape is not bistable.

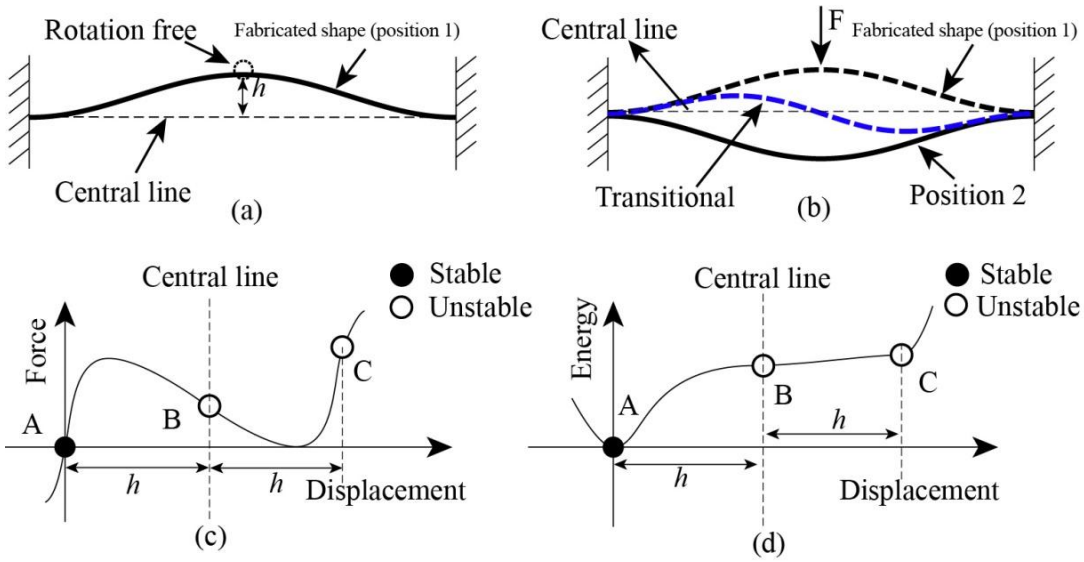

Figure 2 - 3. (a) Single pre-shaped beam; (b) Transitional buckling mode of single pre-shaped beam; (c) Force-Displacement chart of single pre-shaped beam; (d) Energy-Displacement chart of single pre-shaped beam.

2.2.2.2 Central clamped parallel pre-shaped double beams

To increase the energy barrier between the two extreme positions, the central clamped parallel pre-shaped double beams configuration [QIU 01, QIU 04, SAM 06] (figure 2 - 4a) was used as the bistable mechanism. Two parallel pre-shaped beams were clamped at the midpoints. The central clamp constrained the rotation of the midpoints during the switching cycle, so that the transitional buckling mode would be buckling mode 3 (figure 2 - 4b). As discussed in former part, buckling mode 3 stores more energy than mode 2, so, the energy barrier will be high enough to create two local minimal energy points (A and C) for each stable position. The Force-Displacement and Energy-Displacement curves are shown in figure 2 - 4c and d. Similar with figure 2 - 2c, the part (between B and C) of the Force-Displacement curve is negative and there are two stable equilibrium positions (A and C). So, the centrally clamped parallel pre-shaped double beams configuration is bistable.

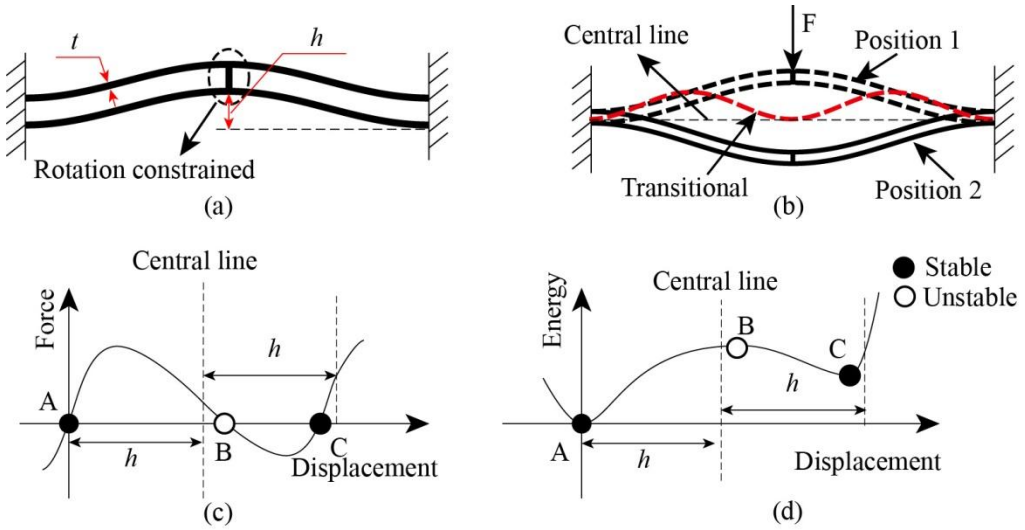

Figure 2 - 4. (a) Centrally clamped parallel pre-shaped double beams; (b) Transitional buckling mode of centrally clamped parallel pre-shaped double beams; (c) Force-Displacement of centrally clamped parallel pre-shaped double beams; (d) Energy-Displacement of centrally clamped parallel pre-shaped double beams.

Although the bistability is achieved, there is a geometrical limit [QIU 01]: the original rise *h* should be more than 2.31 [QIU 01] times of the beam's thickness *t* or it will not be bistable. To have the beam

well bistabled $Q=h/t$ should be more than 6 [QIU 01]. So the stroke, $2\times h$, is bigger than the stroke of pre-compressed beam with the same dimensions (thickness and length). This is not suitable for applications that need precise position output. Furthermore, as we see in figure 2 - 4c, the Force-Displacement curve is not symmetrical with respect to displacement axis, which is not good for applications that there is no preference between the two positions.

2.3 Design of antagonistic double beams

A bistable mechanism based on centrally clamped antagonistic pre-shaped double beams was designed (figure 2-5a), to simplify the pre-compression operation for pre-compressed beam, so that the bistable mechanism could be efficiently produced in bulk fabrication, to lower the geometrical limit Q, in order to have smaller strokes with the same beam thickness (limited by fabrication techniques), and to have symmetrical Force-Displacement behavior.

2.3.1 Design and pre-load

The designed structure consists of two pre-shaped beams, with the same dimensions, which are configured to be antagonistic to each other (figure 2 - 5a). These two beams are embedded in two bracket-like supporting structures and clamped at the midpoints. Between the supporting structures of each beam, a gap equals to $2\times h$ is defined. After the structure is fabricated, it will be firstly pre-loaded by compressing one of the supporting brackets until the gap disappears and secondly the two parts will be fixed together.

According to the third Newton's law of motion, during the pre-load operation, the forces exerted onto two beams' mid-points have the same magnitude. Since the beam used in our design is pre-shaped beam, the Force-Displacement behavior will be similar with the one shown in figure 2 - 4c. Because of the fabrication defects, these two beams are not perfectly with the same strength as they are designed. Therefore, the beam, which is relatively weak (e.g., beam 2 in figure 2 - 5a), will firstly reach its maximal force that it can bear. Then, it will be pushed, by the stronger one (beam 1 in figure 2 - 5a), to the position near its second extreme position. At the same time the force bearable of beam 2 will be largely decreased, thus, force applied on beam 1 will also decrease. Then, beam 1 will recover to the position near its original position and the two beams will reach an equilibrium state. This state will act as the stable position 1 for the whole bistable structure and it can be switched to the stable position 2 by an external force F (figure 2-5a). Based on the designed bistable mechanism, a quadristable mechanism was accomplished as shown in figure 2 - 5b. It is formed by two rows of bistable modules, the internal bistable module is embedded into the external bistable module.

Thus, the bistable mechanism based on centrally clamped antagonistic pre-shaped double beams can lower the difficulty of pre-load operation (especially for multiple rows of beams in pre-compressed beams configuration (figure 2 – 5 b and c). The distance that needs to be compressed during the pre-load operation is defined by the gap between two supporting brackets. So, the pre-load can be realized without the help of external instrument (e.g., linear stage or force sensors used in [ZAID 12]). Furthermore, there is no additional pre-load operation for the quadristable mechanism. It could be realized through only one compression. It is simpler than multistable actuator based on pre-compressed beams (figure 2 - 5c), which needs multiple compressing forces exerted onto the structure at the same time.

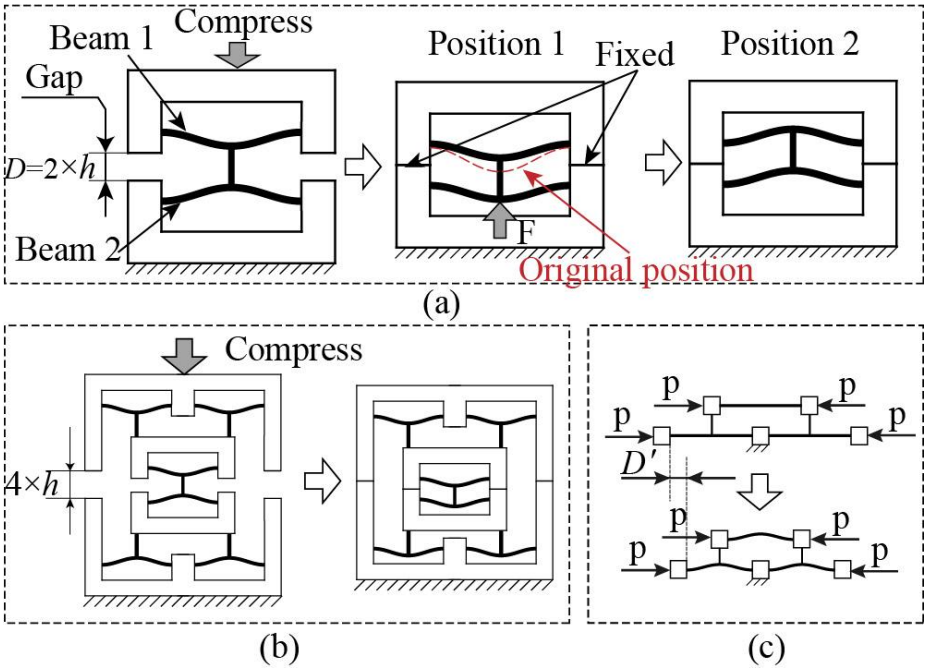

Figure 2 - 5. (a) Pre-load of bistable mechanism based on antagonistic pre-shaped double beams; (b) Pre-load of quadristable mechanism based on antagonistic pre-shaped double beams; (c) Pre-load of quadristable mechanism based on pre-compressed beams.

Moreover, the pre-load operation is less sensitive with pre-load errors. For antagonistic pre-shaped double beams based bistable mechanism, the distance to be compressed (gap D in figure 2 - 5a) equals the stroke $2\times h$. For pre-compressed beam, the distance, D', to be compressed equals to the difference between the length l' before the beam is compressed and length l after the beam is compressed (figure 2 – 6a). The distance D' includes two parts: D_p' which is caused by the compressive axial load p and D_c' which is the difference between l and the arc length s of the compressed cosine shape. According to the Euler-Bernoulli beam theory, before p reaches the critical value p_1 (could be calculated by equation 2.1), the beam will remain in the straight form. Then it is compressed and becomes shorter, this change D_p' can be calculated by the following equation:

$$D_p^{'} = l^{'}\frac{p}{EA} \tag{2.2}$$

Where, E is the elastic modulus of the material, $A = bt$ is the sectional surface area of the beam. When p reaches the critical value p_1 of buckling mode 1, the beam starts to curve and the axial p will stay at p_1 without further increasing. Then the change in length (D_c') is all caused by the curvature of the beam and it could be calculated by:

$$D_c^{'} = s - l = \int_0^l \sqrt{1+\left(\frac{dy(x)}{dx}\right)^2}\,dx - l \tag{2.3}$$

Where, $y(x)$ is the expression of the shape of the cosine curved beam:

$$y(x) = \frac{h}{2}\left(1-\cos\left(x\frac{2\pi}{l}\right)\right) \tag{2.4}$$

Thus, the total difference between l' and l is:

$$D' = l' - l = D'_p + D'_c = l' \frac{p_1}{EA} + \int_0^l \sqrt{1 + \frac{h^2\pi^2}{l^2} \sin^2\left(x \frac{2\pi}{l}\right)} dx - l \tag{2.5}$$

According to the equations presented above, the chart of half stroke *h* versus distance to be compressed *D* for antagonistic pre-shaped double beams and D' for pre-compressed beam was plotted in Matlab and presented in figure 2 - 6b. Apparently, half stroke h of pre-compressed beam is more sensitive with the change of compressed distance. It is obvious that curve for pre-compressed beam increases quite fast when the compressed distance is increased. Moreover, a zoomed view of the starting part of the curve for pre-compressed beam allows to see that before the compressed distance reaches a certain value (i.e., the axial load reaches the critical value for buckling mode 1), the beam stays straight. Once this critical value passed, *h* increases very fast. This characteristic could lead to the difficulty in controlling the half stroke h by the compression pre-load operation. Differently from pre-compressed beam, half stroke of antagonistic pre-shaped double beams has linear relation with the compressed distance. The compressed direction is shifted from the axial direction (the sensitive one) to the normal direction (the insensitive one). Thus, pre-load operation is easier to realize and control.

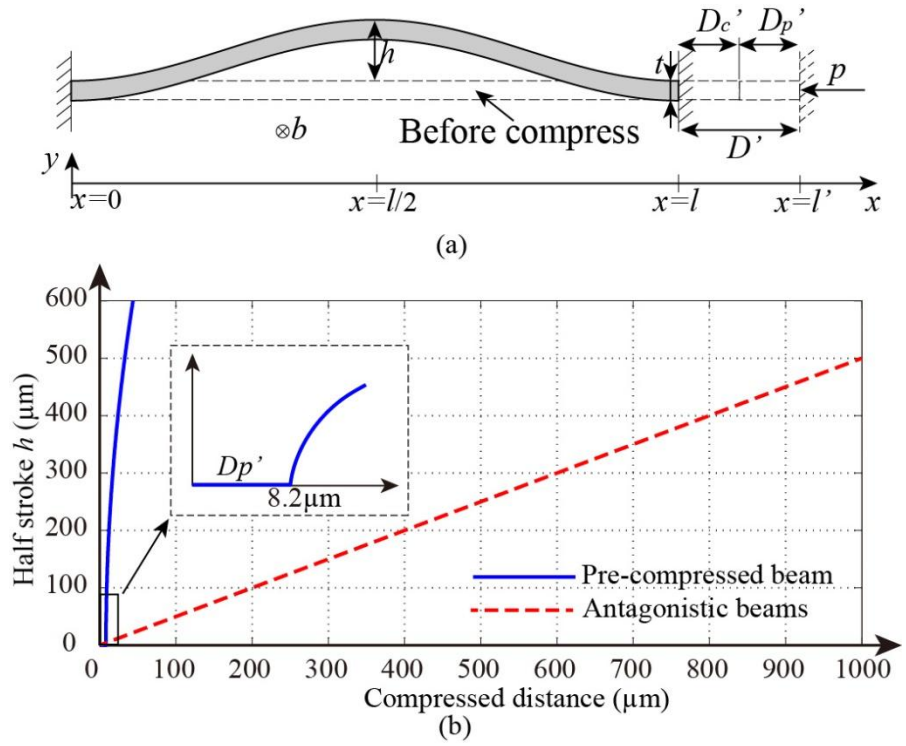

Figure 2 - 6. (a) Illustration of the distance which needs to be compressed for pre-compressed beam; (b) Chart of *h* versus compressed distance *D* for pre-compressed beam and D' for antagonistic double beams.

Let's take the beam with a length of l = 25 *mm*, a thickness of t = 250μm and a half stroke h = 500 μm as an example. The gap $D = 2 \times h$ which is also the stroke would be 1000 μm. For the pre-compressed beam with the same length, the distance D' needs to be compressed to get a same h (500μm) would be 32.9μm. Due to the error of fabrication or compress, if there is a variation of 10μm for D and D'. For antagonistic pre-shaped double beams, the stroke error introduced by the variation of D would have the same value of this variation, i.e., 10μm. But for the pre-compressed beam, the stroke error would be 228μm which is much larger.

2.3.2 Output force and energy analysis

As mentioned before, after the antagonistic pre-shaped double beams are pre-loaded and fixed, the beam 1 stays near its original position, so, the Force-Displacement behavior of beam 1, during the switching

process from position 1 to position 2 should be similar with the behavior of parallel pre-shaped double beams. During the same process, the beam 2 will recover from the position near its second extreme position to the position near its original position. Thus, the Force-Displacement behavior of beam 2 is the mirror of beam 1 with respect to the central line. Moreover, the two beams are antagonistic configured, so, the force of beam 2 should be reversed to below the displacement axis like it is shown in figure 2-7. Then, the total Force-Displacement behavior for whole bistable mechanism is the sum of beam 1 and beam 2. To be clear, the chart shown in figure 2 - 7 is for the state when Q < 2.31. Even if both beam 1 and beam 2 are not bistable, the whole structure is bistable and the force is symmetrical. In the Energy-Displacement chart, it is also obvious that there are two local minimal energy points for both two stable positions and the energy amount at these two points would be the same. Additionally, we can see that the two stable positions are moved for a small distance to the central line, which means the final stroke would be slightly smaller than $2\times h$.

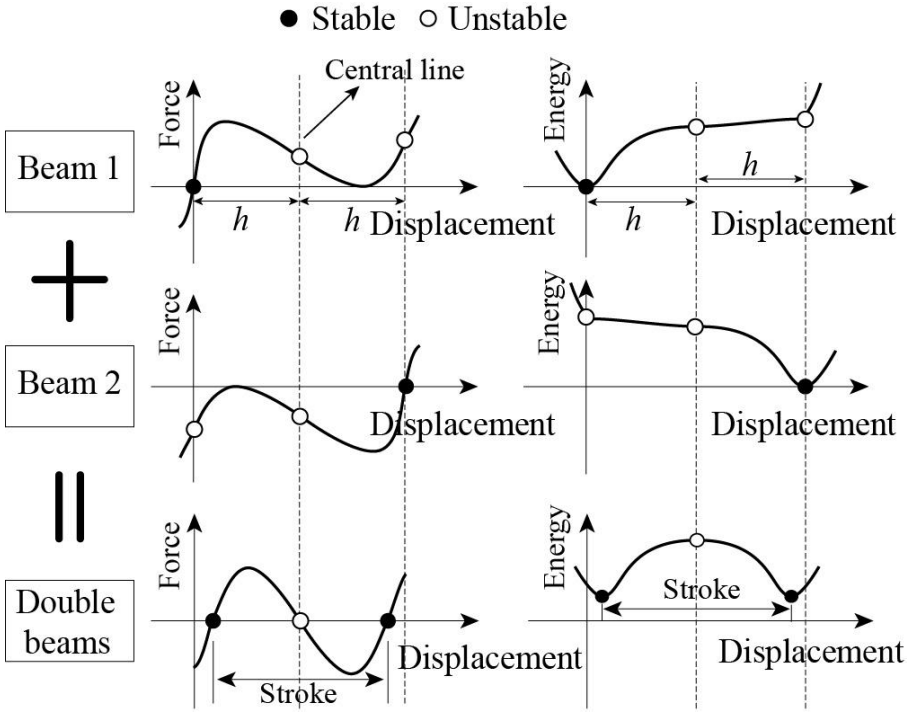

Figure 2 - 7. Force-Displacement and Energy-Displacement charts of the antagonistic pre-shaped double beams based bistable mechanism (Q<2.31).

2.4 Mathematical model

To calculate the force generated by the designed actuator, a model is constructed as shown in figure 2 - 8. The two ends of the beam are fixed. An external force F is applied at the midpoint in the vertical direction. In order to make the figure simple and clear, only one beam was shown in the figure, but, during the constructing of mathematical model, it is assumed that, two beams are used and the rotation of midpoints are constrained. Therefore, transitional buckling mode (deflected shape shown in figure 2 - 8) is the third buckling mode.

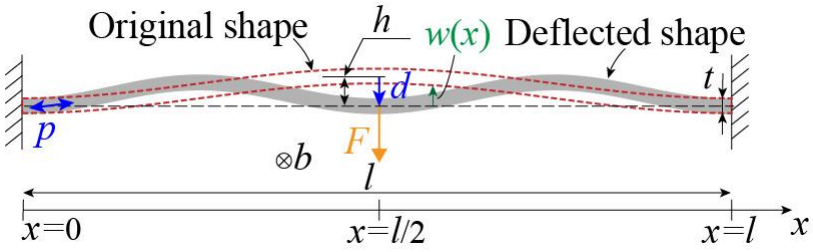

Figure 2 - 8. Model of a single pre-shaped beam with rotation of mid-point constrained.

According to the Euler-Bernoulli beam theory [TIMO 61], the buckled beam with a length of l, a thickness of t, a depth of b and a central original rise of h satisfies the following equation:

$$EI\frac{d^4w}{dx^4}+p\frac{d^2w}{dx^2}=0 \tag{2.6}$$

Where $w(x)$ is the deflection of the beam, E is the Young's modulus, $I = bt^3/12$ is the inertia moment of the cross section with respect to the axis of deflection, p is the axial load. Since both two ends of the beam are fixed, the deflection and rotation at the two ends will stay at 0. Thus, the boundary conditions are:

$$w(0)=w(l)=0 \tag{2.7}$$

$$\left(\frac{dw}{dx}\right)_{x=0}=\left(\frac{dw}{dx}\right)_{x=l}=0 \tag{2.8}$$

Then, the solutions should have the following forms:

$$w(x)=C_1\sin\left(n\frac{x}{l}\right)+C_2\left(n\frac{x}{l}\right)+C_3x+C_4 \tag{2.9}$$

Where, $C_1 \ldots C_4$ are constants, $n^2=pl^2/EI$. With the boundary conditions, it could be inferred that n must satisfy the following equation:

$$\sin\left(\frac{n}{2}\right)\left[\tan\left(\frac{n}{2}\right)-\frac{n}{2}\right]=0 \tag{2.10}$$

So, there are two cases which could meet the equation (2.10). The first case is when:

$$\sin\left(\frac{n}{2}\right)=0 \quad n=(j+1)\pi \quad j=1,3,5... \tag{2.11}$$

$$w(x)=C\left(1-\cos\left(n\frac{x}{l}\right)\right) \quad n=(j+1)\pi \quad j=1,\ 3... \tag{2.12}$$

We can see that, when j = 1, 3..., $w(x)$ is expression of buckling mode 1, 3, ... Then, when:

$$\tan\left(\frac{n}{2}\right)-\frac{n}{2}=0 \tag{2.13}$$

We have the solutions for the second case, which is also the expression of buckling modes 2, 4…:

$$w(x)=C\left(1-\frac{2x}{l}-\cos\left(n\frac{x}{l}\right)+\frac{2\sin\left(n\frac{x}{l}\right)}{n}\right)\quad n=2.86\pi,\ 4.92\pi\ldots\ j=2,4\ldots \tag{2.14}$$

For the pre-shaped beam fabricated with a cosine shape, the original position $\bar{w}(x)$ could be expressed as:

$$\bar{w}(x)=\frac{h}{2}\left(1-\cos\left(2\pi\frac{x}{l}\right)\right) \tag{2.15}$$

When the switching force *F* is applied at the mid-point where $x=l/2$, the mid-point will be deflected by a distance *d*:

$$d=\bar{w}\left(\frac{l}{2}\right)-w\left(\frac{l}{2}\right) \tag{2.16}$$

The arc length *s* will be:

$$s=\int_0^l\sqrt{1+\left(\frac{dw}{dx}\right)^2}\,dx\approx\int_0^l\left(1+\frac{1}{2}\left(\frac{dw}{dx}\right)^2\right)dx \tag{2.17}$$

Then, the axial load *p* could be calculated by:

$$p=Ebt\left(1-\frac{s}{s_{w=\bar{w}}}\right) \tag{2.18}$$

The compressive energy U_c, bending energy U_b, and actuation energy U_f due to the switching force *F* could be calculated by:

$$\partial(U_c)=-p\partial(s) \tag{2.19}$$

$$\partial(U_b)=\partial\left(\frac{EI}{2}\int_0^l\left(\frac{d^2\bar{w}}{dx^2}-\frac{d^2w}{dx^2}\right)^2dx\right) \tag{2.20}$$

$$\partial\left(U_f\right)=-F\partial\left(d\right) \tag{2.21}$$

The total energy U_t is the sum of the above three energies:

$$\partial\left(U_t\right)=\partial\left(U_c\right)+\partial\left(U_b\right)+\partial\left(U_f\right) \tag{2.22}$$

During the switching process, the boundary conditions don't change, so, the deflection *w*(*x*), can be expressed by superposition of an infinite set of buckling modes:

$$w\left(x\right)=\sum_{j=1}^{\infty}A_j w_j\left(x\right) \tag{2.23}$$

Where, A_j and $w_j(x)$ are the amplitude and deflection function of buckling mode *j*. Then, the variance of total energy $\partial\left(U_t\right)$ can be expressed with the superposition *w*(*x*). According the smallest energy theory, A_j should minimize the total energy variance $\partial\left(U_t\right)$, then, we have the following solutions [QIU 04]:

$$F_N(\Delta)=\begin{cases}\dfrac{3\pi^4Q^2}{2}\Delta\left(\Delta-\dfrac{3}{2}+\sqrt{\dfrac{1}{4}-\dfrac{4}{3Q^2}}\right)\left(\Delta-\dfrac{3}{2}-\sqrt{\dfrac{1}{4}-\dfrac{4}{3Q^2}}\right) & p_1\le p<p_2\\ 4.18\pi^4-2.18\pi^4\Delta & p_2\le p<p_3\\ 8\pi^4-6\pi^4\Delta & p>p_3\end{cases} \tag{2.24}$$

Where $F_N = Fl^3/EIh$ is normalized switching force, $\Delta = d/h$ is the normalized deflection, p_1, p_2 and p_3 are the critical axial loads for buckling modes 1, 2 and 3. $Q = h/t$ is the geometry factor. Now we can see that, to let $F_N(\Delta)$ exist when $p_1 \le p < p_2$, Q should satisfy:

$$\frac{1}{4}-\frac{4}{3Q^2}\ge 0 \Rightarrow Q\ge 2.31 \tag{2.25}$$

This is the geometry limit for parallel pre-shaped double beams. If we define the switching force for the antagonistic pre-shaped double beams as F_A, the normalized switching force $F_{NA} = F_A l^3/EIh$, then:

$$F_{NA}(\Delta)=F_N(\Delta)-F_N(2-\Delta) \tag{2.26}$$

The normalized Force-Displacement curves of central clamped parallel pre-shaped beam (F_N in figure 2 - 9) and antagonistic pre-shaped double beams (F_{NA} in figure 2 - 9) are calculated in Matlab environment. As it can be seen in figure 2 - 9, the antagonistic pre-shaped double beams need much smaller Q to be bistable (critical value is Q=1.16). When Q=2, the antagonistic pre-shaped double beams are already well bistabled, while the parallel pre-shaped beam just reaches the critical state when Q=2.31. So, it is possible to get smaller stroke. For example, for medium density fiberboard (MDF) cut by laser, the minimal thickness t that can be reached is about 250 µm, the theoretical minimal stroke for our design could be 580µm (2×Q×t when Q=1.16), while the minimal stroke for parallel pre-shaped beams would be 1155µm (Q=2.31). Furthermore, the force generated by antagonistic pre-shaped double beams is symmetrical in forward and backward directions.

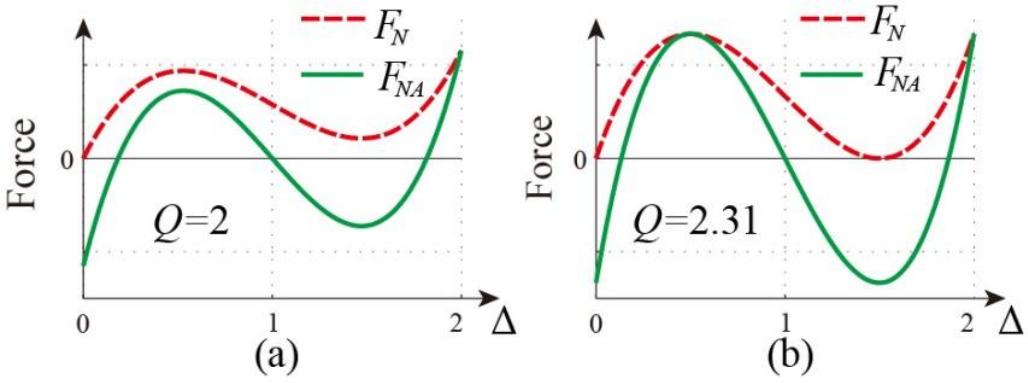

Figure 2 - 9. Force-Displacement curves from Matlab with different value of Q: (a) Q=2; (b) Q=2.31.

So, the designed bistable mechanism based on antagonistic pre-shaped double beams has the advantage of symmetrical force output. In addition, the pre-load operation is simpler than the pre-compressed beam, which leads to the possibility of efficient bulk fabrication. Moreover, the geometrical limit Q is lower than parallel pre-shaped double beam, so that with existing fabrication techniques we can have smaller strokes, which can benefit the applications that need high output resolution.

3 Meso-prototype Fabrication and Test

3.1 Fabrication

In order to validate the bistability of designed bistable mechanism, two kinds of techniques were adopted to fabricate the prototype: 3D printing and laser cutting.

3.1.1 3D printing

At first, the 3D printing technique was employed to fabricate the designed bistable mechanism. The 3D printer is INVision XT from KALLISTO company (figure 2 - 10a). The machine has a resolution of 328×328×606 DPI (Dots Per Inch). The model material is ultra violet (UV) polymer, the supporting material is hydroxied wax. StereoLithography (STL) files are accepted by the machine to construct the model. The STL file can be produced by CAD software CREO.

As mentioned in the previous section, there is the limite of factor *Q* for the pre-shaped beam, so the smallest stroke of the micro-actuator depends on the thickness of the beam. Therefore the thinner the beam is the smaller the stroke can be. Because of the resolution of the machine, the thinnest beam that can be fabricated is 42μm. But this value is given for flat layers. Since the beams are curved, multiple layers are necessary to construct the desired form. For the first time, micro-actuators with a beam of three and four layers thick are fabricated. The general shape of the meso-actuator is shown in figure 2 - 10 b.

Due to the working principle of 3D printer, all the cavaties in the model will be filled by the support matierial (VisiJet SR200) which is a kind of hydroxy wax. So after the micro-actuator was taken out from the work space of the 3D printer, the whole actuator was surrounded by wax (figure 2 - 10c). Before further tests of fabricated meso-actuator, wax need to be removed.

According to the data sheet of the material VisiJet SR200, the melting point is 60^{o}C. So firstly, hot water was used to melt and remove the wax. It was found that the structure was not cleaned very well, the efficiency was low. Then an ultrasound vibrating bath was used to improve the speed and the cleanning effect. After using this machine, the cleaning process was improved but we found that some structures were destroyed by vibration. Moreover, after the cleaning action of hot water, the pre-shaped beam (cosine shape) became straight. In addition, the surface of the material changed into white color (figure 2 - 10d). There are three possible reasons that may have caused the curved beam to be straight: 1) The resolution of the 3D printer is not sufficient to fabricate the cosine shape with a very small amplitude (h = 168um); 2) There is residual stress that remained in the structure after the fabrication process, which may be caused during the solidify process by UV light; 3) The hot water caused shrinkage of the thin part of the structure and the beam was straightened by itself. For the changing of color, the high temperature may be the reason.

After the troubles caused by high temperature, organic solvent came to be another solution for the wax cleaning job. We chose organic solvents ethanol and gasoline to melt the wax.

Gasoline is a very efficiency solvent. Wax was cleaned after a few minutes at room temperature. However, at the same time some material of the bistable actuator was also eroded. The outer support frame was deformed slightly (figure 2 - 10e). The beam was elongated obviously and became very soft. After the gasoline evaporated the beam shrunk to straight like the one cleaned by hot water. The color also changed. The difference is that not only the surface but also deep inside the material the color was changed. The material became a kind of honeycomb-like structure. The material lost its elasticity and became very fragile.

Ethanol is not as efficient as gasoline. Ultrasound vibrating bath was used to accelerate the process at room temperature. The similar problem as cleaned by gasoline came out. The beam was elongated when it was wetted by ethanol and after the ethanol evaporated, the beam shrunk to straight. The color changed to white and structure became fragile. The difference is that the support frame did not have obvious deformation.

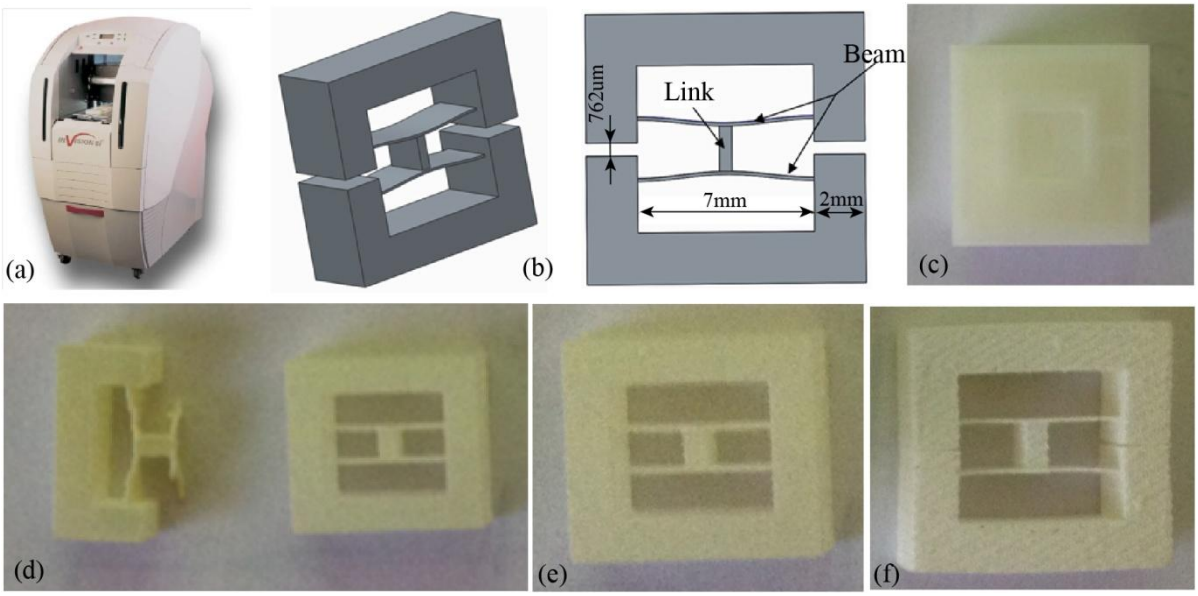

Figure 2 - 10. (a) 3D printer IN Vision XT; (b) CAD model of the designed bistable actuator; (c) Printed bistable actuator with supporting material (wax); (d) Cleaned by hot warter; (e) Cleaned by ethonol; (f) Cleaned by gasoline.

Therefore, this 3D printing process is not suitable for the fabrication of the antagonistic pre-shaped double beams based bistable actuator. Finally a laser cutting process was adopted for the fabrication which will be discussed in the following part.

3.1.2 Laser cutting

After the failure in fabrication with 3D printer, the technique of laser cutting was adopted to realize the designed structure. The laser cutting machine employed was the Trotec Speedy 400 with CO_2 laser and its maximal power is 120W (figure 2 - 11a).

Different materials were tested with the laser cutting machine, includes acrylic, epoxy and medium density fiberboard (MDF). Due to the working principle of laser cutting, there is apparent melting effect on the plastic material (acrylic or epoxy). Therefore, after cutting, the curved beam cannot maintain the designed shape. Finally, it is proven that the MDF material could remain the designed shape after it is cut (and heated) by laser beam. MDF is a composite of wood fibers and resin, so, when it is heated, the wood fiber could offer the support for the structure. Thus, melting effect observed in cutting acrylic or epoxy is largely reduced. However, due to the high temperature of laser beam, the surface of cutting side wall was burnt and carbonized. After the test with different cutting speed, laser power and laser pulse frequency, it was concluded that, cutting process with high power (120W) and frequency (9000kHz) at the speed of 3mm/s could have the least burning effect for the 3mm thick MDF.

A quadristable meso-actuator was fabricated by laser cutting on MDF. It is a combination of two rows (inner row and outer row) of central clamped antagonistic pre-shaped double beams (figure 2 - 11b).

After the pre-load operation (figure 2 - 11b), both the inner and outer row has two stable position, thus, the output point should have four stable positions.

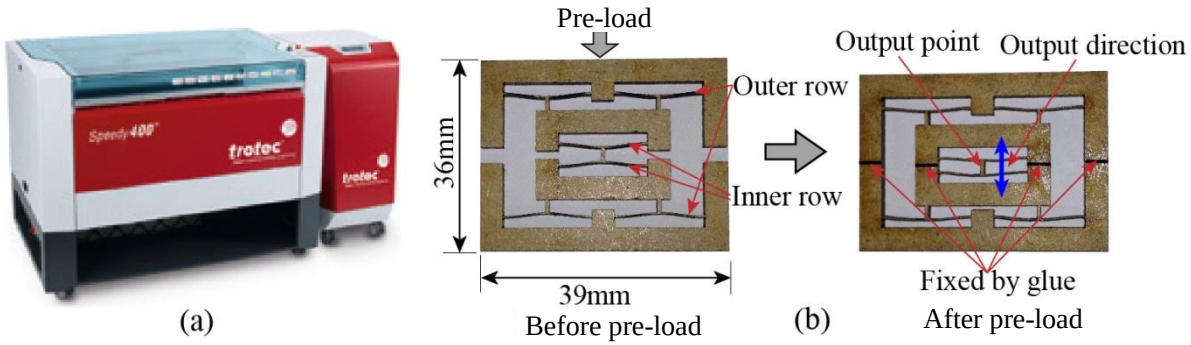

Figure 2 - 11. (a) Laser cutting machine Trotec Speedy 400; (b) Quadristable structure fabricated from MDF by laser cutting.

3.2 Tests

3.2.1 Actuation with linear motor

To test the multistability of the fabricated quadristable actuator, an experimental setup was arranged like it is shown in figure 2 - 12. In order to verify the bistability of designed bistable mechanism based on antagonistic pre-shaped double beams, a linear motor (Newport MFA 25CC) was used to switch the actuator between the stable positions. The optical fiber distance sensor[2] [PREL 06] was used to measure the output movement at the output point. With the aim of improving the sensitivity of optical fiber distance sensor, a small mirror is glued on the output point. The data were collected through National Instruments acquisition card in LabVIEW. The test results are shown in figure 2 - 13.

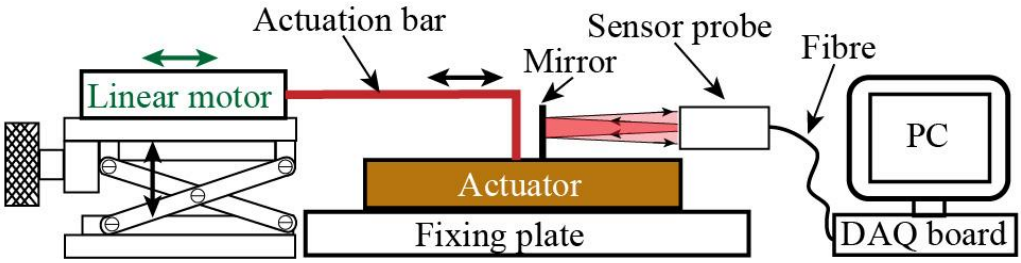

Figure 2 - 12. Schematic of the experimental setup for multistability test with linear motor.

In figure 2 - 13, it is obvious that, in one switching cycle, there are four stable positions: two for inner row and two for outer row (since the stroke for inner and outer is designed with the same value, stable position 2 and 4 are almost at the same position). Thus, the multistability of the designed quadristable actuator is proved. The measured strokes for both inner and outer rows are 970±1 μm over 100 cycles.

If we take the inner row as an example, the zoomed step response (figure 2 - 13) can be divided into two parts. The part indicated by M corresponds to the duration when the bistable double beams were pushed by the linear motor through the actuation bar (A top view schematic of the switching process for inner row is shown in figure 2 - 14). Limited by the maximal speed of linear motor, the gradient of part M is relatively small. After the double beams are pushed across point *b* (figure 2 - 14), which is an equilibrium point, the force needed to switch the double beams becomes negative which means they can reach point c automatically. This is called "snap effect" which is indicated as S in figure 2 - 13 and figure 2 - 14. The time duration of the part *S* is 10 - 20ms which leads to a big gradient of part S in figure 2-13.

[2] See also paragraph 7.2.2 of chapter 3 for additional details on this sensor.

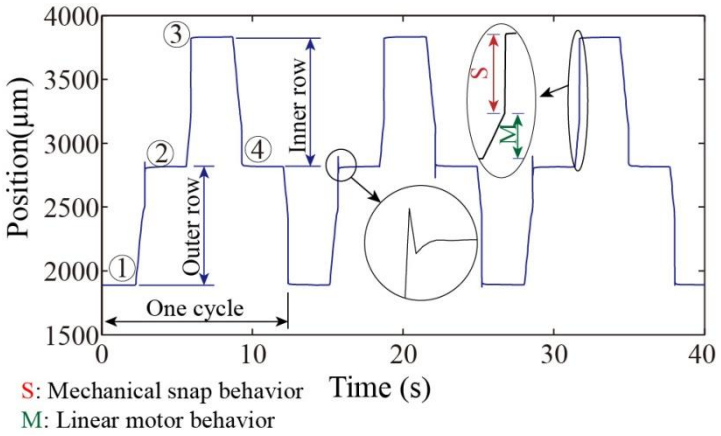

Figure 2 - 13. Multistability and snap time tests of the designed multistable actuator switched by linear motor (l = 15 *mm*, b = 3 *mm*, t = 250 *μm*, h = 500 *μm*).

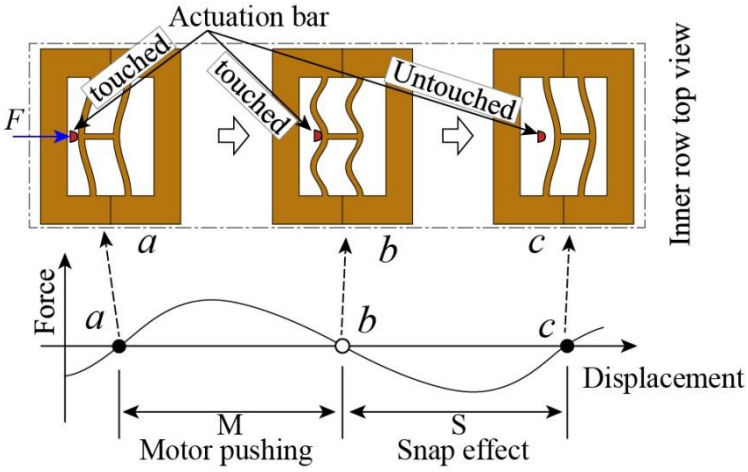

Figure 2 - 14. Snap effect during switching

3.2.2 Actuation with laser heated SMA

Since, the multistable actuator has low level power consumption, it is possible to actuate it with contactless method using laser heated SMA active elements. Due to a reversible diffusionless solid to solid transformation that results in large reversible strains, SMAs are suitable for a wide range of actuators, energy absorption and vibration damping applications [BAXE 12, PERK 75, FUNA 87, DUER 90, OTSU 99, LAGO 08, TAI 11]. Nitinol (Nitinol: alloy of Nickel and Titanium) was chosen for the SMA active elements (bit of sheets) due to its better thermo-mechanical properties as compared to the other shape memory alloys [HUAN 02]. The SMA sheet was purchased from Johnson Matthey company in annealed state. The austenitic warm form is flat and the chemical composition was 55% Ni–45% Ti (wt%). Red laser diode (wavelength λ = 660 *nm*) was used as the energy source for heating SMA elements, because of its high electrical to optical efficiency. Finally, the switching of the inner row of the multistable actuator was realized using two antagonistic SMA elements heated by the laser.

The experimental setup for switching the inner row using laser heated SMA active elements is represented in figure 2-15. In this setup, two SMA active elements with the dimension of 3×1×0.1mm were used. These active elements were fabricated by a laser cutting process (Q-switched Nd:YAG laser at a wavelength of 1064 nm and an average power of 7W).

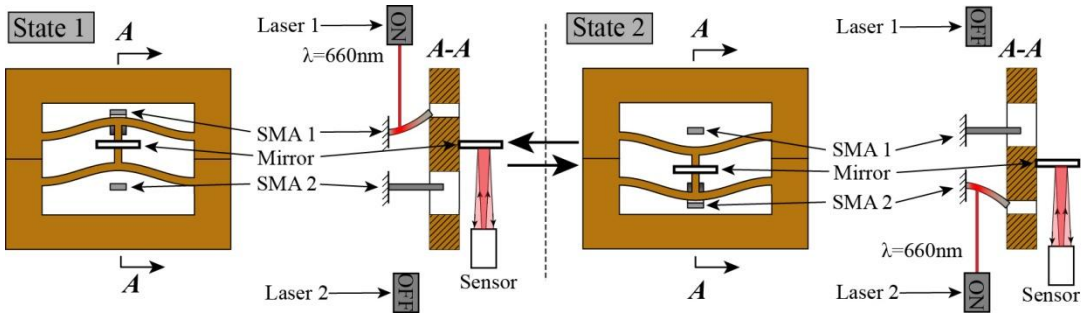

Figure 2 - 15. Experimental setup for switching of the inner row using laser heated SMA sheets.

In figure 2-15, for each stable state, the left side shows the top view, while the right side shows the cross section view. At state 1, the bistable double beam is at its upper stable position. SMA 1 is bent by the beams. Then laser 1 is turned on, SMA 1 is heated to the final transform temperature of the austenite phase. Due to the shape memory effect, the SMA 1 starts to recover its austenitic form, i.e., flat. Thus, a force is exerted on the beams and pushes them towards the lower stable position. When the double beams reach the central position (point b in figure 2-14), the snap effect starts pushing SMA 2. Finally, SMA 2 is bent. After some time, when SMA 1 is cooled down, the beams can be switched back to upper stable position by turning on laser 2 to heat SMA 2.

During the switching process, the movement of the output point, where a mirror is glued, is measured by an optical fiber distance sensor [PREL 06]. The results are shown in figure 2 - 16. The stroke between two stable positions is 681 ± 4 µm over 5 cycles. It is much smaller than the stroke when the actuator is switched by linear motor. Here, one of the SMA active elements is acting as a load during the switching process, e.g., SMA 2 is the load when the double beams are switched from upper stable position to lower stable position. So, there is an equilibrium point when the force of beams equalizes the force generated by SMA active element. Obviously, this point will be reached before the stable point when there is no load. This load effect from SMA active elements can be eliminated by adding a biasing spring to the SMA active elements and create an artificial "two way memory" effect [ALI 10]. This work will be presented in later chapters.

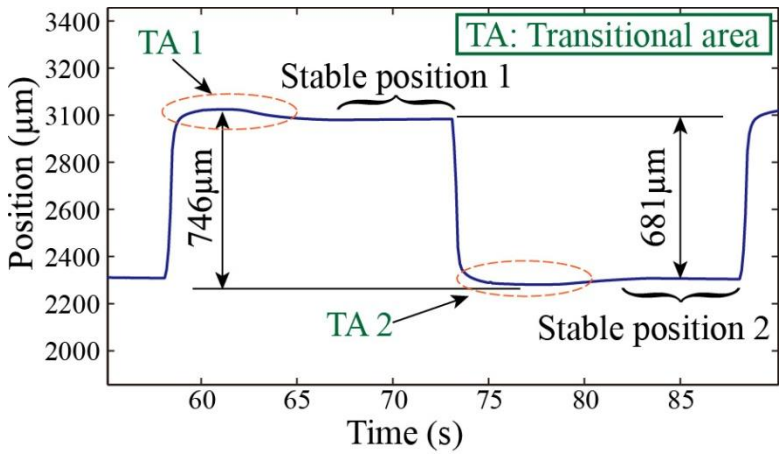

Figure 2 - 16. Test of switching with laser heated SMA active elements (l = 15 *mm*, b = 3 *mm*, t = 250 *µm*, h = 500 *µm*, λ = 660 *nm*).

4 Fabrication of Quadristable Micro-actuator on Silicon

As discussed in former part, the smallest stroke for bistable mechanism based on antagonistic pre-shaped double beams depends on the thickness of beam, i.e., the thinner the beam is the smaller the stroke could be. However, the smallest attainable thickness of beam relies on fabrication

techniques. In former section, the thinnest beam cut by laser on MDF is 250 µm, thus, the stroke of the prototype quadristable actuator is also big (970 µm). In order to reduce the stroke, micro fabrication technique DRIE was employed to manufacture the quadristable micro-actuator on silicon wafer.

4.1 DRIE Technique

DRIE is a highly anisotropic dry etch process. Due to the ability of creating deep penetration and trenches with vertical side walls, it is commonly used for fabrication of micro electro mechanical systems (MEMS) which require features with high aspect ratios. The designed quadristable micro-actuator has uniform cross section, therefore, it can be considered as a 2D design and DRIE is a suitable process for the micro-actuator's manufacturing. Furthermore, in order to constrain the movement of bistable beams in the plane, the beams should have high aspect ratio (*b*/*t*). Thus, DRIE is adopted to realize the fabrication of the designed quadristable micro-actuator.

There are two main DRIE processes with high etching rate: Bosch process and Cryogenic process. Among them, Bosch process is more recognized and commonly used because it can be carried out under ambient temperature while the Cryogenic process needs a very low temperature (-110 ^{o}C) which could lead to some problem like crack of some material. For the fabrication of the quadristable micro-actuator, Bosch process was employed to simplify the fabrication process and avoid the unwanted problem which could be caused by low temperature.

The Bosch process' basic principle of how to create vertical sided wall with high aspect ratio is repeatedly switch between etching and passivation process. Therefore, the previously etched side wall could be protected by passivation layer. The basic steps of Bosch process for silicon substrate are explained in figure 2 - 17.

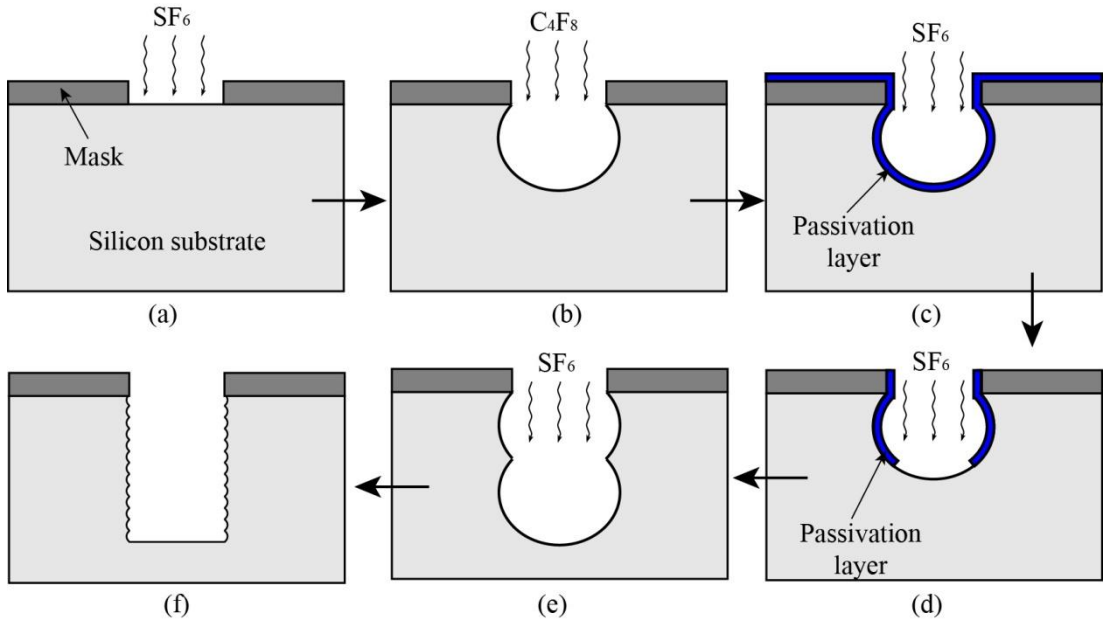

Figure 2 - 17. Bosch etch process: (a) First etch cycle with SF_6; (b) First passivation with C_4F_8; (c) (d) and (e) Second etch cycle; (f) Vertical side wall with multiple etch-passivation cycles.

Firstly, it is assumed that the mask (normally SiO_2 layer) is developed. The first step is started with the etching process using etchant, such as SF_6 gas. Since the simple etching process is isotropic, therefore, after a duration of etching, the unmasked substrate will be etched with a sphere shaped hole. Then, the gas is changed to C_4F_8 and first passivation process is started. After a while, a chemically inert passivation layer will be created on the surface. Then, the gas will be switched back to etchant SF_6. In the second etching process, the ions, which are accelerated in the vertical direction, will mainly

bombard the bottom surface of the etched pit. The passivation layer at the bottom surface will be sputtered off first and the etching gas will create a second sphere shaped pit under the former one. Due to the protection of passivation layer on side wall, the pit etched in the first step will not be enlarged in the second etching cycle. Reducing the duration of etching and passivation cycles, trenches with vertical side walls could be created like it is shown in figure 2 - 17d.

4.2 Mask Design

In etching process, the structured pattern is defined by mask. To achieve better results, mask design should be adjusted with respect to different processes and different substrates. In order to have controlable etching width and better results, the mask was designed to have uniform etching trenches with the width of 50 µm (the dark area in figure 2 – 18b and c). Furthermore, due to the fact that there are some very fragile features (25 µm thick bistable beams), silicon on insulator (SOI) wafer was chosen to protect the beam from breaking during the etching process. Therefore, after the pattern was etched, the structure should be released from the handle layer of SOI wafer. However, there are also some features with big surface area (supporting brackets), which will largely increase the duration of release process. To accelerate this process, "releasing holes" (50×50 µm) are added for those big area features. It can be considered that these "releasing holes" separate these big areas into small pieces. The releasing solvent (normally HF acid was used) could go through these "releasing holes" and remove the insulation layer around all the release holes at the same time. Furthermore, the adding of release holes could also largely reduce the mass of inner row, which is supported by the beams of outer row. With less mass, the stress on outer row's beams is also reduced which leads to longer life span of outer row.

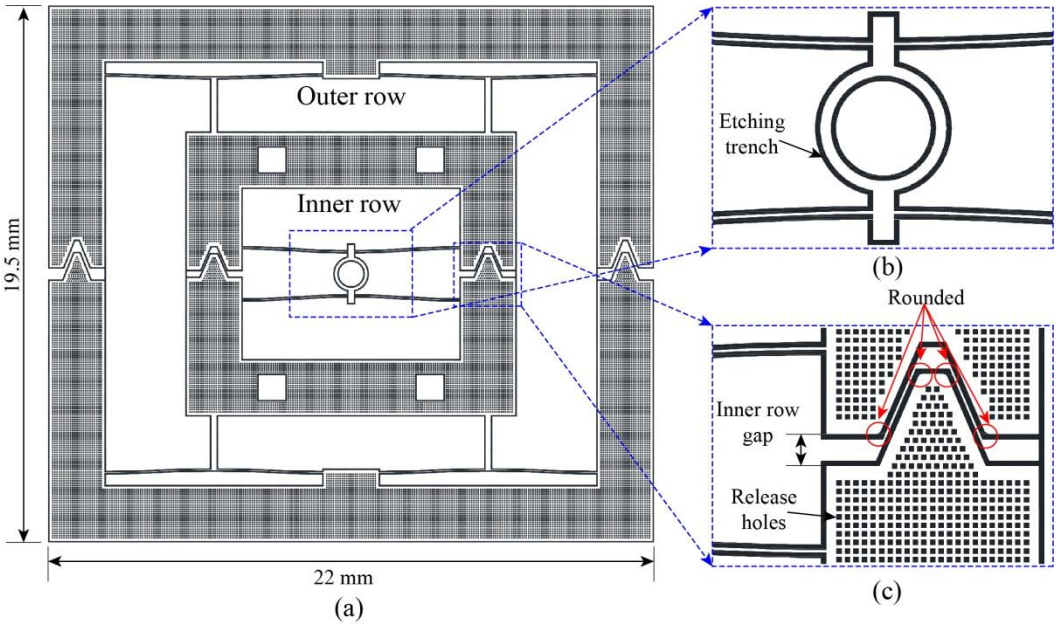

Figure 2 - 18. Photomask of quadristable micro-actuaotr's DRIE farication.

Except the addition of "releasing holes" and smaller size, the design is quite similar with the meso-prototype described in former part. However, some optimizations were done to facilitate the manipulation of micro-devices. The first change is that at the output point (the link part of inner row beams), a circle (figure 2 - 18b) with 1 mm diameter was added for the insertion of an end effector or small mirrors for stroke measurement with fiber optical distance sensor. Another change is at the gap part between supporting brackets (figure 2 - 18c). As it is shown, the flat gap was changed into trapezoidal shape. In this configuration, the flat part will define the gap between two brackets while

the inclined part would help the alignment between two brackets. Considering the fabrication error, there would be conflict at the corner parts, therefore, it is rounded at the corners of the trapezoidal gap.

4.3 Micro-fabrication Workflow

The workflow of the micro-fabrication for quadristable micro-actuator is explained in figure 2 - 19. The SOI wafer, which has a device layer of 400 µm, was used. The insulation and handle layer's thickness is 3.5 µm and 500 µm, respectively. In the first step, the SOI wafer was oxidized in oven at a temperature of 1100 ^{o}C to grow a 4.5 µm thick SiO_2 layer on both top and bottom surface. This SiO_2 layer will be developed as the mask for DRIE process. Then, photoresist resin was spin coated (3500 rpm for 30 s) and soft baked in oven (110 ^{o}C for 15 minutes). After UV light exposure, the exposed resin was removed and hard baking was completed in oven. CHF3 gas was used to remove the unprotected SiO_2 layer and develop the mask for etching process. After mask development, photoresist resin was removed by acetone. Then, the etching process was carried out with repeatedly switched SF6 and C4F8 gases at the temperature of 20 ^{o}C. Finally, the micro-actuator was released from SOI wafer with 50% HF acid.

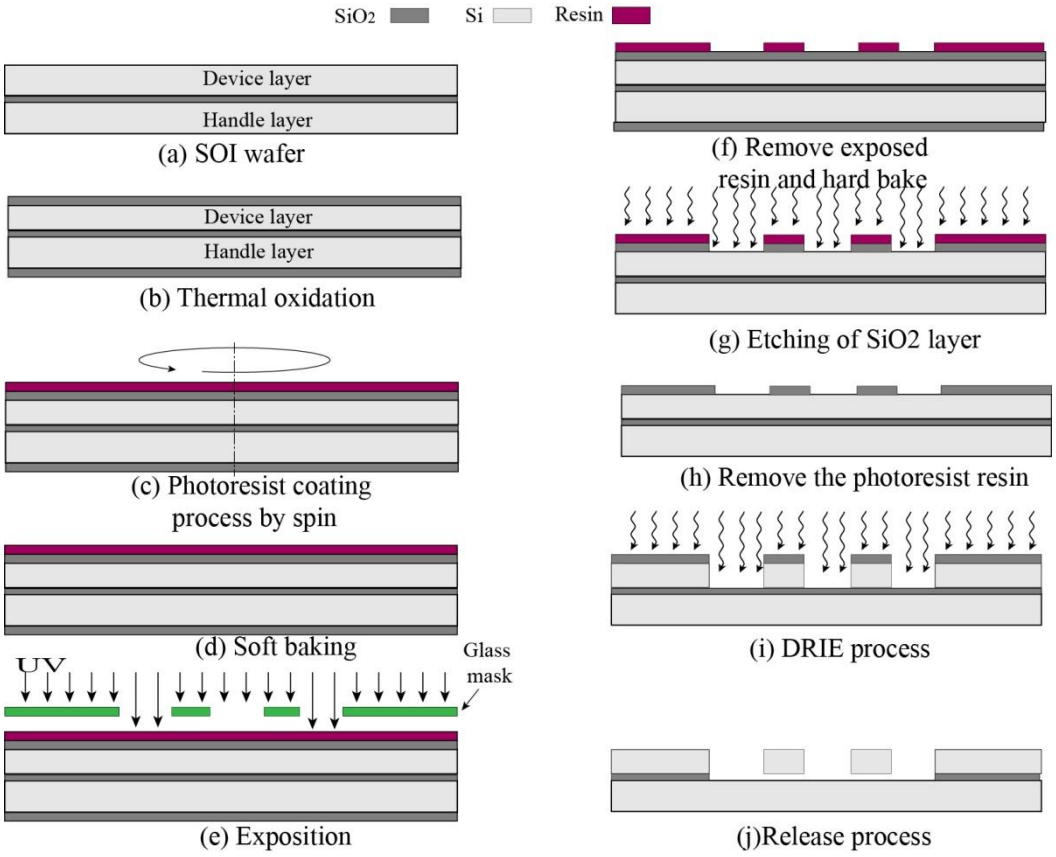

Figure 2 - 19. Micro-fabrication working flow.

The fabricated quadristable micro-actuator is shown in figure 2 - 20. The length of the fabricated bistable beam is 8 mm, the thickness is 25 µm and the original rise *h* of the midpoints for inner row and outer are 150 µm and 100 µm respectively. The inner diameter of the circular central link is 1 mm. Releasing square holes with size of 50 × 50 µm and separated by a distance of 30 µm are etched on the brackets area. The trapezoidal gap was well realized with rounded corners. Furthermore, the side walls of the structure are vertical and smooth.

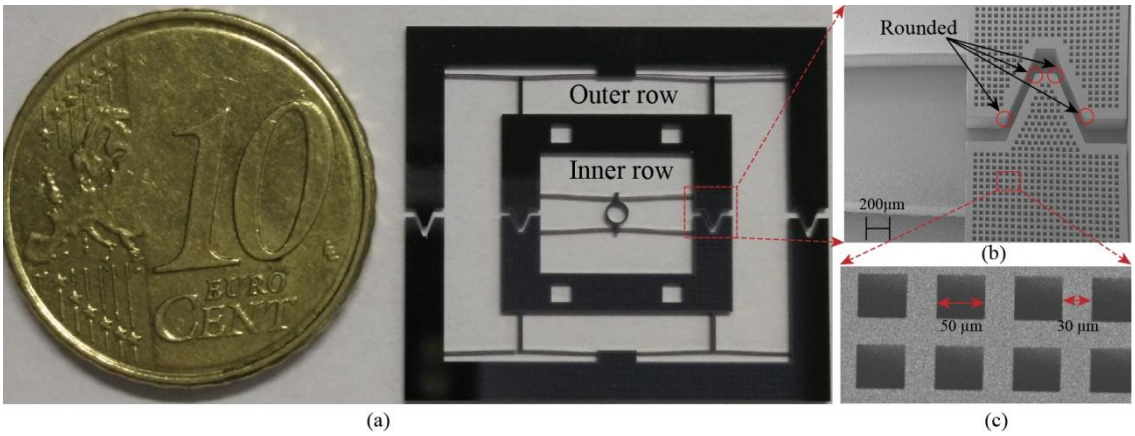

Figure 2 - 20. Fabricated quadriastable micro-actuator on silicon wafer: (a) Quadristable micro-actuator; (b) SEM photo of the trapezoidal gap of inner row; (c) SEM photo of the release holes.

5 Conclusion

A bistable mechanism based on antagonistic pre-shaped double beams was designed, analyzed, fabricated and tested. The bistability is confirmed by mathematical model and experimental results. Moreover, the designed bistable mechanism has the advantage of symmetrical force output as pre-compressed bistable beam, while the pre-load operation is easier than the pre-load of pre-compressed beam. At the same time, the stroke is less sensitive with fabrication assembly errors as compared with pre-compressed beam. Although, pre-shaped beam was employed as the bistable mechanism, the antagonistic configuration has solved the problem of asymmetrical force output for parallel pre-shaped beams configuration. Furthermore, it has lowered (divided by 2) the geometrical limit Q for pre-shaped beam, which could lead to the possibility of smaller output stroke for a given size. Based on the designed bistable mechanism, a prototype of quadristable meso-actuator was fabricated on MDF using laser cutting machine. Limited by the precision of laser cutting machine, the thickness of the beams are 250 µm and the strokes for both inner and outer row are around 970 µm. The prototype's quadristability was validated with the help of a linear motor. At the same time, its inner row was successfully actuated with a wireless approach using laser heated SMA elements. To reduce the stroke of the actuator, a quadristable micro-actuator was fabricated on silicon wafer employing DRIE technique. Bistable beams with 25 µm thickness were realized and the strokes for inner row and outer row were reduced to around 300 µm and 200 µm respectively.

Chapter III

Actuation Method

1 Introduction

As we have mentioned, the multistable micro-actuators have low power consumption level, therefore, it is possible to actuate it with weak and contactless power coupling method like laser or radio frequency electromagnetic waves. However, the exploitation of radio frequency electromagnetic waves need additional circuits to couple the power emitter and receiver. This additional unit would increase the complexity and the mass transported of the system. At the same time, this will need more fabrication process to integrate the additional circuits. Thus, we chose laser heated SMA elements as the contactless actuation approach which is proved to be feasible in [ZAID 12]. In chapter 2, laser heated SMA elements were utilized to actuate the inner row of the prototype quadristable meso-actuator. The experimental results have shown that the exploitation of SMA will largely influence the stroke of bistable beams, because the SMA elements added an extra load on these beams. Therefore, it is necessary to find a way which can recover the SMA elements to its original cold bent state, so that the load effect could be eliminated. In this chapter, the approach of using deposited SiO_2 layer as biasing spring will be presented. Furthermore, the test of the silicon quadristable micro-actuator will be discussed.

2 SMA with SiO_2 Layer

2.1 Working principle

Before the discussion of SMA with biasing SiO_2 layer, it is better to have a look at the situation when there is no biasing spring, so that, we can understand what is the reason that has caused the reduction of stroke and how we could solve the problem.

Figure 3 - 1 presents one switching cycle for the situation that only SMA elements are used to actuate the bistable beam. Since the SMA material we used is a “one way” memory alloy, SMA 1 remains in straight form after it is cooled down (figure 3 - 1c). Thus, when bistable beam is switched back by SMA 2, SMA 1 will act as the load of bistable beam. This is the reason why the stroke is shorter than the original designed stroke.

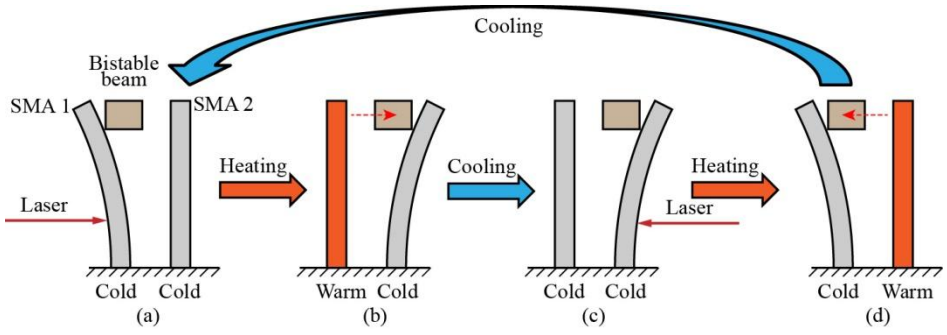

Figure 3 - 1. One actuation cycle of bistable beam with two “one way” SMA elements.

To solve this load effect from SMA elements, it is necessary to re-bend the SMA element after it is cooled down. One of the already proved approaches to bend SMA element after it is cooled down is to deposit a compressive SiO_2 layer on one side of the SMA element and using the SiO_2 layer as the biasing spring [ALI 10].

As shown in Figure 3 - 2a and b, because the thermal expansion ratio of SMA material (Nitinol: 55%Ni - 45%Ti (wt%)) is bigger than SiO_2, after they cooled down from the high temperature of deposition process, SMA material will shrink more than SiO_2 layer. As a consequence, compressive

stress is created in SiO_2 layer. Due to this stress, SMA will be bent together with SiO_2 layer (figure 3 - 2b).

Using the SMA element with SiO_2 layer, which can be regarded as "two ways" memory SMA, bistable beams could be actuated without load effect (figure 3 - 2c - f). Firstly, the bent SMA (SMA 1 in figure 3 - 2c) in cold state is located to the position where there is no contact with bistable beam. Then, SMA 1 is heated by laser and reach the final phase transform temperature (A_f: Austenite final temperature). The martensite phase in SMA 1 is converted into austenite phase which has higher elastic modulus. Due to the shape memory effect and higher elastic modulus, SMA 1 tends to recover the straight memorized shape. This recovery action converts light energy to mechanical energy which is used to switch bistable beam from the left stable position to the right (figure 3 - 2d). Then, laser is turned off, SMA 1 is cooled down, austenite phase retransformed to martensite phase. The SiO_2 layer becomes stronger and bent SMA 1 and itself to the original shape in cold state (figure 3 - 2f). Therefore, when bistable beam is switched back to the left stable position, SMA 1 would not block it in its path. The load effect is eliminated. Bistable mechanism conserves its original designed stroke.

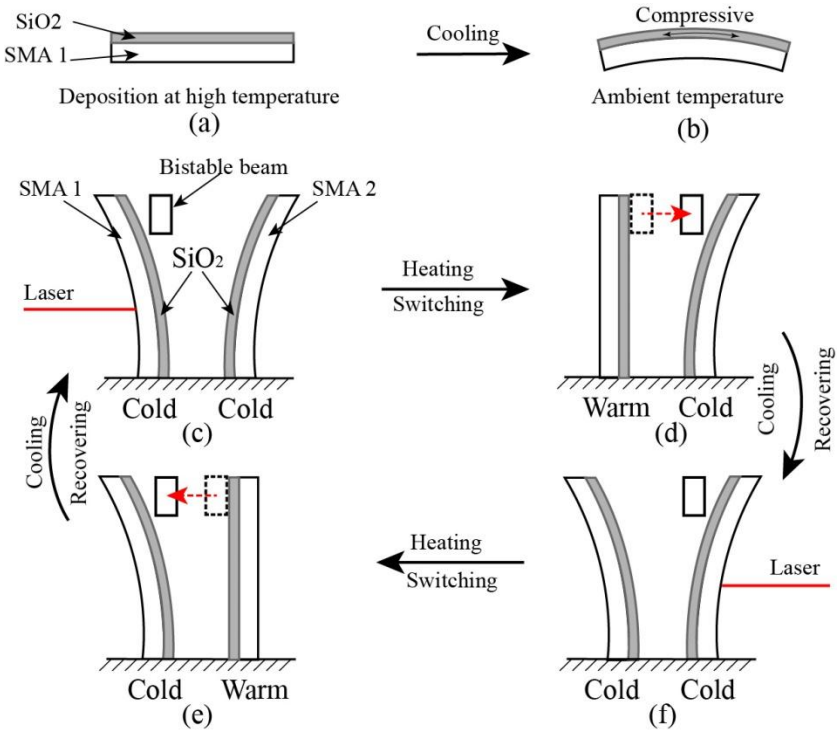

Figure 3 - 2. Compressive SiO_2 layer used as biasing spring for SMA element.

2.2 Mathematical Model

In this part, a mathematical model for SMA element with deposited SiO_2 layer will be constructed. Formulas will be inferred so that we could calculate the stroke of the SMA element.

For the SMA material, the physical properties change with temperature and loads, thus, before creating the model for the SMA element, it is necessary to have a look at these properties [ZAID 11c]. Figure 3 - 3a, shows the phase transformation of SMA material. The shape memory effect is based on phase transformation between martensite and austenite phases. There are four critical temperatures for the phase transformation of SMA. When SMA is heated, the transformation from martensite to austenite phase starts at austenite start temperature (A_s) finishes at the austenite final temperature (A_f). When SMA is cooled down, transformation from austenite to martensite phase starts at martensite start temperature (M_s) and finishes at the martensite final temperature (M_f). The low temperature phase of

SMA is a special martensite which is called thermoelastic martensite. When it is cooled down from high temperature ($T > A_f$) to low temperature ($T < M_f$), the crystalline structure is in twinned state like it is shown in figure 3 - 3a. If load is applied on the twinned crystalline structure and the caused stress reach a certain critical value, the detwinning process will start. This process is similar with the transform from parallelogram to square then to parallelogram. The bonds between atoms are rotated with respect to the atoms, like the rotation of joints, therefore, the necessary force to realize this detwinning process is very small. In the correspondant stress-strain chart, we can see that the curve for this process is almost horizontal which will lead to the result, in the macro view, that the elastic modulus for this part is very small. After the plastic deformation (partially or completely detwinned) is made, if the SMA is heated up to the temperature higher than A_s, the detwinned crystalline (and twinned, if not all of them are detwinned) structure will transform to austenite phase which has more stable crystalline structure (higher elastic modulus). Because the austenite phase has the same shape with twinned martensite phase (self-accommodation property of thermoelastic martensite), the deformation will be recovered completely, if no sliding happened in crystalline structure. This is called shape memory effect.

There is another property of SMA material that is called super elasticity which happens when temperature is higher than A_f. If the stress reaches a certain value (which corresponds to point D in figure 3 - 3b), the stress will cause the transformation from austenite to detwinned martensite. After the load is withdrawn, detwinned martensite phase will retransform back to austenite phase. Due to this reversible phase transformation, SMA material can undertake several times more deformation than normal metal materials without causing plastic deformation. This is called super elasticity.

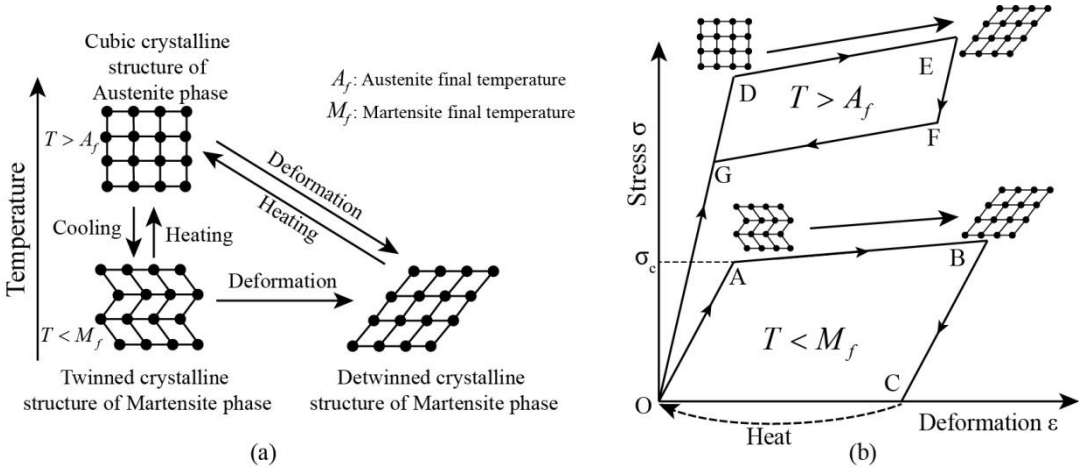

Figure 3 - 3. (a) SMA phase transformation; (b) Simplified Stress-Deformation curve of shape memory effect at low temperature ($T < M_f$) and super elasticity at high temperature ($T < A_f$) [ZAID 11c].

To simplify the model, we assume: 1) When the SMA element is cooled down, the temperature is below M_f, thus, it is completely in martensite phase and when it is re-bent by biasing SiO_2 layer, it is working in the state of OAB in figure 3 - 3b. When the SMA element is heated, its temperature is above A_f, therefore, the whole element is in austenite phase. Furthermore, with the fact that the stress of super elasticity start point (point D in figure 3 - 3b) is higher than the stress of shape memory cycle at any point, therefore, when it is pushing the biasing SiO_2 layer, it is working in the state of OD shown figure 3 - 3b. Based on the second assumption, SMA could be treated as a normal material which has a constant elastic modulus E_{SMA_A} when it is in austenite state.

When SMA is in martensite state, its elastic modulus is not a constant. It could be divided into two parts. First, when stress is smaller than σ_c, which is critical stress (figure 3 - 3b) , it is in twinned

crystalline structure state (OA part in figure 3 - 3b). We denote its elastic modulus as E_{SMA_T}. When stress is bigger than σ_c, the twinned crystalline structure starts detwinning (part AB in figure 3 - 3b), its elastic modulus becomes smaller, which is denoted as E_{SMA_DT}.

To construct the model step by step using superposition method [BREN 49], firstly, we assume that after the deposition process, the element is constrained to flat form and the length of the base material, i.e., SMA. So, there is no stress in SMA. At the same time, because SMA has bigger thermal expansion ratio, there will be compressive stress in deposited SiO_2 layer which is shown in figure 3 - 3a (the twinned and detwinned martensite phase distribution correspond to the final free deformed situation). This stress S could be calculated by following equation:

$$S = E_{SiO_2} \Delta\alpha_{SMA\_SiO_2} \Delta T \tag{3.1}$$

Where, E_{SiO_2} is the elastic modulus of SiO_2, $\Delta\alpha_{SMA\_SiO_2}$ is the thermal expansion ratio difference between SMA and SiO_2 and ΔT is the temperature change between deposition temperature and ambient temperature.

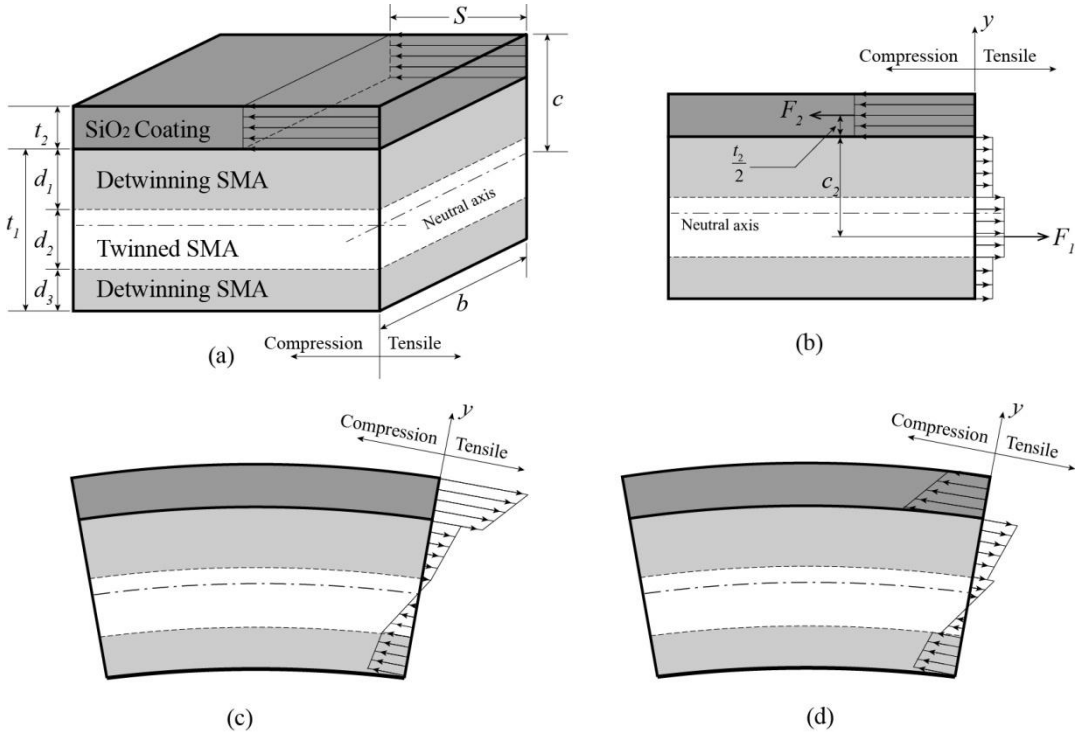

Figure 3 - 4. (a) Stress when both elongation and bending is held; (b) Stress when only elongation is happened; (c) Stress introduced by bending; (d) Stress in the element at free equilibrium stage, i.e., combination of (b) and (d).

Now, if the constrain is partially removed and the element is allowed to elongate, the stress will be like it is shown in Figure 3 - 4b. As we see, both SiO_2 layer and SMA base will slightly elongate, as a consequence, compressive stress in SiO_2 is reduced and tensile stress is created in SMA. Here, we assume that the cross section will always remain in a plane, i.e., elongation or deformation for crystalline twinned and detwinning part is the same. This deformation, ε_1, of SMA is:

$$\varepsilon_1 = \left(\frac{S}{E_{SiO_2}} \right) \frac{E_{SiO_2} t_2}{E_{SMA\_DT}\left(d_1 + d_3\right) + E_{SMA\_T} d_2 + E_{SiO_2} t_2} \tag{3.2}$$

Where, t_2 is the thickness of SiO_2 layer. Parameters d_1, d_3 and d_2 correspond to thickness of two detwinning parts and middle twinned part of SMA. If we consider the force cause by stresses in SMA and SiO_2 as two "point applied" forces: F_1 and F_2 (figure 3 – 4b), they could expressed as:

$$F_2 = F_1 = \varepsilon_1 b\left(E_{SMA\_DT}\left(d_1 + d_3\right) + E_{SMA\_T} d_2\right) \tag{3.3}$$

Here, b is the width of the element. We can see that F_1 and F_2 have formed a force couple and generated a moment M which could be calculated by:

$$M = F_1\left(c_2 + \frac{t_2}{2}\right) \tag{3.4}$$

Where, c_2 is the distance from the action point of F_1 to the intersect surface of SMA and SiO_2 (figure 3 – 4b) and c_2 could be calculated by weighting method:

$$c_2 = \frac{E_{SMA\_DT} d_1 \frac{d_1}{2} + E_{SMA\_T} d_2\left(d_1 + \frac{d_2}{2}\right) + E_{SMA\_DT} d_3\left(d_1 + d_2 + \frac{d_3}{2}\right)}{E_{SMA\_DT} d_1 + E_{SMA\_T} d_2 + E_{SMA\_DT} d_3} \tag{3.5}$$

If the element is completely released, it will be bent and due to the bending deformation, stress will be generated as shown in figure 3 - 4c. This bending caused stress will generate a moment M_b in the opposite direction with M. The schematic of resultant stress distribution is shown in figure 3 – 4d. When $M_b = M$, the element will reach the equilibrium state. If we choose y-axis as shown in figure 3 - 4c, the bending moment will be:

$$\begin{aligned} M_b = & \int_{-(t_1+t_2-c)}^{-(t_1+t_2-c)+d_3} by\left(-\sigma_c - \varepsilon_1 E_{SMA\_T} + \kappa E_{SMA\_DT}\left(y + \left(t_1 + t_2 - c\right) - d_3\right)\right)dy \\ & + \int_{-(t_1+t_2-c)+d_2+d_3}^{-(t_1+t_2-c)+t_1} by\left(\sigma_c - \varepsilon_1 E_{SMA\_T} + \kappa E_{SMA\_DT}\left(y + \left(t_1 + t_2 - c\right) - d_2 - d_3\right)\right)dy \\ & + \int_{-(t_1+t_2-c)+d_3}^{-(t_1+t_2-c)+d_2+d_3} E_{SMA\_T}\kappa b \cdot y^2 dy + \int_{c-t_2}^{c} E_{SiO_2}\kappa b \cdot y^2 dy \end{aligned} \tag{3.6}$$

Here, κ is the curvature. σ_c is the critical stress where the crystalline detwinning started. Parameter c is the distance from neutral axis to the outer surface of SiO_2 (figure 3 – 4a) and c could be calculated by weighting method:

$$c = \frac{E_{SiO_2}\frac{t_2^2}{2} + E_{SMA\_DT} d_1\left(t_2 + \frac{d_1}{2}\right) + E_{SMA\_T} d_2\left(t_2 + d_1 + \frac{d_2}{2}\right) + E_{SMA\_DT} d_3\left(t_2 + d_1 + d_2 + \frac{d_3}{2}\right)}{E_{SiO_2} t_2 + E_{SMA\_DT} d_1 + E_{SMA\_T} d_2 + E_{SMA\_DT} d_3} \tag{3.7}$$

Combine equations (3.4) and (3.6), the curvature κ could be solved. When the SMA element with SiO_2 layer is heated by laser, martensite phase will be converted to austenite phase. The elastic modulus is also increased. Like it is shown in figure 3 – 3b, the stress at any point of the shape memory effect cycle is lower than the stress at point D. So, we can assume that the elastic modulus of SMA, when it is heated, could be considered as a constant and can be denoted E_{SMA_A}. With similar process used for calculating the curvature at ambient temperature, the curvature κ_A, when SMA is heated, could be obtained with following equation [BREN 49]:

$$\kappa_A = \frac{6St_2\left(t_1 + \frac{E_{SiO_2}}{E_{SMA\_A}}t_2\right)\left(t_1 + t_2\right)}{E_{SMA\_A}\left(\frac{E_{SiO_2}}{E_{SMA\_A}}\left(t_1 + t_2\right)^2 + t_1^4\left(1 - \frac{E_{SiO_2}}{E_{SMA\_A}}\right)\right)} \tag{3.8}$$

Then, the stroke $S_{SMA\_SiO_2}$ of SMA element between ambient temperature and heated state is:

$$S_{SMA\_SiO_2} = \delta_{LowTemp} - \delta_{HighTemp} \tag{3.9}$$

$$S_{SMA\_SiO_2} = \frac{1}{\kappa}\left(1 - \cos\left(l_{SMA}\kappa\right)\right) - \frac{1}{\kappa_A}\left(1 - \cos\left(l_{SMA}\kappa_A\right)\right) \tag{3.10}$$

Where l_{SMA} is the length of SMA element, $\delta_{LowTemp}$ and $\delta_{HighTemp}$ is the deflection of the tip with respect to the vertical line for low temperature (ambient temperature) and high temperature (when it is heated by laser) respectively, graphical explanation can be found in figure 3 - 5.

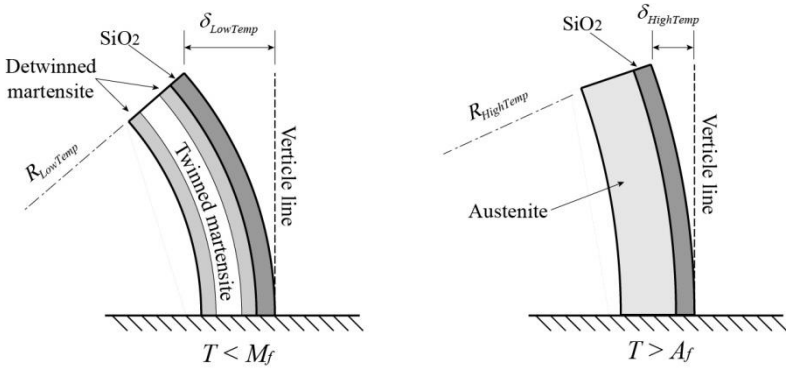

Figure 3 - 5. Deflection of SMA with SiO_2 layer at low temperature and high temperature.

3 SMA Characterization

3.1 SMA Tensile Test

In order to acquire the properties of SMA material we used, the tensile test was carried out. Zwick Roell RetroLine 4505 testing machine was employed to realize the test. The sensor unit has a maximal force tolerance of 500N. Eight samples were tested. Among them, four samples were tested at room temperature, while the other four were heated up to temperatures higher than austenite final temperature. Detailed information of the tests was listed in Table 3 - 1.

Results of tensile tests are shown in figure 3 - 6. We can see that the Stress-strain curves of first four samples are close to each other, though they have different cross sections (widths and thicknesses). Moreover, their trends agree with what is shown in figure 3 - 3b. There are three stages during the charging process. The first stage is similar with normal metal materials, the samples were all in twinned martensite phase and have a relatively stable elastic modulus around 15GPa. With the increasing of charge, when the stress reach a critical value (around 30MPa), the crystalline detwinning of martensite phase started. The elastic modulus decreased to a very small value (about 0.5GPa). As shown in figure 3 - 6, the detwinning part is almost flat, in other words, stress almost stopped increasing with the enlarging of strain. When the deformation reaches about 7%, the detwinning process was finished. The entire sample was in crystalline detwinned state and becomes a normal

metal material. Stress increased with strain. Elastic deformation happened firstly, then, plastic deformation until it was fractured.

Table 3 - 1. Information for contract test of SMA (Nitinol)

Sample	Length (mm)	Width (mm)	Thickness (mm)	Temperature
1	44	7.75	0.05	ambient
2	44	6.63	0.1	ambient
3	44	6.42	0.1	ambient
4	44	7	0.05	ambient
5	44	6.62	0.1	50
6	44	6.75	0.1	62
7	44	7.5	0.05	60
8	44	6.75	0.05	52

There are also three stages for the four samples which were tested at high temperatures (see Table 3-1). At the beginning of the first stage, all four samples had a horizontal shift of stress, which is indicated as "Chuck sliding" in figure 3 - 6. This shift is caused by the gap between different parts of chuck. Because the sample and chuck are surrounded by the oven, the gap was not properly eliminated. In the first stage, all samples were heated up to the temperature higher than austenite final temperature, thus, stress increased linearly with strain. When stress reached a critical value (this value depends on temperature, higher temperature leads to higher critical stress), the stress caused transformation from austenite to martensite started. This process also has very small elastic modulus. When the transformation was completed (where the stress rise fast again in figure 3 - 6), the sample was in detwinned martensite phase and deformed until fracture. We can see that, the heated samples have similar trends, in the third stage, with the room temperature tested ones. This is because they were both in detwinned martensite phase and could be consider as the same material.

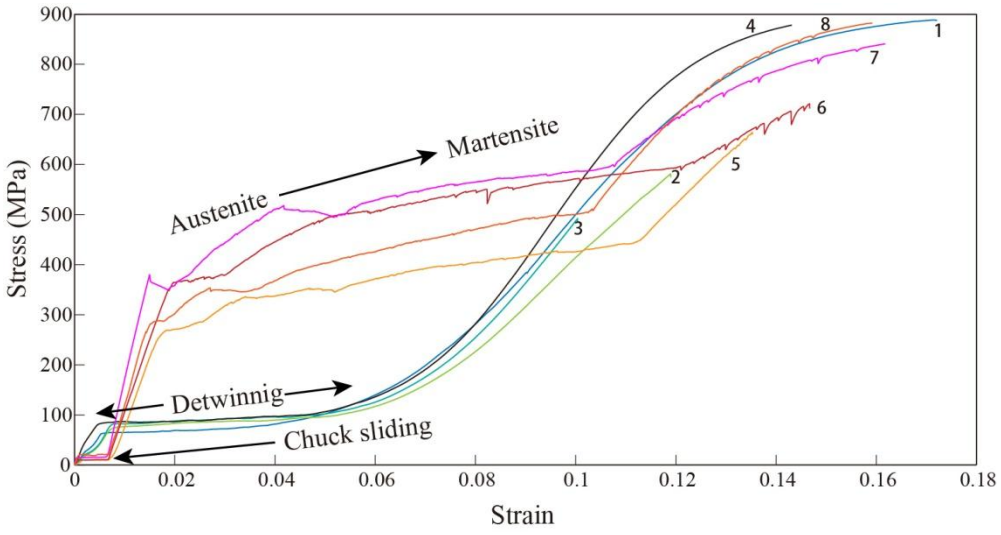

Figure 3 - 6. Stress-strain curves of nitinol tensile tests.

3.2 Phase Transformation under Laser Irradiation

The percentage of the sample (3 × 1 × 0.1 mm) volume, which was transformed into the austenite phase during the martensite to austenite phase transformation, was calculated in former work [ZAID 11c]. The values are tabulated in table 3 - 2 for different laser power values, wherein, V_A represents the volume percentage of austenite phase, V_M represents the volume percentage of martensite phase, V_{AM} is the volume percentage of mixed phase. As it can be seen, 100% phase transformation was achieved for laser power value as low as 40 mW. Therefore, we can guarantee the martensite phase can be transformed into austenite phase completely when the laser power is 100 mW (The value we used for the test).

Table 3 - 2. Percentage of the SMA volume transformed into the austenite phase and the microscopic status for different laser power values

P (mW)	V_A (%)	V_M (%)	V_{AM} (%)	Microscopic status
100	100	0	0	a
90	100	0	0	a
80	100	0	0	a
70	100	0	0	a
60	100	0	0	a
50	100	0	0	a
40	100	0	0	a
30	48	0	52	b

a represents pure austenite phase ($T > A_f$)
b represents pure austenite phase ($T > A_f$) which co-exists with mixed martensite-austenite state ($A_s < T < A_f$)

4 Deposition of SiO_2 layer

The deposition of SiO_2 layer was done in "Laboratoire de Physique de la Matière Condensée (LPMC) in Université Picardie-Jules Verne (UPJV)". Magnetron sputtering deposition was chosen to deposit the SiO_2 layer SMA element. The working principle was explained in figure 3 - 7a. Sputtering deposition is one of the physical vapor deposition processes. The atoms or molecules are bombarded away from the surface of target material (material to be deposited on the substrate) by plasmas particles. In this process, target material was transformed from solid phase directly to gas phase, then condensed on the surface of substrate. Therefore, the target material does not need to be melted firstly, which means the deposition could be carried out at a low temperature (around 200 ^oC). For our application, the substrate material is SMA and the memorized shape was trained at the temperature around 500 ^oC. If SMA is heated too much during the deposition, the memorized shape could be changed, which must be avoided. The magnetron sputtering deposition has added a magnetic field near the target, which can confine the electrons and plasma ions in the space near the surface of target. As a consequence, the density of ions and electron is higher near the target. This largely accelerates the deposition speed. Furthermore, as the plasma is confined to near the target, the chance that ions hit the surface of substrate will be reduced, i.e., damage that may caused by plasma is also reduced. As a conclusion, magnetron sputtering deposition can do the deposition at low temperature with high speed and without causing too much damage to the SMA which make it the best choice for our application.

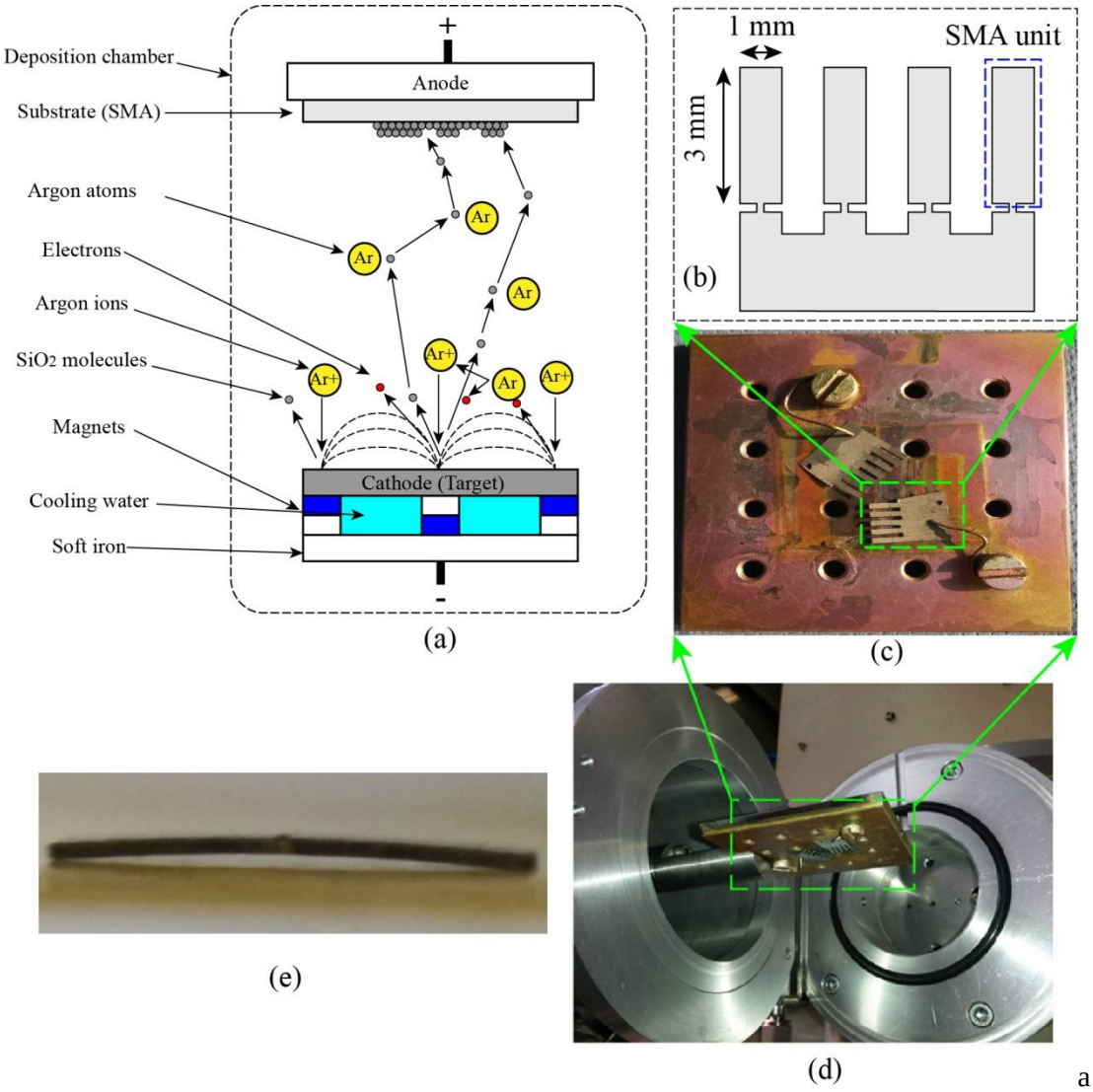

Figure 3 - 7. (a) Schematic of magnetron sputtering deposition; (b) Schematic of the SMA substrate to be deposit; (c) SMA fixed on the sample support of magnetron sputtering depositing machine; (d) Sample support in depositing chamber; (e) Side view of a SMA unit element.

The SiO_2 layer is deposited by magnetron sputtering of a silica target with the argon plasma (pressure 1 Pa; RF power 300 W; growth speed around 2 µm per hour). Before deposition, the SMA element was pickled in HF acid to improve the surface condition. The SMA sheet was pre-cut into the form shown in figure 3 - 7b. Only a very small joint was left between the unit element and the base part, so that, after the deposition of SiO_2, the unit element could be dismounted easily from the base without peeling off the SiO_2 layer. The deposit support and the deposit chamber are shown in figure 3 - 7c and d. The deposited thickness of the SiO_2 layer was 8 µm. A side view of the unit element is shown in figure 3 - 7e, we can see that, after the deposition, the compressive stress in SiO_2 layer has bent the SMA unit element.

5 Stroke test of SMA element with SiO_2 layer

As described in former part, SMA active element with deposited SiO_2 layer could be considered to have a “two way” memory effect. In the application of wireless actuation of the bistable beams, it is expected to switch the beam from one stable position to the other one, then, to recover to the original position automatically after it is cooled down. The stroke of the “two way” memory SMA element should be, theoretically, more than the half stroke of bistable beam, so that the beam can snap to the

other side. In this section, the experimental test for the stroke of SMA element with SiO_2 layer will be presented.

5.1 Calibration of force sensor

In addition to the stroke, the force that could generate the SMA element is also important. The force should be enough to switch the bistable beam. So, force sensor (provided by "Laboratoire de Production Microtechnique (LPM), Ecole Polytechnique Fédérale de Lausanne") was chosen to measure the stroke of SMA element and get the corresponding force at the same time. The force sensor is shown in figure 3 - 8.

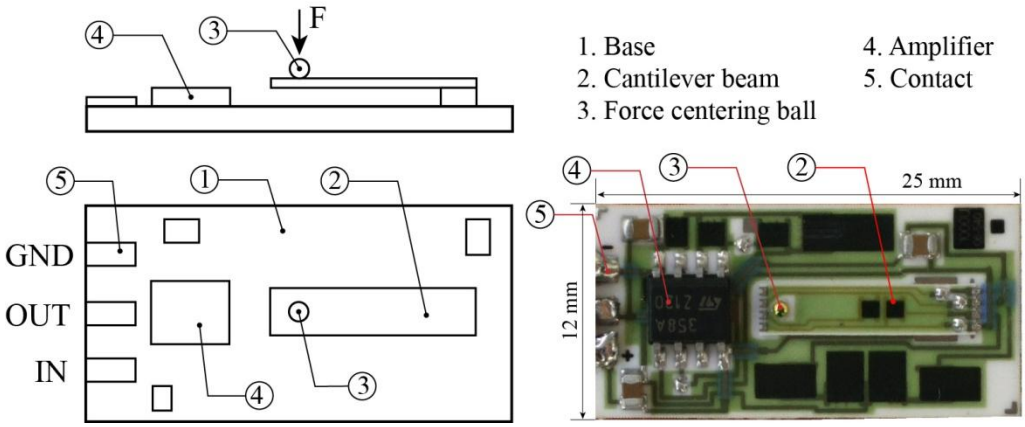

Figure 3 - 8. Schematic and photo of force sensor.

As it is shown, the force sensor is mainly composed of five parts. Among them, the cantilever and amplifier are the most important parts. When force is applied on the centering ball, it will cause the deformation of cantilever which carries a piezoresistive bridge. Therefore, the deformation is transformed into a voltage signal. Finally, the output signal is amplified and carried out by the circuits on the base. The detailed information for the force sensor is listed in table 3 - 2.

Table 3 - 3. Specification of force sensor

Parameters	Value	Unit
Nominal force	1000	mN
Offset at zero force	0.5	V
Span	3	V
Response time	<10	ms
Supply current	<3	mA
Supply voltage	5±0.25	V

In order to use the sensor in a precise way, it is experimentally calibrated by the setup shown in figure 3 - 9. The sensor is fixed on a support board. The support board is installed on a vertical positioner. A lever, whose fulcrum is at the midpoint, is installed on two orthogonal configured linear stages. By adjusting the vertical positioner and linear stages, the left end of the lever was made to have contact with the centering ball of the sensor while the lever is at horizontal position. Precise weight is suspected at the right end of the lever.

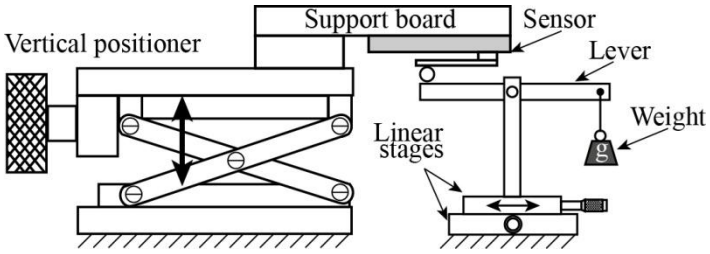

Figure 3 - 9. Experimental setup for the calibration of force sensor.

Weights from 10g to 100g were suspended on the right end of lever and the corresponding output voltages were recorded. The weight was transformed to force using the acceleration of gravity (9.809 m/s^2 for France). The Voltage-Force curve for the calibration of force sensor is shown in figure 3 - 10. We can see that the voltage is linearly increased with force. The function of the trend line is shown in the figure 3 - 10. If we use the trend line as the output function of the sensor, its sensitivity is 2.4 mV/mN.

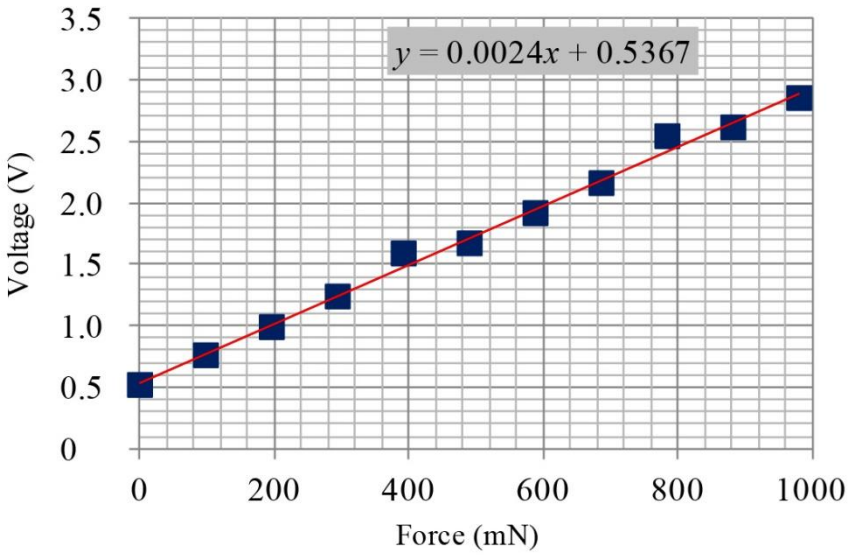

Figure 3 - 10. Voltage-Force curve for the calibration of force sensor.

5.2 Measurement of SMA element's stroke

The stroke of SMA element with deposited SiO_2 layer was measured using the setup shown in figure 3 - 11. The force sensor described in former part is used in the setup. As we see, the sensor is fixed on two linear stages in orthogonal configuration. Firstly, the force centering ball is adjusted to the same height with the SMA element's top end (figure 3 – 11b and c). Then, centering ball was moved slowly towards SMA element until there was a change from the force sensor's output voltage, which means the centering ball starts contacting the SMA element (figure 3 - 11d). Then, a red laser (λ = 660 nm, P = 100 mW) was turned on in order to heat the SMA. When the temperature rises up to the austenitic final temperature, SMA tends to recover the memorized shape, i.e., flat. However, the SMA already has a contact with centering ball. As a consequence, the recovery action exerted a force on the sensor. Keeping the laser on, the force sensor was moved away while the output voltage of force sensor was recorded. This was done until the contact between SMA and centering ball disappeared (figure 3 - 11e). The total movement of force sensor is considered as the stroke of SMA element.

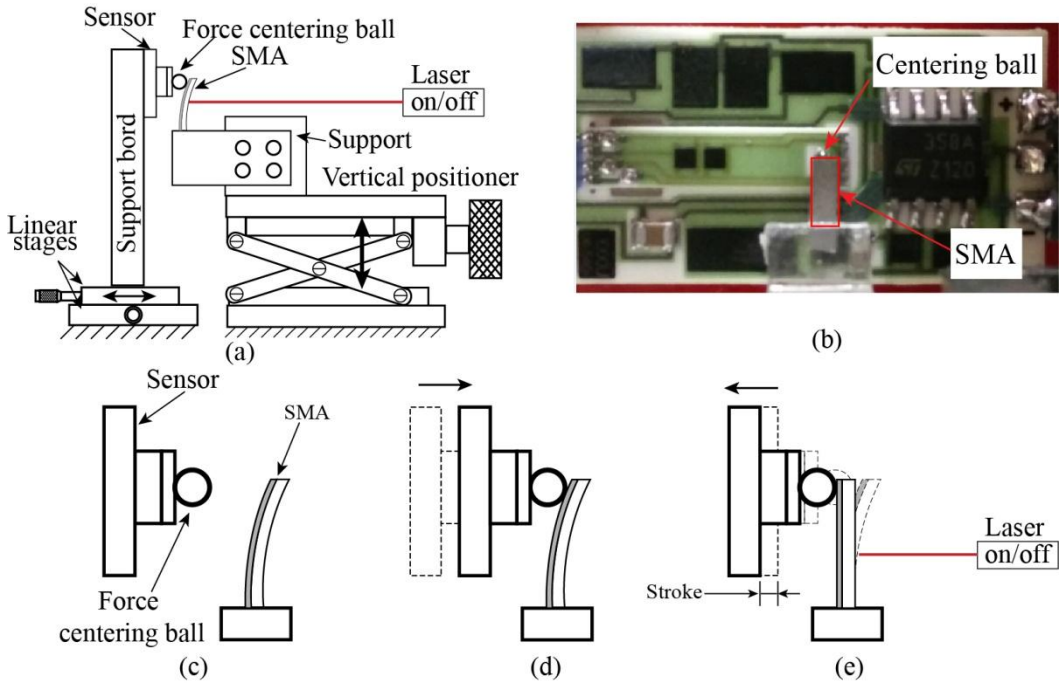

Figure 3 - 11. Measurement of SMA element's stroke with force sensor: (a) Schematic of experimental setup; (b) Photo of force sensor in contact with SMA element; (c) - (e) Stroke measurement process.

The measured results for an SMA element with 8 µm thick SiO_2 layer are shown in figure 3 - 12. As we see, there is output force until the sensor is moved about 300 µm away, which means the stroke is about 300 µm. The inner row has the bigger stroke (300 µm) of the quadristable micro-actuator fabricated on silicon (see chapter 2). Theoretically, after bistable beam is switched to the middle position (150 µm), it could automatically snap to the other stable position. Considering the fabrication defects, there could be a small drift for snap position. Furthermore, to avoid the load effect, 20 µm distance will be preserved between SMA element and bistable beam. Therefore, the stroke of SMA element is enough to switch the bistable beam from one stable position to the other one.

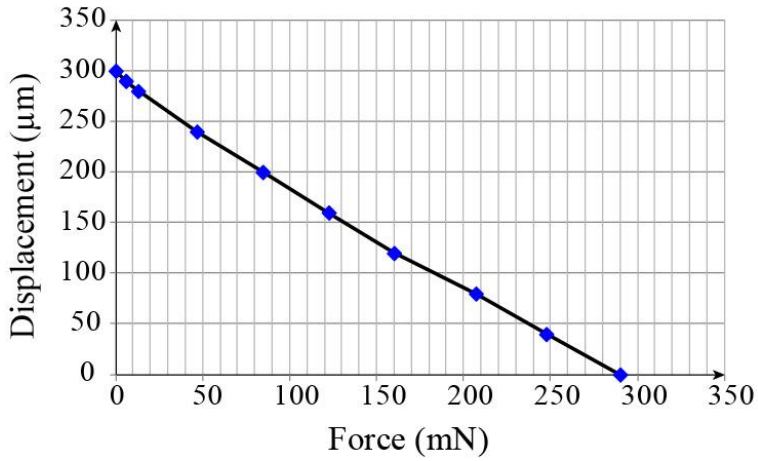

Figure 3 - 12. Displacement-Force curve of a heated SMA element with 8 µm thick deposited SiO_2 layer.

6 Wireless actuation of silicon bistable micro-actuator

In this section, the wireless actuation of the silicon bistable micro-actuator (inner row of the quadristable micro-actuator) is presented. Firstly, a customized support system is designed and fabricated. With this support, the fragile micro-actuator is properly fixed. At the same time, two small mirrors are fixed on the support, so that the bistable micro-actuator can be actuated in two opposite

directions with a single laser source. Then, the experimental setup for wireless actuation is described and the actuation process is explained.

6.1 Support for the silicon bistable micro-actuator

To do the actuation, firstly, the micro-actuator should be properly fixed. Since the silicon bistable micro-actuator is fragile, it is necessary to install it on a special designed support, so that it will not be damaged during the actuation. The customized support is shown in figure 3 - 13. The support system is composed by four parts: lower support, middle spacers, upper support and small fixed mirrors.

The lower support is the base of the support system, on which fixing holes are reserved. The two big holes at the bottom side will be used to fix the entire support system on the experimental table. The other four smaller fixing holes are designed to connect and locate the middle spacers and upper support. Moreover, two slots are reserved for fixing the small mirrors. The lower support was cut from a 3 mm thick poly methyl methacrylate (PMMA) plate by laser cutting machine which was used for the fabrication of prototype quadristable actuator. The upper support is a 0.5 mm thick rectangular frame, which is also cut from PMMA plate. The cavity has the same dimensions with the outer contour of bistable micro-actuator. Two spacers are installed between upper and lower supports. The middle spacers have the same thickness of 3 mm and they are cut from PMMA plate as well.

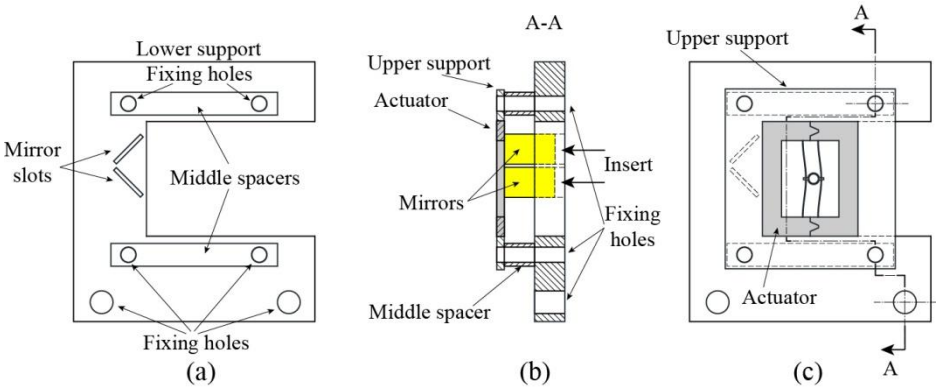

Figure 3 - 13. Support for the silicon bistable micro-actuator: (a) Lower support and middle spacers; (b) Cross sectional view of assembled support; (c) Top view of the assembled support (with bistable micro-actuator installed).

For the assembly, firstly, the silicon bistable micro-actuator will be fitted in the cavity of upper support and fixed by glue. Then, the upper support, middle spacers and lower support are connected by screws through the fixing holes. At last, the small mirrors are inserted into the mirror's slots from the bottom side towards the upper support. The mirrors are 5×5 mm squares and the middle spacer's thickness is 3 mm. As a consequence, part of the mirror stays in the lower support, while the top of the mirror is already in contact with the upper support. Thus, a very small drop of glue into the mirror's slot from the bottom side could fix the mirrors very well and make sure that the reflective surface of the mirror is perpendicular to the lower support plane.

6.2 Wireless actuation : proof of concept

The wireless actuation was carried out by the experimental setup shown in figure 3 - 14. The energy was provided by a 100 mW power laser diode (λ = 660 nm). Firstly, laser beam was focused by lens 1 onto an optical beam steering micro-mirror (S1492, from Mirrorcle Technology). The steering micro-mirror's diameter is 2 mm. It can rotate in the range of $\pm 5^{o}$ with respect to two axes under a numerical control using PC. After the reflection of the micro-mirror, the laser is focused again, with the help of lens 2, onto bistable micro-actuator.

As shown in figure 3 - 14, two SMA elements are integrated in the micro-actuator in order to switch the bistable beams in the two opposite directions. The rotation ability of the steering micro-mirror gives the possibility of heating two SMA elements with a single laser. As we see, SMA 1 can be heated directly. SMA 2 can switch the bistable beams from the left stable position to the right stable one, when the steering micro-mirror is oriented with a pre-calculated angle. In that case, the laser beam can illuminates SMA 2 with reflections onto the two fixed mirrors.

A cross section view of the micro-actuator part is shown in figure 3 - 14, where, SMA active elements are fixed on two precise linear stages which are used to adjust SMA's original position relatively to bistable beams. To avoid the load effect, SMA elements are positioned close to the beam but without contact.

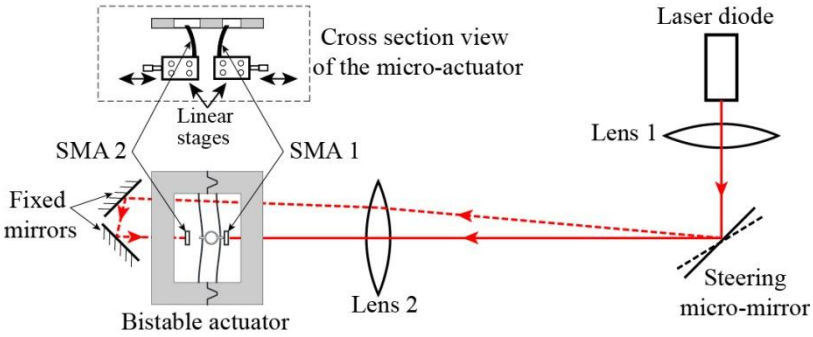

Figure 3 - 14. Experimental setup for wireless actuation of bistable micro-actuator.

The wireless actuation of the silicon bistable micro-actuator was realized successfully. A photo of the setup's top view is shown in figure 3 - 15a. The silicon micro-actuator is fixed in the PMMA support structure. Two small fixed mirrors are located under the upper support behind SMA 2. The side views of micro-actuator when the bistable beams are at the right and left stable position are shown in figure 3 - 15b and c, respectively. Furthermore, in the zoomed view, it is obvious that there is a small gap between SMA and bistable beams at both stable positions, i.e., there is no load effect over SMA elements.

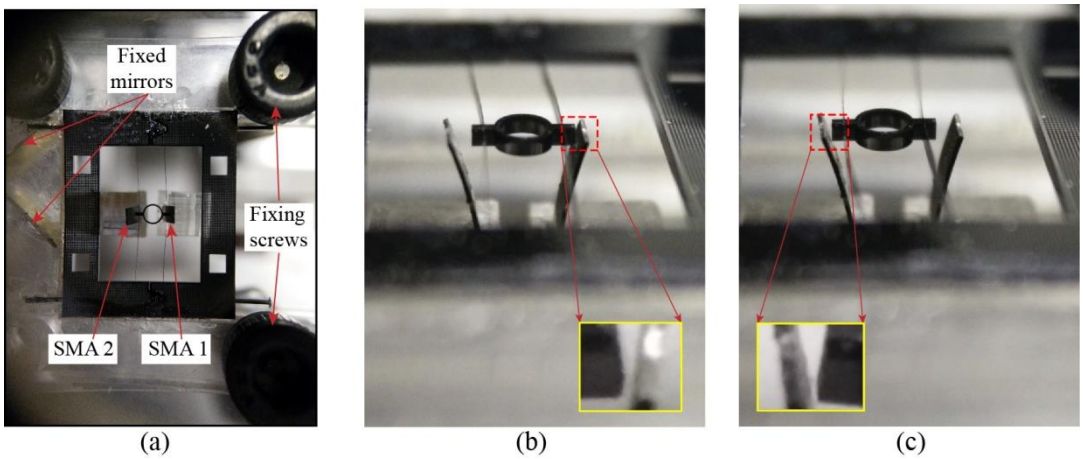

Figure 3 - 15. (a) Top view of real setup; (b) Side view when bistable beam was at the right stable position; (c) Side view when bistable beam was at the left stable position.

As mentioned in former part, the laser needs to be reflected two times to heat SMA 2 and because of the energy loss during reflections, the laser power irradiated on SMA 2 is less than the power on SMA 1. As a consequence, SMA 2 needs to be heated for a longer duration (about 2 s) than SMA 1 (about 1.5 s) to switch the beams.

7 Wireless actuation of the silicon quadristable micro-actuator

After the bistable micro-actuator was successfully actuated, the wireless actuation of quadristable was carried out. New support system was designed and the experimental setup was modified to meet the requirement of actuation for quadristable micro-actuator.

7.1 Support design for silicon quadristable micro-actuator

As describe in chapter 2, the quadristable micro-actuator is a combination of two rows of bistable micro-actuators: inner row embedded into the outer row. Actually, the inner row is the central link of outer row. Thus, when the outer row is actuated, the entire inner row will move with the outer row (figure 3 - 16a). This movement equals to the stroke of outer row (200 µm). If the SMA elements for inner row are relatively fixed to the outer row, when the inner row is at its left stable position and the outer row is at its right stable position, at least 200 µm gap should be reserved between SMA 1 and the central link (figure 3 - 16b), so that when the outer row is switched to the left side, SMA 1 will not block the central link. With this situation, in order to switch the inner row from the left stable position to the right one, SMA 1 should push central link for at least 150 µm (half stroke of inner row) after they started contacting each other. In other words, the stroke of SMA elements should be more than 350 µm (200 µm gap+150 µm half stroke of inner row) which is bigger than the stroke of SMAs' active element. Even if we can get the SMA element with a stroke of 350 µm, when both the inner and outer rows are at the left stable position (figure 3 - 16c) and no initial gap between SMA 1 and central link is anticipated, if SMA 1 is heated, it will push the central link for 350 µm. However, the stroke for inner row is just 300 µm, i.e., after the inner row has reached its right stable position, it will be pushed for additional 50 µm. This over push action will lead to the risk of breaking the inner bistable beam. Therefore, a support system for the inner row's SMA elements is designed and it will be attached on the supporting brackets of inner row and make the SMA elements move together.

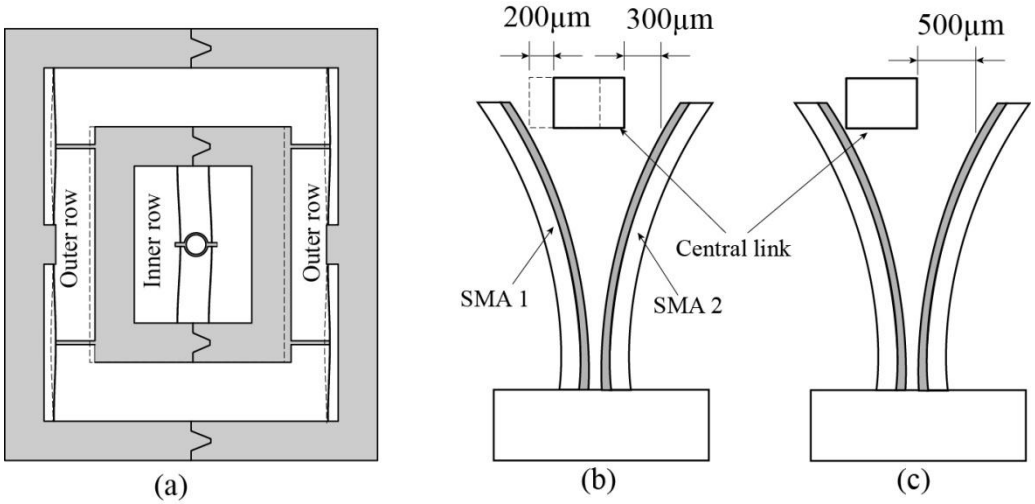

Figure 3 - 16. Situation when the inner row of a quadristable micro-actuator is actuated with SMA elements which is fixed with the outer row: (a) Schematic of quadristable micro-actuator (dashed line is situation when outer row is at the left stable position); (b) The relative position between SMA elements and central link of inner row's bistable beams when outer row is at the right stable position and inner row is at the left stable position (dashed line indicates the position of inner row's central link when the outer row is at the left stable position); (c) The relative position of SMA elements and central link of inner row when both the inner and outer rows are at the left stable position.

The designed support system for the inner row of a silicon quadristable micro-actuator is shown in figure 3 - 17. It is composed of three parts: the upper plate, the lower plate and four spacers. All the

components are cut from 0.5 mm thick PMMA plastic plate by laser machine. On the upper plate, four fixing holes, with the dimension corresponding to the spacers, are cut for the following assembly. Actually, the upper plate is two separated parts that are connected by two very thin links which are called temporary link in figure 3 - 17a. We can see that the fixing holes on upper plate have corresponding holes on the lower plate, thus, the temporary links could simplify the assembling process. After the assembly, they will be removed (figure 3 - 17b). On the lower plate, there are two SMA slots (figure 3 – 17a). Furthermore, some material is removed on both upper and lower plate to reduce the weight of support system. The assembled support system is shown in figure 3 - 17b. Here the support system is zoomed, so that it can be seen clearly. Two SMA elements are already installed in their slots. As indicated, both the upper and lower plates have the same thickness of 0.5 mm and the distance between them is 1.6 mm (defined by the dimensions of spacers). The length of the SMA elements is 3 mm. Therefore, the top end of SMA element is 0.4 mm higher that the top surface of upper plate. This top end will be used to switch the bistable beams, when the support system is fixed onto the quadristable micro-actuator. The support structure will be glued on corresponding areas which are indicated with red hatched rectangles in figure 3 - 17b.

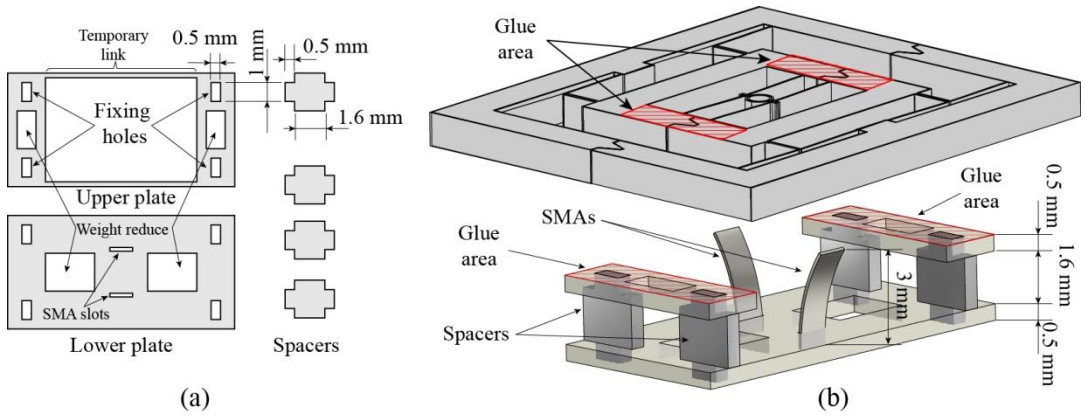

Figure 3 - 17. SMA elements' support system for silicon quadristable micro-actuators inner row: (a) Components of the support system: upper plate, lower plate and four spacers; (b) The assembled support system and the corresponding relationship with quadristable micro-actuator.

For the outer row, SMA elements could be fixed on linear stages like the solution for bistable micro-actuator. However, because of the big size of linear stages, it has increased the dimension of the entire actuator system. To minimize the actuator system, a customized SMA elements support structure is designed for the outer row of the quadristable micro-actuator (figure 3 - 18a). Similar with the inner row support, it is composed of three parts: upper plate, spacers and lower plate. A slot is cut on the lower plate and the SMA element is inserted in the plot.

Similar with bistable micro-actuator, it is necessary to fix the micro-actuator on the experimental table. Since the micro-actuator fabricated with silicon material is fragile, a customized support is fabricated and the micro-actuator is installed in the support (figure 3 – 18b). It can be seen that fixing holes are preserved on the support structure. These fixing holes could be used to install the actuator system on the experimental table by bolts. The bottom and an isometric view of the assembled quadristable micro-actuator system are shown in figure 3 – 18c and d. As it is shown, by using the customized SMA support structures for both inner and outer rows, the dimensions of the system is largely reduced, which will help the future design of the micro-actuators array smart surface.

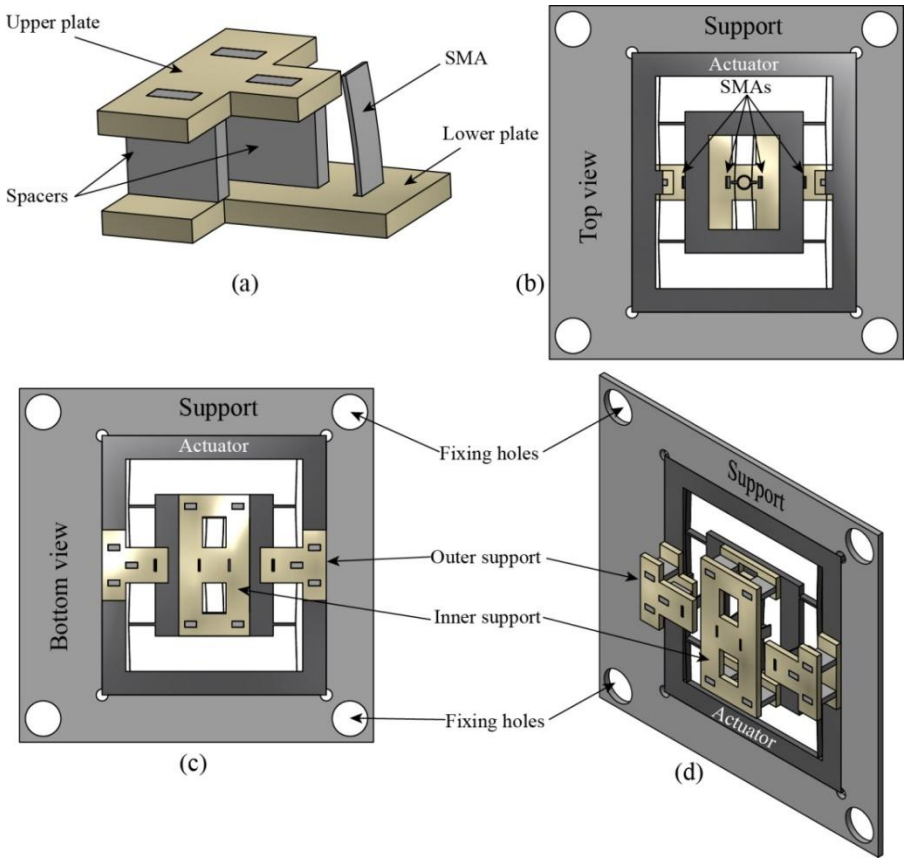

Figure 3 - 18. (a) Outer SMA support; (b) Top view of the support for quadristable micro-actuator; (c) Bottom view of the support for quadristable micro-actuator; (d) Isometric view of the support for quadristable micro-actuator.

7.2 Wireless actuation of quadristable micro-actuator

7.2.1 Experimental setup

In the actuation of the bistable micro-actuator, laser was guided in the horizontal direction and irradiated the SMA elements on the lateral side. For the actuation of the quadristable micro-actuator, four SMA elements have to be employed. In this case, if the laser still comes from the lateral way, more mirrors would be necessary and the system would become complex. Therefore, a new strategy, lighting SMA elements from the top, was utilized for the wireless actuation of quadristable micro-actuator.

The experimental setup is shown in figure 3 - 19. The system was composed of five parts: quadristable micro-actuator, laser and optical guide, steering micro-mirror, distance sensor and controlling program on PC. The quadristable micro-actuator, with four SMA elements installed, was already described in the former part. The laser and optical guide are similar to the one for bistable micro-actuator. The laser source is red laser diode (λ = 660 nm).

Firstly, laser beam is converted to quasi-parallel beam by lens 1 and lens 2. Among them, lens 2 has a small focal length. By adjust the position of lens 1, the laser beam is focused near the focal point of lens 2, thus, after lens 2, the laser beam was converted into a quasi parallel beam with a small diameter because of the steering micro-mirror's diameter (2 mm); if the diameter of laser beam is bigger than 2 mm, a part of the energy will be lost. After the reflection of steering micro-mirror, the quasi-parallel laser beam is focused by lens 3 which has a big focal length to settle the optical components away from the micro-actuator workspace. After lens 3, a fixed big mirror is used to illuminate the quadristable micro-actuator in the top-down direction. The steering micro-mirror is an important part

of the system, because it can rotate precisely under the numerical control on PC. Therefore, we can use one laser source to heat successfully four SMA elements that are necessary to actuate the quadristable micro-actuator.

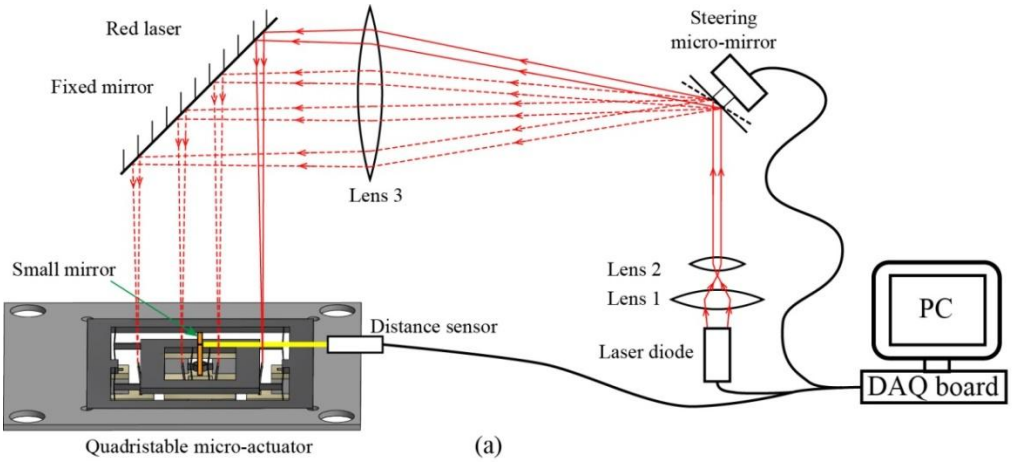

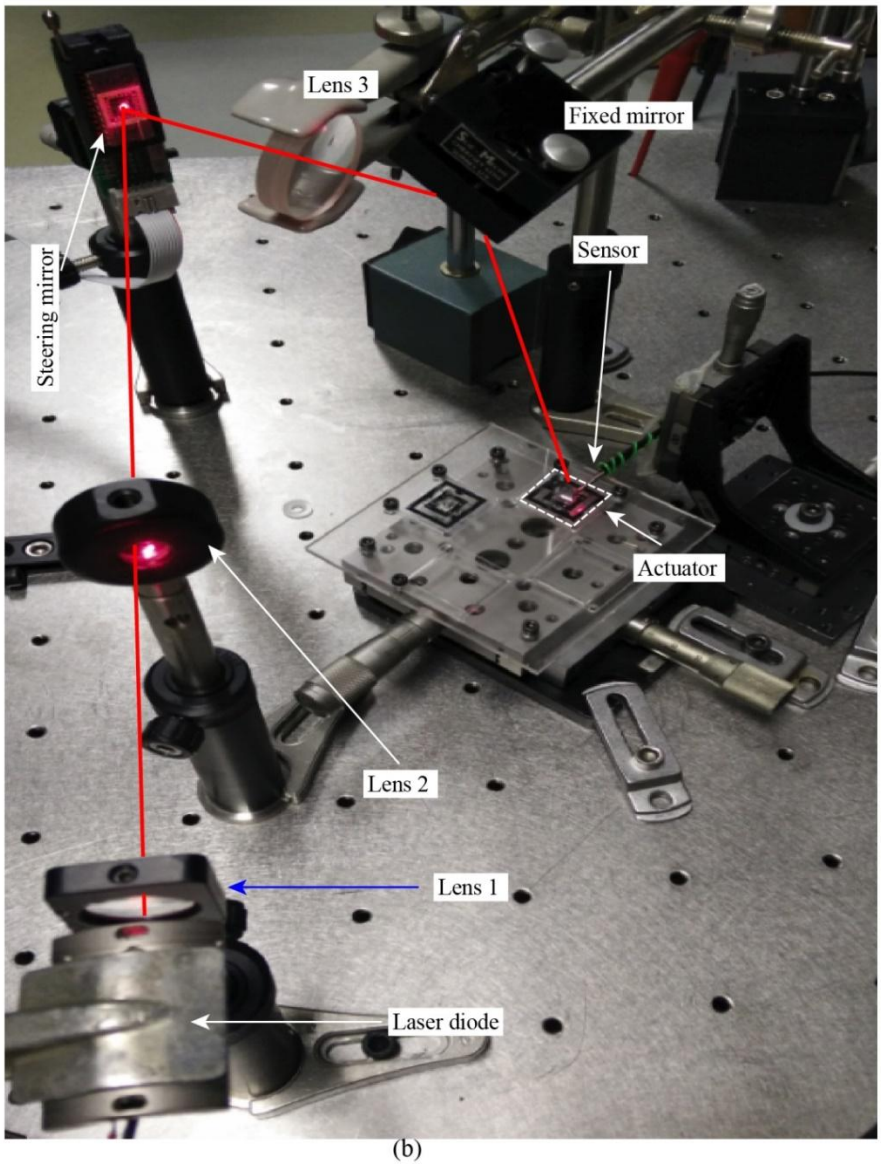

Figure 3 - 19. Experimental setup for quadristable micro-actuator's wireless actuation: (a) Schematic (b) Photograph.

The real experimental setup is shown in figure 3 – 19b. It can be seen that the quadristable micro-actuator is fixed onto a transparent plastic (PMMA) support plate. This support plate is installed onto two orthogonal configured linear stages which could be used to adjust the initial position of the actuator.

7.2.2 Fiber optic distance sensor

As a matter of fact that the micro-actuator can only carry very limited force (around 15 mN), any extra load can influence the output stroke. Therefore, an optical fiber distance sensor [PREL 06] is used to measure the output of the quadristable micro-actuator. This is a non-contact measurement approach and no extra load will be introduced onto the micro-actuator. This characteristic makes it very suitable for our application.

The working principle is explained in figure 3 - 20. As it can be seen, there are two kinds of optical fibers in the probe; the emitter which is located at the central part and the receiver which is located around the emitter (figure 3 – 20a). A laser diode is coupled with the emitter fiber. Light with a certain wavelength is ejected on the mirror through the emitter fiber. Then, the reflected light is collected by the receiver fibers which are coupled with a PIN photodiode (Figure 3 – 20b). Due to photoelectric effect, the photodiode can generate a measurable current and this signal will be amplified with certain circuits then carried out as the output voltage of the sensor. When the mirror is moved away from the sensor's probe, the output will increase first and then decrease, like it is shown in figure 3 - 20c.

The output could be divided into two parts: 1/ in the first part, which is called linear zone, voltage output increases linearly with the increase of distance D, 2/ in the second part, the nonlinear zone, voltage output decreases nonlinearly while distance D is increasing (detecting range is about 2 mm). The linear zone has a linear output and high sensitivity with respect to the change of distance between probe and reflective mirror which make it very good approach for high resolution distance measurement applications. However, the detecting range of linear zone is only about 200 µm. For the applications which need large detecting range, only nonlinear zone is usable. In this case, the nonlinearity could be solved using piecewise interpolation. If the nonlinear zone is divided into multiple small segments, each of them is a linear function of the distance. Therefore, different segments will have different sensitivity. In the practical case, the start part of the nonlinear zone has bigger sensitivity. Thus, it is better to use the start part of the non linear zone to improve the measurement accuracy.

Due to the working principle of optical fiber distance sensor, it is necessary to detect reflected light. So, a small mirror has been fixed onto the output point of the quadristable micro-actuator, i.e., the central link of inner row (shown in figure 3 - 19). Once the light is reflected and detected, the output voltage signal is acquired by NI acquisition card and saved into data file for the post analysis.

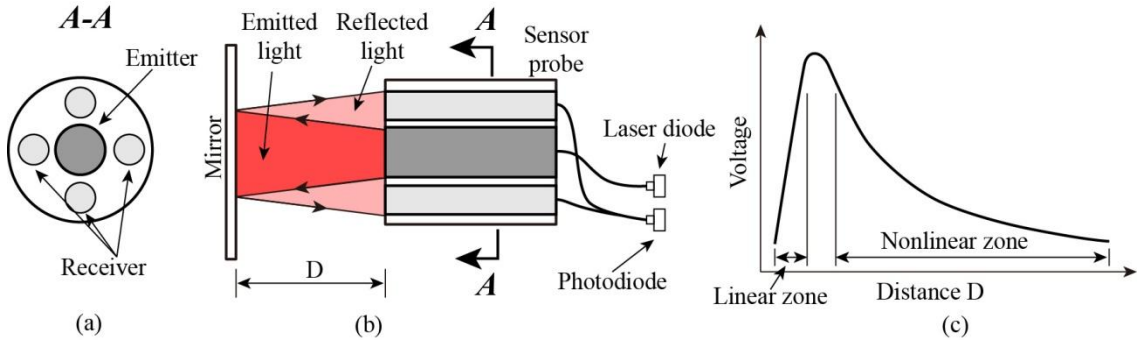

Figure 3 - 20. (a) Cross section view of the optical fiber distance sensor's probe; (b) Optical fiber distance sensor schematic; (c) Output curve of optical fiber distance sensor.

A zoomed view of the quadristable micro-actuator and optical fiber distance sensor is shown in figure 3 – 21a. Because the micro-actuator's beams are very thin, they cannot carry a big mass at the output point. Furthermore, the inertia of big mass will influence the dynamical behavior of the micro-actuator. Since each beam is thin it will act as a spring and if the mass of mirror is big, the snap speed will be slow. Moreover, at the end of the snap effect, mirror with big mass will vibrate which will introduce unwanted output signal. As a consequence, the traditional glass mirror is excluded from the candidate list, because it is heavy and difficult to be fixed. Then, aluminum foil with reflective surface is fabricated then used as the small mirror fixed onto the micro-actuator. A schematic of the small mirror is shown at the left bottom corner of figure 3 – 21a. We can see that, it is not just a simple aluminum foil because a simple piece of foil cannot maintain itself in a plane. So, a small piece of aluminum foil is folded into a dustpan form (without handle part) as indicated in figure 3 – 21a.

There are four advantages of dustpan form. First of all, it will largely increase the structural rigidity, so that the reflective surface will remain in a plane. At the same time, it will not increase too much the weight. Second, it will create a small plane area at the bottom which can facilitate the fixation onto the micro-actuator. In practical case, a small drop of glue is applied onto the bottom side. With the help of a 3D positioner (orthogonal combination of three linear stages), the dustpan form small mirror was located precisely onto the central link part of the micro-actuator. Due the strong and fast-acting adhesive characteristic of glue (cyanoacrylate), once the small mirror touched the central link, it will be firmly fixed instantaneously. The third advantage is that the top part has no side wall, therefore, it is easy to be grabbed by a tweezers without changing its shape, especially the plane reflective surface. Finally, with the fact that laser for actuation comes from top, the dustpan form small mirror can reduce the risk of shading the SMA elements of inner row. By the way, instead of aligning the distance sensor's probe at the center of the small mirror, it is deviated to the left side to avoid the shading of SMA elements for inner row. The calibration curve of optical fiber distance sensor's nonlinear zone with the dustpan form mirror is shown in figure 3 - 21b.

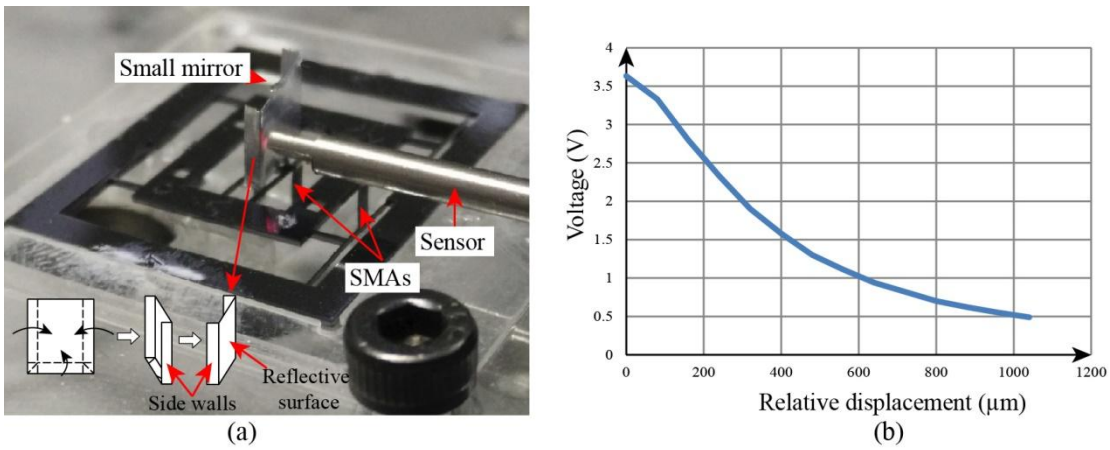

Figure 3 - 21. (a) The quadristable micro-actuator with aluminum foil made small mirror and optical fiber distance sensor; (b) Calibration curve of optical distance sensor's nonlinear zone.

7.3 Experimental results

7.3.1 Proof of concept

With the experimental setup described in precedent part, both the inner row and outer row of the quadristable micro-actuator are actuated over 4000 cycles. Two cycles of actuation, taken within this

set of cycles, are shown in figure 3 – 22a and the photos of actuation for outer row and inner row is shown in figure 3 - 22b.

First of all, it is obvious that both inner row and outer row are bistable, i.e., the actuator is quadristable. The inner row and outer row were actuated in the order: outer row forward → outer row backward → inner row forward → inner row backward. With this actuation order, the output will be in the form which is shown in figure 3 - 22, where output is confined in a small range, so that, we can used the optical fiber distance sensor's high sensitivity detecting range of nonlinear zone. As a consequence, only three stable positions are presented in figure 3 - 22. If the actuation order is: inner row forward → outer row forward → inner row backward → outer row backward, the combination of inner row and outer row will produce four stable positions.

Each cycle has four steps, two steps for inner row's actuation forward and backward, two steps for outer row. Each step's duration is 24 s. In this 24 s, the former 12 s is used to heat the SMA element and the later 12 s is for cooling. The heat duration for this test is long because the SMA elements for outer row need a long time to be heated up to the phase transformation temperature. This is caused by the shading effect from the support brackets of inner row. When laser beam is guided onto the SMA elements of outer row, part of the light energy is blocked by the bracket. As a consequence the energy received by outer row SMA elements is less than the inner row SMA elements. This is also the reason why the duration at stable position of outer row is shorter than the duration of inner row. In fact, the necessary heating duration for inner row's actuation is less than 3 s.

For the stroke, as indicated in figure 3 - 22, the inner row's stroke is 267 ± 3 μm and the outer row's stroke is 187 ± 2 μm over 4000 cycles. However, the designed stroke for inner row is 294 μm. The difference between them is 9% ((designed stroke - experimental stroke)/designed stroke). The designed stroke for outer row is 195 μm and the difference is 4%. These differences are caused by the slight contact between SMA elements and the bistable beams. In the wireless actuation of bistable micro-actuator, SMA elements are fixed on two linear stages, so, the position of SMA elements could be adjusted to be close to the bistable beams but without contact. However, to simplify the system and reduce the dimensions, SMA elements for quadristable micro-actuator are directly fixed onto the support. Once they are fixed by glue, the positions cannot be changed any more. During the solidification process of liquid glue, the volume will change. As a consequence, even if the SMA elements are located to a proper position (close but without contact with bistable beams), when the glue solidified, the position could be slightly changed.

Although there is still slight contact between SMA elements and bistable beams, there are advantages of using SMA elements with SiO_2 layers. First, SMA with SiO_2 layer is an artificial “two ways” memory effect, its recovery dose not depends on the bistable beams force. For the application of silicon quadristable micro-actuator, the force generated by beams are around 15 mN (calculated by the mathematical model in described in chapter 2) which is unable to bent the SMA elements without SiO_2 layer. Secondly, SiO_2 layer possesses a constant physical property and it will always add a constant biasing load on SMA elements. Although SMA is a hysteresis material, every time when SMA with SiO_2 layer is cooled down, it will recover to the same position. Therefore, the stroke is stable, even if the contact has made the experimental stroke smaller than designed stroke, this difference will not increase. The results of actuation over 4000 cycles have shown that the stroke of inner row is around 267 μm with a variation of ± 3 μm. It is similar for the outer row, the variation is even smaller.

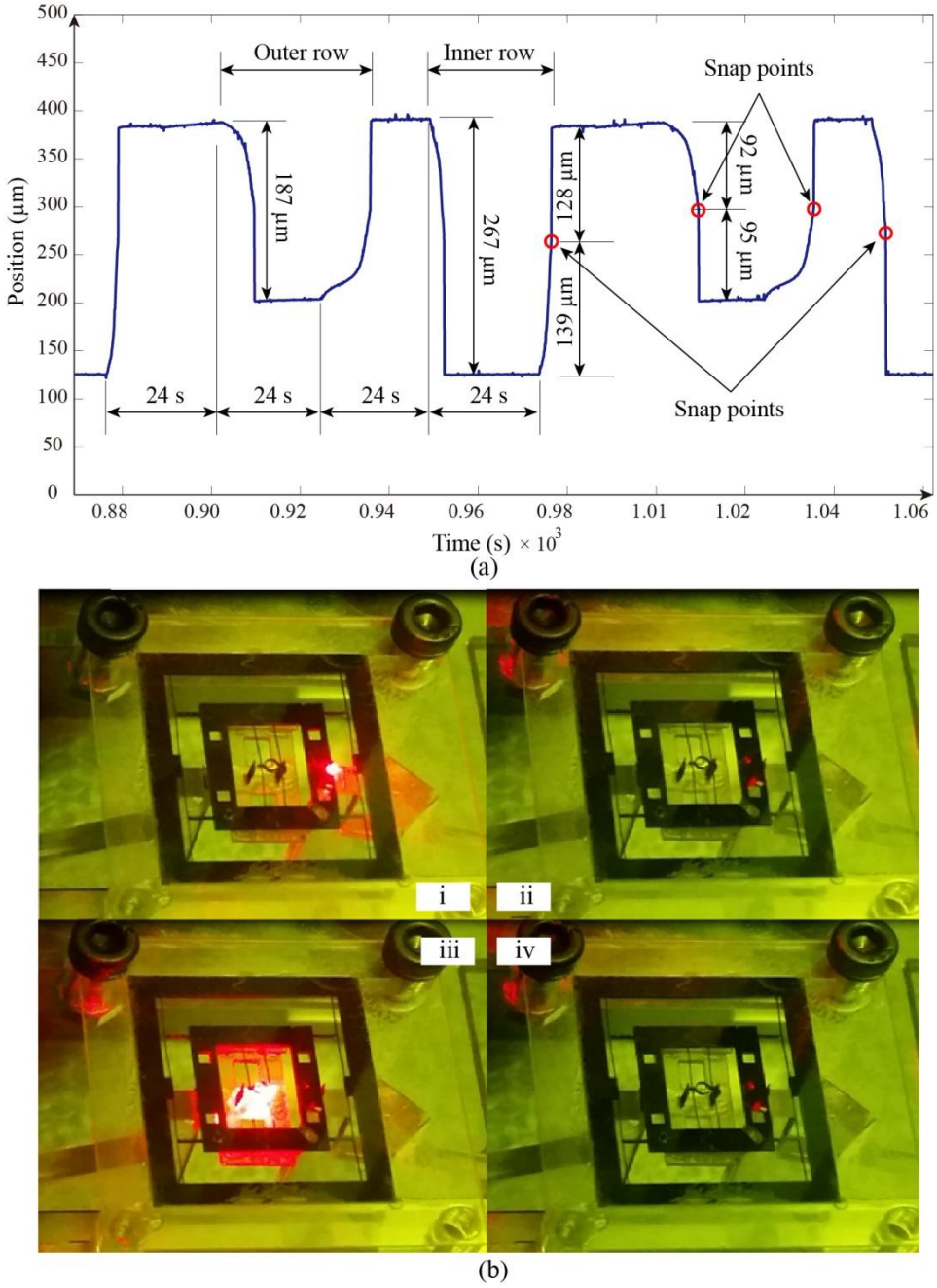

Figure 3 - 22. (a) Two cycles of the actuation of silicon quadristable micro-actuator; (b) Photos of the quadristable micro-actuator in one actuation cycle: i - ii actuation of outer row; iii - iv actuation of inner row.

The snap points for both inner row and outer row are indicated with a red circle in figure 3 - 22. Snap point indicates the position where the force of beam changes from positive to negative. The designed quadristable micro-actuator is base on antagonistic pre-shaped double beams. One of its characteristic is that it has symmetrical output force (take reference from section 2.3.2 of chapter 2). Therefore, theoretically, the snap points should occur at the middle position between the two stable positions. However, because of the fabrication accuracy limit, the meso-scale MDF prototype of quadristable actuator's output is not symmetrical. With the high fabrication accuracy of DRIE technique, it can be seen in figure 3 - 22, the snap points for both inner row and outer row are almost at the middle positions. For the inner row's forward actuation, the distance before snap is 139 µm which is 52% of inner row's stroke. The symmetry of outer row is even better, in its backward actuation, the distance before snap is 49% of outer row's stroke. There could be two reasons that the outer row's symmetry is

better than inner row's. First, for this tested quadristable micro-actuator, the dimensions of outer row's beams are closer to each other (the symmetrical output force is based on the condition that the antagonistic configured two beams are identical to each other). Second, outer row has two pairs of antagonistic pre-shaped double beams, the output behavior is the average results of two pairs beams. The fabrication error follows the normal distribution. According to the statistical law, the average result is closer to the precise value. Therefore, the output behavior of outer row is more symmetrical.

7.3.2 Long-term tests

After the new concept was experimentally verified, a long term test was carried out. In order to reduce the test duration, only the inner row of the silicon quadristable micro-actuator was tested. Because the SMA elements for inner row are easy to be irradiated, in the actuation cycle, one SMA element was heated by 3 s and cooled down by 6 s. Therefore, the duration for one actuation cycle is 18 s (for two SMA elements). After 90 k actuation cycles, the inner row of the micro-actuator is still bistable. The test results for 90 k cycles are shown in figure 3 – 23. It can been seen that the stroke of the inner row increased around 28 μm. This change could be caused by following possible reasons: 1/ Due to the contact between SMA element and the bistable beams, SiO_2 layer was partially removed; 2/ The plastic SMA support structure was deformed because of repeated heating and cooling cycles; 3/ Optical fiber distance sensor's configuration was changed due to external influence, e.g., vibration from the experimental table. The specific reason will be find out in the future work.

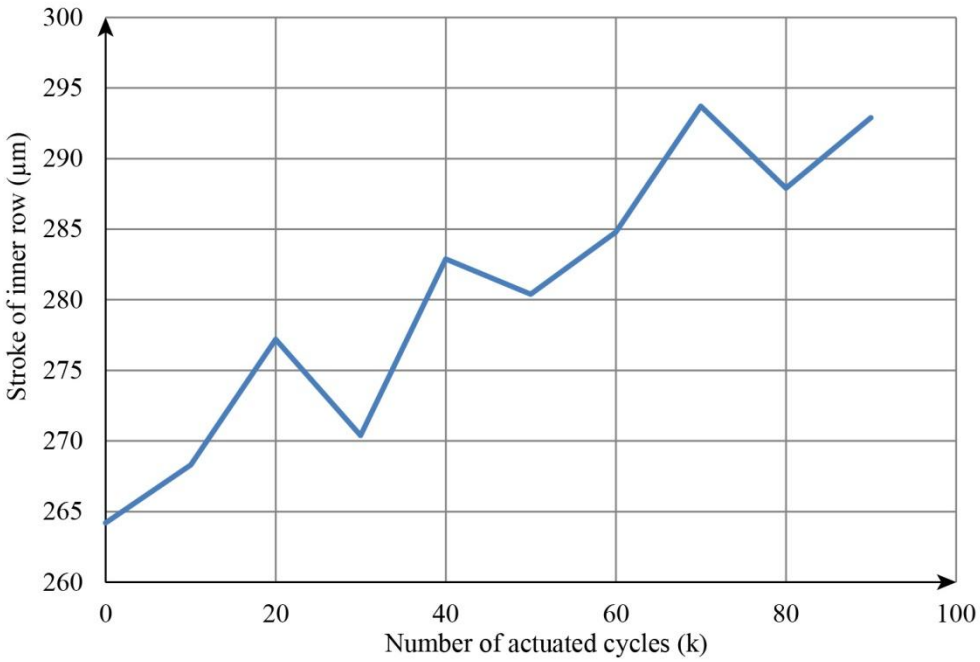

Figure 3 - 23. Long term test of the inner row of the silicon quadristable micro-actuator.

8 Summary

An artificial "two way" memory SMA concept was proposed. Deposited SiO_2 layer was used to bias the SMA element when it was cooled down. A mathematical model of the "two way" memory SMA was constructed. For the properties of SMA material, tensile tests were carried out and the phase transformation relation with laser power, when SMA was under irradiation, was taken as reference from former work. Then, the deposition of SiO_2 layer was realized by Magnetron Sputtering Deposition process and the stroke of the SMA element with 8 μm thick SiO_2 layer was tested with the help of force sensor. Wireless actuation of the silicon quadristable micro-actuator was completed using

the proposed "two way" memory SMA elements. Quadristability of the silicon quadristable micro-actuator was experimentally confirmed. Moreover, the results have demonstrated that the silicon quadristable micro-actuator has more symmetrical output behavior and the "two way" memory SMA has largely reduced the load effect. Furthermore, a long term test for the inner row was carried out. It was proven that the inner row of silicon quadristable micro-actuator can undertake at least 90 k actuation cycles without fracture.

Chapter IV

Micro-actuator with Reducing System

1 Introduction

Quadristable micro-actuator based on antagonistic pre-shaped double beams was designed fabricated and tested. The stroke of the micro-actuator's outer row is around 200 µm. This stroke is still big for a micro-actuator. However, as mentioned, the stroke is limited by the thickness of the beam and geometry factor Q. The geometry factor Q is already lowered by antagonistic configuration from 2.31 to 1.16. The thickness of the beam is reduced to 25µm by using DRIE technique. To reduce the stroke to smaller level, we have chosen the approach of integrating a stroke reducing system into the bistable mechanism, so that, the stroke can be reduced to the micrometer level or even nanometer level. In this chapter, a bistable micro-actuator with stroke reducing structure will firstly be presented. Then, based on the design of bistable micro-actuator with reducing structure, a multistable nano-actuator will be discussed.

2 Bistable micro-actuator with stroke reducing system

2.1 Stroke reducing with flexure hinges connected levers

2.1.1 Proposed design

The designed bistable actuator is shown in figure 4 - 1. There are two main parts: the lower part is the bistable mechanism and the upper part is the stroke reducing structure. Four beams are used in the bistable mechanism to increase the output force. These four beams are parallel configured and clamped at their mid-points. The ends of these beams are fixed by the supporting bracket.

In order to get a big reducing factor, nonlinear reducing principle was adopted. The stroke reducing structure is based on flexure hinges connected levers [QIN 07]. The reducing effect was realized by the rotation of levers. To analyze the working principle, the actual design (figure 4 - 1a) is simplified as the schematic shown in figure 4 - 1b. Levers are considered as rigid and flexure hinges are regarded as a single axis rotational pivot with a torsion spring. Calculation of equivalent stiffness for torsion spring will be discussed in detail in following section. To remain the schematic simple and clear, torsion spring is not shown in the picture.

Like the design of antagonistic pre-shaped double beams, to solve the asymmetrical output force problem, a gap for pre-load is defined between bistable mechanism part and stroke reducing structure. After pre-load action, levers AI and JH, which are the fixing structures, will be fixed onto the supporting bracket. Due to the fact that bistable mechanism should be capable to drive reducing structure so that output of bistable module could be transferred and reduced through reducing system, four (calculated by the mathematical model which will be discussed in later part) parallel central clamped pre-shaped beams are used to make the bistable beams stronger than the reducing structure. Thus, when the actuator is pre-loaded, lever DE will be pushed upward to D'E' as shown in figure 4 - 1c. In a sequence, hinge B will move to B', hinge C will move to C'. Since the reducing structure is symmetrical, hinges G and F will move correspondingly. Then, if the bistable beams are switched from one stable position to the other, it will cause the movement of lever DE. As demonstrated above, it will cause the movement of lever CF. This movement of CF will be taken as the final output (reduced stroke).

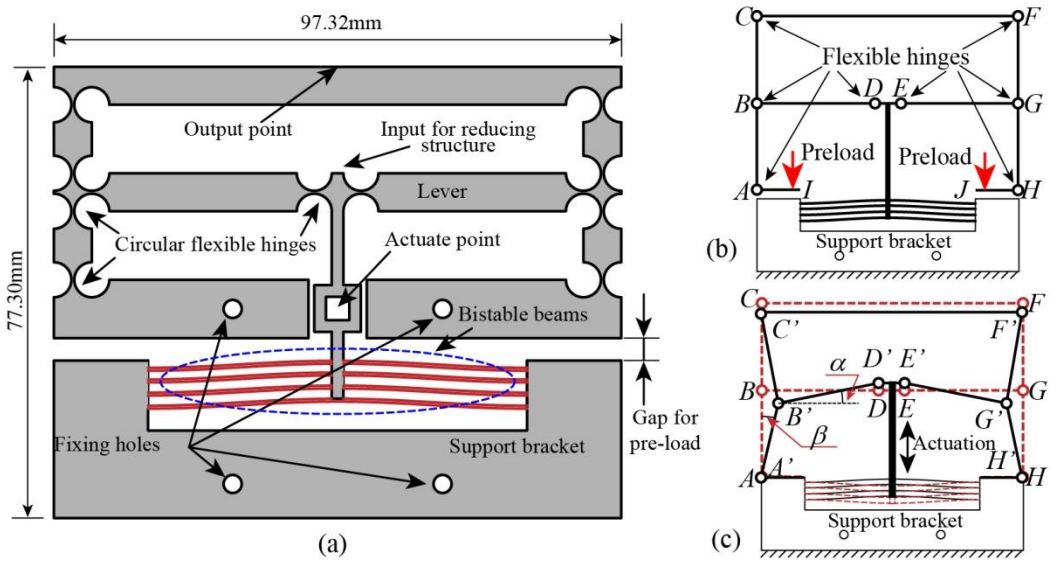

Figure 4 - 1. Bistable actuator with stroke reducing structure: (a) Actual design of the bistable actuator with reducing structure; (b) Simplified schematic of the designed bistable actuator before pre-load; (c) Schematic of the designed bistable actuator after pre-load.

2.1.2 Flexure hinge

As shown in figure 4 - 1, flexure hinges have been chosen as the revolute joints in the stroke reducing system. Flexure hinges have been commonly used as substitutes for mechanical joints in design of micro devices. It has the advantages of no friction losses, no need of lubrication, no hysteresis, no clearance and wear. The limit of flexure hinge is that the movement is limited in a narrow range. In our design, precision is the major requirement and the movement is small. Therefore, flexure hinge is the perfect choice for our design.

In compliant mechanism applications, flexure hinges are commonly made of rectangle blank by removing two symmetrical cut-outs with circular, filleted leaf or elliptic shapes as shown in figure 4 - 2 [TIAN 10]. They have low revolute stiffness in one axis and high stiffness in other degrees of freedom. Among them the circular hinge has the highest stiffness while the filleted leaf hinge has the lowest stiffness, the performance of elliptical hinge is between the two other ones. Moreover, the flexible portion of filleted leaf hinge is bigger than the other two, thus, filleted leaf hinge has the biggest revolute range. It can be easily inferred that the circular hinge has the lowest output range and the elliptical hinge is between the former two. Although filleted leaf hinge have a big output range, it is not as precise as circular hinge. In practical scenario, pure moment load is very rare. It is always accompanied by the translational load. The center of rotation can be changed due to the coupled translational load. This change can be largely limited in circular hinge. Therefore, circular hinge was chosen as the revolute joints in the stroke reducing system.

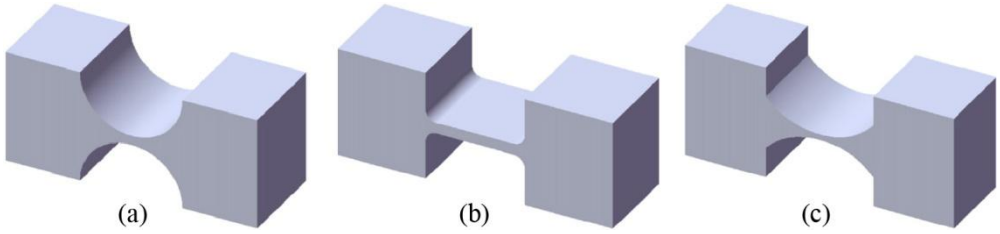

Figure 4 - 2. Single axis revolute flexure hinges: (a) Circular hinge; (b) Filleted leaf hinge; (c) Elliptical hinge [TIAN 10].

An illustration of single axis circular hinge is shown in figure 4 - 3. In the figure, r is the radius of the circular hinge, t_h is the thickness of the thinnest part, b is the depth.

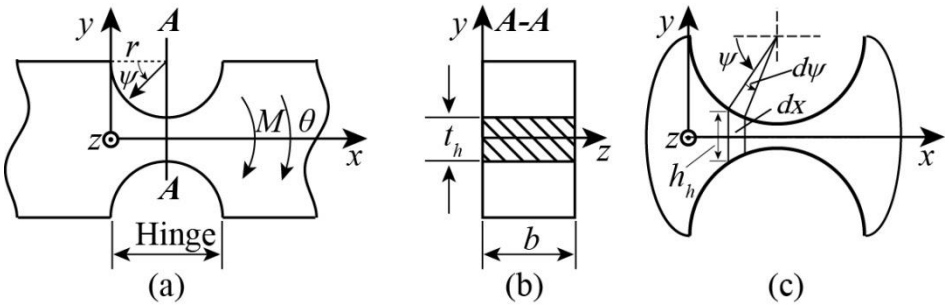

Figure 4 - 3. Single axis circular flexure hinge: (a) Front view; (b) Sectional view of ***A*-*A***; (c) Coordinates transform.

When moment *M* is applied on the flexure hinge, the hinge will be rotated by a small angle θ. If the projection (in plane *xy*) of neutral plane (coincided with *xz* plane before applying load) is expressed as:

$$y = f(x) \tag{4.1}$$

According to the integral theory, the gradient of the neutral plane could be expressed as:

$$\tan\theta = \frac{dy}{dx} \approx \theta \quad x \in [0,\ 2r] \tag{4.2}$$

To calculate the rotation angle θ, the hinge part is divided into small segments. Each segment can be considered as a beam with a length of *dx* and a constant cross section. Once the rotation of each segment is worked out, the total rotation can be calculated by the sum of the rotations of all these small segments. According to mechanics of material theory [TIMO 61], the curvature of the neutral plane of the segment *dx* can be expressed as:

$$\frac{1}{\rho(x)} = \frac{M(x)}{EI(x)} \tag{4.3}$$

Where $\rho(x)$ is the radius of curvature for neutral plane's projection, *M*(*x*) is the moment applied onto the segment *dx*, *E* is Young's modulus of material, *I*(*x*) is the inertial moment of the segment *dx*. Using calculus, the curvature of neutral plane can be calculated and approximated (when deformation is small) as [TIAN 10]:

$$\frac{1}{\rho(x)} = \frac{\left|\frac{d^2y}{dx^2}\right|}{\left(1+\left(\frac{dy}{dx}\right)^2\right)^{3/2}} \approx \pm\frac{d^2y}{dx^2} \tag{4.4}$$

Here, the symbol of the curvature is determined by the direction of the rotation. Therefore, when curvature is positive, with equation (4.3) and (4.4) we get:

$$\frac{M(x)}{EI(x)} = \frac{d^2y}{dx^2} \tag{4.5}$$

Multiply *dx* at two sides of equation (4.5) and apply the integral once, we get the total rotation angle:

$$\theta = \frac{dy}{dx} = \int_0^{2r}\frac{d^2y}{dx^2}dx = \int_0^{2r}\frac{M(x)}{EI(x)}dx \tag{4.6}$$

Here, with the small range ($x \in [0,\ 2r]$), *M*(*x*) can be considered as a constant value. Therefore, the rotational stiffness of the flexure hinge is:

$$k_h = \frac{M}{\theta} = \frac{1}{\int_0^{2r} \frac{dx}{EI(x)}} \tag{4.7}$$

With the help of figure 4 - 3c, equation (4.7) can be converted into polar coordinate system. As shown:

$$dx = rd\psi \sin\psi \tag{4.8}$$

$$I(x) = \frac{bh_h^3(x)}{12} = \frac{b\left(2r + t_h - r\sin\psi\right)^3}{12} \tag{4.9}$$

Therefore, the rotational stiffness, k_h, expressed in polar coordinate system will be:

$$k_h = \frac{1}{\int_0^{\pi} \frac{12r\sin\psi}{Eb(2r + t_h - 2r\sin\psi)^3} d\psi} \tag{4.10}$$

2.1.3 Reducing factor

Output stroke is decided by two factors: the original stroke of bistable beams and the reducing factor of reducing system. The original stroke is simply defined by the mid-point's original rise *h* of the pre-shaped beam. Therefore, the reducing factor will be calculated in the following part.

When *DE* is moved by the output of beams to *D'E'* (figure 4 – 4a), it will cause the rotation of *BD*. Because the movement is much smaller as compared to the length of *BD*, the angle α between *BD* and *B'D'* is small. Supposing the length of *BD* is L_1 and the distance between *DE* and *D'E'* is Δ_1, then α can be expressed by (figure 4 – 4b):

$$\alpha = \frac{\Delta_1}{L_1} \tag{4.11}^3$$

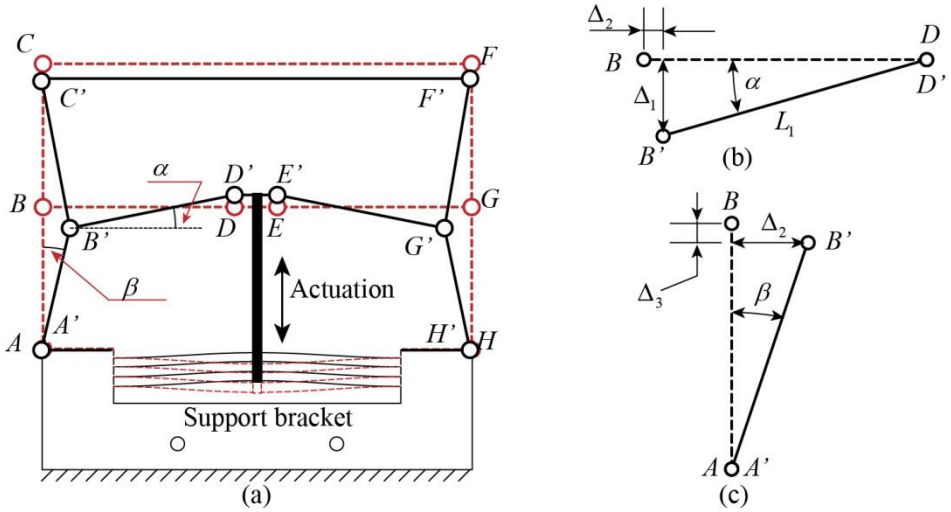

Figure 4 - 4. Illustration of the reducing effect of the flexure hinges connected levers.

This rotation will cause a small horizontal movement of hinge *B* (figure 4 – 4b). The horizontal distance Δ_2 between *B* and *B'* is:

$$\Delta_2 = L_1(1-\cos\alpha) \approx L_1\left(1-\left(1-\frac{\alpha^2}{2}\right)\right) = L_1\frac{\alpha^2}{2} \tag{4.12}$$

[3] The movement of hinge *B* in vertical direction is small, so, it is neglected in this equation.

Then Δ_2 will cause the rotation of *BA* (figure 4 – 4c). The angle β between *BA* and *B'A'* is:

$$\beta = \frac{\Delta_2}{L_2} \tag{4.13}$$

Where L_2 is the length of *BA*. Then rotation β will cause a small vertical movement of hinge B. As a consequence, the vertical distance Δ_3 between B and B' is:

$$\Delta_3 = L_2(1-\cos\beta) \approx L_2\frac{\beta^2}{2} \tag{4.14}$$

Here *BA* and *BC* have the same length, so the distance between *CF* and *C'F'* i.e. the output Δ_4 equals:

$$\Delta_4 = 2\times\Delta_3 = L_2\beta^2 \tag{4.15}$$

Then the reducing factor R_1 is:

$$R_1 = \frac{\Delta_1}{\Delta_4} = \frac{4L_1^{\,2}L_2}{\Delta_1^{\,3}} \tag{4.16}$$

2.1.4 Reacting Force of Reducing Structure

After the reducing effect of *BD* the displacement Δ_2 is relatively small (about 50 times smaller than Δ_1). The force caused by the rotation of *BA*, *BC*, *GH* and *GF* is very small. To simplify the calculation only the force of hinge *B D E* and *G* are considered. The reaction of reducing structure can be regarded as a spring. According to Hook's low, when *DE* is pushed to *D'E'*, the work, W_1, done to the reducing structure is:

$$W_1 = \frac{1}{2}k_{r1}\Delta_1^{\,2} \tag{4.17}$$

Where, k_{r1} is the stiffness factor of the reducing structure. Then, the energy stored in hinges *B, D, E* and *G* is:

$$E_{w1} = 4\cdot\frac{1}{2}k_h\alpha^2 = 2k_h\frac{\Delta_1^{\,2}}{L_1^{\,2}} \tag{4.18}$$

According to the law of conservation of energy:

$$W_1 = E_{w1} \tag{4.19}$$

Using equations (4.17) and (4.18), equation (4.19) becomes:

$$\frac{1}{2}k_{r1}\Delta_1^{\,2} = 2k_h\frac{\Delta_1^{\,2}}{L_1^{\,2}} \tag{4.20}$$

Then, the equivalent stiffness of the stroke reducing structure is:

$$k_{r1} = 4\frac{k_h}{L_1^{\,2}} \tag{4.21}$$

Here, k_h is the rotational stiffness of flexible hinge which is a constant value for a given design. Therefore, the reacting force of the stroke reducing structure can be calculated as:

$$F_{r1} = k_{r1}\Delta_1 = 4\frac{k_h}{L_1^{\,2}}\Delta_1 \tag{4.22}$$

Here F_{r1} is the reacting force. As we see, F_{r1} is a linear function with respect to Δ_1. If we define the downward direction as positive for switching force and let:

$$n_b \frac{EIh}{l^3} F_N(1) = F_{r1}(\frac{1}{2}\Delta_1) \tag{4.23}$$

Here, $F_N(1) = F_N(\Delta)_{\Delta=1}$, is the normalized switching force at middle (half stroke) position of pre-shaped beam (equation (2.24)). Parameter n_b is the number of pre-shaped bistable beams ($n_b = 4$). The reacting force of reducing structure will cross the central point of the switching force of the beams (figure 4 – 5a). Then the resultant force will be symmetrical with respect to the axis of displacement as shown in figure 4 – 5b. As it can be seen, a part of the resultant force is positive and the other part is negative. That means the actuator with the stroke reducing structure is bistable. As it can be seen, at the end of the reacting force curve, the force is not zero. This is because an initial biasing force is added by making the gap, between bistable beam's supporting bracket and reducing structure, bigger than the stroke of bistable beams. In this configuration, the reacting force curve's slope could be small, so that the resultant force can have bigger amplitude and the bistable beam can be more bistable.

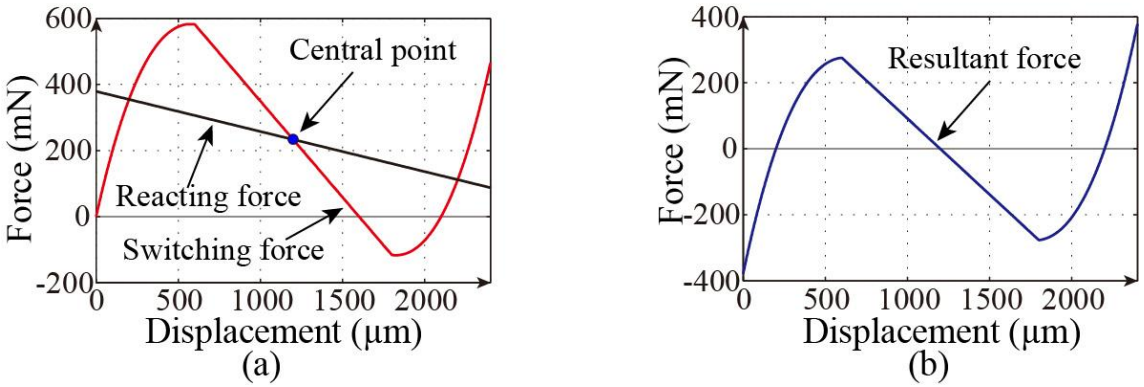

Figure 4 - 5. (a) Switching force for beams and reacting force for reducing structure; (b) Resultant force for the actuator (*l=65mm, h=1200μm, t=450μm, b=3mm, E=3GPa, t_h=0.5mm, r=3mm, L_1=38.16mm*)

As a primary conclusion of this part, the flexure hinges connected levers can be used as reducing structure for pre-shaped bistable beams. By antagonistically configuring the bistable beams and reducing structure, the whole actuator can have a symmetrical output force.

2.2 Hybrid stroke reducing design

A hybrid reducing structure is designed. As shown in figure 4 - 6, the first reducing lever is replaced by flexible beams. The difference between flexible beams and flexible hinges connected levers is that deformation occurs on every point along the beam. For flexure hinges connected levers, deformation only happened at the hinges. So, flexible beam can tolerate more deformation than flexure hinges connected levers which have the same length. Moreover, several flexible beams can be configured in parallel to share the deformation. So with same input, flexible beam can be shorter than lever. The total length of two levers (*BD* and *EG* in figure 4 - 1) is 76.3mm, while the total length of flexible beams (*BD* and *EK* in figure 4 - 6) is 31.0mm.

After analyzing the first reducing structure, we found the output point may have horizontal vibration during the switching process. In the hybrid design the output point is connected with fixing part by two beams we call overshoot resistance in figure 4 - 6.

Moreover, in the first design, the output direction of stroke reducing structure is in opposite direction of input, which can cause some strange output problem. For example, during *DE* is pushed to *D'E'*, the force applied will cause the elastic deformation of *BA* and *GH*. The deformation will appear directly in the output without reducing. So it can be relatively big as compared with output caused by rotation of lever *BA*, *BC* and *GF*, *GH*. But the deformation is in opposite direction with the output.

In the hybrid design, lever *BA*, *BC* and *KJ*, *KL* are not vertical, a small angle of 1.2^o is added so that the input, output and elastic deformation of *BA* and *KL* will be in the same direction. To reduce the width of stroke reducing structure without changing the reducing factor too much, three flexible beams are parallel configured to share the deformation. Here the three beams are adjusted to have the same deflectable length (*BD* + *EK* = *FG* = *HI*) by adding a deflection resistance as shown in figure 4 - 6. Then the deformation of each beam is approximately one third of the total deformation.

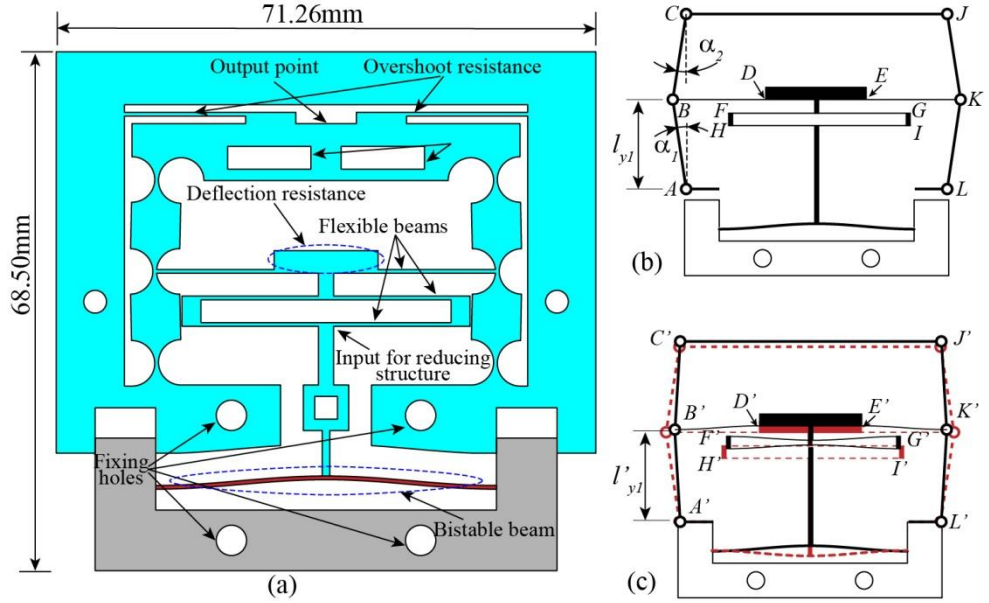

Figure 4 - 6. Hybrid stroke reducing structure: (a) The actual appearance; (b) Simplified schematic; (c) Preloaded schematic.

2.2.1 Flexible beam

The flexible beams used in the hybrid reducing structure can be regarded as a beam with two ends supported by slider linkage as shown in figure 4 - 7. Δ_5 is the deflection at the midpoint of the flexible beam, which is caused by bistable beam. Δ_6 is the movement of one end. According to the symmetry, the movements at the two ends have the same value. δ_x is the deflection of the beam at point *x*. F_{r2} is the force applied at the midpoint. l_d is the length after deflection.

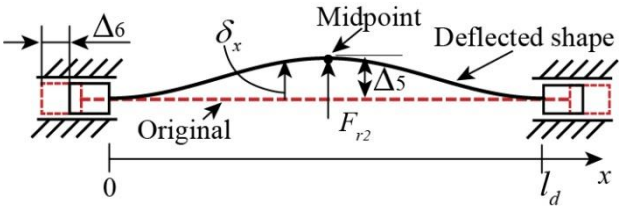

Figure 4 - 7. Schematic for deflected flexible beam.

It is obvious that the deflected shape is symmetrical with respect to the midpoint. The deflection, δ_x, of the left half part ($x \in [0, l_d/2]$), can be calculated by Direct Integration Method as follow:

$$M(x) = \frac{1}{EI_d}\frac{F_{r2}}{8}\left(l_d - 4x\right), x \in [0, \frac{l_d}{2}] \tag{4.24}$$

$$\theta(x) = \int M(x)dx = \frac{1}{EI_d}\frac{F_{r2}}{8}\left(l_d x - 2x^2\right) + C_1, x \in [0, \frac{l_d}{2}] \tag{4.25}$$

$$\delta_x = \int \theta(x)dx = \frac{1}{EI_d}\frac{F_{r2}}{8}\left(\frac{l_d x^2}{2} - \frac{2}{3}x^3\right) + C_1 x + C_2, x \in [0, \frac{l_d}{2}] \tag{4.26}$$

Where $M(x)$ is the internal moment, θ_x is the rotation at x, E is the Young's modulus, $I_d=bt_d^3/12$ is the inertia moment with respect to the axis of deflection, t_d is the thickness of the flexible beam and C_1 and C_2 are constants for integral. With the fact that both the rotation θ and deflection δ are zero at $x=0$, we know that $C_1=C_2=0$. So the deflection at midpoint is:

$$\Delta_5 = \delta_{\frac{1}{2}l_d} = \frac{F_{r2} l_d^{\,3}}{192 E I_d} \tag{4.27}$$

Therefore, the reacting force of the hybrid stroke reducing structure F_{r2} is:

$$F_{r2} = \frac{192 E I_d}{l_d^{\,3}} \Delta_5 \tag{4.28}$$

We can see that reacting force of the hybrid design is also a linear function with respect to the deflection at midpoint. So if let:

$$\frac{EIh}{l^3} F_N(1) = F_{r2}\left(\frac{1}{2}\delta_{\frac{1}{2}l_d}\right) \tag{4.29}$$

$F_N(1) = F_N(\Delta)_{\Delta=1}$ is the switching force of pre-shaped beam (equation (2.24)). Similar with the former reducing design, the diagram of reacting force, which is straight line, will cross the central point of the switching force's diagram (figure 4 - 8). As a consequence, the resultant force will be symmetrical with respect to the displacement axis. Furthermore, although, only one pre-shaped beam was employed in the hybrid design, it is still bistable. Similarly with the first design, there is an initial biasing force to reduce the slope of reducing system's reacting force curve. Because of this initial biasing force, the reacting force is not zero at the end of the curve.

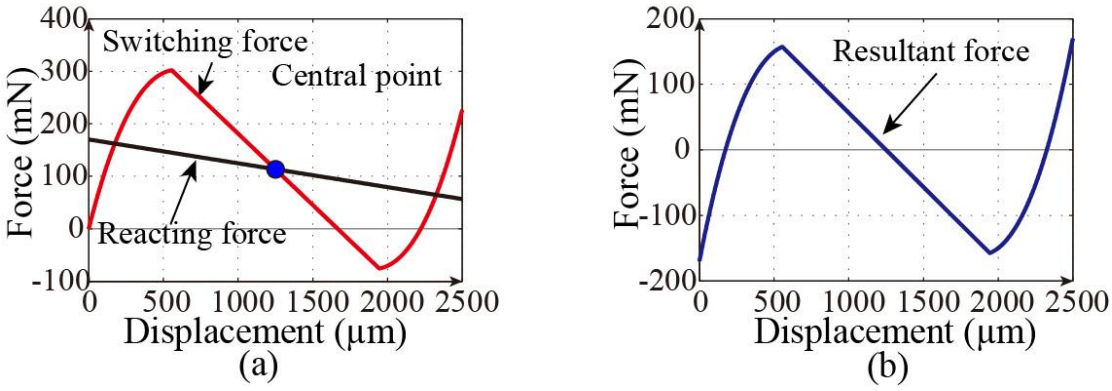

Figure 4 - 8. (a) Switching force for pre-shaped bistable beam and reacting force for reducing structure; (b) Resultant force for the actuator ($l=45mm$, $h=1250\mu m$, $t=450\mu m$, $b=3mm$, $E=1.86GPa$, $t_d=450\mu m$, $l_d=31.03mm$).

So, the hybrid reducing design can largely reduce the dimensions of the reducing structure. At the same time, because of the small stiffness of flexible beam, only one bistable pre-shaped beam is necessary to drive the reducing structure. Moreover, the initial angle of the levers in second reducing level may eliminate the unwanted output behavior caused by elastic deformation of levers.

2.2.2 Reducing factor of hybrid design

In the hybrid reducing design, first reducing level is accomplished by a flexible beam. When the beam is deflected, it causes the movement of its ends. Then, this small movement causes the rotation of flexible hinges connected levers, which is the second reducing level.

The reducing effect of the first reducing level is caused by the difference in length before and after the flexible beam is deflected. Since we have the expression of deflected beam ((4.26)), we can get the arc length *s* (could be used as the length before deflection) of the deflected beam using calculus method:

$$\begin{aligned} s &= 2\int_0^{\frac{l_d}{2}} \sqrt{1+\left(\frac{d\delta_x}{dx}\right)^2}\,dx \\ &= \frac{1}{4EI_d}\int_0^{\frac{l_d}{2}} \sqrt{{F_{r2}}^2 x^2 (l_d-2x)^2 + 64E^2{I_d}^2}\,dx \\ &= 2\int_0^{\frac{l_d}{2}} \sqrt{576{\Delta_5}^2 x^2 (l_d-2x)^2 + 1}\,dx \end{aligned} \tag{4.30}$$

Because the structure is symmetrical, the movement at one end Δ_6 is half of the difference between l_d and *s*.

$$\Delta_6 = \frac{1}{2}(s - l_d) \tag{4.31}$$

Then Δ_6 will cause the rotation of *BA* and *BC* (figure 4 - 6), If we define the length of *BA* as l_1 and the vertical component of l_1 as l_{1y}, then:

$$l_{1y} = l_1 \cos\alpha_1 \tag{4.32}$$

The vertical component, after *BA* is rotated, l'_{1y} is:

$$l'_{1y} = \sqrt{{l_1}^2 - (l_1 \sin\alpha_1 - \Delta_6)^2} \tag{4.33}$$

Similarly we define the length of *BC* as l_2, then:

$$l'_{2y} = \sqrt{{l_2}^2 - (l_2 \sin\alpha_2 - \Delta_6)^2} \tag{4.34}$$

The output Δ_7 for the second reducing level is:

$$\Delta_7 = (l'_{1y} - l_{1y}) + (l'_{2y} - l_{2y}) \tag{4.35}$$

So, the reducing factor for the hybrid reducing design is:

$$R_2 = \frac{\Delta_7}{\Delta_5} \tag{4.36}$$

2.3 Fabrication and test

2.3.1 Fabrication

Meso-actuators with two kinds of stroke reducing structures were fabricated by laser machining (Trotec speedy 400) of medium density fiberboard material (figure 4 - 9). It can be seen that the dimensions of second design is smaller even after the vibration resistance part was added. Between the reducing structure and bistable beam a square cavity (actuate point) is added, so that the actuator can be switched by linear motor through a thin steel bar.

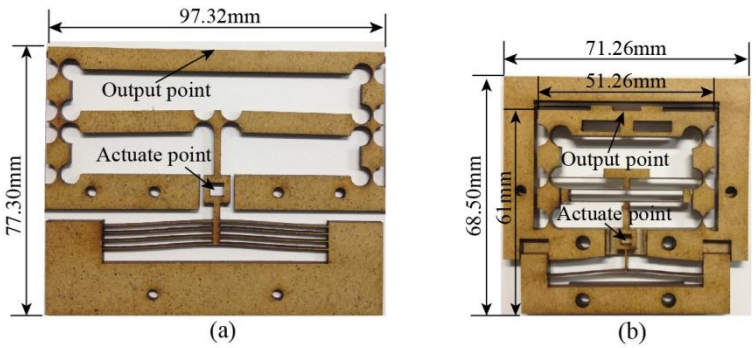

Figure 4 - 9. Fabricated bistable micro-actuator: (a) with purely flexible hinges based reducing structure; (b) with hybrid reducing structure

2.3.2 Test and comparison

The outputs of both designs were measured by fiber optic distance sensor. The sensitivity of the sensor depends on the reflection coefficient of the illuminated surface. To increase the sensitivity of the sensor, a small gold coated silicon mirror was glued at the output point. A linear motor (Newport MFA 25CC) was used to automatically switch the beam from one stable position to the other. The data was collected through National Instruments acquisition card in LabVIEW. The schematic of experimental measurement setup is shown in figure 4 - 10.

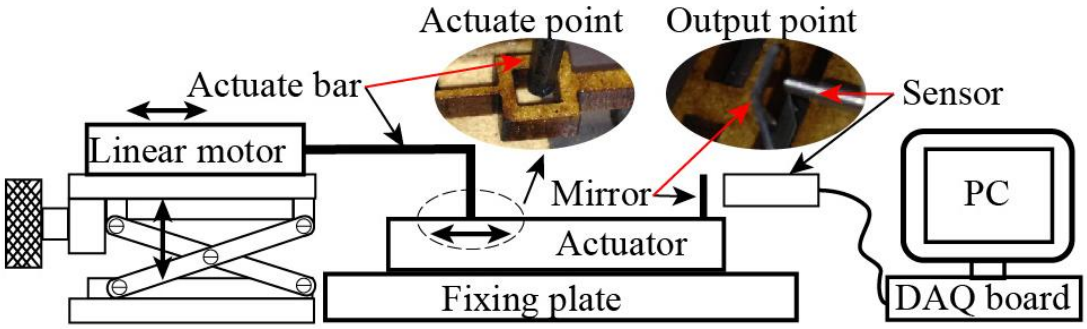

Figure 4 - 10. Experimental setup for measuring the output of the bistable actuator with stroke reducing structure.

The output measurements for both designs are shown in figure 4 - 11. We can see that in figure 4 - 11a the output has a very big overshoot. Following reasons may have caused that: 1/ The mobile mass for the output part of the structure is too big; 2/ There are horizontal vibrations at the output point; 3/ The snap effect was too strong.

Therefore, in the second design, some unnecessary material is removed at the output part and two thin beams (overshoot resistance in figure 4 - 6a) were added to avoid the vibration of output part in horizontal direction. The experimental results proved that the hybrid design works very well. The overshoot disappears in the output of the hybrid design. Moreover, in the first design input and output for reducing structure are in opposite directions. So, when the bistable actuator was switched from one position to the other, the force applied on reducing structure would cause elastic deformation of lever *BA* and *GH* (figure 4 - 1b). This will add an output in the reverse direction with output caused by real input. In the hybrid design, an original angle of 1.2^o (α_1 and α_2) is added for the vertical levers (*AB*, *BC*, *KL* and *KG* in figure 4 - 6), so that all the input, output and elastic deformation will be in the same direction.

We can see that in figure 4 - 11b, the unwanted output caused by elastic deformation at one stable position has already disappeared. At the other position, a very small elastic deformation effect still remains. It can be caused by fabrication defects. Because the angle added is small, when the structure

is not fabricated perfectly symmetrical, it is possible that when it is actuated at one position the rotation of the vertical bar will be a little bigger than 1.2^o. Then the elastic deformation occurs in opposite direction again. As the actuating process going on the angle of the vertical bar will be smaller than 1.2^o, then the output becomes normal. This problem can be solved by increasing the original angle.

In figure 4 - 11b, the snap effect is very clear. That means as the linear motor switching the bistable beam slowly, when the beam comes to snap point where the force change the direction, the beam will switch itself very fast. The part of the curve before snap strongly depends on the linear motor used to switch. If a faster motor is employed, this part will be steeper.

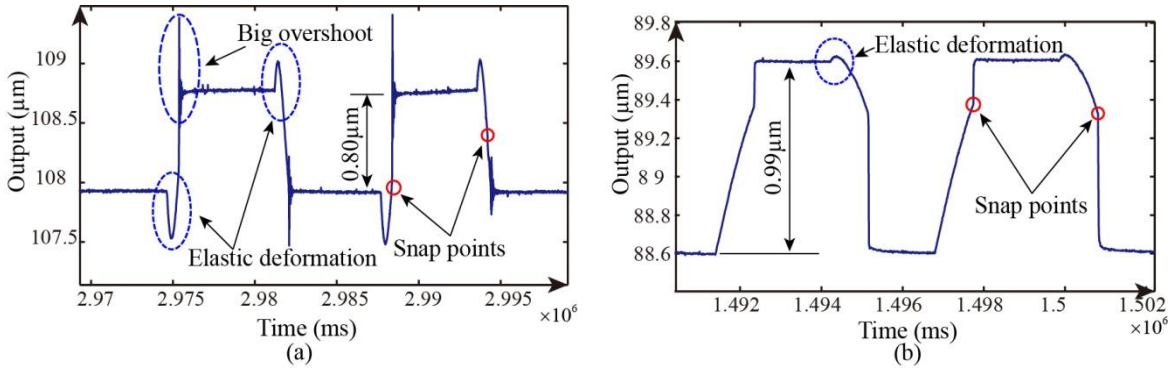

Figure 4 - 11. Output measurement: (a) Purely flexible hinges connected levers based stroke reducing design; (b) Hybrid design.

It is clear that both of the two designs are bistable. The first has an output of 0.8 μm while the second has a output of 1.0 μm. The input for both of them is 2.38 mm. Although the reducing factor for the second design is smaller, it has smaller dimension which is also important for micro-actuators. Moreover, the second design has solved the problems observed in the first one.

2.4 Summary

Bistable micro-actuator with two kinds of stroke reducing structure were designed, fabricated and tested. Both of the two designs are bistable. Although problems of big overshoot and unwanted output behavior are observed in the first design, the problems are solved in the second design by adding the vibration resistant part and an initial angle of the lever (vertical one) in the second reducing level. It is proved that the integration of a reducing structure can solve the midpoint rotation problem for a single pre-shaped beam to make it bistable. Then the flexure hinges connected levers and flexible beams can be used together in stroke reducing structure. Moreover, several flexible beams can be connected in parallel to share the deformations. This kind of hybrid design can largely reduce the size of the reducing structure.

3 Multistable nano-actuator

3.1 Proposed design

In former part, a bistable actuator with a stroke reducing structure has been designed fabricated and tested. However, the bistable actuator has only two output positions. It is difficult to realize some complex tasks. Furthermore, the output of the designed bistable actuator with reducing structure has an output around 1 μm and the dimensions of the actuator are at the level of several centimeters which is too big for the micro-actuator. Therefore, it is decided to design a multistable actuator by combining

several of the bistable actuators designed in former part. To minimize the dimensions of the actuator, new fabrication techniques will be adopted such as DRIE.

The designed multistable actuator is shown in figure 4 - 12. It is formed by four bistable modules which are coupled through a parallel coupling system. This coupling system has not only the coupling function but also the reducing effect. The outputs of these four bistable modules are combined to a series of outputs distributed over an axis.

Using different reducing factors for bistable modules, different output combination strategies can be available for various applications. In order to have submicrometric until nanometric output resolution, the thickness of bistable beams should be reduced. Therefore, the laser cutting process for previous bistable design is not capable to realize the fabrication any more. So, the multistable nano-actuator is expected to be fabricated on silicon wafer using micro-fabrication technique DRIE.

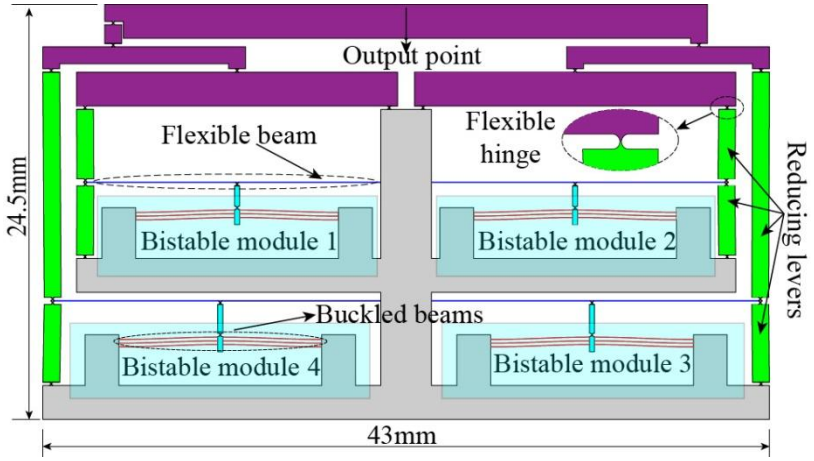

Figure 4 - 12. Multistable nano-actuator.

3.2 Bistable module

One of the four bistable modules (bistable module 1) is shown in figure 4 - 13. Similarly with the hybrid bistable design, central clamped pre-shaped beams were used as the bistable element. However, the bistable beams need to drive the reducing structure and the coupling system, so, three (by calculation) parallel pre-shaped beams are used to increase the force. Another difference is that, one end of the flexible beam is fixed to have more stable output behavior. Because of the fixed end, the reducing structure is no more symmetrical, so during the switching, the central input point of the flexible beam will move in horizontal direction. Therefore, two extra flexure hinges *G* and *F* were added to decouple the bistable beams and the flexible beam. To simplify the assembly, no more preload is employed in the bistable modules. As a consequence, the absence of preload will lead to an asymmetrical Force-Displacement output behavior, it is not a big problem with the nano-actuator in which has been integrated a reducing structure with a big reducing factor. Because output force of bistable beams will be amplified by the same value of reducing factor at output point, the output force in both output direction will largely exceed the requirement for nano-applications. As a consequence, the output force limit in both directions only depends on the strength of the structure. It is like the case that the peak of a sinusoid waveform is cut because of saturation effect of oscilloscope. So the force output of bistable module with reducing structure could be regarded as symmetrical in a general way.

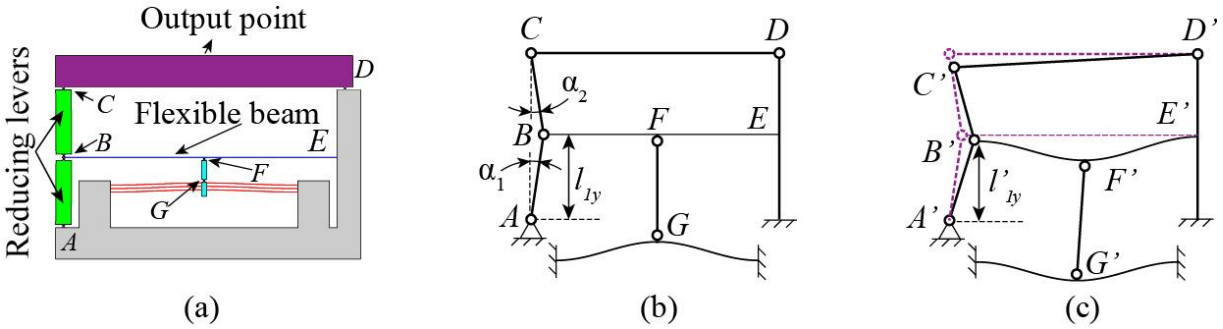

Figure 4 - 13. Flexible hinges based stroke reducing structure: (a) Bistable module 1; (b) Schematic of reducing structure; (c) Actuated reducing structure.

In [QIU 04], it is reported that when the geometry factor Q is bigger than 6, central clamped pre-shaped beams will be well bistabled. But for a given length *l*, bigger *Q* will create bigger internal stress. In order to avoid enlarging the length of the beam too much and to have the beam well bistabled, *Q* is chosen to be 7. Then with a given thickness of beam $t=20\mu m$, the central original rise $h=Q\cdot t$ will be $140\mu m$ and the stroke is about two times of *h*, i.e. $280\mu m$. Obviously the stroke is too big for a nano-actuator, then a flexure hinges based stroke reducing structure is monolithically integrated.

In figure 4 - 13a, *A*, *B*, *C*, *D*, *F* and *G* are circular flexure hinges (a zoomed view of circular flexure hinge is shown in figure 4 - 12). If we consider the flexure hinges as frictionless rotational revolute joints, the bistable module 1 can be simplified to the schematic shown in figure 4 - 13b. The specific reducing factor depends a lot on the original angles between *AB* and *BC* with respect to the vertical direction, i.e. α_1 and α_2 (figure 4 - 13b). The smaller the angle is the bigger the reducing factor will be.

According to former section, when the reducing structure is not properly configured, it has the unwanted output behavior (figure 4 – 11a and figure 4 - 14). When the bistable element is switched between two stable positions, it will generate an approximate square waveform input for the reducing structure. But the output is not a square-like waveform. When it starts from stable position 1 to stable position 2, the output goes to the inverse direction for a small distance, then, turned back to the stable position 2. Similar case happened when it came back to position 1. This causes the output of switching process inconsistent.

This problem could be caused by two reasons: the non-monotonic output and the elastic deformation of lever. If we just consider the lever *AB* and rotate it from *AB* to *AB*' (figure 4 - 14), the trace of *B* is an arc. So the component movement in vertical direction, i.e., the output, will firstly increase then decrease. This is the non-monotonic output of rotational lever. So, to avoid the problem, trace of *B* should not pass the vertical line where the maximum output occurs. Furthermore, when the beam *BE* is deflected, a force with the same direction will apply on *BA* and this force will cause a small elastic deformation of *BA*. In our case, *BA* will be compressed. So, *BA* becomes shorter. This deformation is much smaller than the output of *B*, but it will be added directly to the final output without reduction effect. So, when it is compared to the final output it will cause a visible change on the output behavior. When this elastic deformation happens in the opposite direction, it can cause the same unwanted behavior shown in figure 4 - 14.

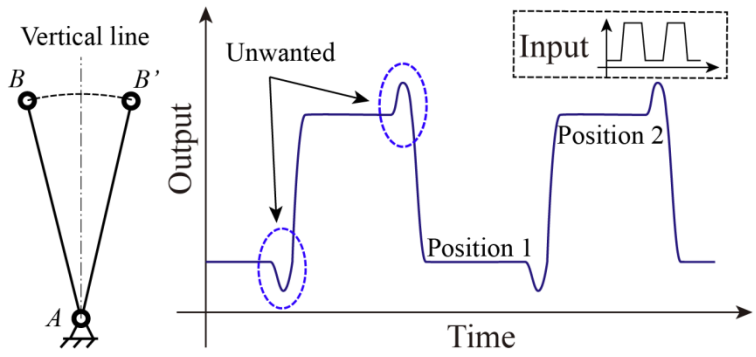

Figure 4 - 14. Illustration of the unwanted behavior in output.

In our case, the bistable beams are originally designed to be upward buckled, so that when the bistable beams are switched to the other stable position, the force in lever *GF*, which connect bistable beams and the reducing structure, is always a tensile force. This will assure that *GF* will not be twisted due to flexure hinges *G* and *F*. In this configuration, the force applied on *AB* is in downward direction and will cause an elastic deformation in the same direction. As the deflection of beam *BE* will always generate a movement of *B* towards the right side, the original position of *AB* is chosen on the right side of the vertical line, in order to make the output in the same direction with the elastic deformation.

3.3 Reducing Factor

The first reducing level of multistable nano-actuator's reducing structure is quite similar with the hybrid reducing structure in former section (figure 4 - 15). Here input (movement of the midpoint) is defined as Δ_8 and output is denoted as Δ_9. The deflecting force is F_d. The main difference is that one end of the flexible beam is fixed. Thus, output equals to the difference between the already deflected length l_d and the arc length s (in former design, the output is half of the difference between l_d and s). Therefore, using equation (4.30), the output of the first reducing level could be expressed as:

$$\Delta_9 = s - l_d = 2\int_0^{\frac{l_d}{2}} \sqrt{\frac{576\Delta_8^{\,2}x^2}{l_d^6}(l_d - 2x)^2 + 1}dx - l_d \tag{4.37}$$

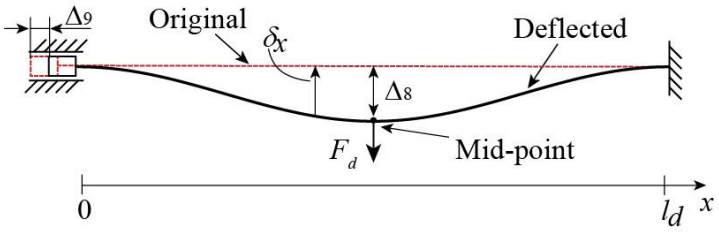

Figure 4 - 15. Flexible beam for the first reducing level of the multistable nano-actuator.

The second reducing level is the same with the former design, thus according equations (4.34) and (4.35), output of bistable module 1, i.e., Δ_{10} will be:

$$\Delta_{10} = \frac{1}{2}\left[(l_1\cos\alpha_1 - \sqrt{l_1^{\,2} - (l_1\sin\alpha_1 + \Delta_9)^2}) + (l_2\cos\alpha_2 - \sqrt{l_2^{\,2} - (l_2\sin\alpha_2 + \Delta_9)^2})\right] \tag{4.38}$$

Where, l_1 and l_2 are the lengths of levers *BA* and *BC*. Because the output is taken from the midpoint of lever CD and flexure hinge D is fixed, the output is half of the vertical movement of hinge C. Thus, a coefficient 1/2 is added. The total reducing factor R_{M1} for bistable module 1 is:

$$R_{M1} = \frac{\Delta_{10}}{\Delta_8} \tag{4.39}$$

The reducing factors R_{M2}, R_{M3} and R_{M4} for other three bistable modules can be calculated with the same method.

3.4 Coupling the four bistable modules

To form a multistable actuator, the outputs of bistable modules should be coupled. There are two kinds of coupling strategies: serial coupling (figure 4 - 16a) and parallel coupling (figure 4 - 16b). Serial coupling is simple. The output of module 1 is directly linked to module 2. When module 1 is actuated the whole module 2 will act as the load for module 1. Different from serial coupling, in parallel coupling, two bistable modules are at the same level and they are coupled through coupling structure. The coupling structure in miniature design is normally levers connected by flexible hinges which is a lighter load. At the same time, the coupling structure has a stroke reducing effect. Like it is shown in figure 4 - 16b, the final output is the weighted average of output 1 and 2.

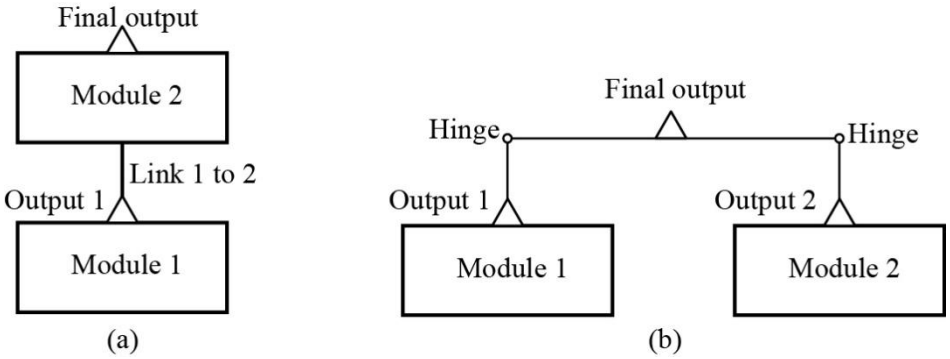

Figure 4 - 16. Coupling strategies: (a) Serial coupling; (b) Parallel coupling.

In our design, each bistable module has a reducing structure with relatively weak output stiffness. If serial coupling strategy is exploited, when pre-module (e.g., module 1 in figure 4 - 16a) drives the whole following module (e.g., module 2 in figure 4 - 16a), there could be big vibrations. Therefore, the parallel coupling strategy was chosen (figure 4 - 17). Furthermore, in parallel strategy, coupling structure gives an additional reducing effect.

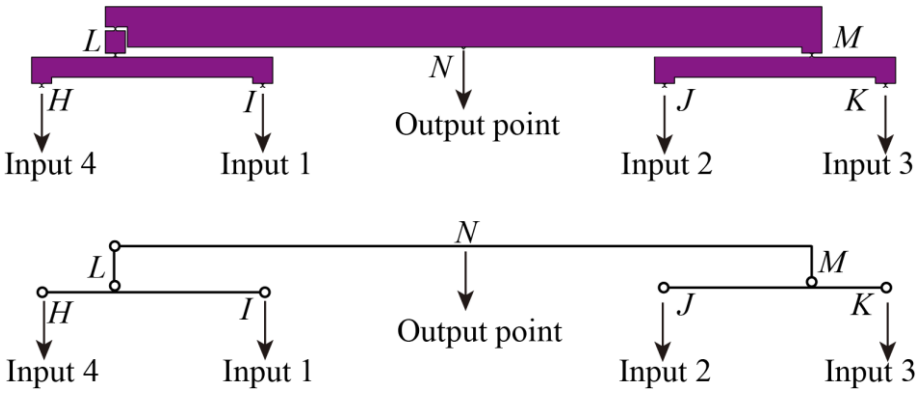

Figure 4 - 17. Parallel coupling structure used in this design (upper part) and simplified schematic (lower part).

3.5 Output strategies

Since there are four bistable modules coupled in the nano-actuator and the final output is the combination of the outputs from the four bistable modules, it is possible to have different output strategies by giving each bistable module a certain stroke and reducing factor. Here, four bistable

modules were designed with same original strokes, i.e., 280 µm. Using different reducing factors, these four modules can have different strokes at the output point.

The most common desired output strategy is to have continuous and linearly distributed output positions over an axis. For the purpose, the strokes of four modules at the output point can be, e.g., 10nm, 20nm, 40nm and 80. Then the combined outputs can be those given in table 4 - 1.

Table 4 - 1. Combination of bistable modules' outputs for continuous linear distribution

Number	M1 10nm	M2 20nm	M3 40nm	M4 80nm	Movement (nm)
0	×	×	×	×	0
1	●	×	×	×	10
2	×	●	×	×	20
3	●	●	×	×	30
4	×	×	●	×	40
5	●	×	●	×	50
6	×	●	●	×	60
7	●	●	●	×	70
8	×	×	×	●	80
9	●	×	×	●	90
10	×	●	×	●	100
11	●	●	×	●	110
12	×	×	●	●	120
13	●	×	●	●	130
14	×	●	●	●	140
15	●	●	●	●	150

● Module is actuated

× Module is not actuated

For applications that need big and small steps at the same time, continuous and linearly distributed outputs may not be the best choice. For example, in applications where high speed (big step) and high resolution (small step) are required. For this scenario, it is possible to separate the continuous output range into two discontinuous ranges by increasing the stroke of bistable module 4. Furthermore, if both bistable module 3 and 4's strokes are increased, the combined output could be four separate zones distributed over the range (figure 4 - 18).

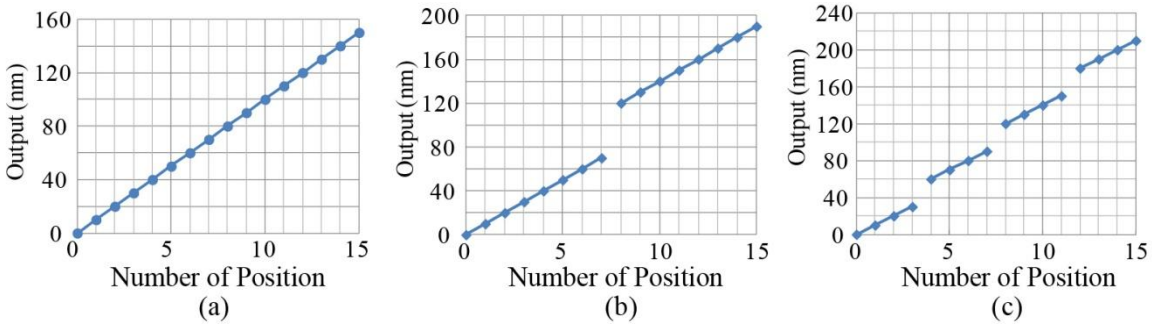

Figure 4 - 18. Output strategies: (a) Single continuous zone, strokes for four bistable modules are 10, 20, 40 and 80nm; (b) Two separate zones, strokes for four bistable modules are 10, 20, 40 and 120nm; (c) Four separate zones, strokes for four bistable modules are 10, 20, 60 and 120nm.

Therefore, the designed multistable nano-actuator could have different output strategies. According to the requirements of applications, outputs with different steps could be generated.

3.6 Simulation

3.6.1 Stress Verification

The designed multistable nano-actuator is expected to be fabricated on silicon wafer in the future. Since it is a monolithic structure and the flexible parts are expected to be deformed elastically, it should be assured that the internal stress generated during the actuation would not pass the elastic limit of silicon material. Figure 4 - 19, b and c shows the stress simulated when all four bistable modules are actuated (in ANSYS). The elastic limit of silicon has been chosen at 120MPa. The simulation reported a global maximum stress of 81MPa. The position where the maximum stress occurs corresponds to the hinge *B* (figure 4 - 13). In fact, as we see in figure 4 - 19a, there are two flexure hinges at *B*. These two hinges were utilized to share the deformation at *B*, so that the maximum stress can be reduced.

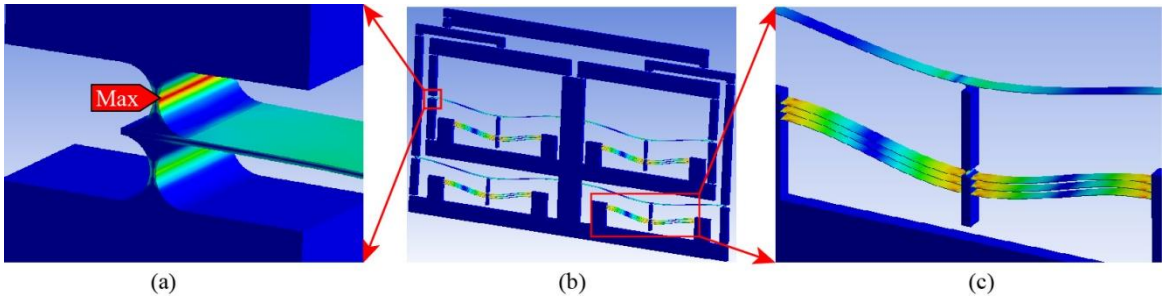

Figure 4 - 19. Stress simulation for the multistable nano-actuator: (a) Location of global maximum stress; (b) The global result; (c) Stress of one bistable module. (The deformation is visually enlarged four time of the real scale)

3.6.2 Simulation of bistable module

The forces of bistable modules are analyzed in FEM software ANSYS. The forces from mathematical model and FEM model for bistable module 4 are shown in figure 4 - 20. It can be seen that these two results are quite close to each other except the part near the two peaks. The difference between them is due to the simplification in the mathematical model. As a matter of fact, in the mathematical model, only the first three buckling modes are considered because the influence of higher buckling modes is relatively small as compared to the first three ones. In FEM analysis, the nonlinear method is used. It is closer to the real behavior of buckling beam. So in the following section the simulation results will be used to decide the reducing factor and get the expected outputs.

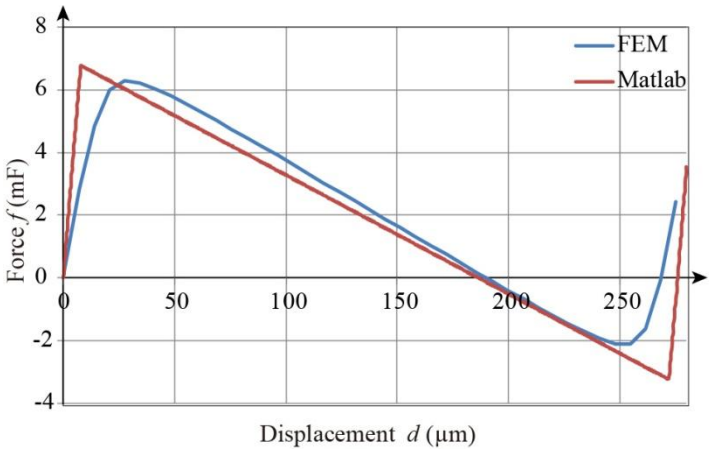

Figure 4 - 20. Comparison of mathematic model and FEM model for switching force

3.6.3 Simulation of reducing structure

The outputs of the multistable nano-actuator are simulated in FEM software ANSYS and compared with mathematical model (table 4 - 2). The results shown here correspond to the situation when only one of the four bistable modules is actuated. Firstly, we found that the biggest difference between two models reached 4.4% which is unacceptable for an accurate model. After a carefully analysis, it was found that the values α_1 and α_2 (coming from Computer Aided Design model) used for FEM analysis were slightly bigger than the ones used in mathematical model. That is why the FEM results are always bigger than the results from mathematical model. As we see in table 4 - 2, after correcting the angle values, the difference between the two models are quite close to each other. Then, by properly actuating the four bistable modules, we can get linearly distributed outputs over an axis from about 10nm to 150nm.

Table 4 - 2 Output of four bistable modules

	Module 1	**Module 2**	**Module 3**	**Module 4**
Stroke (µm)	275.4	275.4	275.4	275.4
Output of mathematical model before angle correction(nm)	10	20	40	80
Output of mathematical model after angle correction(nm)	10.3	20.7	41.6	83.3
Output of FEM (nm)	10.3	20.7	41.8	81.7
Difference before angle correction (%)	3.2	3.7	4.4	2.1
Difference after angle correction (%)	-0.1	0.1	0.4	-2

3.6.4 Deflection under gravity

The exploitation of flexible hinges has led to the possibility of monolithically integration of a stroke reducing structure. However, due to the weak stiffness of flexure hinges, the mobile part of the nano-actuator may be deflected by gravity. In order to verify if the error introduced by this deflection is small enough as compared to the output stroke, the deflection under gravity was simulated in ANSYS. The results are shown in figure 4 - 21.

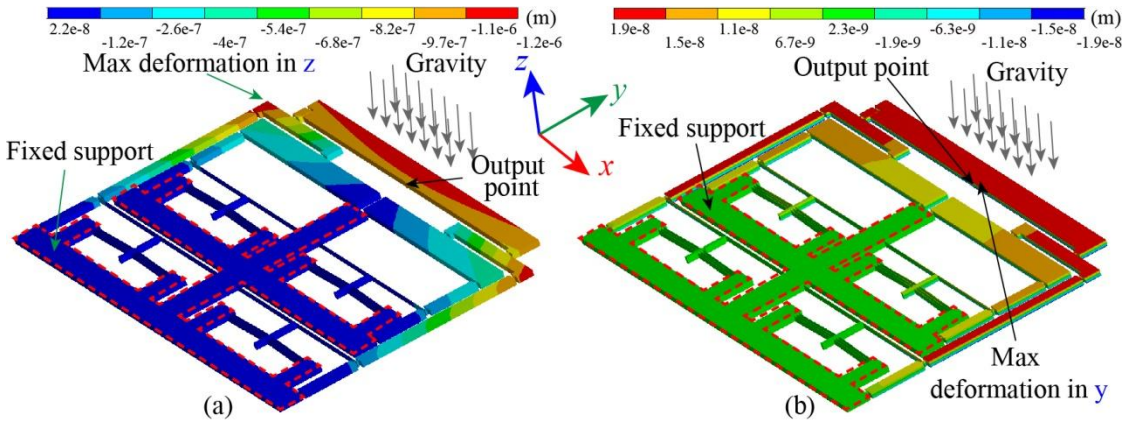

Figure 4 - 21. Deformation of multistable nano-actuator under gravity without support: (a) Deformation in z-axis; (b) Deformation in y-axis (direction of actuation).

In the simulation, the fixed part of the multistable nano-actuator was constrained with a fixed support. The standard gravity was applied in the negative direction of z-axis. Firstly, the maximal stress is 9.6

MPa which occurs at the flexure hinges. This value is much smaller than the stress limit of silicon material (120 MPa for the elastic limit), which means the nano-actuator will not break under gravity. Then, the deformation in z-axis is presented in figure 4 - 21a, the maximal deformation occurs at the output part. The deflection at output point in z-axis is 1.06 µm. This deflection will cause the movement in y-axis, which is the axis of actuation. The deformation in y-axis is presented in figure 4 - 21b. It can be seen that the maximal deformation is also at the output part and the deformation (movement) at output point due to the gravity in y-axis is 17.2 nm. Since the minimal output stroke of the multistable nano-actuator is designed to be 10 nm, this deformation caused by gravity is too big as compared with output stroke. Therefore, it is necessary to introduce some supporting mechanism to reduce the influence caused by gravity.

One approach to solve the gravity caused deflection problem is using half-sphere beads [KHAN 12]. However, multiple flexure hinges are utilized in the nano-actuator, to effectively support the mobile parts, it is necessary to support at multiple locations. Due to the error of fabrication, the radius of half-sphere beads are not exactly the same value, thus, when the supporting location is more than three, not all the beads will have a contact which the ground. Another solution is to use complete sphere sapphire beads dropped into through-holes [KHAN 14], which could theoretically maintain all the supporting points in contact with the ground. The location of holes for supporting beads and the supporting principle is shown in figure 4 - 22.

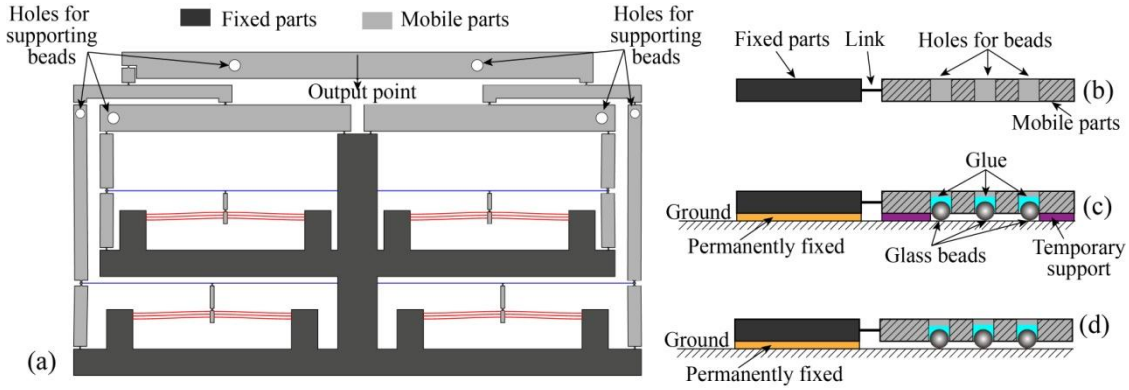

Figure 4 - 22. Support strategy of multistable nano-actuator: (a) Location of holes for supporting beads; (b), (c) and (d) Illustration of the supporting procedures.

In figure 4 - 22a, the dark grey area is the fixed part and the light grey part is the mobile part. The mobile part need to be supported was divided, by flexure hinges, into five parts: four reducing structure for four bistable modules and the coupling system. One supporting beads was added for every reducing structure of bistable module. Two beads were added for the coupling system at the output lever, which is the biggest mobile mass in coupling system. Though, the reducing structure for each bistable module is slightly different, the whole nano-actuator could be regarded as a symmetrical structure. Thus, these supporting beads were symmetrically located.

To explain the supporting mechanism, the nano-actuator could be abstracted as the structure shown in figure 4 - 22b, which includes the fixed part and mobile part (with through-holes for beads) connected by flexible link (flexure hinges). Firstly, the mobile part should be adjusted to the same height with fixed part with temporary support (figure 4 - 22c). The supporting beads (made from glass material) will be dropped from the topside of via holes. Diameters of through-holes were designed to be slightly bigger than the beads, so that the beads could fall freely, under the gravity, until they contact with the ground. A small amount of glue is applied into the through-holes to fix the supporting beads. After the glue dried, the temporary support could be removed (figure 4 - 22d). In this scenario, all beads are

theoretically possibly in contact with the ground. The simulated deflection of multistable nano-actuator under gravity including supporting beads is shown in figure 4 - 23.

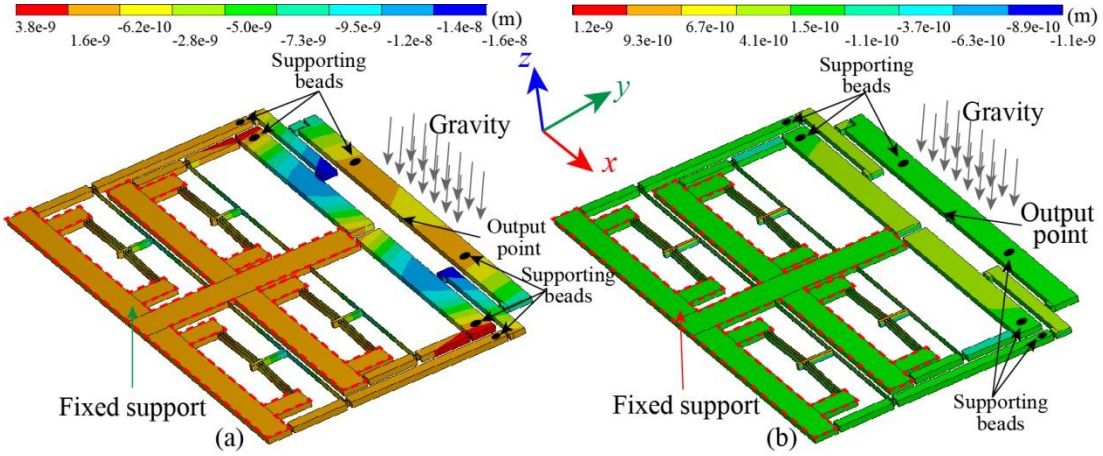

Figure 4 - 23. Deformation under gravity of multistable nano-actuator with supporting beads: (a) Deformation in z-axis; (b) Deformation in y-axis.

As we see in figure 4 - 23a, the maximal deformation in z-axis of the nano-actuator has been theoretically reduced from 1.2 µm (without support) to 16nm (with support) and the deformation at output point is 0.7nm. In the actuation direction (figure 4 -23b), i.e., y-axis, the maximal deformation is 1.2 nm and the deformation at output point is 0.04 nm which is negligible as compared with the smallest output stroke (10 nm) of the nano-actuator.

3.6.5 Modal analysis

As shown in figure 4 - 22b, the structure of the multistable nano-actuator could be regarded as two masses (fixed part and mobile part) connected with flexure hinges which is also a mass spring vibration system. The natural frequency could be calculated as:

$$f = \frac{1}{2\pi}\sqrt{\frac{k}{m}} \tag{4.40}$$

Where f is the natural frequency, k is the stiffness factor of spring, m is the mass. According to this equation, we can see that, when the stiffness factor of the spring is small, the natural frequency could be low. In the multistable nano-actuator, due to the utilization of flexure hinges, the stiffness of the link (spring) between fixed part and mobile part is weak. Therefore, it is possible that the structure has low natural vibration frequency. To calculate the natural vibration frequency, the modal analysis is carried out with FEM in ANSYS. The first ten vibration modes are presented in figure 4 - 24.

Mode	Frequency (Hz)
1	700.46
2	998.87
3	1115.3
4	1228.6
5	1253.3
6	1544.6
7	1605.9
8	1669
9	1723.7
10	1972.5

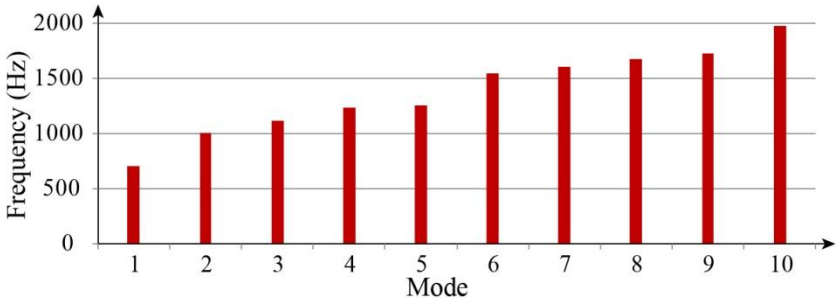

Figure 4 - 24. Modal analysis of multistable nano-actuator

It can be seen that, the first vibration mode occurs at the frequency of 700Hz. The designed nano-actuator is expected to be actuated with laser heated SMA element, which is a kind of thermal

actuation. Due to the working principle of SMA element and the fact that it is heated with laser (low power energy transfer), the frequency of actuation for the designed nano-actuator will be much lower (several hertz) than the first vibration mode. So, the actuation force from SMA element will not cause the resonance problem.

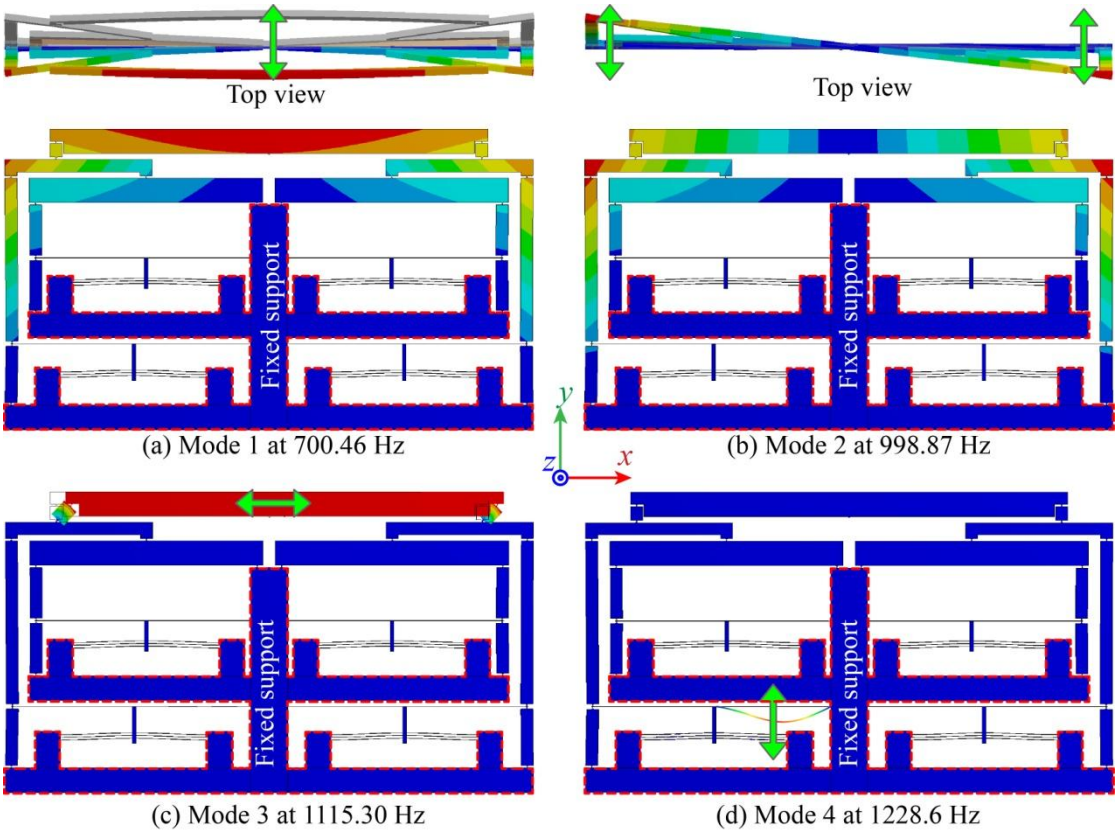

Figure 4 - 25. First four vibration mode shapes of multistable nano-actuator.

The first four mode shapes of the nano-actuator are shown in figure 4 - 25. It is obvious that the first vibration mode shape is the bending in z direction at 700 Hz. The second mode shape is the torsion with respect to y-axis at about 1 kHz. The third mode shape is the vibration of the output lever in x-axis at about 1.1 kHz. Modes 4 to 7 are the vibrations of the reducing flexible beams of bistable modules 4, 3, 2, 1. We can see that, in the modal analysis, the output part is a free end, if a flexible link is added to the output part, it will increase the connection stiffness between fixed part and mobile part, so that the vibration modes could be augmented. Thus, faster actuation method could be used to achieve higher output speed without causing the resonance.

3.7 Conclusion

A multistable nano-actuator was designed and analyzed. Mathematical model was constructed to support the design. Furthermore, the designed actuator is analyzed in FEM software. The FEM simulation results are in good agreement with the mathematical model. The actuator has 16 uniformly distributed output positions from 0nm to 150nm with a constant step of 10nm between two positions. As future work, this design will be first fabricated on silicon wafer and second experimentally evaluated.

The exploitation of flexible hinges has led to the possibility of monolithically integrate of stroke reducing structures, however, due to the weak stiffness of flexure hinges, the mobile part of the actuator should be supported. Therefore, friction will be introduced in. To reduce the friction effect,

the sapphire supported mobile part will be sliding on a flat surface coated with low coefficient of friction materials, e.g., Teflon.

4 Summary

In this chapter, a bistable micro-actuator with reducing structures was designed, fabricated and tested. Two kinds of reducing mechanisms were designed for the bistable micro-actuator. The experiment results proved the bistable micro-actuator with both two kinds of reducing structure was bistable. Both of two designs have a output stroke around 1 μm. The hybrid reducing design validated the theory that a single pre-shaped beam with reducing structure could also be bistable. Furthermore, the exploitation of flexible beam in the hybrid reducing design can largely reduce the dimensions of the reducing system.

Based on the design of bistable micro-actuator with hybrid reducing system, a multistable nano-actuator was designed and verified via simulation. The multistable nano-actuator has coupled four bistable modules, thus, the actuator has 16 output positions in total. Minimal output stroke could be as small as 10nm. By giving different reducing factor for each bistable modules, it can have several output combination strategies. The internal stress during switching was verified by simulation as well as the force output of a single bistable module. Modal analysis was also carried out to analyze the dynamic behavior. Furthermore, to reduce the influence caused by deflection under gravity, a supporting mechanism using through-holes filled by complete sphere beads was proposed and verified through simulation.

Chapter V

Conclusion and Perspectives

In this work, a bistable mechanism based on antagonistic pre-shaped double beams was proposed. Employing the proposed bistable mechanism, a quadristable micro-actuator was designed. In order to validate the quadristability of the device, a meso-scaled prototype was fabricated from MDF by laser cutting. After the quadristability was experimentally confirmed, a quadristable micro-actuator was realized on SOI wafer using DRIE technique. Strokes for inner row and outer row were reduced to 300 µm and 200 µm respectively. For the actuation of the quadristable micro-actuator, laser heated SMA elements with deposited SiO_2 layer were used to realize the optical wireless actuation. With the help of a laser beam steering micro-mirror, both inner row and outer row were successfully actuated. In order to further reduce the stroke, a bistable actuator with stroke reducing structure was designed and a prototype cut from MDF was tested. Bistability was validated and a stroke of 1 µm was experimentally achieved. Based on this bistable module, a multistable nano-actuator, which contains four parallel coupled bistable modules, was designed and simulated. The simulated results have indicated that it was capable of outputs 16 discrete stable positions available from 0 nm to 150 nm with a step of 10 nm between two stable positions.

First, literatures related to the buckled beams based bistable mechanisms were reviewed. The bistable buckled beams could be categorized into basic groups: pre-compressed beam, pre-stressed beam and pre-shaped beam. They have advantages as well as disadvantages when compared with each other. Pre-compressed bistable beam has symmetrical output force which leads to an identical stability for both stable positions. With given maximal output force and stroke, symmetrical output behavior could maximize the bistability and enhance the tolerance to disturbances and fabrication errors. For our scenario, the bistable actuator's basic task is forward and backward movement between two stable positions having the same priorities. Therefore, symmetrical output force is an attracting merit for our application. However, the pre-compressed bistable beam needs a pre-load operation, i.e., a compression, to obtain a buckled shape. In order to get the desired stroke, which depends on the rise of the mid-point of the beam, the pre-load compression needs to be carried out with the help of precise linear stage. This will largely increase the complexity of the system. Furthermore, stroke of pre-compressed bistable beam is very sensitive with the variation of compressed distance, which makes the pre-load operation difficult to control.

Pre-stressed bistable beam's principle is similar with pre-compressed bistable beam; the unique difference is that the pre-load operation is realized by the residual stress which is intentionally introduced in the fabrication process by the difference of thermal expansion ratio between two materials. The advantage of pre-stressed bistable beam is that no pre-load operation is required after fabrication. However, the amplitude of the residual stress is also difficult to control. Furthermore, if the fabricated bistable actuator's stroke is not as wanted, it is not possible to do an adjustment.

Pre-shaped bistable beam is the approach which needs no pre-load operation. The beam is fabricated with the designed shape without stress. Stroke is defined at the design step if the fabrication error is negligible. This characteristic makes it applicable for bulk fabrication. However, at least two parallel pre-shaped beams should be connected at the mid-points to get a bistable actuator. Moreover, there is geometrical limit for the pre-shaped beam, which makes the stroke of pre-shaped bistable beams bigger than the stroke of pre-compressed beam considering the same thickness for each of them. Finally, a set of two beams joined at their midpoints lead to asymmetrical output force.

Based on the research of literatures and analysis of different beams, a bistable mechanism based on antagonistic pre-shaped double beams was proposed. It has combined the advantages of both pre-compressed bistable beam and pre-shaped beam. As it is based on pre-shaped beam, the pre-load operation is largely simplified as compared to the process to pre-compressed beam. The pre-load direction is changed to the vertical direction instead of longitudinal direction. The stroke is very less

sensitive with the variation in vertical direction which means the tolerance for pre-load error is enhanced. Moreover, the pre-load operation for multistable actuator could be accomplished in one single action. Therefore, it is possible to fabricate and assemble rapidly and efficiently micro-actuators for smart surfaces application (2D array of micro-actuators). Furthermore, the utilization of two antagonistically configured pre-shaped beams makes the bistable mechanism capable to provide a symmetrical output force. At the same time, the geometrical limit for pre-shaped beam is lowered to the half value of parallel pre-shaped double beams, which has enabled the proposed bistable mechanism to have smaller stroke with same beam thickness.

On the basis of parallel pre-shaped double beams' mathematical model, the model for antagonistic pre-shaped double beams was constructed. Based on the model, a quadristable actuator was designed. It was the combination of two rows of bistable beams. One inner row was embedded into the outer row. This inner row acts as the central link. Each row has two stable positions, thus, the entire actuator has four stable positions. The designed quadristable actuator was simulated in FEM software ANSYS. The simulation confirmed the prediction from mathematical model. The bistable mechanism based on antagonistic pre-shaped double beams has symmetrical output force. The Force-Displacement curve of the output point from mathematical model and FEM simulation are coherent with each other. The difference between the two curves is relatively big around the force peak part. This difference is caused by the simplification in mathematical model which has only taken the first three buckling modes into account.

In order to experimentally validate the designed quadristable actuator, two rapid prototyping processes, 3D printing and laser cutting, were used to fabricate the meso-scaled actuator. The 3D printing technique was firstly employed. Unfortunately, the process of removing support material did damage to the thin pre-shaped beam. The bistability was lost. After all, a prototype was successfully realized using medium density fiberboard by laser cutting machine. Bistable beams with a minimal thickness of 250 µm were achieved.

An experimental setup was established to test the fabricated prototype of quadristable actuator. Firstly, a linear motor was used to switch the actuator between different positions. A small gold coated mirror was fixed onto the output point and optical fiber distance sensor was utilized to measure the position changes of the output point. The results indicated that both the inner row and outer row were bistable. The quadristability of the designed actuator was experimentally validated. Both inner row and outer row has a stroke around 970 ± 1 µm. After the validation of the quadristability, a wireless actuation for the inner row of the prototype was carried out with laser heated Shape Memory Alloy (SMA) elements. Two red laser diodes (P = 100 mW, λ = 660 nm) were used provide the heat source for two small SMA elements (0.1 × 1 × 3 mm). The inner row was successfully and wirelessly actuated, however, due to the load effect of SMA elements, the stroke (681 ± 1 µm) is smaller than when it is switched by linear motor (no load applied).

After the quadristability of the designed actuator was experimentally validated with a laser cut prototype, an optimized quadristable micro-actuator was fabricated on SOI wafer using micro-fabrication technique DRIE. Because the minimal stroke of the bistable mechanism depends on the thickness of beams, DRIE, which could produce much thinner beam, was employed to manufacture the bistable beams. Specifically, Bosch process was adopted to realize the fabrication, because it can produce true vertical side wall with high aspect ratio by alternatively repeating the etching and passivation processes. The high value elastic modulus of silicon material guaranteed the strength of thin beam. The crystal micro-structure led to the long life cycles. SOI wafer has protected the thin beam from breaking during etching process. According to the characteristics of the manufacturing process, some optimizations were done on the basis of designed quadristable

meso-actuator. First, the gap between supporting brackets was changed into a trapezoidal form, so that the two sides of the gap could be automatically aligned with their central line. Second, a small circular (1 mm diameter) structure was integrated to the central link of inner row, in order to install end effector or other necessary components (e.g., mirrors). Third, small releasing holes were done in the quadristable micro-actuator to accelerate the releasing process. After photo lithography, SiO_2 etching, silicon etching and releasing processes, a quadristable micro-actuator was fabricated. The thickness of the pre-shaped bistable beams was 25 µm. The strokes of inner row and outer row were 300 µm and 200 µm, respectively.

For the wireless actuation of the silicon quadristable micro-actuator, SMA elements with deposited SiO_2 layer were used as an artificial "two way" memory SMA, in order to eliminate the load effect. In this two way memory concept, SiO_2 layer was acting as the biasing spring for the SMA element. Due the bigger thermal expansion ratio, SMA material (Nitinol) shrinks more than SiO_2 layer when they were cooled down from high deposition temperature. Therefore, compressive stress was created in SiO_2 layer and this compressive stress has bent SMA element. When the SMA element was heated up, the shape memory effect tried to make recover the SMA to its straight form. As a consequence, curvature became smaller. Since one end of the SMA element was fixed, thus the other end did the work due to the load on it. When heating was stopped, temperature of SMA decreased, then, SMA element was re-bent by SiO_2 layer. A force sensor was used to quantitatively measure the displacement of the artificial "two way" memory SMA element and its corresponding output force. Firstly, the force sensor was calibrated using a lever and suspended precise weights. Then, a setup was established for the measurement. The measurements showed that 100 µm thick SMA with 8 µm thick SiO_2 layer were capable of 300 µm output displacement. The maximal output force (290 mN) appeared at the position when displacement was zero. The displacement of the SMA element is more than the half stroke of both inner row and outer row, thus, it is enough to switch the inner row and outer row. The necessary force of switching the silicon micro-actuator was less than 20 mN, therefore, the force generated by SMA element is also sufficient.

Wireless actuation of the fabricated silicon micro-actuator was realized in two different heating directions. First, the inner row of the quadristable micro-actuator, which could be considered as a bistable micro-actuator, was actuated by two SMA elements which were heated in horizontal direction. Two SMA elements with SiO_2 layer were fixed on two linear stages, so that their initial positions could be easily adjusted to make sure there was no contact between SMA elements and bistable beams during the cooling phase. In the optical system used to heat the SMA elements, an optical beam steering micro-micro was used to change the orientation of laser beam. With the help of another fixed small mirror, which was located behind the second SMA element, the two SMA elements were successfully actuated by the use of one single laser. Test results indicated that load effect could be completely eliminated using artificial "two way" memory SMA elements on the condition that the initial position of SMA elements were well adjusted. Due to the fact that when laser beam comes from the horizontal direction, most of the energy was transmitted to the SMA elements, the necessary heating duration is short (around 2 s).

For the wireless actuation of both inner row and outer row of the silicon quadristable micro-actuator, customized SMA support was designed for the inner row. SMA elements for inner row have to follow the movement of the inner row when it was actuated by the outer row. In order to simplify the structure, SMA elements for outer row were also installed on customized support. For the aim of detecting the output displacement using optical fiber distance sensor, a very light reflective surface, folded from aluminum foil, was glued on the central link of inner row. In the actuation for both inner row and outer row, four SMA elements, located along a line, have to be heated. If the laser comes in the horizontal direction like it was in the configuration of bistable micro-actuator, SMA elements for

inner row will be shadowed by the one for outer row. Thus, for the actuation of quadristable micro-actuator, the laser comes from the top of the actuator in the downward direction. Similarly with the setup for bistable micro-actuator, optical beam steering micro-mirror was integrated in the optical system, in order to irradiate four SMA elements with one single laser diode.

The measured movement data was acquired in Labview environment through NI acquisition card. The results have shown that both inner row and outer row were bistable, i.e., the micro-actuator is quadristable. The measured stroke of inner row was 267 ± 3µm (which was 9% smaller than the designed stroke) over 4000 cycles. For outer row, the measured stroke was 187 ± 2 µm (which was 4% smaller than designed stroke). Although the SMA elements with SiO_2 layer could eliminate the load effect, it is based on the condition that the relative initial position of SMA, with respect to bistable beam, is well adjusted without contact. However, when the SMA elements were installed on the support structure, it was difficult to adjust the initial position. Therefore, the stroke was still slightly influenced by the load effect coming from the SMA elements, but influence was much smaller than it was without SiO_2 layer. Due the precise fabrication, two antagonistic pre-shaped beams were more identical to each other. It has led to a more symmetrical output force than the one of the prototype which was fabricated by laser cutting machine on MDF. For the inner row, the total stroke was divided by the snap point into two parts which were 52% and 48% respectively. Due to the average effect, the outer row, which was composed by two pairs of antagonistic pre-shaped double beams, had a more symmetrical output behavior. The distances on two sides of the snap point were 51% and 49% of the total stroke, respectively.

After the successful test of silicon micro-actuator (bistable and quadristable), a bistable actuator with stroke reducing structure was designed. The bistable mechanism was also based on pre-shaped beam. One of the antagonistic pre-shaped beams in former design was replaced by a lever based reducing structure. The reducing structure contains two reducing levels. The first level had constrained the mid-point's rotation of pre-shaped beam. A meso-scaled prototype of the bistable actuator with reducing structure was fabricated by laser cutting machine on MDF. Both the initial stroke (stroke before reducing) and final stroke (stroke after reducing) were measured using optical fiber distance sensor. The actuator was bistable and the stroke was reduced from 2.4 mm to 1 µm.

In order to have multiple output strokes, a multistable nano-actuator was designed and simulated. It was composed by four bistable modules. Each bistable module was based on the design of bistable actuator with reducing structure. The output of four bistable modules were coupled in a parallel configuration by a flexure hinges connected levers based structure. The combined output had 16 discrete stable positions from 0 to 150 nm with step of 10 nm. A 3D model was constructed and simulated in ANSYS. The simulation results were coherent with the results from analytical model in Matlab. Since this design was expected to be fabricated on silicon material using micro-fabrication technique, a stress simulation was carried out with respect to the properties of silicon material to ensure that the compliant structure will not break during actuation. The simulated results indicated that the maximum stress was less than the elastic limit, which means the structure should be strong enough.

For perspectives, using the antagonistic pre-shaped double beams based bistable mechanism as elementary units, a concept of silicon wafer based smart surface for micro conveyance applications was proposed.

As shown in figure 5 - 1, via the micro fabrication techniques (e.g., DRIE), it is possible to fabricate very thin pre-shaped beams. Due the small value of beam thickness, which is the key parameter of bistable mechanism, the overall dimensions of a bistable module could be largely reduced. Thus, a big number of bistable modules could be directly fabricated on a single wafer. For the pre-load operation of antagonistic pre-shaped double beams, it is possible to fabricate two beams that the original shapes

are curved away from each other. Then, a buckle structure will be added on two beams. Using small gripper, two beams could be easily buckled together. Finally, two beams will act as a whole part and it will have the same output behavior as the antagonistic configuration.

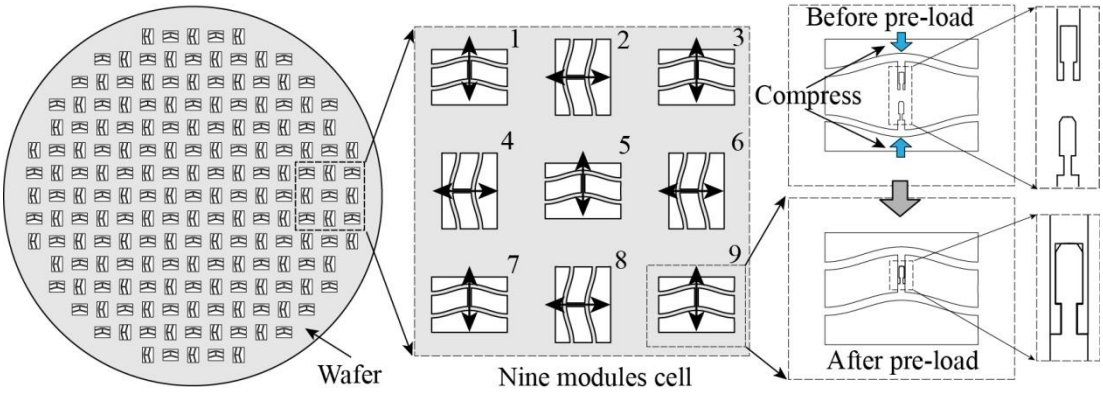

Figure 5 - 1. Wafer conveyance based on bistable actuator array (10cm wafer with 4x3mm bistable module).

As shown in figure 5 - 1, the output directions of elementary bistable units are configured in x- and y-direction with a certain pattern. If a conveyance plate is settled on top of the smart surface and dimensions of the plate cover at least four bistable modules at any time, it is possible to generate a 3-DOF (degree of freedom) movement by individually controlling these bistable modules. Figure 5 – 2 presents the control strategy of 3-DOF movements by using nine bistable modules. For the movement along x-axis, bistable modules 2, 4, 6 and 8 should move in the same direction together (figure 5 - 2a). Similarly for the movement along y-axis, modules 1, 3, 5 (not necessary), 7 and 9 should be actuated in the same direction (figure 5 - 2b). Besides the translation along x- and y-axis, a rotation degree of freedom with respect to z-axis can be generated by coupling the two translational movements (figure 5 - 2c). It is also possible to have the movement along diagonal direction by combining the movement along x- and y-axis.

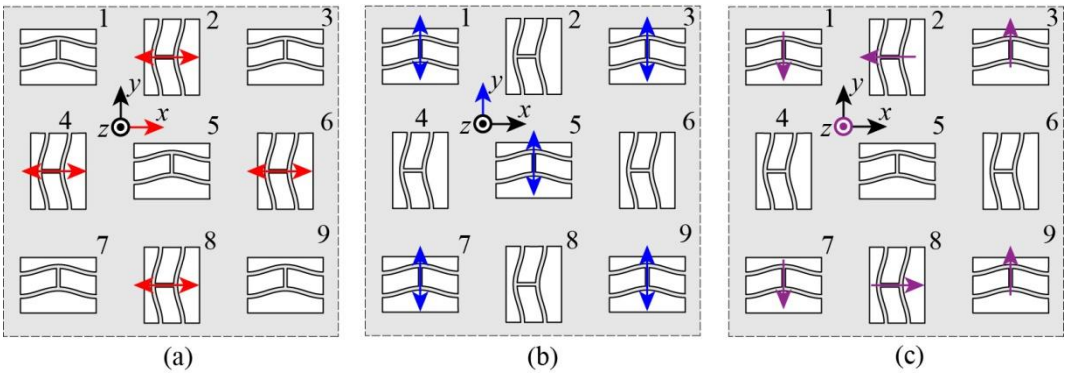

Figure 5 - 2. Control strategy of wafer conveyance: (a) Movement in x-axis; (b) Movement in y-axis; (c) Rotation with respect to z-axis.

Moreover, the silicon quadristable micro-actuator without reducing structure will be optimized to make the actuation of outer row easier. Then, smart surface based on the quadristable micro-actuator will be constructed. The smart surface based on quadristable micro-actuator could have different strokes for inner row and outer row. This characteristic will enable the smart surface to have the ability of big moving speed (using big stroke) and precise output (using small stroke) within one system.

For the aspect of actuator with reducing structure, the bistable one will be firstly fabricated using DRIE to verify the feasibility of the design on silicon material. Then, the multistable nano-actuator will be realized on silicon material and should provide a nano-scaled output. Furthermore, the

multistable nano-actuator could also be used to form a smart surface which should be able to realize more complex tasks.

Annex I: List of Publications

[1] X. Liu; F. Lamarque; E Doré; P Pouille, "Multistable wireless micro-actuator based on antagonistic pre-shaped double beams", *Smart Mater. Struct.*, vol.24, no.7, 075028 (7pp), June 2015.

[2] Xingxing LIU, Hani AL HAJJAR, Frédéric LAMARQUE, Emmanuel DORE, Olivier CARTON, Andreas ZEINERT and Stéphane CHARVET, "An Optical Wireless Bistable Micro-actuator", IEEE *ICMA 2015*, August 2 to August 5, 2015, Beijing, China.

[3] Xingxing Liu; Lamarque, F.; Dore, E.; Prelle, C., "Design and simulation of a multistable nano-actuator," *Mecatronics (MECATRONICS), 2014 10th France-Japan/ 8th Europe-Asia Congress on* , vol., no., pp.313,318, 27-29 Nov. 2014.

[4] Liu X., Lamarque F., Doré E., Petit L., Pouille P., Duhamel Y., "A bistable micro-actuator with stroke reducing structure," *Proceedings of the ASME 2014 12th Biennial Conference on Engineering Systems Design and Analysis (ESDA2014)*, June 25-27, 2014, Copenhagen, Denmark.

Bibliography

[ABDE 11] Abdelnour K, Stinchcombe A, Porfiri M, Zhang J and Childress S, 2011, "Wireless powering of ionic polymer metal composites toward hovering micro swimmers", *IEEE/ASME Trans. Mechatronics*, 17 924–35.

[ABOU 14] Jacob Aboudi, Xiaojing Zheng, Ke Jin, "Micromechanics of magnetostrictive composites", *International Journal of Engineering Science*, Volume 81, August 2014, Pages 82-99, ISSN 0020-7225.

[ALI 10] Ali M S M and Takahata K, 2010, "Frequency-controlled wireless shape memory alloy microactuators integrated using and electroplating bonding process", *Sensors Actuators A* 163 363–72.

[ALI 11] Ali M S M and Takahata K, 2011, "Wireless microfluidic control with integrated shape-memory-alloy actuators operated by field frequency modulation", *J. Micromech. Microeng*. 21 075005.

[ANDO 12] B. Andò, S. Baglio, M. Baù, A.R. Bulsara, V. Ferrari, M. Ferrari, G. L'Episcopo, "A Nonlinear Energy Harvester by Direct Printing Technology", *Procedia Engineering*, Volume 47, 2012, Pages 933-936, ISSN 1877-7058.

[ANDO 14] B. Andò, S. Baglio, A.R. Bulsara, V. Marletta, A bistable buckled beam based approach for vibrational energy harvesting, Sensors and Actuators A: Physical, Volume 211, 1 May 2014, Pages 153-161, ISSN 0924-4247.

[BAGL 02] S. Baglio, S. Castorina, L. Fortuna, N. Savalli, "Modeling and design of novel photo-thermo-mechanical microactuators", *Sensors and Actuators A: Physical*, Volume 101, Issues 1–2, 30 September 2002, Pages 185-193, ISSN 0924-4247.

[BART 12] Barth, J.; Megnin, C.; Kohl, M., "A Bistable Shape Memory Alloy Microvalve With Magnetostatic Latches", *Journal of Microelectromechanical Systems*, vol.21, no.1, pp.76,84, Feb. 2012.

[BAXE 12] T Baxevanis, Y Chemisky and D C Lagoudas, 2012, "Finite element analysis of the plane strain crack-tip mechanical fields in pseudoelastic shape memory alloys", *Smart Mater. Struct.*, 21094012 (10pp).

[BOEI 08] Jeroen de Boeij, Lomonova, E., Duarte, Jorge, "Contactless Planar Actuator with Manipulator: a Motion System without Cables and Physical Contact between the Mover and the Fixed World", *Industry Applications Society Annual Meeting*, 2008. IAS '08. IEEE , vol., no., pp.1,8, 5-9 Oct. 2008.

[BOHR 94a] K.-F. Böhringer, B. R. Donald, R. Mihailovich, and N. C. MacDonald, "A Theory of Manipulation and Control for Microfabricated Actuator Arrays", *Proc. IEEE Workshop on Micro Electro Mechanical Systems* (MEMS), Oiso, Japan (January 1994).

[BOHR 94b] K.-F. Böhringer, B. R. Donald, R. Mihailovich, and N. C. MacDonald, "Sensorless Manipulation Using Massively Parallel Microfabricated Actuator Arrays", *Proc. IEEE International Conference on Robotics and Automation* (ICRA), San Diego, California (May 1994). Nominated for Best Conference Paper Award.

[BOHR 96] K.-F. Böhringer, B. R. Donald, and N. C. MacDonald, "Single-Crystal Silicon Actuator Arrays for Micro Manipulation Tasks", *IEEE Workshop on Micro*

Electro Mechanical Systems (MEMS), San Diego, California (February 1996).

[BRAG 11] F. Braghin, S. Cinquemani, F. Resta, "A model of magnetostrictive actuators for active vibration control", *Sensors and Actuators A: Physical*, Volume 165, Issue 2, February 2011, Pages 342-350, ISSN 0924-4247.

[BREN 49] Abner Brenner and Seymour Senderoff, "Calculation of stress in electrodeposits from the curvature of a plated strip", *Part of the Journal of Research of the National Bureau of Standards*, Volume 42, February 1949.

[BYUN 11] Donghak Byun, Jongho Choi, Kyoungrae Cha, Jong-oh Park, Sukho Park, "Swimming microrobot actuated by two pairs of Helmholtz coils system", *Mechatronics*, Volume 21, Issue 1, February 2011, Pages 357-364, ISSN 0957-4158.

[CART 10] R. Carta, J. Thoné, R. Puers, "A wireless power supply system for robotic capsular endoscopes", *Sensors and Actuators A: Physical*, Volume 162, Issue 2, August 2010, Pages 177-183, ISSN 0924-4247.

[CARV 10] Carvalho Pde T, Silva IS, Reis FA, Perreira DM and Aydos RD, 2010, "Influence of ingaalp laser (660nm) on the healing of skin wounds in diabetic rats", *ACTA CIRURGICA BRASILEIRA*, vol. 25, pp. 71-79, January.

[CHAL 11] Chalvet, V., Zarzycki, A., Haddab, Yassine; Lutz, P., "Digital microrobotics based on bistable modules: Design of a non-redundant digital micropositioning robot", *IEEE International Conference on Robotics and Automation* (ICRA), vol., no., pp.3628,3633, 9-13 May 2011.

[CHAL 13] Chalvet, V., Haddab, Y., Lutz, P., "A Microfabricated Planar Digital Microrobot for Precise Positioning Based on Bistable Modules", *IEEE Transactions on Robotics*, vol.29, no.3, pp.641, 649, June 2013.

[CHEN 08] Qiao Chen; Haddab, Yassine; Lutz, P., "Digital Microrobotics Based on Bistable Modules: Design of Compliant Bistable Structures", *IEEE/ASME International Conference on Mechtronic and Embedded Systems and Applications*, MESA 2008., vol., no., pp.36,41, 12-15 Oct. 2008.

[CHEN 09a] Chen G., Wilcox D.L., Howell L.L., "Fully compliant double tensural tristable micromechanisms (DTTM)", *J. Micromech. Microeng.*, 19(2), 025011, 2009.

[CHEN 09b] Chen Guimin, Aten Quentin T., Zirbel Shannon, et al. "A Tristable Mechanism Configuration Employing Orthogonal Compliant Mechanisms", *J. Mechanisms Robotics* 2, 014501 (2009) (6 pages).

[CHEN 10] Chen G., Gou Y. and Yang L. 2010 "Research on Multistable Compliant Mechanisms: The State of the Art", *Proceedings of the 9th International Conference on Frontiers of Design and Manufacturing*, July 17~19, 2010, Changsha, China.

[CHEN 11] Chen Guimin, Gou Yanjie, Zhang Aimei. "Synthesis of Compliant Multistable Mechanisms Through Use of a Single Bistable Mechanism", *J. Mech*. Des. 133, 081007 (2011) (9 pages).

[CHEN 15] Jinglong Chen, Chunlin Zhang, Minglong Xu, Yanyang Zi, Xinong Zhang, "Rhombic micro-displacement amplifier for piezoelectric actuator and its linear and hybrid model", *Mechanical Systems and Signal Processing*, Volumes 50–51, January 2015, Pages 580-593, ISSN 0888-3270.

[CHEN 98] K-S Chen et al, "Silicon strength testing for mesoscale structural applications", *MRS Spring Meeting Symposium*, *MRS Symposium Proceeding* Vol. 518, pp.

123-130, 1998.

[CHER 08] Cherry, B.B., Howell, L.L., Jensen, B.D., "Evaluating three dimensional effects on the behavior of compliant bistable micromechanisms", *J. Micromech. Microeng.*, 18(9), 095001, 2008.

[DAVI 14] Edward Davies, David S. George, Malcolm C. Gower, Andrew S. Holmes, "MEMS Fabry–Pérot optical accelerometer employing mechanical amplification via a V-beam structure", *Sensors and Actuators A: Physical*, Volume 215, 15 August 2014, Pages 22-29, ISSN 0924-4247.

[DELE 11] Anne Delettre, Guillaume J. Laurent and Nadine Le Fort-Piat, "2-DOF Contactless Distributed Manipulation Using Superposition of Induced Air Flows", *IEEE/RSJ International Conference on Intelligent Robots and Systems*, IROS'11., Sep 2011, San Francisco, CA., United States.

[DUER 90] Duerig T, Melton K, Stöckel D and Wayman C (ed) 1990, "Engineering Aspects of Shape Memory Alloys", (London: Butterworth–Heinemann).

[ELLI 10] Elliott, G., Raabe, S., Covic, G.A., Boys, J.T., "Multiphase Pickups for Large Lateral Tolerance Contactless Power-Transfer Systems", *IEEE Transactions on Industrial Electronics*, vol.57, no.5, pp.1590,1598, May 2010.

[EMIR 14] Vela Emir, Hafez Moustapha and Régnier Stéphane, "Contactless automated manipulation of mesoscale objects using opto-fluidic actuation and visual servoing", *Review of Scientific Instruments*, 85, 055107 (2014).

[FUKU 04] Y Fukuta, M Yanada, A Ino, Y Mita, YA Chapuis, S Konishi, H Fujita, "Conveyor for pneumatic two-dimensional manipulation realized by arrayed MEMS and its control", *Journal of Robotics and Mechatronics* 16, 163-170, 2004.

[FUKU 06] Yamato Fukuta, Yves-André Chapuis, Yoshio Mita, and Hiroyuki Fujita, "Design, Fabrication, and Control of MEMS-Based Actuator Arrays for Air-Flow Distributed Micromanipulation", *Journal of Micro Electro Mechanical Systems*, vol. 15, NO. 4, August 2006.

[FUNA 87] Funakubo H (ed) 1987 "Shape Memory Alloys", (London: Gordon and Breach)

[HABI 12] Amirali Habibi, Eugen Dedu, Julien Bourgeois, Guillaume J. Laurent, Nadine Le Fort-Piat. "Distributed Pneumatic MEMS for Fast Conveyance of Fragile Objects", JRWRTC'12, 6th Junior Researcher Workshop on Real-Time Computing, joint to RNTS'12, the Int. Conf. on Real-Time and Network Systems, Jan 2012, France. pp.33 - 36, 2012.

[HOWE 01] Howell L.L., "Compliant Mechanisms", Wiley, New York, 2001.

[HUAN 02] Huang W, 2002 "On the selection of shape memory alloys for actuators Mater.", Des. 23 11–9.

[HYUN 14] Choi, Hyunchul, Jeong, Semi, Lee, Cheong, Go, Gwangjun, Kwon, Kiduk, Ko, Seong Young, Park, Jong-Oh, Park, Sukho, "Biomimetic swimming tadpole microrobot using 3-pairs Helmholtz coils", 2014 *5th IEEE RAS & EMBS International Conference on Biomedical Robotics and Biomechatronics*, vol., no., pp.841,844, 12-15 Aug. 2014.

[IMBO 14] Imboden, M., Morrison, J., Lowell, E., Han, H., Bishop, D.J., "Controlling Levitation and Enhancing Displacement in Electrostatic Comb Drives of MEMS Actuators," Journal of Microelectromechanical Systems, vol.23, no.5, pp.1063,1072, Oct. 2014.

[JANS 06] Michael Jansen, Brad D. Cantos, Glen P. Carey, Rene Dato, Giorgio Giaretta, Sascha Hallstein and William R. Hitchens, 2006, "Visible laser and laser array sources for displays" *Proc. SPIE 6135*, 61350T, January.

[JENS 03] Jensen B.D., Howell L.L., "Identification of compliant pseudo-rigid-body mechanism configurations resulting in bistable behavior", *Trans. ASME, J. Mech. Design*, 125, 701-708, 2003

[JENS 99] Jensen B.D., Howell L.L., Salmon L.G., "Design of two-link, in-plane, bistable compliant micro-mechanisms", *Trans. ASME, J. Mech. Design*, 121(3), 416-423, 1999

[JEON 07] Jong Up Jeon, Kyu-Yeol Park, Toshiro Higuchi, "Contactless suspension and transportation of glass panels by electrostatic forces", *Sensors and Actuators A: Physical*, Volume 134, Issue 2, 15 March 2007, Pages 565-574, ISSN 0924-4247.

[JEON 99] Jong Up Jeon, Shao Jü Woo, Toshiro Higuchi, "Variable-capacitance motors with electrostatic suspension", *Sensors and Actuators A: Physical*, Volume 75, Issue 3, 8 June 1999, Pages 289-297, ISSN 0924-4247.

[JOUL 47] Joule, J.P. (1847). "On the Effects of Magnetism upon the Dimensions of Iron and Steel Bars". *The London, Edinburgh and Dublin philosophical magazine and journal of science* (Taylor & Francis).

[KARU 10] S. Karunanidhi, M. Singaperumal, "Design, analysis and simulation of magnetostrictive actuator and its application to high dynamic servo valve", *Sensors and Actuators A: Physical*, Volume 157, Issue 2, February 2010, Pages 185-197, ISSN 0924-4247.

[KHAN 12] Khan, M.U., Bencheikh, N., Prelle, C., Lamarque, F., Beutel, T., Buttgenbach, S., "A Long Stroke Electromagnetic XY Positioning Stage for Micro Applications," *IEEE/ASME Transactions on Mechatronics*, vol.17, no.5, pp.866,875, Oct. 2012.

[KHAN 14] Khan, Muneeb Ullah, "Contribution to the design and fabrication of an integrated micro-positioning system", thesis in Université de Technologie de Compiègne, 2014, 2014COMP1671, pp 135-137.

[LAGO 08] Lagoudas D C (ed) 2008 "Shape Memory Alloys: Modeling and Engineering Applications", (New York: Springer)

[LASZ 10] Karolina Laszczyk, Sylwester Bargiel, Christophe Gorecki, Jerzy Krężel, Piotr Dziuban, Małgorzata Kujawińska, Damien Callet, Sven Frank, "A two directional electrostatic comb-drive X–Y micro-stage for MOEMS applications", *Sensors and Actuators A: Physical*, Volume 163, Issue 1, September 2010, Pages 255-265, ISSN 0924-4247.

[LEE 10] Lee J S, Gutta S, Yim W and Kim K J, 2010, "Preliminary study of wireless actuation and control of IPMC actuator", *Proc. IEEE/ASME Int. Conf. on Adv. Intelligent Mech.* (Montréal, 6–9 July) pp 157–62.

[LIU 00] LIU Wei, "Computer aided calculation of angle stiffness of single axis flexible hinge", *Optics and Precision Engineering*, vol. 02, 2000.

[LUKE 10] Luke J. Currano, Miao Yu, Balakumar Balachandran, "Latching in a MEMS shock sensor: Modeling and experiments", *Sensors and Actuators A: Physical*, Volume 159, Issue 1, April 2010, Pages 41-50, ISSN 0924-4247.

[MAO 10] Shengping Mao, Hong Wang, Yibo Wu, Jun Tang, Guifu Ding, "A latching

bistable microswitch using dual-beam electrothermal actuation", *2010 5th IEEE International Conference on Nano/Micro Engineered and Molecular Systems (NEMS)*, , vol., no., pp.732,735, 20-23 Jan. 2010.

[MAST 03] Masters N.D., Howell L.L., "A self-retracting fully compliant bistable micromechanism", *J. Microelectromech. Syst.*, 12, 273-280, 2003

[MATI 10] Laëtitia Matignon, Guillaume J. Laurent, Nadine Le Fort - Piat, Yves-André Chapuis. "Designing Decentralized controllers for distributed-air-jet MEMS-based micromanipulators by reinforcement learning". *Journal of Intelligent & Robotic Systems*, 2010, 59 (2), pp.145-166.

[MIAZ 00] K. Miazato, D. F. de Sousa, A. Delben, J. R. Delben, S. L. de Oliveira and L. A. O. Nunes 2000 "Up conversion mechanisms in Tm3+ doped lead fluoroindogallate glasses", *Journal of Non-Crystaline Solids*, vol. 273, issues 1-3, pp. 246-251, August.

[MOBE 12] Sebastian Möbes, Benoît Piranda, Guillaume J. Laurent, Julien Bourgeois, Cédric Clévy, et al.. "Toward a 2D Modular and Self-Reconfigurable Robot for Conveying Microparts", *2nd Workshop on Design, Control and Software implementation for distributed MEMS*, dMEMS'12, Apr 2012, Besançon, France.

[MORA 08] Artur Moradewicz, Marian P. Kaźmierkowski, "Resonant converter based contactless power supply for robots and manipulators", *Journal of Automation, Mobile Robotics & Intelligent Systems*, vol 2, N° 3, 2008.

[MORA 10] Moradewicz, A.J., Kazmierkowski, M.P., "Contactless Energy Transfer System With FPGA-Controlled Resonant Converter", *IEEE Transactions on Industrial Electronics*, vol.57, no.9, pp.3181,3190, Sept. 2010.

[NI 14] Yuan Ni, Zongquan Deng, Xiang Wu, Junbao Li, Long Li, "Modeling and analysis of an over-constrained flexure-based compliant mechanism", *Measurement*, Volume 50, April 2014, Pages 270-278, ISSN 0263-2241.

[OTSU 99] Otsuka K and Wayman C M (ed) 1999, "Shape Memory Materials" (Cambridge: Cambridge University Press)

[OWEN 06] Owen, R.B., Maggiore, M., Apkarian, J., "A high-precision, magnetically levitated positioning stage: toward contactless actuation for industrial manufacturing", *IEEE Control Systems*, vol.26, no.3, pp.82,95, June 2006.

[PANE 07] I.Z. Pane and T. Asano, 2007, "Fabrication of bistable pre-stressed curved-beam," *Proc. of 20th International Conference on Microprocesses and Nanotechnology*, pp. 390-391, November, 2007, Kyoto, Japan.

[PANE 08] I.Z. Pane and T. Asano, 2008, "Investigation on bistability and fabrication of bistable prestressed curved beam" *Japanese journal of Applied Physics*, vol. 47, pp. 5291-5296, 2008.

[PANE 09] I.Z. Pane and T. Asano, 2009, "Analysis and fabrication of ampere-force actuated bistable curved beam", *Japanese Journal of Applied Physics*, vol. 48, pp. 06FK08:1-06FK08:4, 2009.

[PAPA 07a] Papastergiou, K.D.; Macpherson, D.E., "An Airborne Radar Power Supply With Contactless Transfer of Energy—Part I: Rotating Transformer", *IEEE Transactions on Industrial Electronics*, vol.54, no.5, pp.2874,2884, Oct. 2007.

[PAPA 07b] Papastergiou, K.D., Macpherson, D., "An Airborne Radar Power Supply With Contactless Transfer of Energy—Part II: Converter Design", *IEEE*

Transactions on Industrial Electronics, vol.54, no.5, pp.2885,2893, Oct. 2007.

[PEND 07] Pendleton T.M., Jensen B.D., "Development of a tristable compliant mechanism", *Proc. 12TH IFToMM World Congress*, A835, 2007.

[PERK 75] Perkins J (ed) 1975, "Shape Memory Effects in Alloys" (New York: Plenum).

[PETI 14] Petit, L., Hassine, A, Terrien, J., Lamarque, F., Prelle, C., "Development of a Control Module for a Digital Electromagnetic Actuators Array", *IEEE Transactions on Industrial Electronics*, vol.61, no.9, pp.4788,4796, Sept. 2014.

[PHAM 11a] Huy-Tuan Pham, Dung-An Wang, "A quadristable compliant mechanism with a bistable structure embedded in a surrounding beam structure", *Sensors and Actuators A: Physical*, Volume 167, Issue 2, June 2011, Pages 438-448, ISSN 0924-4247.

[PHAM 11b] Huy-Tuan Pham, Dung-An Wang, "A constant-force bistable mechanism for force regulation and overload protection", *Mechanism and Machine Theory*, Volume 46, Issue 7, July 2011, Pages 899-909, ISSN 0094-114X.

[PREL 06] Prelle C, Lamarque F and Revel P, 2006, "Reflective optical sensor for long-range and high-resolution displacements", *Sensors Actuators A* 127 139–46.

[QIN 07] QIN Yu, FENG Zhi-jing, "Simulation and Experiment of Nano-positioning Compliant Mechanism for Motion Reduction", *Nanotechnology and Precision Engineering*, vol. 5, No. 1, Mar, 2007.

[QIU 01] Qiu, J., Lang, J.H., Slocum, AH., "A centrally-clamped parallel-beam bistable MEMS mechanism", *The 14th IEEE International Conference on Micro Electro Mechanical Systems*, 2001. MEMS 2001., vol., no., pp.353,356, 25-25 Jan. 2001.

[QIU 04] JIN Qiu, J.H. Lang, and A.H. Slocum, 2004, "A curved-beam bistable mechanism", *Journal of Micro electro mechanical Systems*, vol. 13, pp. 137-145, 2004.

[SAM 06] Han Jeong Sam, Müller Claas, Wallrabe Ulrike, et al., "Design, Simulation, and Fabrication of a Quadstable Monolithic Mechanism With X- and Y-Directional Bistable Curved Beams", *J. Mech.* Des. 129, 1198-1203 (2006) (6 pages).

[STRA 12] Stranczl, M., Sarajlic, E., Fujita, H., Gijs, M.A.M., Yamahata, C., "High-Angular-Range Electrostatic Rotary Stepper Micromotors Fabricated With SOI Technology", *Journal of Microelectromechanical Systems*, vol.21, no.3, pp.605,620, June 2012.

[SYMS 03] Syms, R.R.A, Zou, H., Stagg, J., Moore, D.F., "Multistate latching MEMS variable optical attenuator", *IEEE Photonics Technology Letters*, vol.16, no.1, pp.191,193, Jan. 2004.

[SYMS 05] Syms, R.R.A, Zou, H., Boyle, P., "Mechanical stability of a latching MEMS variable optical attenuator", *Journal of Microelectromechanical Systems*, vol.14, no.3, pp.529,538, June 2005.

[TAI 11] Tai N T and Ahn K K, 2011, "Adaptive proportional–integral–derivative tuning sliding mode control for a shape memory alloy actuator", *Smart Mater. Struct.* 20 055010

[TALB 06] A. TALBI, O. Ducloux, N. Tiercelin , Y. Deblock, P. Pernod, V. Preobrazhensky, "Vibrotactile using micromachined electromagnetic actuators

Array", *Journal of Physics*, Conference Series 34 (2006) 637–642.

[TANG 14] Tang, H.; Li, Y., "A New Flexure-Based Yθ Nanomanipulator With Nanometer-Scale Resolution and Millimeter-Scale Workspace", *IEEE/ASME Transactions on Mechatronics*, vol.PP, no.99, pp.1,11, june, 2015.

[TIAN 10] Y. Tian, B. Shirinzadeh, D. Zhang, Y. Zhong, "Three flexure hinges for compliant mechanism designs based on dimensionless graph analysis", *Precision Engineering*, Volume 34, Issue 1, January 2010, Pages 92-100, ISSN 0141-6359.

[TIMO 61] Timoshenko, S. P., and Gere, J. M. 1961 "Theory of Elastic Stability", 2nd ed., McGraw-Hill, New York.

[UMIT 08] Sönmez Ümit, Tutum Cem C., "A Compliant Bistable Mechanism Design Incorporating Elastica Buckling Beam Theory and Pseudo-Rigid-Body Model", *J. Mech.*, Des. 130, 042304 (2008) (14 pages).

[UNAM 13] Unamuno, A; Blue, R., Uttamchandani, D., "Modeling and Characterization of a Vernier Latching MEMS Variable Optical Attenuator", *Journal of Microelectromechanical Systems*, vol.22, no.5, pp.1229,1241, Oct. 2013.

[UNAM 06] Unamuno, A, Uttamchandani, D., "MEMS variable optical attenuator with vernier latching mechanism", *IEEE Photonics Technology Letters*, vol.18, no.1, pp.88,90, Jan. 1, 2006.

[WANG 09] Dung-An Wang, Huy-Tuan Pham, Yi-Han Hsieh, "Dynamical switching of an electromagnetically driven compliant bistable mechanism", *Sensors and Actuators A: Physical*, Volume 149, Issue 1, 15 January 2009, Pages 143-151, ISSN 0924-4247.

[WANG 13] Dung-An Wang, Jyun-Hua Chen, Huy-Tuan Pham, "A tristable compliant micromechanism with two serially connected bistable mechanisms", *Mechanism and Machine Theory*, Volume 71, January 2014, Pages 27-39, ISSN 0094-114X.

[WIKI 14] Wikipedia, "Compliant mechanism", http://en.wikipedia.org/wiki/Compliant_ mechanism

[WILC 05] Wilcox D.L., Howell L.L., "Fully compliant tensural bistable micromechanisms (FTBM)", *J. Microelectromech. Syst.*, 14(6), 1223-1235, 2005

[XU 10] Qingsong Xu, Yangmin Li, "Analytical modeling, optimization and testing of a compound bridge-type compliant displacement amplifier", *Mechanism and Machine Theory*, Volume 46, Issue 2, February 2011, Pages 183-200, ISSN 0094-114X, http://dx.doi.org/10.1016/j.mechmachtheory.2010.09.007.

[XU 11] Xu Yang, Chen Meng, Pang Qingsheng, Chang Liang, Bai Zhenao, Ai Qingkang and Li Gang, 2011, "The Research of Red Beam Generation By Frequency-Doubling of a Nd-YAG Laser", *International Coriference on Electronics and Optoelectronics* (ICEOE 2011), Jul, 2011, Harbin.

[XU 14] Qingsong Xu, "Design and Smooth Position/Force Switching Control of a Miniature Gripper for Automated Microhandling", *IEEE Transactions on Industrial Informatics*, vol.10, no.2, pp.1023,1032, May 2014.

[ZAID 10] Sajid Zaidi, Frédéric Lamarque, Christine Prelle, Björn Hoxhold, Emmanuel Doré, Philippe Pouille and Stephanus Büttgenbach, 2010, "Bistable Curved-Beam Actuated by Optically Controlled Shape Memory Alloy", *IEEE/ASME International Conference on Advanced Intelligent Mechatronics*,

Montréal, Canada, July 6-9, 2010.

[ZAID 11a] Zaidi S., Lamarque, F., Prelle, C., Dore, E., "Dynamic characterization of remotely triggered digital actuator", 2011 *IEEE International Conference on Mechatronics* (ICM), vol., no., pp.678,683, 13-15 April 2011.

[ZAID 11b] Zaidi S, Lamarque F, Favergeon J, Carton O and Prelle C, 2011, "Wavelength selective shape memory alloy for wireless micro-actuation of a bistable curved-beam", *IEEE Transactions on Industrial Electronics*, Vol 58, n°12, pp.5288-5295, (Dec 2011).

[ZAID 11c] Sajid ZAIDI, "Contactless Energy Transfer and Control Strategy for a Bistable Micro-Actuator", Thesis of PhD degree, in University of Technology of Compiegne, 10th of June, 2011.

[ZAID 12] S Zaidi1, F Lamarque, C Prelle, O Carton and A Zeinert, 2012, "Contactless and selective energy transfer to a bistable micro-actuator using laser heated shape memory alloy", *Smart Mater. Struct.*, 21 (2012) 115027

[ZHU 14] Yuchuan Zhu, Liang Ji, "Theoretical and experimental investigations of the temperature and thermal deformation of a giant magnetostrictive actuator", *Sensors and Actuators A: Physical*, Volume 218, 1 October 2014, Pages 167-178, ISSN 0924-4247.

[ZOLT 12] Zoltan Szabo, Eniko T. Enikov, "Development of Wearable Micro-Actuator Array for 3-D Virtual Tactile Displays", *Journal of Electromagnetic Analysis and Applications*, 2012, 4, 219-229.